# APPLICATIONS OF LUMINESCENT SOLAR CONCENTRATORS

QUINN DAIGLE

A THESIS SUBMITTED TO
THE FACULTY OF GRADUATE STUDIES
IN PARTIAL FULFILLMENT OF THE REQUIREMENTS
FOR THE DEGREE OF
MASTER OF APPLIED SCIENCE

GRADUATE PROGRAM IN MECHANICAL ENGINEERING
YORK UNIVERSITY
TORONTO, ONTARIO.

JULY 2020

# Abstract

Luminescent solar concentrators (LSCs) are a promising technology because they are inexpensive, lightweight, aesthetically versatile, and offer wavelength-selective transparency. This thesis investigates the use of LSCs for building energy applications, with emphasis on thermal energy utilization. A spectral modeling method is developed to analyze the benefits of integrating LSCs into greenhouse rooftops, solar thermal collectors, and solar air heaters. Results show red LSCs can increase greenhouse profits by up to 40%. Furthermore, a novel experimental method wherein Newton's law of cooling is used to determine the thermal energy generated by LSCs is demonstrated. The thermal energy generated by LSCs can be used to substantially reduce building energy consumption. By integrating LSCs into solar thermal collectors the temperature of the collector fluid can be increased from ~140°C to over 200°C. Despite these advances, the efficiency of LSCs must be improved to realize their full potential and make widespread commercialization viable.

## Acknowledgments

Thank you to my Supervisor, Prof. O'Brien for providing guidance and feedback through this project. Thank you to my Co-Supervisor, Dr. Ijaz Rauf for his help and support. Thank you to Peter Fung for his help in the lab during his time as a lab assistant. An additional thank you to Joecy Peters for her support and encouragement throughout this process.

# Table of Contents

# List of Tables

# List of Figures

# List of Acronyms

BGR – blue green red

BY– blue yellow

BYO – blue yellow orange

BYR – blue yellow red

InGaAs – Indium Gallium arsenide

LSC – luminescent solar concentrator

MP – melting point

NIR – near-infrared radiation

PMMA – (Acrylic) polymethyl methacrylate

PPFD – photosynthetic photon flux density

PV- photovoltaic

QD- quantum dots

QY – quantum yield

RGB – red green blue

RYB – red yellow blue

SAH – solar air heater

SR – spectral response

TIR – total internal reflection

UV – ultraviolet

MMA - methyl methacrylate

AIBN – azobisisobutyronitrile

# List of Symbols

$\beta$ – tilt angle of the collector

$\varepsilon_g$ – emittance of the cover

$\varepsilon_p$ – emittance of the plate

$\sigma$ – radiation heat loss coefficient

$A_c(\lambda)$ – absorbance of the clear acrylic sheet

$A_c$ – collector area

$A_{dye}(\lambda)$ – amount of light absorbed by the dye within an acrylic sheet

$A_f(\lambda)$ – absorbance of a fluorescent acrylic sheet

$A_{frame}$ – area of panel framing

$A_{roof}$ – area of roof

C – simplified parameter representing numerical equation given by $520(1-0.000051\beta^2)$ for $0° < \beta < 70$

ΔP – the ratio between the power measured from the PV cell before vs after being attached to the LSC waveguide

E – light emissions from the LSC

e – simplified parameter representing numerical equation give by $0.430(1-100/T_{pm})$

f – simplified parameter representing numerical equation given by $(1+0.089h_{air} – 0.1166 h_{air}\varepsilon_p)(1+0.07866*N)$

$h_{air}$ –wind heat transfer coefficient ($W/m^2$ °C)

$I(\lambda)$ – incident light intensity

$I_{cell}$ –current measured from the PV cell prior to attaching to the LSC waveguide

$I_{LSC}$ – current measured from the PV cell after being attached to the LSC waveguide

$I_{sc}$ – short circuit current

k – thermal conductance coefficient

L – length

$L_c$ – length of frame columns

$L_{panel}$ – length of panel

$L_r$ – length of frame rows

N – number of glass covers

$N_p$ – number of panels

$\eta_{dye\text{-}Optical}$ – the efficiency with which light power absorbed by the dye is subsequently reemitted and incident onto the edges, or sidewalls, of the fluorescent LSC sheets

$\eta_{host}$ – host efficiency

$\eta_{host\text{-}edge}$ – the efficiency with which heat absorbed by the acrylic sheets is conducted to its sidewalls

$\eta_{EQE}(\lambda)$ – external quantum efficiency

$\eta_{QY}$ – quantum yield efficiency

$\eta_{Self}$ – self absorption efficiency

$\eta_{Stokes}$ – Stokes shift efficiency

$\eta_{abs}$ – dye absorption efficiency

$\eta_{opt}$ – optical efficiency

P – power

$P_{Cell}$ – power observed from the PV cell before being attached the LSC waveguide

$P_{dye}$ – radiant power absorbed the dye within an acrylic sheet

$P_{dye\text{-}internal\_loss}$ - portion of the radiant energy absorbed by the dye ($P_{dye}$) that is converted to thermal energy within the acrylic sheet due to non-unity quantum yield, Stokes shift, and absorption of reemitted photons in the acrylic sheet

$P_{dye\text{-}Optical}$ – radiant power absorbed by the dye that is reemitted to the edge of the acrylic sheet

$P_{edge(host)}$ – total thermal power provided by the frame of the clear (host) module

$P_{edge(LSC)}$ – total thermal power provided by the frame of the LSC module

$P_{host}$ – total thermal power generated in the acrylic host when subjected to illumination

$P_{host(abs)}$ – radiant power absorbed by the acrylic host, through absorption of incident and emitted photons, non-unity quantum yield and Stokes shift.

Pl – perimeter

$P_{LSC}$ – power observed from the PV cell after being attached the LSC waveguide

$P_{TIR}$ – probability of TIR

$Q_D$ – heat loss through ducting

QE – quantum efficiency

$Q_{fin}$ – heat loss through LSC (fin losses)

$Q_u$ – useful heat output

R – reflection

$r_1$ – inner radius

$r_2$ – ducting radius

$R^2$ – regression value for curve of best fit

$r_3$ – insulation radius

RD – measured reflection spectrum

$R_d$ – ratio of ducting insulation circumference

$R_{fin}$ – thermal resistance of fin

$R_{LSC}$ – thermal resistance of LSC

$R_T$ – total thermal resistance

S – incident irradiance onto the absorber for a collector

$S_0$ – initial vibration energy level

$S_1$ – excited vibration energy level

$S_{LSC}$ - the amount of light captured by the LSC dye multiplied by the optical efficiency of the panel

SR – spectral response

t - thickness

T- transmission

$T_a$ – ambient temperature (K)

TD – measured diffuse transmission spectrum

$T_d$– diffuse light component of the transmission (calculated)

$t_{frame}$ – thickness of panel frame

$T_i$ – inside temperature

$T_{in}$ – inlet temperature

$T_{out}$ – outlet temperature

$T_{pm}$ – mean plate temperature (K)

TS – measured linear transmission spectrum

$T_s$ – spectral (linear) light component of the transmission (calculated)

$TS_c$ – spectral (linear) light component of the transmission from a clear sample

$u_{LSC}$ – heat loss co-efficient through LSC (fin losses)

$U_b$ – heat loss from the bottom of a flat plate collector

$U_e$ – heat loss from the side of a flat plate collector

$U_L$– heat loss from a flat plate collector

$U_t$ – heat loss from the top of a flat plate collector

$U_T$ – total heat loss coefficient

$V_{cell}$ – voltage measured from the PV cell prior to attaching to the LSC waveguide

$V_{LSC}$ – voltage measured from the PV cell after being attached to the LSC waveguide

$V_{oc}$ – open current voltage

# 1. Introduction and Background

## 1.1 Solar Power and Renewable Energy

Climate change is one of the prominent obstacles to future stability, putting pressure on researchers, industries, and governments to develop clean technologies to reduce greenhouse gas emissions globally. Progress towards reducing human impacts is being made in a wide range of fields including increased efficiency of products, carbon capture, renewable energy developments, and electrification. Despite efforts, more still needs to be done to transition into a low-carbon society. The IEA predicts that between 2018 and 2050, global energy demand will increase by ~50% [1], making clean energy generation a key factor in reducing human impacts on greenhouse gas generation. Solar energy may prove to be a key factor in the energy solution. The sun can provide about 1000 $W/m^2$ of energy to the Earth's surface on a clear day, resulting in a total of 89,300 TW of radiant power [2]. Considering a global electricity consumption of ~30,000 TWh (in 2019) [3] solar energy provides enough energy in 33 minutes to supply all electricity needs across the world for 1 year. Despite this, finding the land for solar energy harvesting can sometimes be difficult due to land-use competition. However, solutions such as rooftop solar systems or integrated solar windows for buildings can minimize land use. Houses and office buildings account for nearly 40% of the overall energy use in the United States [4] and 36% of global energy consumption [5]. In Canada, 17% (1,517.5 PJ) of all energy used is consumed by households and 83% of all residential energy use was for space and water heating [6]. Residential energy use in Canada released 66.2 MT of GHG in 2013 [6]. Traditionally, energy must be generated off-site and transported to the location using expensive transmission systems. Of this energy, 41% is estimated to be used for space and water heating and 15% is used for cooling [7].

It is estimated that the energy needs for a residential unit are ~0.03641$W/m^2$ (3.14 kwh/day) of floor area, by the national association of home builders for homes built between 2000 and 2009 [8]. The consensus on available building rooftop space for PV varies between 5-100% as reported by NREL [9]. Electric power from solar windows can be added to the generation mix, but typically suffer from low efficiencies of around 1-2%, although it is estimated that 140 $W/m^2$

could be generated from glazed commercial windows [10]. The company, Solar Windows, estimates that generating electricity from windows could reduce the energy costs of large buildings by up to 50% [11].

The development of solar windows offers the additional benefits of reducing the incoming heat load during hot months, thus lowering cooling bills while concurrently generating electricity. Solar windows are transparent solar collectors that can be used as windows in buildings. They typically harvest energy from the non-visible regions of the solar spectrum (sometimes with minimal absorption in the visible spectrum as well) to minimize the visual impact. Solar windows have seen renewed interest in recent years with developments on ultraviolet (UV) and near-infrared (NIR) luminescent solar concentrators (LSCs) [12] as well as transparent perovskite solar cells [13] and solar films [11]. Despite these advancements, there has been little implementation of solar windows into buildings.

LSCs have interested researchers for years with the promise of low-cost solar energy capture coupled with selective transparent properties. LSC technology has been around for nearly 40 years and have been suggested for various solar harvesting applications [14] [15]. However, most research on LSCs has been on lab-scale samples to increase their low efficiency and performance. A large gap in research exists before realizing the application of solar energy harvesting using LSCs for greenhouses, solar windows, or solar thermal collecting applications.

LSCs have the potential to be developed for use in both transparent applications, such as windows, as well as for traditional solar generation, such as rooftop panels or co-generation solar heaters, however, none have thus far made it to widescale commercial use indicating that more research on their development and applications is required. This thesis aims to evaluate the readiness and suitability of using LSCs to harvest and convert solar energy to thermal energy for various applications such as buildings, greenhouses, and flat-plate solar thermal collectors.

## 1.2 Luminescent Solar Concentrators

LSCs are optical devices that are used to concentrate solar energy incident onto their planar surface onto their sidewalls, which can potentially be used for photovoltaic or thermal

applications. LSCs are composed of a transparent waveguide that has been impregnated with fluorescent dye particles that are capable of absorbing and re-emitting photons. Light passes through the surface of the transparent flat planar waveguide where some light is absorbed by the fluorescent dye particles; the rest is transmitted through the waveguide. If the absorbed light is re-emitted by the dye particle (dependant on the dye's quantum yield) there is a probability of the emitted photon being trapped within the waveguide. Total internal reflection (TIR) can occur within the waveguide (if the photon is emitted at an angle that is greater than the critical angle for TIR) and the photon can be transported to the edge of the waveguide where it can be harvested (usually by solar cells). **Figure 1.1** depicts the cross-section of an LSC with various interaction mechanisms.

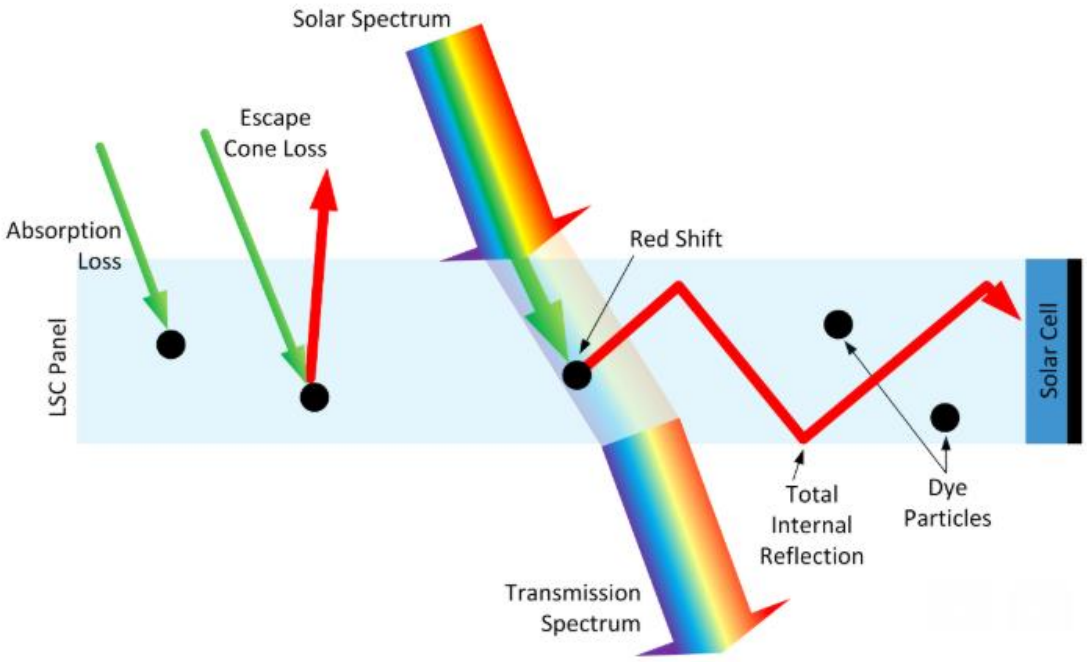


**Figure 1.1.** Light interactions in LSCs. Cross-section view of the various mechanism of an LSC using a dye that absorbs green light and emits red light.

LSCs usually have large surface areas and small thicknesses which offers the advantages of being able to concentrate incident light, both direct and diffuse, from a large surface to a small profile edge for harvesting. The concentration ratio for LSCs is related to their surface area compared to their edge thickness and can theoretically offer higher concentration ratios than

traditional geometric concentrating devices without the need for solar tracking systems [16]. LSCs can be transparent and can be tuned to selectively capture light over a specific wavelength range through the exclusive choice of fluorescent dyes. These properties give LSCs the potential to be used in various applications, such as windows, greenhouses, or tandem cell collectors. The fluorescents used in LSCs are usually organic dyes, quantum dots, or rare-earth metals, although organic dyes are the most common [17].

### 1.2.1 Fluorophores

There are three main types of fluorophores used in LSC devices; organic dyes, quantum dots and rare-earth materials. An ideal fluorescent material would have a wide absorption range, a large Stokes shift with no overlapping absorption/emission spectra, a quantum yield of 1 (unity), high stability and lifespan and high solubility in the host material. In practice, no ideal dyes currently exist. Ideally, the emission spectrum of the dye occurs in the NIR spectral region where it can be used most efficiently by Si cells [18]. Lumogen Red 305 (organic dye) is considered the state-of-the-art fluorophore and is often used for comparison of LSCs.

Organic dyes are the most commonly used fluorophores in LSC devices reported in the literature. organic dyes are often used in LSCs due to their high quantum yields, good solubility, and relatively large absorption range [19]. Organic dyes suffer from long tails on the absorption/emission spectrum leading to high self-absorption losses, making it crucial to have high quantum yield for use in LSC applications since each re-absorption event could lead to the loss of the photon. Rhodamine, coumarin and perylene based dyes are the 3 most commonly used, with a renewed interest in the development of perylene dyes due to their potential for improved photostability and quantum yields [20]. The best organic dyes currently available on the market are the Lumogen ® series by BASF [19]. Organic dyes can readily be dissolved into polymer materials such as PMMA for the creation of LSC waveguides.

When a photon with appropriate energy strikes an electron in the fluorescent dye molecule, the energy becomes absorbed by the electron and it moves to an excitation state at the next vibrational energy level ($S_0 \rightarrow S_1$) [21]. The electron then decays back to its original energy level, $S_0$ by releasing a photon [21]. This process occurs within $10^{-8}$ s and thus the time between

when an electron is excited and when it returns to its normal state is ~10 ns [21]. This process is usually depicted using a Jablonski Diagram, as shown in **Figure 1.2**. $S_2$ in this figure is a secondary vibration level that the electron could be excited to if the incident photon has enough energy; however, this level quickly ($10^{-12}$ s) decays back to $S_1$ in a process called internal conversion [21]. This loss of energy during the rapid decay from $S_2$ to $S_1$ is one of the causes of the Stokes shift in the emission spectrum [21]. This process also means that the emission spectrum is red-shifted with respect to the excitation wavelength, as extra energy above the $S_1$ level is quickly lost [21]. This process is known as Kasha's Rule. As the electron decays from $S_1$ to $S_0$ through the release of a photon, it generally decays to a slightly higher energy level than $S_0$ and then returns to $S_0$ through thermalization [21].

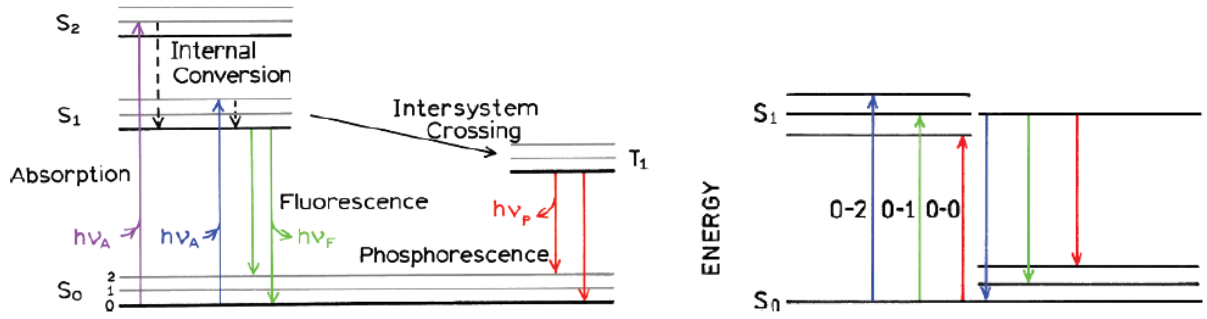


**Figure 1.2.** Jablonski diagram showing the mechanisms of fluorescence decay. Image from J. R. Lakowicz, "Introduction to Fluorescence" in *Principles of Fluorescence Spectroscopy*, Springer © US, 2006, pp. 5, 8.

Due to the mechanisms involved in fluorescence decay, the emission spectrum is usually a mirror image of the absorption spectrum [21]. Both the absorption and emission spectrum usually contain one main peak, with an offset of 50 - 100 nm between peaks [17]. **Figure 1.3** illustrates the symmetry between the emission and absorption spectrum along with the effect of Stokes shift.

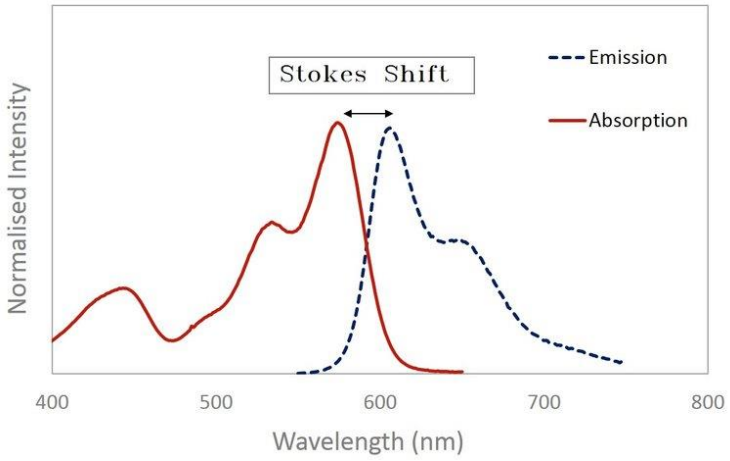


**Figure 1.3**. Absorption and emission spectrum of lumogen red 305 fluorescent dye. From M. Gajic and G. Rosengarten, "Non-imaging technologies for designing a hybrid photovoltaic and solar thermal collector," *RMIT University, Thesis* ©. 2018. [19].

The quantum yield, defined as the number of photons emitted vs the number of photons absorbed, can be very near unity for some dyes. It is important to remember that even at unity the energy yield is always less due to Stokes shift. For fluorescents with longer absorption wavelengths, the quantum yield generally decreases, resulting in low quantum yields for fluorophores that work in the infrared range [17] [21], making the production of suitable NIR dyes difficult. Despite the challenges, dyes with emission between 700-800 nm and quantum yields ranging between 50-90% based on terrylenediimides and violanthrones have been reported [22] [23] [24].

The effect of re-absorption in organic dyes can be reduced by the addition of dimethyl sulfoxide (or other high mobility molecules) to the host matrix which increases the Stoke shift and thus increases the gap between the absorption and emission spectra [25]. This effect is caused due to the decrease in Stokes shift observed when particles are embedded in a rigid matrix compared to a mobile matrix (liquid) and is attributed to the reorientation of the polar solvent molecules caused by an increased dipole moment of the dye particles while in an excited state [25].

Organic dyes also suffer from a relatively short lifespan in comparison with PV cells, caused by fluorescence quenching [19]. Fluorescence quenching is a term used to describe various

mechanisms that reduce the fluorescent intensity of a fluorophore. The performance of an LSC will degrade over time due to the increasing fluorescence quenching in the sample, as shown by Sark et al, 2008 [26]. However, degradation of LSC panels can be reduced by the addition of UV blockers and other additives as shown by L. R Wilson [17] and C. Corrrado et al [27]. Commonly used organic dyes in LSC applications from Lumogen ® series by BASF are listed in Table 1.1 (data provided by BASF data sheets and reported by L. R. Wilson [17] [28]).

**Table 1.1**. BASF Lumongen series dyes. [17] [28]

| Name | Type |
|---|---|
| Violette 570 | napthalimide |
| Gleb 083 | perylene |
| Gleb 170 | perylene |
| Orange 240 | perylene |
| Rot 305 | perylene |

In addition, some NIR dyes produced by BASF for LSC applications are KF402, NIR1, NIR3, with reported quantum yields of up to 92% [24]. Testing by L. R. Wilson has shown that they perform with quantum yields between 60-80% and that the addition of these NIR dyes into an LSC leads to a reduced efficiency due to increased losses as a result of multiple re-absorption events and low quantum yields [29]. Rot 305 was concluded to be the most suitable dye (of the dyes listed in Table 1.1) due to high performance and slow degradation in PMMA [29]. It was also shown that the addition of dye mixtures did not significantly improve the efficiency of the panel with the exception of adding a small amount of Violett 570, which led to a small increase [29]. This was concluded to be due to the increase in re-absorption instances when multiple dyes are mixed (i.e. the emission from one dye becomes readily absorbed by another dye, leading to high re-absorption) which is in correlation with results from other researchers [29]. L. R. Wilson goes on to predict an optimal efficiency of 3.75% for a 10 cm x 10 cm LSC with a back reflector, using 350 ppm Rot 305 and 50 ppm Violette 570 [29]. To make use of the NIR dyes, they must be placed in a separate panel and stacked, which was found to lead to an increase to 4.62% overall efficiency when stacked with the Rot 305 (350), Violette 570 (50) panel mentioned above [29]. Similarly, Zastrow et al [30] were able to achieve 4% power conversion efficiency using a

double stacked 40 cm x 40 cm LSC with GaAs cells. Currie et al [31] reported a power efficiency of 5.5% using a combination of luminescence and fluorescence. An efficiency of 2.7% power conversion efficiency was reported from a 5 cm x 5 cm LSC with a single InGaAs cell and a record of 7.1% power efficiency was reported for a 5 cm x 5 cm cell using four GaAs cells with a back reflector and a combination of Rot 305 and CRS040 dyes by Slooff et al [32] [33].

### 1.2.2 Waveguide

The waveguide material used in LSC applications should have a high optical clarity, coupled with a high index of refraction. As can be seen from Equation 1.2, a higher index of refraction leads to a greater degree of TIR. In practice, the index of refraction is limited for materials with high optical clarity. Different materials such as PMMA, quartz, B270 glass polycarbonate I, and Polycarbonate II are suitable materials, with PMMA being the most used. In a study by Kastelijn et al [34] these 5 types of materials were tested for use in LSCs and it was found that the difference in performance was minimal. PMMA is generally used due to its ease in fabrication and the ability to easily dissolve organic dyes into the solution. PMMA has a high optical clarity of ~90% in the visible light region and is inexpensive. PMMA does suffer some degradation in UV light that limits its lifespan, however, the application of UV coatings can extend its life [29] [27]. The melting temperature is sometimes a concern for applications such as solar thermal collectors. The melting temperature of PMMA is 160 °C, thus limiting its use in high-temperature thermal collector applications. When used in applications in which high temperatures are expected, quartz (MP =1715 °C), B270 glass ( MP =1033 °C), or polycarbonate (MP = 288 °C) should be used.

Various edge geometries of the waveguide have been explored, such as tappers or V-grooves to improve the LSC performance by enhancing the optical path of light through the waveguide with miniscule results. In a review conducted by L. R. Wilson, it was concluded that the performance increase achieved was not worth the additional processes required [29].

The efficiency has been reported to decrease with increasing LSC area due to increased host absorption and self-absorption losses [35] [29] [36] [27] [19]. This effect is due to the increasing host absorption, imperfect TIR, and self-absorption losses with increasing size. Note that by

increasing the thickness, the concentration of dye required is reduced to achieve the same absorption.

### 1.2.3 Raytracer

The effects of size on LSCs were modeled using a simulation program developed by L. R. Wilson [35] and presented in Luminescent Solar Concentrators: A Study of Optical Properties, Re-absorption and Device Optimisation [29] which was designed to model LSC behaviour. The results from the program were compared against the results from a Monte-Carlo raytracing program Raylene, for verification by the creator. The program generates photons emitted from random points and directions and models their behavior based on probability as they interact with an LSC with variable dyes, sizes and concentrations. The program uses absorption and emission spectra from various Lumogen ® dyes in combination with the optical properties of PMMA, the AM 1.5 solar spectrum, and the quantum efficiency spectrum of Si-PV cells to estimate the solar to electrical efficiency based on the input parameters (dye type, concentration, LSC size, reflectors, cell type). Using this program to model the performance of LSCs comprising various Lumogen ® dyes as a function of their size (using square panels), the effect of size on the efficiency of the LSCs can be visualized (**Figure 1.4**). The optical efficiency of a panel can be extracted from the program as well, allowing for comparisons in later chapters.

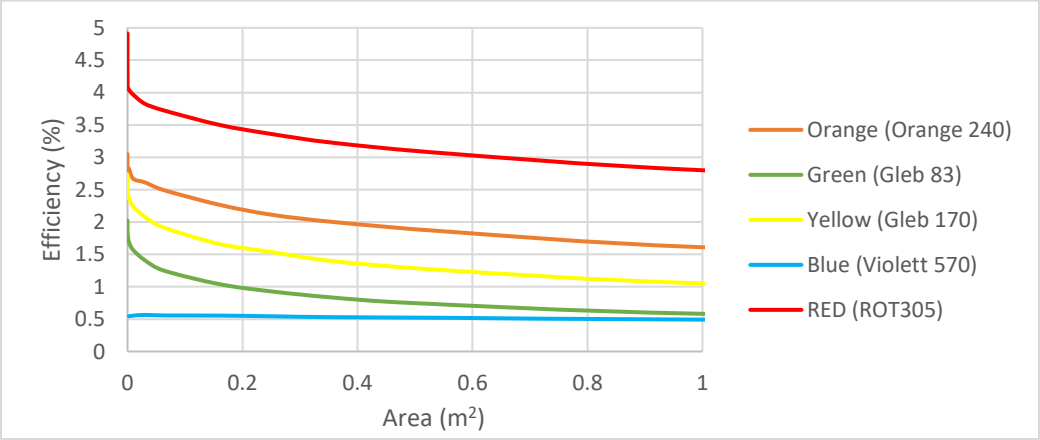


**Figure 1.4.** The efficiency vs size curve for various dyes in 3mm thick LSCs using a square shape, PMMA host material and a concentration of 400 ppm. Data obtained from LSC Raytracer developed by L. R. Wilson [35] [29].

It can be noted that the efficiency increases drastically as the LSC panel gets very small (less than 0.05 $m^2$). The exception is with the Violette 570, which appears to hold a near-constant efficiency with increased size. The reduction in efficiency with increasing size marks one of the major challenges with using LSCs in real-world applications.

## 1.3 PV Cells

To convert concentrated light from LSCs into electricity, solar PV cells are attached directly to the waveguide. The materials used to attach the cells must be optically clear with a similar index of refraction to that of the waveguide to prevent losses at the interface. The power observed from a cell is the product of the incident light available at the interface, given by the optical efficiency of the LSC and the solar cell efficiency. Because of the narrow emission spectra generally seen in LSC fluorescence, PV cells can be selected that operates optimally in that range for increased performance. The small cell size required also allows for more expensive and efficient cells to be used economically. Despite this, Si cells are commonly used in research, although some researchers have used GaAs or GaInP cells to achieve higher efficiencies. For convenience, Si cells are used in this thesis.

GaAs cells have a higher bandgap than Si cells (1.43 eV compared to 1.11 eV) resulting in less wasted energy when used on LSCs that emit in the visible light region, however, GaAs cells suffer from a cut-off wavelength of only 873 nm, making them unsuitable for most NIR applications. For LSCs designed to operate in the NIR region, Si cells are a better choice due to a high efficiency in this region and a cut off wavelength of ~1100 nm.

### 1.3.1 $V_{oc}$ and $I_{sc}$

The IV (current-voltage) curve (example shown in

**Figure 1.5)** is typically used to show the performance of solar cells. The $I_{sc}$ or short circuit current is the current measured across the cell when the voltage across the cell electrodes is zero. The $V_{oc}$, or open-circuit voltage, is the voltage measured across the cell when the current is zero. $I_{sc}$ will increase with increasing irradiance on the solar cell. The $V_{oc}$ is a function of the bandgap of the cell.

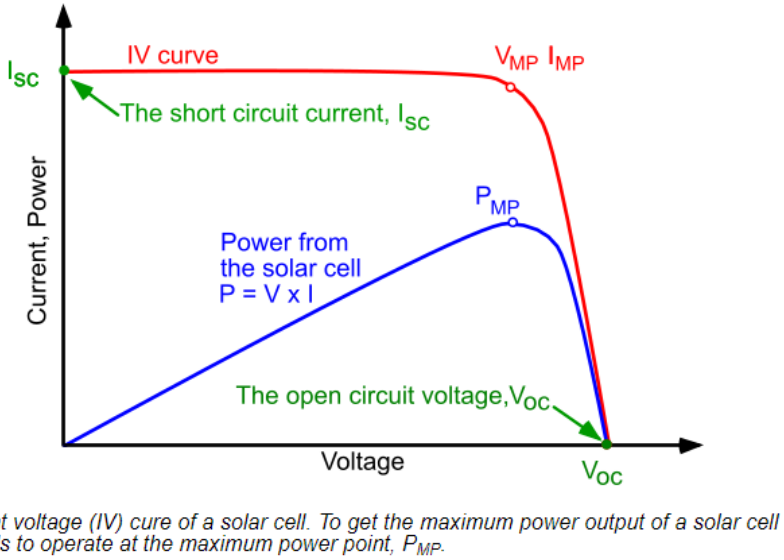


*Current voltage (IV) cure of a solar cell. To get the maximum power output of a solar cell it needs to operate at the maximum power point, $P_{MP}$.*

**Figure 1.5.** IV curve for a solar cell. Image from PV Education ©, IV curve [37]

To obtain the IV curve, a device must be used that varies the resistance and concurrently measures the voltage and current through the circuit. Measuring the open-circuit voltage and short circuit current and using the formula $P = I_{sc} \cdot V_{oc}$ overestimates the power produced by the cell; however, by multiplying the power by the fill factor of the cell, the maximum power output can be found. The fill factor can vary between 40-85%. In this thesis, a fill factor of 80% was assumed based on the specifications obtained for the Si-cells used.

To determine the response of a solar cell to incident light, it is important to know the external quantum efficiency, internal quantum efficiency and spectral response. The quantum efficiency of a solar cell is the ratio of incoming photons of a given wavelength to the ratio of electrons in the output current from the cell. The external quantum efficiency includes optical losses, such as reflection or transmission, whereas the internal quantum efficiency considers only the photons

that are absorbed in the PV cell. The quantum efficiency gives the number of output electrons per photon, whereas the spectral response compares incoming power at a given wavelength to the power generated by the cell. High energy photons exhibit low spectral response efficiency because they possess much higher energy than the output of the electron from the cell (i.e. electrons generated by high energy photons thermalize before contributing to the output current from the PV cell). The excess energy from electrons generated through the absorption of high energy photons, which is any energy above the bandgap of the material, is thermally absorbed by the PV cell. The bandgap of Si-based PV cells is 1.12 eV. Photons that have less energy than the bandgap do no generate electrons. The spectral response for a Si-cell is shown in **Figure 1.6**.

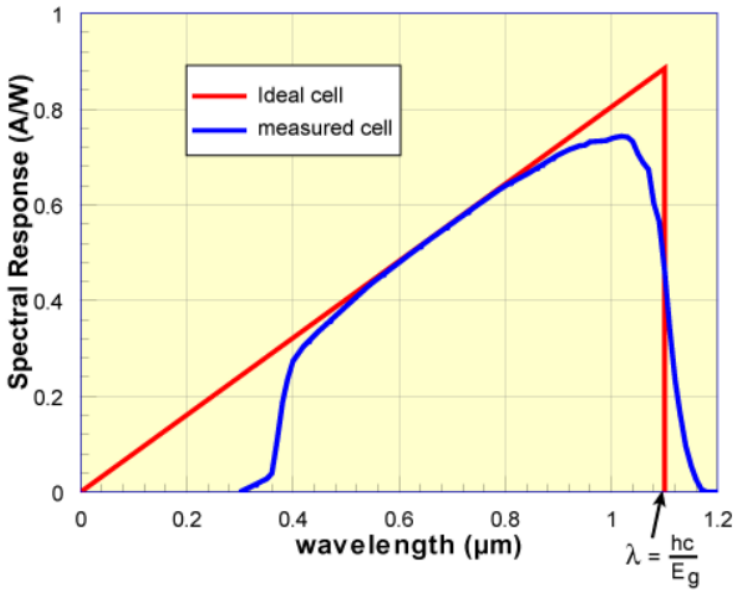


**Figure 1.6.** Spectral response of a silicon solar cell. Image from PV Education ©2019 [38]

Additionally, the spectral response for Si PV cells can be calculated using Equation 1.1. Note that this equation is not valid for wavelengths above the cut-off (1100 nm).

Equation 1.1

$$SR = \frac{QE * \lambda\ (nm)}{1239.8} \qquad \text{For: } 400nm < \lambda < 1100\ nm$$

## 1.4 Loss Mechanisms in LSCs

Several loss mechanisms are present which influence the solar-to-electric conversion efficiencies of LSCs. These loss mechanisms have been dutifully explored by previous authors such as A. P. Green [16] and L. R. Wilson [29] and will be summarized here.

The first loss encountered by light as it enters the LSC is the reflection from the top surface of the collector [16]. This loss is dependant on the properties of the waveguide and is around 4% for PMMA based waveguides. This loss can be expressed as the fraction R, where R is the loss due to the Fresnel reflection value of the surface, and (1-R) is the fraction of incident light transmitted into the sheet [17].

The absorption efficiency describes the percentage of light incident onto an LSC that is absorbed by the dye. This value is dependant on the absorption spectrum of the dye and thus a dye that absorbs a wide range of wavelengths will have a higher absorption efficiency than one with a narrow range of absorbed wavelengths if other parameters (quantum absorption, dye concentration, thickness) are constant. The optimal efficiency for an LSC with Si cells that absorbs all light with wavelength under 950 nm and emits light with a wavelength between 950-1000 nm would have an absorption efficiency of 0.71 [17]. In practice, the maximum absorption efficiency of an LSC panel using a single dye type is much lower (0.15-0.25).

The light entering the waveguide interacts with the fluorescent particles where it is absorbed, if it is within the absorption spectrum of the particle, and re-emitted based on the quantum yield of the fluorescence. The quantum yield is the probability that a fluorescent particle re-emits a captured photon (rather than thermal absorption of the energy) and is between 0.95 and 1 for the most commonly used organic dyes [16] [17] [14] [39].

Due to the random orientation of dye particles the light is re-emitted randomly from each dye particle leading to an average isotropic emission within the waveguide [17]. The emitted light must strike the surface of the waveguide sheet at an angle greater than the critical angle for total internal reflection or else it can escape [16]. These losses are known as the escape cone losses and are dependant on the probability of total internal reflection ($P_{TIR}$). The probability of total

internal reflection can be calculated using Snell's laws of refraction and is based on the difference in the refractive indices of the host material used in the waveguide and the surrounding air, as shown in Equation 1.2. For PMMA with a refractive index of 1.5, the $P_{TIR}$ is ~75% and thus escape cone losses are ~25% [16] [17] [14].

Equation 1.2 $$P_{TIR} = \sqrt{1 - \frac{1}{n^2}}$$

Photons emitted from fluorescent particles have a longer wavelength and thus lower energy than the photons absorbed by these particles [16]. This effect is described by Stokes shift and the Stokes efficiency is the fraction of the energy of the emitted photon compared to the energy of the absorbed photon. A Stokes efficiency of 0.75 is common for LSCs [16] [17].

Once an emitted photon is trapped from TIR, it must travel through the host material that makes up the waveguide until it is harvested from the edge of the LSC sheet. Theoretically, TIR should be 100% efficient, however, surface imperfections such as scratches, dust or water droplets can cause the light to be scattered and escape [17]. TIR losses are sometimes grouped in with host material losses for simplicity. There is a chance that the photon will be absorbed by the host material, determined by the host efficiency. Host efficiency is the fraction of emitted photon energy that is transmitted to the LSC edges. The host efficiency can be calculated by using the absorption coefficient of the material (found experimentally using the Beer-Lambert law) and multiplying by the average path length of a photon captured within the waveguide [16]. For PMMA, the host efficiency for light with wavelengths between 360- 700 nm is between 0.95 – 0.98 (based on transparency) for most LSC devices. LSCs that utilize longer wavelengths (such as infrared) will have higher host absorption losses unless careful selection of host material is used [17]. Most of the light lost due to host losses will become heat, however, some of these losses are also due to scattering caused by imperfections in the host matrix resulting in escaped light [16] [40]. In addition to the losses due to host absorption and scattering, losses are also present due to the imperfect total internal reflection losses. Combined, the host efficiency losses result in a decreasing efficiency with larger LSC panels due to increasing losses with increased travel distance. This is shown in an experiment by J. Mugnier [40] and described by A. Green

[16] in which the addition of mirrors to the opposite edge of an LSC is expected to give nearly double the output on the collector edge, however a significantly lower increase was observed.

LSCs also suffer from self-absorption losses because a photon that is emitted by a dye particle can be re-absorbed if it interacts with another dye particle due to overlapping absorption and emission spectra. Overlapping emission and absorption spectra are caused by small Stokes shifts and long absorption tails that are common among organic dyes [17]. When self-absorption occurs, the photon has another chance to be thermally absorbed due to non-unity quantum yield or to escape, thereby contributing to escape cone losses. Thus, re-absorption can lead to a significant decrease in efficiency. Some of these re-absorption events can re-capture a photon that would otherwise have escaped and re-direct it towards the LSC sidewalls; however, the occurrence of these events is small due to the short pathlength and thinness of the waveguide compared with its length and width. Photons can be emitted and re-absorbed multiple times and the number of times this occurs is dependant on the type and concentration of fluorescence used within the waveguide and the travel distance of the photon. The self-absorption efficiency for organic dyes is usually between 40-80% for a sheet with a single dye [17]. The losses due to self-absorption is the main reason why the addition of multiple dyes in a single LSC panel does not result in a significantly increased efficiency and can even reduce the efficiency of the device, as shown by L. R. Wilson [17]. To avoid this problem while using multiple dyes to increase the absorption range of an LSC panel, multiple sheets with unique dye's and an air gap between each can be used.

In summary, the overall optical efficiency of an LSC panel can be described, as proposed by Goetzberger et al [14] , by multiplying the efficiency of each of the loss mechanisms as shown in Equation 1.3.

Equation 1.3

$$\eta_{opt} = (1 - R) * P_{TIR} * \eta_{abs} * \eta_{QY} * \eta_{Stokes} * \eta_{host} * \eta_{Self}$$

Where R is the reflection losses, $P_{TIR}$ is the probability of total internal reflection (escape losses), $n_{abs}$ is the dye absorption efficiency, $\eta_{QY}$ is the quantum yield efficiency, $\eta_{Stokes}$ is the Stokes shift efficiency, $\eta_{host}$ is the host efficiency and $\eta_{Self}$ is the self-absorption efficiency. The values obtained by Geotzberger et al [14] and reported by L. R. Wilson [17] for a 40 cm x 40 cm x 0.3 cm LSC are shown in Table 1.2.

**Table 1.2.** Efficiency values for an LSC. Values were determined experimentally and reported by Geotzberger et al [14] for a 40 cm x 40 cm x 0.3 cm LSC

| Quantity | Value |
|---|---|
| 1-R | 0.96 |
| $P_{TIR}$ | 0.75 |
| $n_{abs}$ | 0.2-0.3 |
| $\eta_{host}$ | 0.9-0.95 |
| $\eta_{QY}$ | 0.95-1.0 |
| $\eta_{Stokes}$ | 0.75 |
| $\eta_{Self}$ | 0.75 |
| $\boldsymbol{\eta_{opt}}$ | 0.07-0.12 |

Due to the difficulty in measuring some of these quantities experimentally, LSC devices are often modeled using Monte Carlo raytracing programs to determine self-absorption losses, mean path length, escape losses and optical efficiency [16] [17]. Once an optical efficiency has been found for an LSC, the amount of electricity that can be generated by attaching a solar cell can be calculated by using the external quantum efficiency spectrum $\eta_{EQE}(\lambda, \theta)$ at the attached face [16]. This expression is a function of wavelength and angle and represents the ratio between the number of electrons in the external circuit generated within the PV cell and the number of photons incident onto its surfaces; However, the angle for LSC applications is usually considered to be normal, and thus the external quantum efficiency is simplified to $\eta_{EQE}(\lambda)$ [16]. A

compilation of reported efficiencies for both organic dye and quantum dots has been created and reported by G. Maja [19], as shown in Table 1.3.

**Table 1.3.** Compilation of LSC efficiencies reported in literature. Compiled by G. Maja [19]. M. Gajic and G. Rosengarten, "Non-imaging technologies for designing a hybrid photovoltaic and solar thermal collector," *RMIT University, Thesis,* 2018 pg. 23,24.

| Reference | Concentration | PCE | Optical Efficiency | Size | Note |
|---|---|---|---|---|---|
| (Mansour et al. 2002) | Various | Not reported | Average 30 % | 5 x 4 x 0.3 $cm^3$ | Outdoor testing |
| (Slooff et al. 2008) | LumRed305 0.01 %wt and Yellow CRS040 Coumarine 0.003 %wt | 7.1 % | Optical efficiency 24 % Solar cell efficiency 29 % | 5 x 5 x 0.5 $cm^3$ | World record LSC |
| (Sark et al. 2008) | LumRed305 unreported conc | 2.5 % | Optical efficiency 13 % Solar cell efficiency 18.6 % | Unreported | Good report of photodegradation |
| (Goldschmidt et al. 2009) | Unreported conc | 6.7 % | Optical efficiency 43 % Solar cell efficiency 15.4 % | 2 x 2 x 0.3 $cm^3$ | Obtained high optical efficiency with band stop filter |
| (Desmet et al. 2012) | LumRed305 115ppm and Blue Perylene 75ppm | 4.2 % for stack | Optical efficiency 27.1 % Solar cell efficiency 15.6 % | 5 x 5 x 0.5 $cm^3$ | |
| (Liu & Li 2015) | Three dye LSC | 1.4 % | EQE up to 30 % Solar cell efficiency 11.7 % | 5 x 5 x 0.5 $cm^3$ | |
| (Vishwanathan et al. 2015) | LumRed305 200ppm | 2.9 % straight, 2.4 % bent | Optical efficiency 19 % Solar cell efficiency 15 % | 10 x 10 x 0.3 $cm^3$ | Compared flat and bent configurations |
| (Chou et al. 2015) | Coumarin C440 174.2 mg/L , Disodium fluorescein (DSF) 824.24 mg/L | 4.92 % with stack of two | Optical efficiency 31.21 % Solar cell efficiency 15.8 % | 5 x 5 x 0.5 $cm^3$ | World record silicon based LSC |
| (Tummeltshammer et al. 2016) | LumRed305 10ppm - 150ppm | Not reported | Investigates wavelength dependent optical efficiency | 6 x 6 x 0.5 $cm^3$ | |
| (Krumer et al. 2017) | LumRed305 4ppm - 153ppm | 2.3 % | 15.13 % | 3.5 x 10 x 1 $cm^3$ | Liquid waveguide |

*Table 2.3: Key organic dye based studies in the literature*

| Reference | Concentration | QY | Efficiency | Size | Note |
|---|---|---|---|---|---|
| (Chatten et al. 2004) | CdSe/CdS, conc not reported | 0.5 | PCE 4 % with GaAs cells | 4.2 x 1 x 0.5 $cm^3$ | First QD LSC experiments |
| (Wang et al. 2010) | CdSe/ZnS and 50 uM PbS | 0.12 | PCE 3.3 % with cells on all edges | 4.5 x 1.2 x 0.4 $cm^3$ | |
| (Coropceanu & Bawendi 2014) | CdSe/CdS 20 %wt | .4 | Optical efficiency 10.2 % | 21.5 x 1.3 x 28 $cm^3$ | |
| (Coropceanu & Bawendi 2014) | CdSe/CdS 0.5 %wt | .86 | Optical efficiency 48 % at 400 nm | 2 x 2 x 0.2 $cm^3$ | |
| (Meinardi et al. 2014b) | CdSe/CdS 0.05 %wt | .45 | Optical efficiency 10.2 % | 21.5 x 1.35 x 0.5 $cm^3$ | |
| (Meinardi et al. 2015) | CISe coated with ZnS 0.5 %wt | .4 | Optical efficiency 3.27 % | 12 x 12 x 0.3 $cm^3$ | |
| (Knowles et al. 2015) | $CuInS_2$/CdS 0.5 %wt | .86 | Unreported | 120 x 1 $cm^3$ liquid waveguide | Well matched to solar spectrum |
| (Zhou et al. 2016) | $CuInS_2$/CdS 0.5 %wt | .4 - 0.5 | Optical efficiency 6.1 % | 5 x 1.5 x 0.3 $cm^3$ | Near IR QD |
| (Zhao et al. 2016) | CdSe/$Cd_xPb_{1-x}S$ 0.5 %wt | .4 | PCE 1.15 % | 7 x 1.5 x 0.3 $cm^3$ | |
| (Meinardi et al. 2017) | Si QD 0.09 %wt | .46 | PCE 2.85 % | 12 x 12 x 0.26 $cm^3$ | First to use silicon QD |
| (Waldron et al. 2017) | PbSe QD 12.7 uM | > 0.7 | PCE 4.74 % | 2.1 x 2.1 x .49 $cm^3$ | Record QD performance |

*Table 2.4: Key quantum dot based studies in the literature*

## 1.5 Thesis Goals and Overview

Thesis goals:

- Determine the current state of LSCs
- Evaluate the potential for LSCs in greenhouse applications, with regards to the potential symbiotic relationship between microclimate and selective solar absorbance.
- Create a modeling method to estimate the working parameters of LSCs, such as optical power at the LSC edges, transmission, and absorption for aid in the design of LSCs for various applications. The model should be able to account for various configurations and irradiance profiles and provide details of the energy flow through the LSCs.
- Explore the use of LSCs in solar heating applications, such as LSC solar collectors, hybrid solar collectors, and co-generation solar collectors. Measure the thermal and electrical output from LSCs and analyze their potential in these applications.

The goal of this thesis is to investigate applications that make use of LSCs unique spectral and optical properties to evaluate the potential for using LSC technology in real-world applications. Due to LSCs low electrical performance, they will never be competitive with traditional solar PV for pure electrical gain. The research explores the potential use and benefits of using LSC

technology in applications in which the LSCs make use of their selective transparency and other beneficial properties for added value, such as agrivoltaics, solar heaters, and co-generation solar modules. To make the design of LSCs for these applications more efficient, a mathematic model for estimating the performance of both single and stacked LSCs should be created. This model will allow for the analysis/simulation of multiple design variations without the time and cost-intensive process of building and testing each design variation.

Additionally, commonly found fluorescent acrylic from commercial suppliers was examined for use in LSC experiments and designs. This accelerated the research in this thesis pertaining to the applications of LSCs by reducing the time-intensive and difficult process of creating LSC waveguides and samples. By showing that commercially available fluorescent acrylic can perform satisfactorily as an LSC, testing and experimenting with large LSCs in various applications can be expedited. An overview of this thesis is detailed below.

Chapter 2 examines the use of LSCs in greenhouse applications. A review of microclimates in greenhouses is conducted to determine how the use of LSC rooftops will affect crop growth and resource use. Thus, this chapter's goal is to explore the claim made by previous authors that LSCs can find use in greenhouse roof applications. This chapter also introduces the use of spectral modeling as a tool for the design and analysis of LSCs.

Chapter 3 details the fabrication and testing of PMMA based LSCs. Various manufacturing methods are examined and solar cells are attached to LSCs to measure output. This chapter uses commercially available fluorescent acrylic in place of waveguides created in the lab with the goal of verifying these purchased LSCs provide suitable samples for the experimental research conducted in this theses. This allows for faster experiments and prototypes for application-based research due to a reduction in fabrication time, large available sizes and low cost.

Chapter 4 uses transmission and reflection data from fluorescent acrylic samples to build a model of energy flow through single or multi-panel LSCs under variable irradiance profiles. Thermal experimentation was completed simultaneously in which thermal power output at the edge of the LSCs was measured allowing for the dye efficiency of the samples to be determined and

verifying the modeling results. This modeling system can be used in the design of LSCs for various applications due to its ability to track all energy flows and to accommodate different configurations, allowing the designer to find the optimal configuration for a specific application.

Chapter 5 uses the modeling method created in Chapter 4 to design and analyse LSCs for solar thermal applications. The designs are compared against traditional flat-plate thermal collectors for discussion purposes and to determine the suitability of LSCs in thermal applications.

Chapter 6 investigates the effect on the performance of integrating LSC covers and ducting with existing flat plate thermal collector designs as well as examines the case for co-generation LSC electric/thermal collectors.

Chapter 7 concludes the thesis, highlighting key take away information from the various chapters and draws overall conclusions from the completed work.

# 2. Greenhouse Applications of LSCs

This chapter investigates the suggested application of using LSCs in greenhouse roofs. First, an investigation into the suitability of LSCs in greenhouse applications will be conducted to determine the requirements for an LSC integrated system. To go into more detail about the effect of LSCs on greenhouse crop photosynthetic action, spectral modeling methods are created. The goal of this chapter is to analyse the effects of LSCs on greenhouse crops to support the claim that this is an application worth pursuing. The results from this chapter indicate that LSCs are likely suitable in greenhouses when used in hot sunny climates from a microclimate/crop yield perspective. Initial modeling also found that LSCs may increase greenhouse profits by up to 40% using the conditions and parameters stated herein.

## 2.1 Introduction to Greenhouse Applications

It has been suggested by previous authors that LSCs may find applications in greenhouses and agrivoltaics, due to their unique spectral selectivity. Plants generally absorb blue and red light and reflect yellow/green light, thus allowing the yellow/green light to be harvested without an impact on the growth of the plants. The general photoactive spectrum of light for plants is shown in **Figure 2.1**, which provides the spectral absorption of the main pigments present in most plants. At ~525 nm to 600 nm the absorption of light is at a minimum: this correlates' well with the use of Lumogen Red 305 dye which has a peak absorbance between ~525-580 nm.

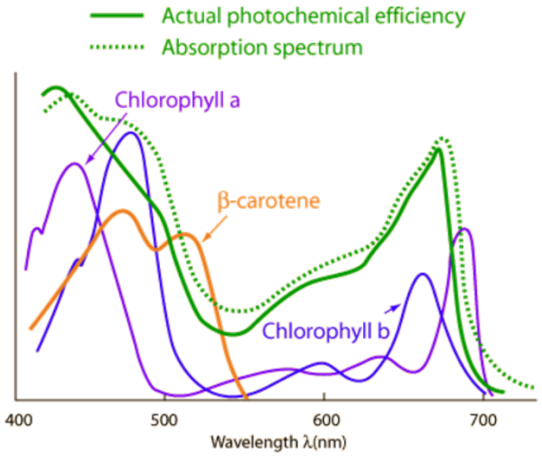


**Figure 2.1**. Absorption and photochemical efficiency of pigments in plants. Image is from hyper physics© [41].

In a study done by C. Corrado et al [27], red LSC panels were integrated into a greenhouse and monitored for one year. The study concludes that the average large greenhouse only requires 1/3 roof coverage to produce all the electricity required to cover the demand for the operation of the greenhouse. The study also notes that initial plant trials indicate neutral to positive effects on the crops. Additionally, the study investigated several stabilizing additives and tested the performance of the panels over accelerated weathering conditions and estimates an extended life of up to 20 years [27]. To get a better understanding of the effect of LSC on crops a literature review was conducted to analyse the micro-climates within the greenhouse. Additionally, a simple profit estimation model was developed for greenhouse economics associated with integrating LSCs into a greenhouse roof that was completed to provide support for the use of LSCs in greenhouse applications.

### 2.1.1 Greenhouse micro-climate review

To better understand the connection between greenhouse parameters and their effects on plant growth, an understanding of the photosynthesis process is required. The leaves in the plant contain various pigments that absorb energy from a light source to convert $CO_2$ and water into carbohydrates which can be stored or used for energy. Various factors influence the rate of photosynthesis, such as light intensity, temperature, $CO_2$ concentrations and water. Generally, the rate of photosynthesis increases with increasing light intensity, up until a saturation point, at which point increasing the light intensity increases the leaf temperature resulting in higher water evaporation. At higher photosynthetic rates more $CO_2$ and water must be captured and supplied to drive the reaction. $CO_2$ is captured by cells on the bottom of the leaf called Stoma, which open and close during respiration. As photosynthetic rates increase the respiration rate also increases to supply enough $CO_2$. Respiration uses energy from the plant and thus the net growth is dependant on the difference between the incoming energy from photosynthesis and the energy used for respiration. During respiration, water vapour can escape through the open stoma and thus increased respiration rates also increase the transpiration (water loss through leaves). Increasing the $CO_2$ concentrations in the surroundings leads to an increase in the amount of $CO_2$ the leaf can capture while minimizing the duration of time the stoma is open for, reducing transpiration and energy loss through respiration. Increasing the temperature also increases the

respiration rate (and transpiration rate), as the plant allows more water to evaporate from its leaves to regulate its temperature through evaporative cooling.

### 2.1.2 Greenhouse parameters

The climate in a greenhouse consists of multiple parameters that have complex effects on the growth and yield of crops. Both energy balance and mass balance must be considered while analysing the climate in a greenhouse and establishing relationships between crop yields and measurable parameters. It is important to note that no direct relationship is currently known. The parameters that are relevant while studying greenhouses are; temperature, incoming photosynthetic photon flux density (PPFD), relative humidity and $CO_2$ concentrations. Each parameter has a complex relationship with both other parameters and with the effect on crops. This problem is illustrated below in the diagram from A. Pawlowski et al, 2009.

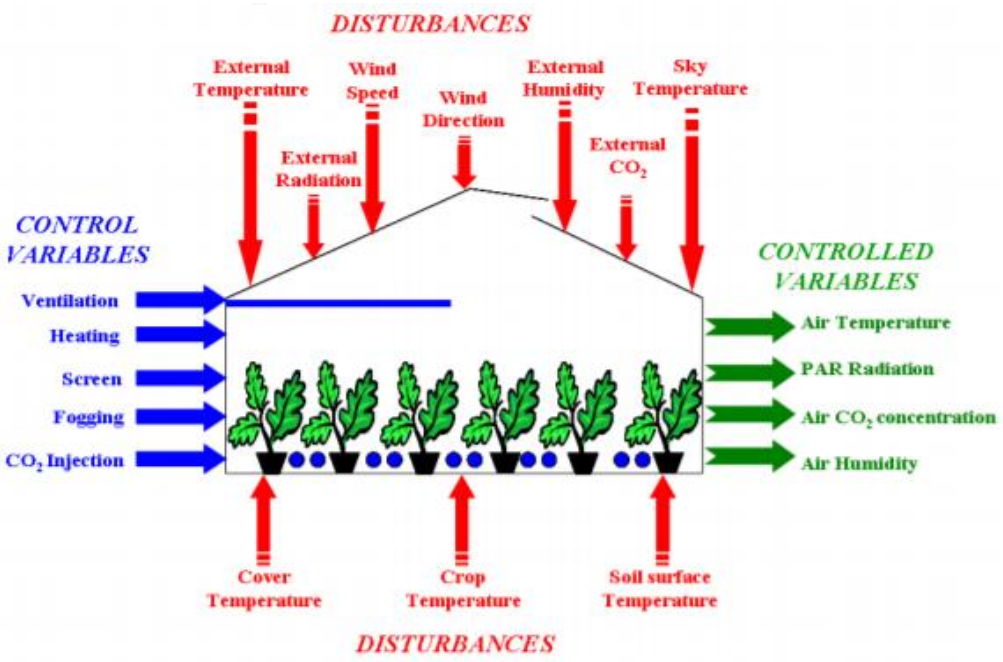


**Figure 2.2.** Greenhouse parameters. Picture from A. Pawlowski, J. L. Guzman, F. Rodriguez, M. Berenguel, J. Sanchez and S. Dormido, "Simulation of Greenhouse Climate Monitoring and Control with Wireless Sensor Network and Event-Based Control," Sensors, vol. 9, pp. 235, 2009 ©

The temperature must be constrained to a certain range to prevent negative effects on the crop. This temperature range is suggested as 22-28 ° C during the day and 15-20 ° C during the night [42]. Increasing the temperature increases the respiration rate of the crop which can have

positive effects on plant growth as long as the photosynthetic output of the plant can keep up; the maximum photosynthetic output occurs when the chloroplasts reach their max absorption capacity [43]. Higher respiration rates use more energy and thus the respiration rate should be balanced with the photosynthetic rate to prevent energy waste and plant stress [43]. This is shown in a study by O. Körner et al [44], who reported that photosynthetic rates increase with temperature to a maximum and then begins to decrease. Increasing the $CO_2$ concentrations and increasing solar radiation was shown to increase the optimal temperature for photosynthesis [44]. Increasing atmospheric $CO_2$ concentrations increases the photosynthesis of the plant, up to a point, dependant on a variety of conditions.

The relative humidity of the greenhouse is directly related to temperature. Relative humidity in greenhouses has been known to affect the growth of the plant and water consumption in various studies, due to its effect on transpiration rate of the crop [43] [45]. The relative humidity is typically kept between 60-70% for greenhouse tomatoes. Low relative humidity increases the transpiration rate of the crop and thus increases the amount of water required [46]. Excessive transpiration rates cause plant stress, disrupt the nutrient supply and reduce plant health [43]. The transpiration rate is also linked to the respiration rate; increasing the $CO_2$ concentration can reduce the plants' need for respiration and thus also reduce the transpiration rate [43].

### 2.1.3 Controlling parameters of a greenhouse

Temperature, relative humidity and $CO_2$ concentration are the main controllable parameters in a greenhouse. Their effects on crop growth have been described above. Temperature can be controlled through ventilation, active cooling systems or shading. Ventilation decreases the relative humidity and $CO_2$ concentrations inside the greenhouse through air exchange with the outside environment, however, it can be done cheaply using vents or fans. Nearly all greenhouses use ventilation to prevent excessive temperatures and crop damage. Shading can limit the amount of incoming solar radiation and have a detrimental effect on crop growth. Active cooling systems, such as air-conditioning systems, are expensive and energy-intensive. The advantage of shading and active cooling systems over ventilation is the ability to cool the greenhouse without reducing the relative humidity and $CO_2$ concentrations, both of which can have negative effects on crop growth and resource use. Relative humidity and $CO_2$ concentration

can both be controlled by adding more of the respective resource, water and $CO_2$, into the greenhouse environment. LSCs reduce the incoming solar radiation and can thus reduce the temperature inside the greenhouse and prevent excessive venting. This can help minimize resource use as well as reduce transpiration stress and heat stress in the crop during periods of high solar irradiance.

During the hot summer months, temperatures outside can reach over the desired 28 °C, even in colder regions such as Canada. Techniques such as whitening, in which a semi-transparent white cover is placed over the greenhouse is often used to help reduce the temperature as well as reduce the incoming photosynthetic flux density to prevent damage from oversaturation of the plant leaves. The use of LSCs in greenhouses can mimic the effect of whitening while making use of the blocked energy to produce electricity. Unlike whitening, LSCs are directly integrated into the greenhouse and thus are more suitable for warm climates that need shading/cooling for a longer duration throughout the year.

### 2.1.4 LSCs for use in greenhouse roofs

LSCs are likely to benefit crops through decreased temperatures caused by the reduction of light entering the greenhouse. This is similar to the reasons why greenhouses sometimes use green glass to provide shading to the crop without reducing the amount of useful light the plants receive. Additional benefits may include reduced water, $CO_2$ and electricity use for the greenhouse operator. Due to the low absorbance of green/yellow light in the range of 520-575 nm, LSCs that absorb these wavelengths are expected to have a low impact on the photosynthetically active light in the greenhouse. It is also worth considering that LSCs down-convert the absorbed light, thus converting captured green/yellow light into red, which is more efficiently absorbed by plants. Since 25% of the light absorbed by LSCs is lost through escape cone losses, a net increase in red light will be available in the greenhouse. Despite low absorption in the green/yellow range, it is unclear what the effect of removing most of the yellow and green light will have on the crop yield. To determine the effect on the photosynthetic action of crops in a greenhouse using LSCs, more information is needed about the spectral transmission and absorption for LSC panels, which is addressed in the following section. To produce an

estimate of the profits obtainable by integrating LSCs into greenhouse roofs and to explore initial parameters, a simple model was created and applied.

## 2.2 Spectral Modeling Methods

Five fluorescent acrylic sheets, coloured blue, green, yellow, orange and red, were acquired from Plastic World (plasticworld.ca). Additionally, a clear acrylic sheet, to be used as a reference, was acquired from the same source. The transmission and reflection of each sheet was measured and recorded using a UV-Vis Spectrometer (Shimadzu UV-2600 spectrophotometer) at each wavelength from 300 to 1400 nm at 1 nm increments. Both the diffuse transmission (TD) and the specular (linear) transmission (TS) were measured, where TS is the direct transmission, excluding the diffuse component. The reflection spectra (RD) was measured using an integrating sphere that captured both the diffuse and spectral reflection. The incident angle for the reflection spectra measurements was 4°. For each acrylic sheet, the absorption was calculated using TS, TD and RD as described below.

The absorption of each sample can be calculated by starting with Equation 2.1.

Equation 2.1 $$Absorption = 100 - T - R$$

where T is the transmission and R is the reflection. The transmission can be further broken down into two components, $T = T_d + T_s$ where $T_d$ is the diffuse component and $T_s$ is the specular component. For non-fluorescent samples the measurement $TS = T_s$, and $TD = T = T_d + T_s$. In the case of fluorescent samples, the measurement *TD* changes to include the emissions *E*, which represent the escape losses from the dye, such that $TD = T_d + TS + E$.

$T_d$ can be approximated by finding the difference between the *TD* and *TS* measurement of a clear sample made from the same host material (PMMA) to isolate for the host diffusion. This value represents the scattering caused by the host material. This is depicted in **Figure 2.3**.

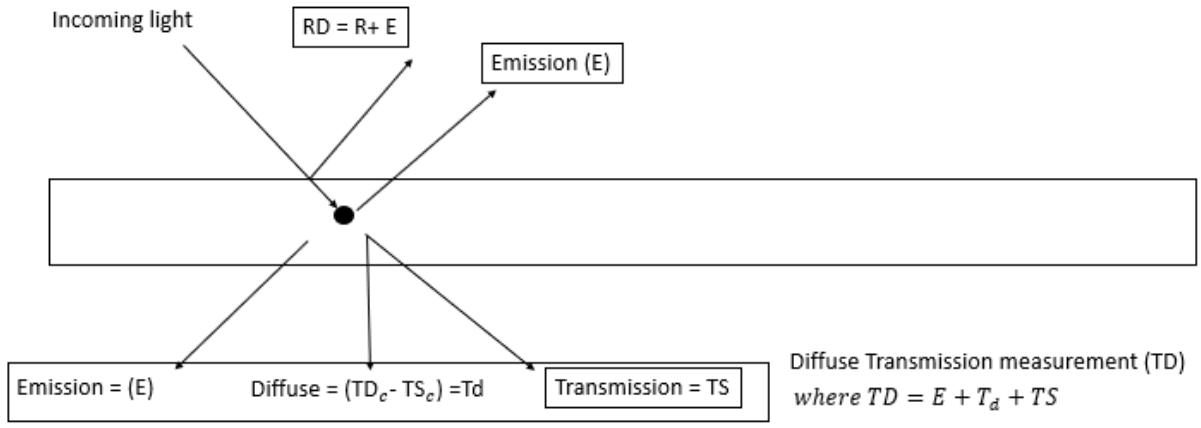


**Figure 2.3.** Light pathways through an LSC sample

Substituting into Equation 2.1, the equation for absorption becomes $Absoprtion = 100 - TD - RD + 2 * E$ where $E = TD - T_d - TS$. Substituting for *E* and noting that each measurement (*TD*, *TS* and *RD*) are functions of wavelength, this equation can be further combined to give Equation 2.2.

Equation 2.2

$$A_f(\lambda) = 100 - TS(\lambda) - RD(\lambda) + (TD(\lambda) - TS(\lambda)) - 2T_d(\lambda)$$

Noting that both the fluorescent dye and the acrylic matrix within the sheets contribute to the absorbance spectra, the absorbance for the clear sheet, $A_c(\lambda)$, was subtracted from the absorbance for each fluorescent sheet, $A_f(\lambda)$ to determine the amount of light captured by the dye, $A_{dye}(\lambda)$, as shown in Equation 2.3.

Equation 2.3

$$A_{dye}(\lambda) = A_f(\lambda) - A_c(\lambda)$$

The amount of light energy absorbed by the dye within each fluorescent sheet was determined as the summation of the incident light intensity at each wavelength, $I(\lambda)$, multiplied by the dye absorbance spectrum, $A_{dye}(\lambda)$. As shown in Equation 2.4 this summation is taken over the spectral region from $\lambda$ = 220 nm to 1400 nm to find the radiant power captured by the dye, $P_{dye}$.

Additionally, Equation 2.4 can be used to determine the radiant power absorbed by the clear acrylic (host) sheet, $P_{host(abs)}$, by substituting $A_c(\lambda)$ in place of $A_{dye}(\lambda)$.

Equation 2.4

$$P_{dye} = \sum_{\lambda=220\ \mathrm{nm}}^{1400\ nm} I(\lambda) \cdot A_{dye}(\lambda)$$

Only a portion of the light energy captured by the dye will make it to the edge of the fluorescent acrylic sheets due to emission, escape cone, and absorbance losses. Considering these losses, the amount of light power that propagates to the edge of the fluorescent LSC sheets, $P_{dye\text{-}Optical}$, is given by Equation 2.5.

Equation 2.5

$$P_{dye-\,Optical} = \eta_{dye-optical} \cdot \sum_{\lambda=220\ \mathrm{nm}}^{1400\ nm} I(\lambda) \cdot A_{dye}(\lambda)$$

Where $\eta_{dye-Optical}$, referred to herein as the optical dye efficiency (or just dye efficiency), is the efficiency with which light power absorbed by the dye is subsequently emitted and incident onto the edges, or sidewalls, of the fluorescent LSC sheets. Thus, $\eta_{dye-Optical}$ accounts for emission, escape-cone, and transmission losses in the host matrix. $\eta_{dye-Optical}$ can be determined experimentally using Equation 2.6 or by using Raytracer simulations.

Equation 2.6

$$\eta_{dye-Optical} = \frac{P_{edge(LSC)} - P_{edge(host)}}{P_{dye}}$$

$P_{edge\ (host)}$ is the power observed experimentally at the edge from a clear acrylic sheet and is caused by radiant power absorbed by the host matrix, $P_{host(abs)}$, which generates thermal energy, some of which will be conducted and transferred to the aluminum frame.

## 2.3 Economic Analysis Methods

A set of equations was created to investigate the effects of the integration of LSCs into greenhouses on profits. The model aims to set the groundwork for the basic design and estimation of LSC profits in greenhouses. The problem arises because larger LSC panels produce less electrical energy, due to increased transmission losses as emitted photons propagate within the LSC, but also require less frame structure which minimizes the amount of shading on crops. In contrast, decreasing the size of the LSC generates more electricity but reduces crop yields due to the increase in shading from the increased frame area required to support more panels. In practice, the thickness of the frames is going to be a set value based on structural requirements and the physical requirements of being able to hold the LSC panels with integrated solar cells and wiring. To find the results for a wide range of inputs, a set of equations was developed to estimate the electricity and crop yields for a given panel size and frame thickness, for a simple square greenhouse. The calculations and assumptions were programmed into MATLAB. The edge length of each panel as well as the frame thickness were set as vectors, with the results plotted in a 3D plot for both frame thickness and panel edge length. The goal was to estimate the profitability of LSC use in greenhouses and to demonstrate the impacts of design limits and choices, namely panel size and frame thickness. The results can be used as an estimate to determine the conditions under which LSCs are profitable, and how profitable they are. This represents a more in-depth profit analysis for LSC utilization in greenhouses than previously seen in the literature and highlights important design criteria for maximizing profit for a real greenhouse.

### 2.3.1 Calculations

The basic profit/cost function is given by Equation 2.7:

Equation 2.7

$$Profit = Yield_{electricity}(kWh) * Price_{electricity} + Yeild_{crop} * Price_{crop} - Cost_{operation}$$

The model uses a fixed sample roof area of 100 $m^2$ and it is assumed that the roof is square. The number of panels required for a specific frame thickness and panel size is calculated using

Equation 2.8. It is assumed that the LSC panels are square and that the frame thickness is uniform.

Equation 2.8

$$N_p = \frac{A_{roof}}{\left(L_{panel} + t_{frame}\right)^2}$$

The area of the framing is calculated by first determining the number of rows and columns to fill the square roof area based on the frame thickness and panel size.

Equation 2.9

$$N_r = \frac{\sqrt{A_{roof}}}{L_{panel} + t_{frame}}$$

Next, the length of the rows and columns need to be determined. To do this, the rows are taken to be full length (the span of the roof) and the columns are assumed to be interrupted by the rows to avoid double counting, as illustrated in **Figure 2.4**.

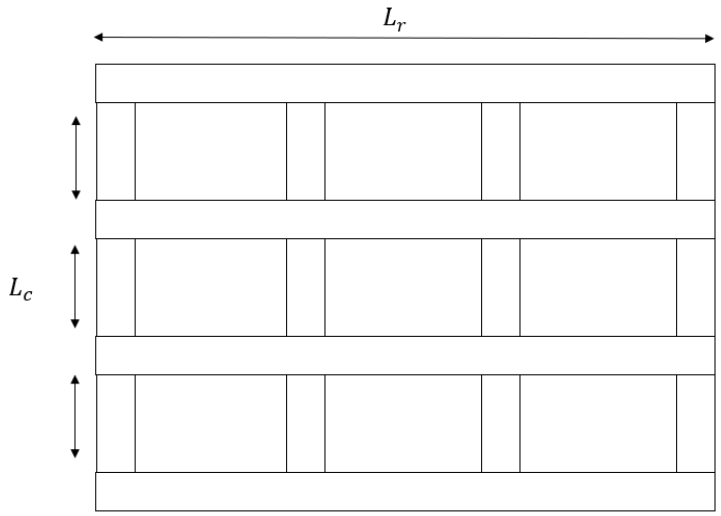


**Figure 2.4.** Frame layout for frame area calculations. The rows are shown to run the entire span whereas the columns are interrupted by the rows to avoid double counting the area.

The net length of the frames in the column is determined by multiplying the number of panels in a row by the length of each panel. Finally, the total area of the frame can be found using Equation 2.10

Equation 2.10

$$A_{frame} = t_{frame} * (N_r + 1) * (L_c + L_r)$$

The shading factor of the frame is then calculated by taking the ratio of frame area to the total roof area, as per Equation 2.11.

Equation 2.11

$$Shading\ \% = \frac{A_{frame}}{A_{roof}}$$

It has been widely accepted that the fraction of shading in greenhouses is equal to the fraction of lost profits. The model calculates the amount of shading based on the ratio of frame area to the roof area and uses that shading ratio to determine the decrease in crop yields. An additional parameter was included to ignore shading under a certain percentage, to account for the baseline shading from a traditional greenhouse. For example, if the ratio of structural members to the roof area for a traditional greenhouse is 10%, and the model allows for any shading less than 10% to not affect crop yields. Due to a lack of data on traditional frame shading, for the results presented herein, it is assumed that frame shading values of less than 10% do not reduce crop production. This would correlate to a greenhouse with 1 $m^2$ panels and ~5 cm thick frames. It is also assumed that the LSC panels themselves have a neutral effect on the crop yield, shading, and operating costs. This assumption is made based on the conclusions from several authors, such as Huyskens-Keil et al [47], who found an increase in tomato crop yields despite the addition of solar panels due to improved microclimates, R. Hassanien et al [48] who found that the addition of semi transparent solar panels into greenhouse roofs did not have a significant effect of tomato crop yields, and C. Corrado et al [27] who states that the integration of LSCs into greenhouses will likely have a neutral to slightly positive effect on crops, despite the removal of some photosynthetically active light.

### 2.3.2 Profit calculations: Electricity

The profit from electricity generation is calculated using the total LSC area, the monthly average irradiance, the respective electrical efficiency for the specified panel size, and the cost value of the produced electricity. The mean average irradiance tables were obtained from Natural Resources Canada and provide the monthly average irradiance for a south-facing roof with a tilt equal to the latitude in the Toronto, Ontario region [49]. When multiplied by the panel efficiency and total panel area, the number of kWh generated for that month can be estimated. The cost of electricity was varied depending on the peak wholesale rates of electricity in Ontario; 13.4 c/kWh in the summer and 9.4 c/kWh in the winter. The efficiency of the LSCs based on the edge length of a square PMMA panel was determined using L. R. Wilsons raytracer program [35] to plot the efficiency of a Lumogen Red 305 LSC over a range of edge lengths. The panel parameters were 3 mm thick PMMA with a dye concentration of 400 ppm. Polycrystalline Si-PV cells were coupled on all 4 edges of the LSC panel. 500,000 photons were generated for each simulation. The results from this plot are shown in **Figure 2.5**. Note that a sensitivity test was completed to determine the effects of changing the number of photons. Also, considering the probabilistic nature of the simulations, the variation in results from running the simulation with the same input parameters multiple times was monitored. Running the simulation with the same input setting over 5 iterations resulted in a standard deviation for the efficiency of 0.018% using 500,000 photons. Doubling the number of photons used in the simulation and repeating for 5 iterations, the standard deviation was reduced to 0.0064 and resulted in a difference between the average of the two samples of 0.007 % efficiency. This is smaller than the number of significant digits used, thus verifying that 500,000 photons and 1 simulation run is appropriate. A polynomial function was fit to the plot of the electrical efficiency as a function of the side length of the LSC, and the coefficient of determination (or $R^2$ value) was 0.99. This function, shown in **Figure 2.5**, is used to approximate the efficiency of the LSC panels at any size, although extremely small sizes or sizes larger than $4m^2$ should be used with caution.

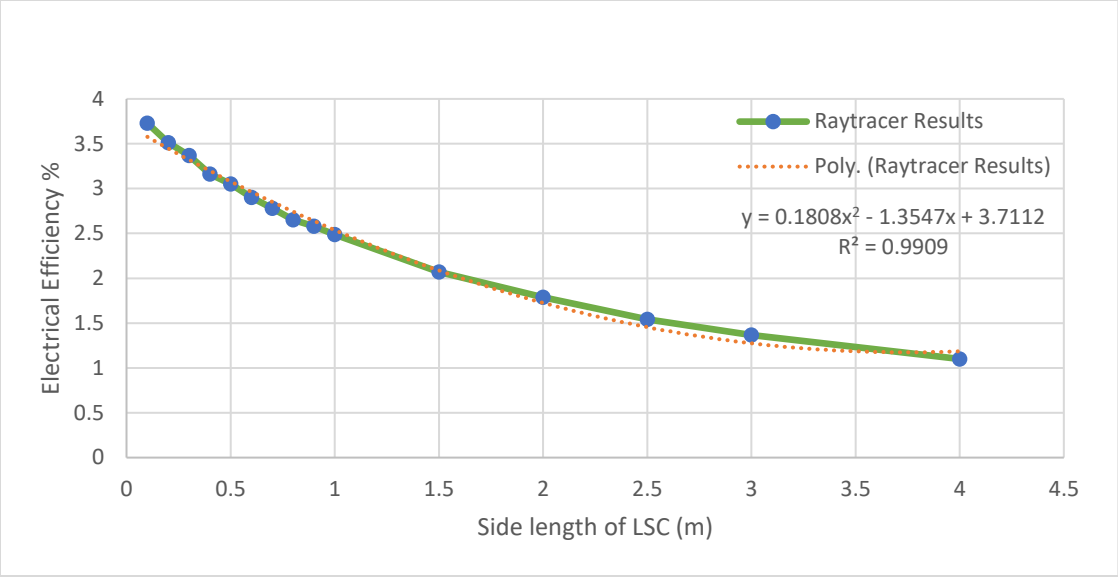


**Figure 2.5**. Raytracer results for the electrical efficiency of a square LSC panel using Lumogen Red dye. A polynomial function is shown along with the $R^2$ value.

Additionally, the model allows for the exposed frame to be covered with solar cells to produce additional electricity. The cells are assumed to be Si-PV with an efficiency of 18%.

### 2.3.3 Profits: Crops

The profit estimates from the crops are determined by taking the average crop value produced in Ontario and reducing the value based on the estimated reduction in yield due to shading, where the reduction in yield is determined by (100 % - % shading). As discussed previously, a buffer of 10% is added to account for frame shading of a traditional greenhouse. Using data obtained from Alberta.ca [50] it was found that tomato crops (a common greenhouse crop) produce between 50 to 70 kg of tomatoes per $m^2$ on an annual basis, depending on the grower's skill and setup. The median value of 60 kg/$m^2$ was chosen to represent the yield of tomatoes. Stats Canada: "Area, production and farm gate value of marketed fruits" [51] reports an average farm gate value of $2 per kg of tomatoes resulting in a net crop value of $120/$m^2$. Additionally, the net profit of a greenhouse can be estimated by deducting the operating costs. The operating costs of a greenhouse obtained from Stats Canada: "Greenhouse, Sod and Nursery Industries" [52] was found to be $101.33 /$m^2$.

## 2.4 Results and Discussions

### 2.4.1 Spectral modeling results

**Figure 2.6** shows the measured transmission spectrum for each sample of coloured acrylic. **Figure 2.7** shows the resulting dye absorption spectrum calculated from the transmission and reflection spectra. The absorption spectrum from the red fluorescent sample falls closest to the area of reduced photosynthetic efficiency shown in **Figure 2.1** thus making it the most suitable candidate for use in greenhouse roofs.

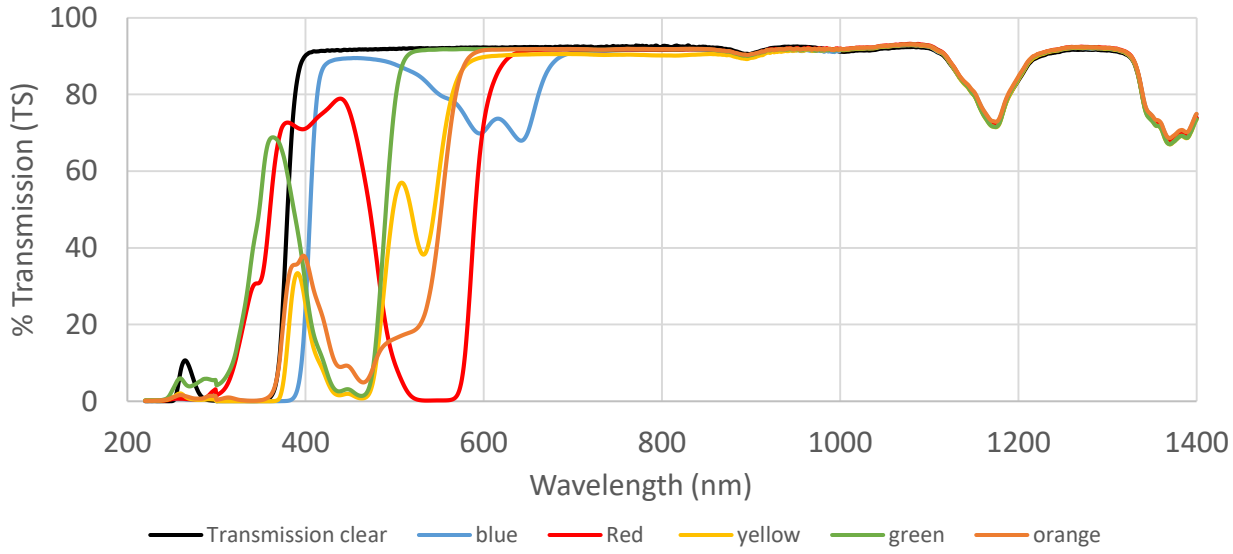


**Figure 2.6.** Measured transmission (TS) from each fluorescent sample

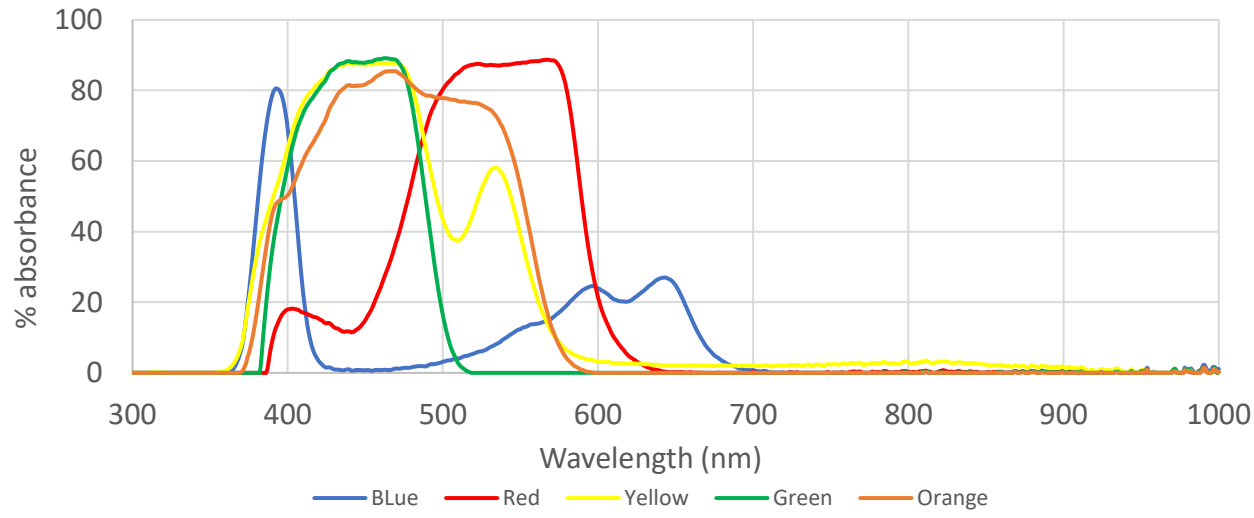


**Figure 2.7.** $A_f(\lambda)$ for each fluorescent sample

There is ~160 W/m$^2$ of light available from the AM 1.5 Solar spectrum between 575 nm and 700 nm. Using spectral modeling methods for the red fluorescent sample, it is estimated that an additional 17.41 W/m$^2$ of light between 575 and 700 nm will enter the greenhouse due to escape losses of photons emitted from the dye within the red acrylic LSC panel (12.14% increase). According to a study by K.J McCree [53] on the action spectrum of photosynthesis in crop plants, the average relative action for tomato crops is 0.475 for light between 400 nm to 500 nm, 0.645 for light between 500 nm to 600 nm and 0.9725 for light between 600-700 nm. The relative action is the rate at which carbon dioxide is taken up divided by the amount of energy received by the leaf [53]. Note that the action spectrum for blue light is relatively low, likely because the photons carry more energy than needed to drive the reaction resulting in heat generation and reduced energy efficiency. Using the transmission and absorption spectra for a red LSC panel and using Equation 2.3 and Equation 2.4 a red LSC will block 139.28 W/m$^2$ and transmit 208.15 W/m$^2$ (400-700 nm). An additional 17.41 W/m$^2$ (25%*0.5*139.28) of red light with a wavelength of ~622 nm will be transmitted due to escape cone losses. The transmitted light from a red panel and its relative action is compared against the transmission and relative action from a plexiglass (clear) panel in **Table 2.1**.

**Table 2.1** Relative photosynthetic action in a greenhouse using LSCs

| Wavelength (nm) | Transmission LSC (W/m$^2$) | Transmission clear (W/m$^2$) | Relative Action (%) ($CO_2$ uptake/energy) | Photosynthetic action LSC | Photosynthetic action (Clear) |
|---|---|---|---|---|---|
| 400-500 | 69.26 | 105.99 | 0.475 | 32.89 | 50.34 |
| 500-600 | 25.96 | 124.39 | 0.645 | 16.74 | 80.23 |
| 600-700 | 115.31 + 17.41 | 117.1 | 0.972 | 129.00 | 113.82 |
| sum | 225.56 | 345.79 | | 178.63 | 244.39 |

This indicates that the use of a red LSC panel will result in 73.1% of the photosynthetic action of a clear panel, a 27% decrease in net photosynthetic action, and a net 35% shading factor. Despite a lower photosynthetic action from this analysis, multiple other parameters influence the crop

yield, as discussed previously. Multiple studies have shown increased crop yields despite reduced irradiance. A study by D. Dannehl et al [47] found a 31.8% increase in crop yield despite an 11% shading factor. A. Baille et al [54] observed increased crop health after using a shading technique called whitening with a net decrease in solar irradiance of 50% during periods of high solar irradiance. R. Hassanien et al [55] observed no decrease in the growth rate of lettuce plants under a 40% high shading value than a traditional polyethylene greenhouse, caused by integrating semi-transparent solar cells into the roof of a greenhouse. In a separate study, R. Hassanien et al [48] showed no impact on tomato yields despite a 40% higher shading compared with a polyethylene cover. Additional studies have also noted similar effects, wherein shading has resulted in either a beneficial or negligible effect on crop yields [56] [57]. For comparison, whitening is a technique often used to provide shade and reduce temperatures in the greenhouse, with common shading values up to 40% [58]. These results go against the general rule of thumb that 1% shading = 1% decrease in crop yields, however, these studies all improve the internal micro-climate of the greenhouse thus mitigating the effects of shading. Note that previous authors, such as C. Corrado et al [27] have made the assumption that LSC panels will have a neutral to positive effect on greenhouse crops. These results neither support nor disprove that assumption and thus a dedicated study that compares the crop yields from a greenhouse using red LSC panels to a control greenhouse should be completed.

### 2.4.2 Profit estimation results

The results are shown in **Figure 2.8**, **Figure 2.9**, and **Figure 2.10** which illustrate the increase/decrease in profit and shading of a greenhouse as a function of panel size and frame thickness. The results shown in these figures were determined assuming the greenhouse roof area is 100 $m^2$, the frame thickness varies between 0.01 and 6 cm, and the LSC panel side length varies between 0 and 2 m. It is assumed that shading less than 10% does not reduce crop yields. All values are expressed per $m^2$.

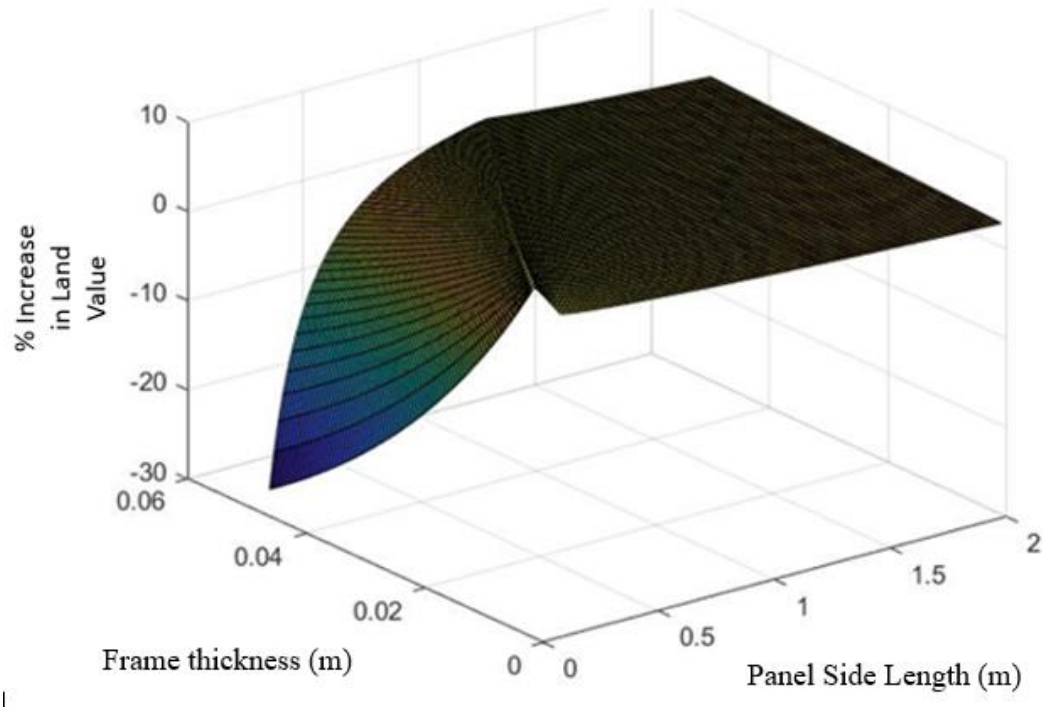


**Figure 2.8.** The % increase in land value as a function of frame thickness and panel size.

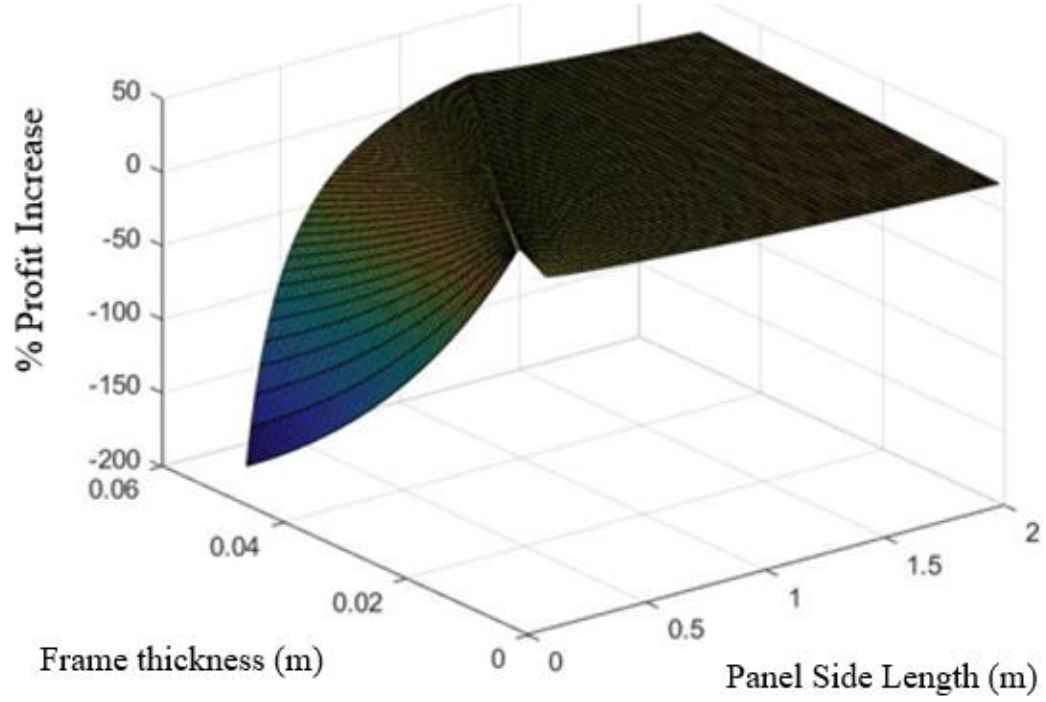


**Figure 2.9.** The % increase in final profit (after expenses) as a function of frame thickness and panel length.

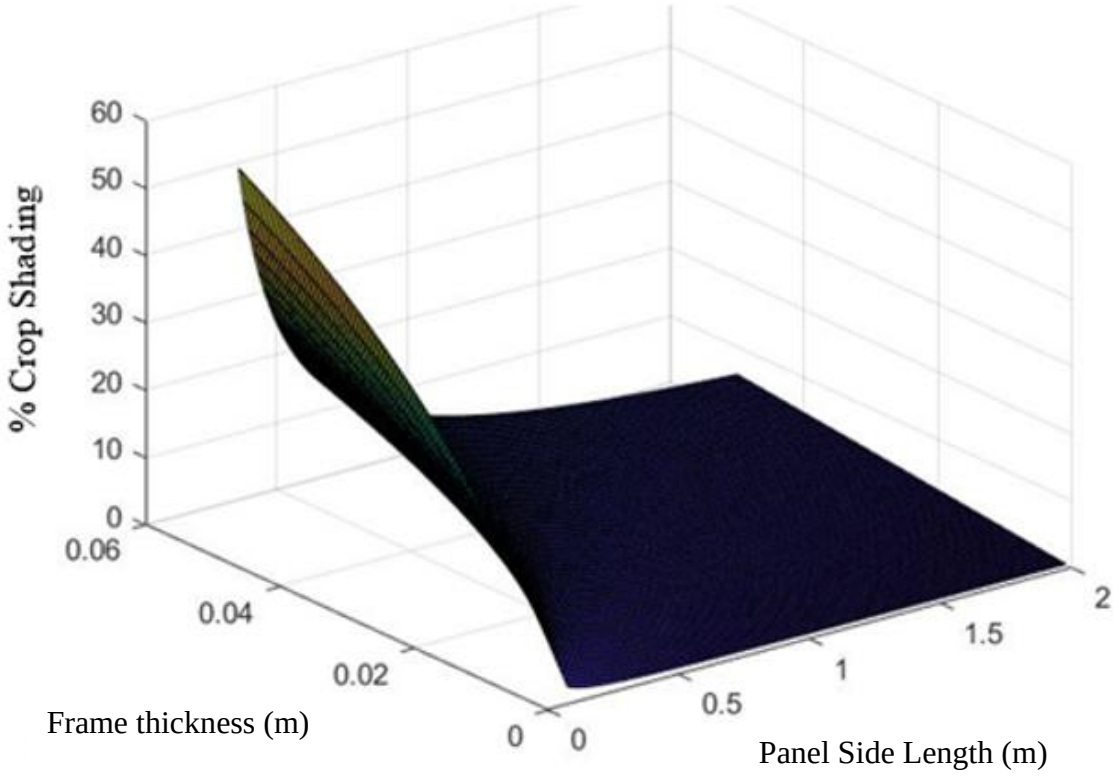


**Figure 2.10**. Image showing the % of shade generated as a function of panel length and frame thickness

As expected, as the panel size decreases and the frame coverage increase, the amount of shading increases steeply, resulting in a decreased profit and land value. In contrast, as the size of the panels increases, the effects of the frame become less significant due to the decreased number of panels and thus the amount of frame area required, but so does the profits from the electricity, thus the profit approaches the baseline crop profits. An optimal peak exists at which the maximum profits increase occurs. It is assumed that frame thickness will be a non-controllable aspect of the design, and thus for a required frame thickness, an optimal panel side length can be found which correlates to the maximum increase in profits. Note the profit increase refers to the increase or decrease in the net profit after expenses in the greenhouse where the land value gains represent the increase in the net value of the land per square meter. Adjusting the range for a more realistic scenario in which the minimum panel length is 0.5 m, the plots shown in **Figure 2.11** are created.

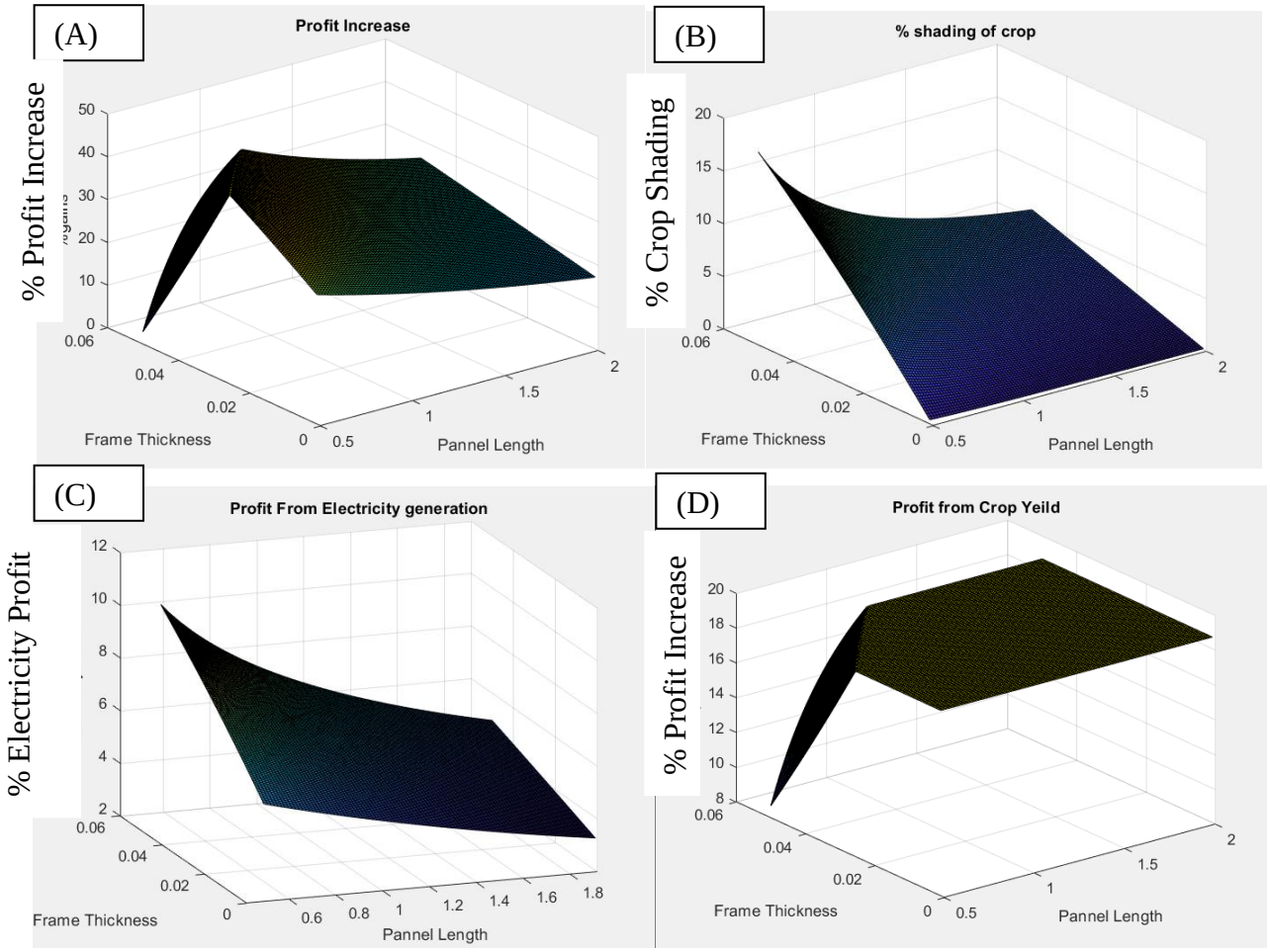


**Figure 2.11.** Greenhouse LSC results. (A) shows the % increase in profits (after expenses) for a greenhouse as a function of frame thickness and panel size. (B) shows the amount of shade generated as a function of frame thickness and panel size. (C) show the profits directly generated from the electrical generation of the LSC and (D) shows the profits generated from the crop yield.

The largest profit increase occurs when the panel length is 0.5 m and the frame thickness is 0.025 m. Under these parameters, the crop yield is 60 kg/$m^2$ or \$120/$m^2$. The electricity generated is 6671.84 kWh/year with an estimated value of \$7.6 / $m^2$. This represents a 6.3% increase in revenue. If operating costs are included, (\$101/$m^2$ ) the net profit without the electricity is \$18.67/$m^2$ and \$26.3/$m^2$ with the electricity generation, representing a 40.7% increase in profits.

The increased frame thickness generates increased profits due to the PV cells on its surface, up until it reaches the 10% shading value at which the crop yield begins to decrease. If the simulation is run without solar cells on the frame, the maximum profit gains decrease to 29% ($24.0/m$^2$, with $18.67 /m$^2$ profit generated by the crop and $5.3/m$^2$ generated from electricity) for a frame with the minimum thickness of 0.001 m and remains relatively steady until the frame thickness reaches 0.025 m (26% profit gains, $23.5 /m$^2$, with $4.9/m$^2$ generated from electricity), at which point it drops drastically. The results show that panels up to 2 $m^2$ in size can generate a 26% increase in profits for a greenhouse with PV cells on the frame and 17% without them.

## 2.5 Conclusions

This chapter builds the case for LSC integration into greenhouse roofs by showing that red LSCs may form a symbiotic relationship with the crops allowing for both improved microclimate due to reduced temperatures and thus ventilation times. When using spectral modeling to estimate the effect of using red LSCs on the photosynthetic action of crops, it was found that the addition of commercially purchased red fluorescent panels resulted in a 35% shading factor. This shading value is similar to the shading factor from commonly used techniques, such as whitening, which is used during hot months and can provide shading values of higher than 40%. However, due to the selective properties, the LSC reduces the net photosynthetic action of the crops by 27% (at 35% shading), rather than by 1% for each percent of shading caused by traditional shading methods, such as whitening. This indicated that the LSCs may improve the crop yields when compared to crops grown in greenhouses that utilize high whitening values due to reduced disruption on the photosynthetic action over traditional shading methods. The review of microclimates in greenhouse indicated that the shading caused by LSCs may improve the crop yield when compared to non shaded greenhouses in hot climates due to improved microclimate from shading, which is supported by various studies, although a real world comparison study should be conducted to authenticate this conclusion. It should be noted that the dye concentration used in the LSCs could be varied causing different amounts of shading and effecting LSC collection performance. Finally, it is worth pointing out that traditional shading techniques have the advantage of being removable, thus allowing them to be used only when required; in contrast, LSCs may be integrated into greenhouse rooftops as a permanent fixture, which would limit their suitability to hot, sunny climates.

The profit simulation analysis shows that the integration of LSCs into a theoretical greenhouse can raise the profits from a greenhouse by as much as 40.7% of the generated electricity is sold at wholesale Ontario prices, under the assumptions described. The model demonstrates the relationship between panel size and frame thickness and their impacts on profits and crop yields. This provides a useful tool in designing the parameters for a real greenhouse and supports the idea that LSCs can increase profits for greenhouses under certain conditions. Future work to build and test a greenhouse with integrated LSC panels should be completed to determine the actual crop yields and electrical yields; the methods above can provide a starting place.

The use of LSCs in greenhouses has thus been shown to be worth further investigation, especially when used in hot, sunny conditions and as such, further research into the implementation of such a system should be conducted with a focus on electricity output and crop yields. It is suggested that two similar greenhouses be constructed, one using a traditional roof, and one using an LSC roof, where crop yields from each greenhouse could be studied and compared, along with electricity production, thus laying the groundwork for future commercialization and implementation in the climate zone.

The need for a system in which to track the energy flow through an LSC can be of vital use in designing and analysing the suitability of LSCs for specific applications. A preview of the usefulness of such a system was demonstrated by using the transmission through an LSC panel was used to predict the photosynthetic action of crops. More work on this modeling system to experimentally determine the dye efficiency and modeling accuracy is conducted in later chapters. Additionally, the fluorescent acrylic used in the analysis within this chapter should be verified for suitability as an LSC, as done in the next chapter. Combined, this allows for the investigation into additional applications for LSCs, such as thermal collectors and transparent windows.

# 3. Fabrication and Testing of PMMA Based LSCs

## 3.1 Introduction

This chapter details the testing of LSCs to determine the ability to use commercially available fluorescent acrylic for fabricating LSC modules in place of fabricating LSCs in the lab. Initially, traditional methods of creating LSC waveguides were explored in the lab, such as PMMA polymerization casting, spin coating and custom mould casting; however, various defects were present, and the size was limited by available lab equipment. The methods and results used for fabricating LSCs in the lab are described in full in

# 4. References


[1] EIA. Energy Information Administration, "International Energy Outlook 2019," EIA, 2019.

[2] J. Tsao, N. Lewis and G. Crabtree, "Solar FAQs," U.S Department of Energy, 2006.

[3] IEA, "World Energy Outlook 2019," IEA, 2019. [Online]. Available: https://www.iea.org/reports/world-energy-outlook-2019/electricity. [Accessed 12 05 2020].

[4] R. F. Service, "Skyscrapers could soon generate their own power, thanks to see-through solar cells.," Science, AAAS, 28 june 2018. [Online]. Available: https://www.sciencemag.org/news/2018/06/skyscrapers-could-soon-generate-their-own-power-thanks-see-through-solar-cells. [Accessed 12 05 2020].

[5] International Energy Agency, "Energy Efficiency, Buildings," Availible: https://www.iea.org/topics/energyefficiency/buildings, 2019.

[6] Office of Energy Efficiency, "Energy Efficiency Trends In Canada 1990 to 2013," Natural Resources Canada, 2016.

[7] U.S Department of Energy., 2011 Buildings Energy Data Book, 2001.

[8] P. Emrath and J. Miller, "How much Energy Homes Use and Why," National Association of Home Builders, 2014.

[9] NREL, "Estimating Rooftop Suitability for PV: a Review of Methods, Patents and Validation Techniques," NREL, Denver, 2013.

[10] CSIRO, "Windows will soon generate electricity," CSIRO, April 2020. [Online]. Available: https://www.csiro.au/en/News/News-releases/2020/Windows-will-soon-generate-electricity. [Accessed 12 05 2020].

[11] "Solar Window Technologies," Solar Window Technologies, [Online]. Available: https://www.solarwindow.com/technology/. [Accessed 12 05 2020].

[12] C. J. Traverse, R. Pandey, M. C. Barr and R. R. Lunt, "Emergence of highly transparent photovoltaics for distributed applications," *Nature Energy*, vol. 2, pp. 849-860, 2017.

[13] J. Yu, J. Sun, N. Chandrasekaran, C. Dunn, A. Chesman and J. Jasieniak, "Semi-transparent Perovkite solar cells with a cross-linked hole transport layer," *Nano Energy,* no. https://doi.org/10.1016/j.nanoen.2020.104635, 2020.

[14] A. Goetzberger and V.Wittwer., "Flourescent planar collector-concentrators: A Review.," *Solar Cells,* vol. 4, no. 3, p. 23, 1981.

[15] A. Goetzberger, "Thermal Energy Conversion With Fluorescent Collector-Concentrators," *Solar Energy ,* vol. 22, pp. 435-438, 1979.

[16] A. P. Green, "Optical Properties of Luminescent Solar Concentrators," in *University of Sheffield*, England, 2014.

[17] L. R. Wilson, B. C. Rowan, N. Robertson, B. Richards, A. C. Jones and O. Moudam, "Characterization and reduction of re-absorption losses in luminescent solar concentrators," *Applied Optics*, vol. 49, no. 9, pp. 651-1661, 01 03 2010.

[18] B. S. Richards and K. R. McIntosh, "Ray-tracing simulations of luminescent solar concentrators containing multiple luminescent species," *Proceedings of the 21st EU PVSEC, Dresden,* pp. 185-188, 2006.

[19] M. Gajic and G. Rosengarten, "Non-imaging technologies for designing a hybrid photovoltaic and solar thermal collector," *RMIT University, Thesis. ,* 2018.

[20] G. Griffini, L. Brambilla, M. Levi, M. DelZoppo and S. Turri, "Photodegradation of a perylene-based organic Luminescent solar concentrator: Molecular Aspects and device implications," *Solar Energy Materials and Solar Cells,* vol. 111, pp. 41-48, 2013.

[21] J. R. Lakowicz, "Introduction to," in *Principles of Fluorescence Spectroscopy*, Springer US, 2006, pp. 1-23.

[22] F. Holtrup, G. M• uller, S. H. Quante, d. Feyter, F. d. Schryver and k. Mullen, "Terrlenimides: New NIR flourescent dyes.," *Chem. EUR. J. ,* vol. 3, no. 2, pp. 219-225, 1997.

[23] F. Nolde, J. Qu, C. Kohl, N. Pschinirer, E. Reuther and K. Mullen, "Synthesis and modification of terrylenendiimides as high-performance fluorescent dyes.," *Chem. Eur. J.,* no. 11, pp. 3959-3967, 2005.

[24] G.Wagenblast and G.Seybold, "New Perlene and Violanthrone Dyestuffs for Flourescnets collectors.," *Dyes and Pigments,* vol. 11, pp. 303-317, 1989.

[25] R. Sah and G. Baur, "Influence of the solvent matrix on the overlapping of the absorption and emission bads of soulte fluorescnet dyes.," *Appl. Phys.,* vol. 23, pp. 369-372, 1980.

[26] W. G. v. Stark, K. W. J. Barnham, L. H. Slooff, A. J. Chatten, A. Buchtemann, A. Meyer, S. J. McCormack, R. Koole, D. J. Farrell, R. Bose, E. E. Bende, A. R. Burgers, T. Budel and J. Quilitz, "Luminescent solar concentrators- A review of recent results," *Optics Express,* vol. 16, no. 26, pp. 21773-21792, 2008.

[27] C. Corrado, S. W. Leow, M. Osborn, I. Carbone, K. Hellier, M. Short, G. Alers and S. A. Carter., "Power Generation Study of Luminescent Solar Concentrator Greenhouse," *Renewable Sustainable Energy,* vol. 8, no. 043502-10, 2016.

[28] BASF, "Lumogen F Dyes," BASF, [Online]. Available: http://www2.basf.us/additives/pdfs/lumvio570.pdf. [Accessed 20 03 2020].

[29] L. R. Wilson, "Luminescent Solar Concentrators: A study of Optical properties re-absorbtion and device optimization," *Heriot-Watt University, School of Engineering and Physical Sciences,* vol. Doctor of Philosphy Thesis Submission, 2010.

[30] A. Zastrow, "Ph.D Thesis," *Frieburg,* 1981.

[31] M. Currie., "High-efficiency organic solar concentrators for photovoltaics," *Science,* vol. 321, no. 226, 2008.

[32] L. Sloof, E. Bende, A. Burgers, T.Budel, M.Pravettoni, R. Kenny and E. Dunlop, "A luminescent solar concentrator with 7.1% power conversion efficiency," *Phys. Stat. Sol. (RRL),* vol. 2, no. 6, pp. 257-259, 2008.

[33] L. Slooff, R. Kinderman, A. Burgers, A. Buchtemann, R.Danz, T. Meyer, A. Chatter, D. Farrell, K. Barnham and J. V. Roosmalen, "The luminescent concentrator illuminated," *Proc. SPIE 6197 Photonics for Solar Energy Systems,* 2006.

[34] M. Kastelijn, M. Bastiaansen and C. Debije, "Influence of waveguide material on light emission in luminescent solar concentrators," *Optical Materials,* vol. 31, no. 11, pp. 1720-1722, 2009.

[35] L. R. Wilson, *LSC Simmulation Code.,* 2010.

[36] C. Tummeltshammer, A. Taylor, A. Kenyon and I. Papkonstantinou, "Losses in Luminescent Solar Concentrators Unveiled," *Solar Energy Materials and Solar Cells,* vol. 144, pp. 40-47, 2016.

[37] C.Honsberg and S. Bowden, "IV curve," PV Education, 2019. [Online]. Available: https://www.pveducation.org/pvcdrom/solar-cell-operation/iv-curve. [Accessed 23 03 2020].

[38] C. Honsberg and S. Bowden, "PV Education - Spectral Response," [Online]. Available: https://www.pveducation.org/pvcdrom/solar-cell-operation/spectral-response. [Accessed 29 3 2020].

[39] L. R. Wilson and B. Richards, "Measurement method for PLQY of fluorescent organic dyes," *Applied Optics,* vol. 48, pp. 212-220, 2009.

[40] J. Mugnier, Y.Dordet, J. Pouget and B. Valeur, "A photometric approach of fluorescent solar Concentrators. Role of Diffuse Reflectors and Spectral Sensitivity of Solar Cells," *Revue Phys. Appl.,* vol. 22, pp. 89-100, 1987.

[41] R. Nave, "Light Absorption for Photosynthesis," HyperPhysics Project, Georgia State University, [Online]. Available: http://hyperphysics.phy-astr.gsu.edu/hbase/Biology/ligabs.html. [Accessed 29 07 2020].

[42] R. Hassanien, E. Hassanien, M. Li and F. Yin, "The integration of semi-transparent photovoltaics on greenhouse roof for energy and plant production," *Renewable Energy,* vol. 121, pp. 377-388, 2018.

[43] D. R. Holding and A. M. Striech, "Plant Growth Processes: Transpiration, Photosynthesis and Respiration," University of Nebraska, 2013.

[44] O.Korner, E. HeuVelink and Q.Niu, "Quantification of temperature, CO2 and light effects on crop photosythesis as a basis for model-based greenhouse climate control," *Journal of Horticultural science and biotechnology,* vol. 84, no. 2, pp. 233-239, 2009.

[45] K. Aberkani, X. Hao, D. d. Halleux, M. Dorais, S. Vineberg and A. Gosselin, "Effects of Shading Using a Retractable Liquid Foam Technology on Greenhouse and Plant Micro-Climates," *HorTechnology,* vol. 20, no. 2, pp. 283-291, 2010.

[46] R. Hassanien and E. Hassanien, "Influences of greenhouse-integrated semi-transparent photocoltaics on microclimate and lettuce growth," *International Journal of Agricultural and Biological Engineering,* vol. 10, no. 6, pp. 11-20, 2017.

[47] D. Dannehl, J.Suhl, S. Huyskens-Keil, C. Ulrichs and U. Schmidt, "Effects of a special solar collector greenhouse on water balance, fruit quantity and fruit quality of tomatoes," *Agricultural Water Management.,* vol. 134, pp. 14-23, 2014.

[48] R. Hassanien, M. Li and F. Yin, "The integration of semi-transparent photovoltaics on greenhouse roof for energy and plant production," *Renewable Energy,* no. https://doi.org/10.1016/j.renene.2018.01.044, 2018.

[49] NRC, "Photovoltaic and Solar Resource Maps," Natural resources Canada, 2019. [Online]. Available: https://www.nrcan.gc.ca/18366. [Accessed 04 02 2019].

[50] "Commercial Greenhouse Tomato Production," Alberta, [Online]. Available: https://www.alberta.ca/commercial-greenhouse-tomato-production.aspx. [Accessed 02 02 2019].

[51] Statistics Canada, "Table 32-10-0364-01. Area, Production and farm gate value of marketed fruits," [Online]. Available: https://doi.org/10.25318/3210036401-eng.

[52] Statistics Canada, "Tables 22-202-X; Greenhouse, Sod and Nursery Industries," Stats Canada, 2018. [Online]. Available: https://www150.statcan.gc.ca/n1/en/catalogue/22-202-X. [Accessed 02 02 2019].

[53] K. Mcree, "The Action Spectrum, Absorbance and Quantum Yield of Photosynthesis in Crop Plants," *Agric. Meterol. ,* vol. 9, pp. 191-216, 1970.

[54] A. Baille, C. Kittas and N. Katsoulas, "Influence of whitening on greenhouse microclimate and crop energy partitioning," *Agricultural and Forest Meteorology,* vol. 107, no. 01681923, pp. 293-306, 2001.

[55] R. Hassanien, E. Hassanien and L. Ming, "Influences of greenhouse-integrated semi-transparent photovoltaics on microclimate and lettuce growth," *Int J Agric & Biol Eng,* vol. 10, no. 6, 2017.

[56] M. Cossu, L. Murgia, L. Ledda, P. Deligios, A. Sirigu, F. Chessa and A. Pazzona, "Solar radiation distribution inside a greenhouse with south-oriented photovoltaic roofs and effects on crop productivity," *Applied Energy,* 2014.

[57] Y. Araki and S. I. k. Murakami, "Effects of Shading on Suimmer Spinach," *Journal of Agricultural Engineering,* 2017.

[58] M. d. l. Á. Moreno-Teruel, D. Valera, F. D. Molina-Aiz, A. López-Martínez, A. Peña, P. Marín and A. Reyes-Rosas, "Effects of Cover Whitening Concentrations on the Microclimate and on the Development and Yeild of Tomato Inside Mediterranean Greenhouses," *Agronomy,* vol. 10, no. 237, 2020.

[59] B. Rowan, L. R. Wilson and B. Richards, "Advanced Material concepts for Luminescent Solar Concentrators," *IEEE Journal of Selected Topics in Quantum Electronics,* vol. 14, no. 5, pp. 1312-1322, 2008.

[60] L. Desmet, A. J. M. Ras, D. k. .. deBoer and M. Debijie, "Monocrystalline silicon photovoltaic luminescent solar concentrator with 4.2% power conversion efficiency," *Opt. Lett. 37, 3087-3089 (2012).*

[61] B. Wishwanathan, A. reinders, D. deBoer, L. Desmet, A. Ras, F. Zahn and M. Debije, "A comparison of performance of flat and bent photovoltaic luminescent solar concentrators," *Solar Energy,* vol. 112, pp. 120-127, 2015.

[62] W. G. A. Geotzberger, "Solar Energy Conversion with Flourescent Collectors," *Appl. Phys.,* vol. 14, pp. 123-139, 1977.

[63] W.Stahl, V.Wittwer and A.Goetzberger, "Thermal Conversion With Fluorscent concentrators," *Solar Energy Vol. 36,* vol. 36, no. 1, pp. 27-35, 1986.

[64] A.Goetzberger, "Thermal Energy Conversion With Fluorescent Collector-Concentrators," *Solar Energy,* vol. 22, pp. 435-438, 1979.

[65] C. T. O'Sullivan, "Newtons Law of Cooling- A critical Assessment,," *AM.J Phys.,* vol. 58, no. 10, p. 956.

[66] M. Vollmet, "Newton's Law of Cooling Revisted," *Eur. J. Phys.,* pp. 10063-1084, 2009.

[67] A.Goetzberger and V.Wittwer., "Flourescent planar collector-concentrators: A Review.," *Solar Cells,* vol. 4, no. 3, p. 23, 1981.

[68] Arkema, "Plexiglas," Altuglas Internation. Arkema Inc. , Philadelphia, 2000.

[69] W. Stahl, V.Wittwer and A. Goetzberger, "Thermal Conversion With Fluorscent concentrators," *Solar Energy Vol. 36,* vol. 36, no. 1, pp. 27-35, 1986.

[70] J. A. Duffie and W. A. Beckman, Solar Engineering of Thermal Processes, Fourth Edition, US: John Wiley & Sons., 2013.

[71] NREL, "Reference Solar Spectral Irradiance: ASTM G-173," Gov., [Online]. Available: https://rredc.nrel.gov/solar//spectra/am1.5/ASTMG173/ASTMG173.html. [Accessed 01 08 2019].

[72] NREl, "Reference Solar Spectral Irradiance: ASTM G-173," [Online]. Available: https://rredc.nrel.gov/solar//spectra/am1.5/ASTMG173/ASTMG173.html. [Accessed 05 11 2019].

[73] Energy Star, "ENERGY STAR® for Windows, Doors, and Skylights Version 6.0".

[74] R. L. a. B. Krittakom, "A study: Thermal Efficiency of Solar Air heater with Wire mesh Stainless Installation: Using Solar Simulator," *Journal of Physics: Conference Series,* vol. 1039 012044, 2018.

[75] E. Loh and D. Scalapino, "Luminescent solar concentrators: effects of shape on efficiency," *Appl. Opt.,* vol. 25, no. 2, pp. 1901-1907, 1986.

[76] M. S. D. Cardona, M.Carrascosa, F. Meseguer, F. Cusso and F. Jaque, "Edge Effect on Luminescent Solar Concenctrators," *Solar Cells,* vol. 15, pp. 225-230, 1985.

[77] ThorLabs, [Online]. Available: Thorlabs.com. [Accessed 08 2019].

[78] "Flourescent Acrylic - Alibaba," 20 01 2020. [Online]. Available: https://www.alibaba.com/trade/search?fsb=y&IndexArea=product_en&CatId=&SearchText=fluorescent+acrylic.

[79] F. Struckmann, "Analysis of a Flat-plate Solar Collector," *Heat and Mass Transport,* 2008.

[80] E. E. a. R. E. U.S Department of Energy, "Energy Efficiency Trends in Residential and Commercial Buildings," U.S Department of Energy, 2008.

[81] G. Liu, R. Mazzaro, Y. Wang, H. Zhao and A. Vomiero, "High Efficiency sandwich structure luminescent solar concentraotrs based on colloidal quantum dots," *Nano Energy,* vol. 60, pp. 119-126, 2019.

[82] N. Aste, L. Tagliabue, C. Pero and D. T. R. Fusco, "Performance analysis of a large-area luminescent solar concentrator module," *Renewable Energy,* vol. 76, pp. 330-337, April 2015.

[83] L. Witmer, Solar Thermal Energy for Utilities and Industry, PennState, Department of Energy and Mineral Engineering, 2013.

[84] H. Bhowmilk and R. Amin, "Efficiency Improvement of flat plate solar collector using reflector," *Energy Reports,* vol. 3, pp. 119-123, 2017.

[85] S. Agbo and E. Okoroigwe, "Analysis of Thermal Losses in the Flat-Plate Collector of a Thermosyphon Solar Water Heater," *Research Journal of Physics,* vol. 1, pp. 35-41, 2007.

[86] L. &. B. A. &. D. M. Slooff, "Reduction of escape cone losses in luminescent solar concentrators with cholosteric mirrors.," *Proc SPIE,* no. 10.1117/12.794522. , 2008.

[87] "Fluorescence guide," Abcam, 2020. [Online]. Available: https://www.abcam.com/secondary-antibodies/fluorescence-guide. [Accessed 18 03 2020].

[88] J. R. Lakowicz, "Principles of Flourescence Spectroscopy," vol. 3, Springer Science + Business Media, 1983.

[89] G. S. a. G. Wagenblast., "New perylene and violanthrone dyestuff for flourescent collectors.," *Dyes and pigments,* vol. 11, pp. 303-317, 1989.

[90] M. Debije, K. -P. Tuenissen, M. Kastelijin, P. Verbunt and C. Bastiaansen., "The effect of a scattering layer on the edge output of a luminescent solar concentrator," *Solar Energy Materials and Solar Cells,* vol. 93, pp. 1345-1350, 2009.

[91] L. H. Slooff, E. E. Bende1, A. R. Burgers, T. Budel, M. Pravettoni, R. P. Kenny and E. D. Dunlop, "A luminescent Solar Concentrator with a 7.1% power conversion Efficiency," *Phys. Stat. Sol,* vol. 2, no. 6, pp. 257-259, 2008.

[92] Lexico, "UK Dictionary: Definition: Quantum Dot," Oxford. [Online].

[93] M. Samadpour, "Efficiency of CdS/CdSe/ZnS quantum dot sensitized solar cells perpared by ZnS Treatment from methanol Solvent," *Solar Energy,* vol. 144, pp. 63-70, 2016.

[94] M. G. Hydahl, S. T. Bailey and B. P. Wittmershaus, "Photo-stability and performance of CdSe/ZnS quantum Dots in Luminescent Solar Concentrators," *Solar Energy,* vol. 83, no. 4, pp. 566-573, 2009.

[95] Z. Krumer, S. J. Pera, R. J. v. Dijk-Moes, Y. Zhao, A. F. d. Brouwer, E. Groeneveld and W. G. v. Stark, "Tackling self-absorption in luminescent solar concentrators with type-II colloidal quantum dots," *Solar Energy Materials and Solar cells,* vol. 111, pp. 57-65, 2013.

[96] C. D. M. Donega, "Formation of nanoscale spatially indirect excitons: evolution of the type-ii optical character of CdTe/CdSe heteronanocrystals," *Physical Review B,* vol. 81, p. 165303, 2010.

[97] K. Knowles, T. Kilburn, D. Alzate, S. McDowall and D. Gamelin, "Bright CuInS2/CdS nanoCrystal phosphors for high-grain full spectrum luminescent solar concentrators," *Chemical Communications,* vol. 51, no. 44, pp. 9129-32, 2015.

[98] D. Waldron, A. Preske and J. Zawodny, "PbSe quantum dot based luminescent solar concentrators," *nanotechnology,* vol. 28, no. 9, p. 095205, 2017.

[99] L. R. Wilson, "Luminescent Solar Concentrators: A Study of Optical Properties, Re-Absorption and Device Optimization," Heriot-Watt University, School of Engineering and Physcial Sciences, Edinburgh, 2010.

[100] D. Holding and A. Streich, Plant Growth Processes; Transpiration, Photosynthesis and Respiration, Universityof Nebraska, 2013.

[101] L. Wilson, B. Rowan, N. Robertson, B. Richards, A. Jones and O. Moudam, "Chareacterization and reduction of reabsorption losses in luminescent solar concetrators," *Applied Optics,* 01 03 2010.

[102] W. Stahl, V. Wittwer and A. Goetzberger, "Thermal Converions with Flourescent Concentrators," *Solar Energy,* vol. 36, no. 1, pp. 27-35, 1986.

[103] International Energy Agency, "Energy Technology Perspectives," IEA, Availible: https://www.iea.org/etp2017/, 2017.

[104] A.P.Green, "Optical Properties of Luminescent Solar Concentrators," in *University of Sheffield,* England, 2014.

[105] L. Slooff, A. Burgers and M. Debije, "Reduction of escape cone losses in luminescent solar concentrators with cholosteric mirrors.," *Proc SPIE,* no. 10.1117/12.794522., 2008.

[106] L. R. Wilson, *LSC simmulation Code*, 2010.

[107] F. Meinardi, H. MCDaniel, F. Carulli, A. Colombo, K. A. Velizhanin, N. S. Makarov, R. Simonutti, V. I. Klimov and S. Brovelli, "Highly Efficiency large area colourless Luminescent solar concentrators using heavy-metal-free colloidial quantuym dots," *Nature Nanotechnology*, vol. 10, 2015.

[108] F. Mateen, M. Ali, S. Y. Lee, S. H. Jeong, M. J. Ko and S. Hong, "Tandem Structured luminescent solar concentrator based on inorganic carbon quantum dots and organic dyes," *Solar Energy*, vol. 190, pp. 488-494, 2019.

[109] A. I. Olivia, R. Castro-Rodriguez, O. Solis-Canto, V. Sosa, P. Quintana and J. L. Pena, "Comparison of properties of CdS thin films grown by two techniques," *Applied Science*, vol. 205, no. 1-4, pp. 56-64, 2003.

[110] C. Chou, M. Hsu and F. Chen, "Flexible luminescent waveguiding photovoltaics exhibiting strong scattering effects from the dye aggregation," *nano energy*, vol. 15, pp. 729-736, 2015.

[111] C. Corrado, S. Leow, M. Osborn, I. Carone, K. Hellier, M. Short, G. Alers and S. Carter, "Power generation study of luminescent solar concentrator Greenhouse," *Renewable and Sustainable Energy*, vol. 8, p. 043502, 2016.

Appendix A: Fabrication Methods for LSC Waveguides.

In general, the fabrication of LSCs is time consuming, difficult, and can be limited (by size) in a lab setting. As an alternative to creating LSC waveguides in the lab, commercially available fluorescent acrylic (PMMA) samples were purchased from a local supply store (Plastic World (http://plasticworld.ca/) and tested to determine their suitability as LSC waveguides. Fluorescent acrylic is available in sheets up to 4 feet by 8 feet in size with high-quality surface properties (made from industrial manufacturing and possesses no visible defects) and can be purchased in a variety of colours. Although the exact dye properties are unknown, the use of commercially available fluorescent acrylic reduce time and complexity in fabricating waveguides and allow for rapid prototyping of LSC modules for application testing. The use of commercially available fluorescent acrylic waveguides has been previously unreported; thus the main goal of this section is to evaluate if commercially available fluorescent acrylic samples perform satisfactorily in LSC applications. Once verified for suitable use as an LSC waveguide, the commercial fluorescent acrylic can be used for future experiments, such as thermal heating.

In this chapter, fabrication and testing of LSC modules using commercially available fluorescent acrylic waveguides is completed by attaching solar cells to the waveguide and measuring the electrical power generated under illumination. In addition to optical characterization through reflection and transmission measurements, measuring the electrical output from PV cells attached to the sidewalls of the commercial acrylic sheets is used to verify their performance by comparing them to the results reported in the literature. Additionally, insights into methods of how to cut solar cells to size for lab experiments are discussed in this chapter. Suggestions are made to overcome commonly overlooked problems that arise while attaching the solar cells to the waveguide.

A phenomenon is explored in which the edge illumination intensity varies from the middle of the sidewalls to the corners for a square/rectangular sample. Additional insights into fabrication methods are reported, such as cutting the solar cells to size and methods to overcome commonly overlooked problems that arise while attaching the solar cells using epoxy.

## 3.2 Materials and Methods

Various samples were created using different sized waveguides and fabrication techniques. The general techniques used are detailed in the following sections, with specifics given for each sample.

### 3.2.1 Waveguides

The waveguide material used in the fluorescent acrylic samples is acrylic, or polymethyl methacrylate (PMMA). PMMA is commonly used as a waveguide and has a strong presence in previous literature due to its excellent optical properties for LSC applications; namely its high transparency, UV resistance and index of refraction [59]. It should be noted that PMMA is limited by its melting temperature (~160 °C) when used in high-temperature applications, such as LSC thermal collector systems. For this chapter, red fluorescent acrylic (PMMA) purchased from Plastic World (http://plasticworld.ca/, colour code 9095) was used. The sheets were 4.7 mm thick and precut into 30 cm x 30 cm squares. The acrylic was cut to the final LSC dimensions by using a laser cutter, and the edges were then squared using sandpaper to remove the slight angle left by the laser cutter. Four different sizes of LSC waveguides were used: 35 x 35 mm squares, 35 x 50 mm rectangles, 35 x 60 mm rectangles and 12 cm x 12 cm squares. The 35 x 35 mm squares, 35 x 50 mm rectangles, 35 x 60 mm rectangles are grouped and referred to as “small LSCs” whereas the larger 12 cm x 12 cm LSCs are referred to as “Large LSCs”.

### 3.2.2 Photovoltaic cells

The solar cells used were 6” x 6”, 4.14 W grade A polycrystalline silicon (c-Si) photovoltaic (PV) cells purchased from MISOL with a manufacturer claim of 17.2% efficiency and a fill factor of 78.54%. The c-Si PV cells came in 15 cm x 15 cm sheets and without electrical connections. Few papers have provided details about the process used to cut the solar cells to the required size, with some opting to purchase custom made cells for their applications.

### 3.2.3 Cutting the solar cells/ PV cell preparation

The c-Si PV cells had to be cut to a suitable size of ~5 mm wide by 3.5-12 cm long to adhere to the edge of the fluorescent PMMA sheets (depending on the sample). Initially, a glass cutter was used to cut the cells down to size, however, due to the brittleness and fragility of the PV cells it

was very difficult to accurately cut them to the appropriate size. During the cutting process, the cells would often break, and the edge profile was extremely jagged and rough. To solve this problem a Dremel tool fitted with a diamond disk blade was used. A rig was designed to hold the Dremel and allow it to travel along one axis to enable a straight cut with the goal of improved cutting accuracy and to avoid vibrations and shaking that occur from cutting by hand as shown in **Figure 4.1**. The rails used in the rig are aluminum rods purchased from MetalSupermarkets.com. The rig was designed on SOLIDWORKS and 3D printed using MakerBot 3D Printers.

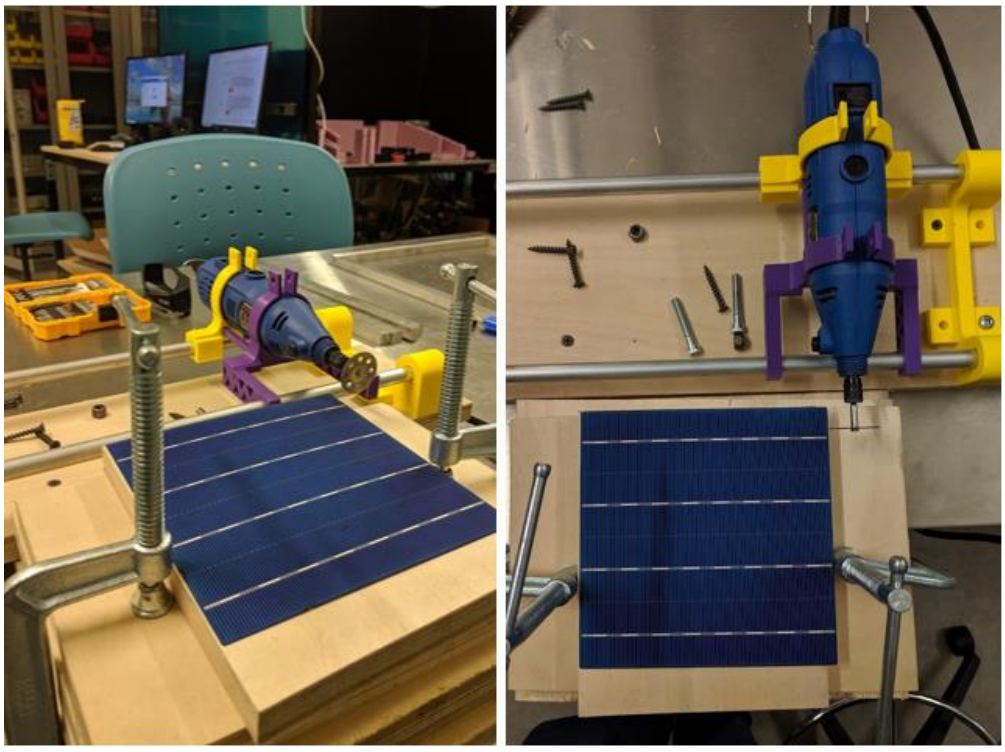

**Figure 4.1.** 3D printed Dremel cutting rig for cutting solar cells

The Dremel cutting rig was able to consistently provide a visibly accurate and straight cut, as shown in **Figure 4.2**.

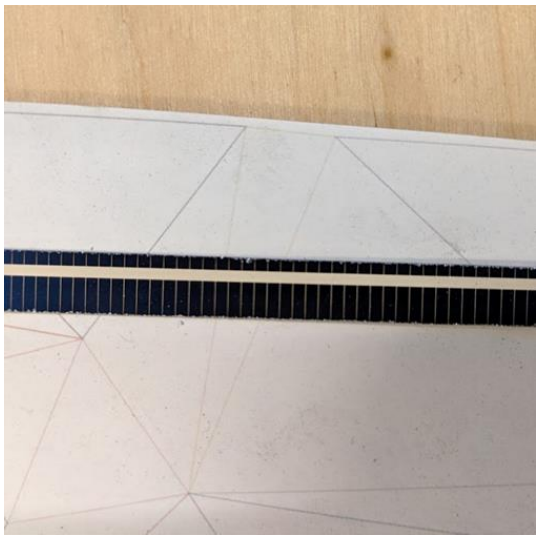

**Figure 4.2**. Solar cell that has been cut to size

### 3.2.4 Soldering and electrical connections

While cutting the solar cell, it is crucial to ensure that the resulting cell has a soldering connection on both the front and back surfaces. Tabbing, which is a thin conductive strip, was soldered to the front and back busbar on the solar cell (the thick white line on the solar cell in **Figure 4.2**) to provide the required electrical connections. A flux pen was used prior to soldering to help the solder flow and form a stronger connection. Once tabbing had been applied along both contacts, an additional piece was added at a 90-degree angle to provide for easy connections once the cell is attached to the LSC waveguide. Note that as the length of the cell increases, the difficulty for soldering increases as well. This is because the tabbing must run along the length of the cell and as the cell gets longer the thermal stresses caused by the high-temperature solder and the difference in thermal expansion of the tabbing and cell cause the cell to bend or break. If the tabbing is first tacked to both sides of the cell before completing a full soldered pass, successful fabrication is likely. This is because the heat from the soldering iron can pass through the cell to the tabbing on the opposite side, since both sides now have tabbing and are being heated, the thermal stresses are more evenly distributed. This method was used to create the connections for 5 mm by 10 cm long cells. Alternatively, conductive adhesives could be used to make the electrical connections and prevent bending of the cell.

### 3.2.5 Attaching the solar cell to the waveguide

The final fabrication step is attaching the PV cells to the waveguide. The following section goes over the various methods used to attach the solar cells to the waveguide, referred to as either the "direct gluing method", "glue gap method" or "3D printed frame" method. Adhesives are typically used and should contain the following properties; High optical clarity (non-yellowing), a similar index of refraction to the host material, good bonding between materials and high toughness (to account for thermal stresses). Three different types of epoxy/glue were chosen. Epoxy Adhesive Optically Clear High Impact, Two-part, Low Viscosity, AA-BOND from Atom Adhesives was chosen for its clear optical properties, index of refraction similar to that of the acrylic/PMMA and ability to be cured at room temperature. In addition, commonly found Krazy glue and Gorilla super glue were used to directly glue the PV cells to the waveguide.

Care must be taken to prevent glue fillets from forming while gluing the solar cells directly to the LSC waveguide. If the adhesive is applied to the face of either the cell or the edge of the LSC and clamped together, fillets will form where the glue has been pushed out from the clamped surfaces. These fillets can cause trapped light to escape from the waveguide, as shown in **Figure 4.3**. A light ray that would have otherwise been reflected due to TIR and been absorbed by the cell can escape by traveling through the optically coupled glue fillet. This method is referred to as the "direct gluing method" in this text.

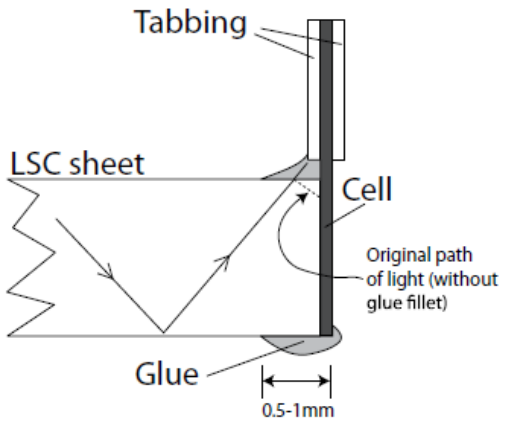


**Figure 4.3.** LSC internal losses due to glue fillet. Figure from L. R. Wilson, "Luminescent Solar Concentrators: A Study of Optical Properties, Re-Absorption and Device Optimization", page 94. ©2010 [29]

L. R. Wilson [29] estimates that the effect of a fillet that extends 0.2 mm on the front and rear surface will contribute to a 13% reduction in incident light on a PV cell located at the sidewall of the LSC. Since avoiding the formation of some size of glue fillets is nearly impossible, it has been suggested that a 1 mm thick mirrored coating could be applied to the perimeter of the upper and lower surfaces of the LSC prior to gluing, which could then reflect any light that would otherwise be lost through the fillet.

To prevent the unwanted issues caused by fillets completely, an alternative solution was created which separates the solar cell from the waveguide as shown in **Figure 4.4**. This method is referred to as the "glue gap method" in this text. The waveguide and solar cell are both placed in a mould, with a small (~1-2 mm) gap between them. The gap is then filled with the adhesive epoxy using a needle and allowed to dry. This method was the primary method used to attach solar cells to the waveguide. The molds were designed on SOLIDWORKS and 3D printed to fit the size of the LSC. This method also provides support and protection for the extruding part of the solar cell with the tabbing. Due to the high accuracy of 3D printing, the additional thickness added by the tabbing on the solar cell can also be accommodated by adding a small 0.5 mm setback on the mould wall, ensuring the cells sits flat against the mould wall despite the tabbing. Additional epoxy can be added to cover the entire surface of the waveguide with a thin layer for added protection, weather resistance and UV protection. Care should be used to ensure the epoxy used has high optical properties and suitable weather resistance/hardness.

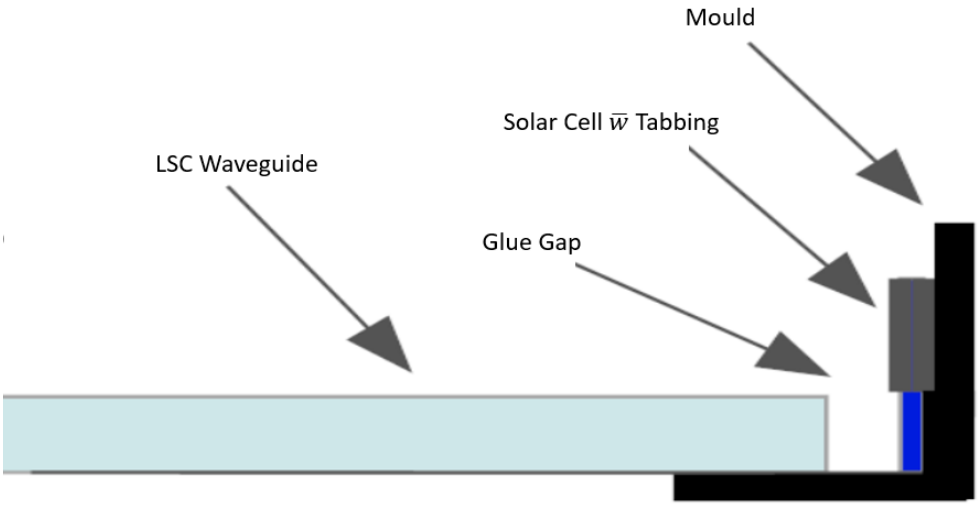


**Figure 4.4.** 3D printed mould design used to attach solar cells and prevent glue fillets.

To help fill the gap with epoxy, a funnel-shaped design was included in the mould with an opening at the bottom that enters the gap. This allowed the glue to be poured into the funnel, eliminating the need to accurately fill the gap (shown in **Figure 4.6**). **Figure 4.5** shows various assembled LSCs created using this method. Note that black tape was used to cover any part of the solar cell extruding from the edge of the waveguide to ensure that all light received is a result of fluorescence in the waveguide.

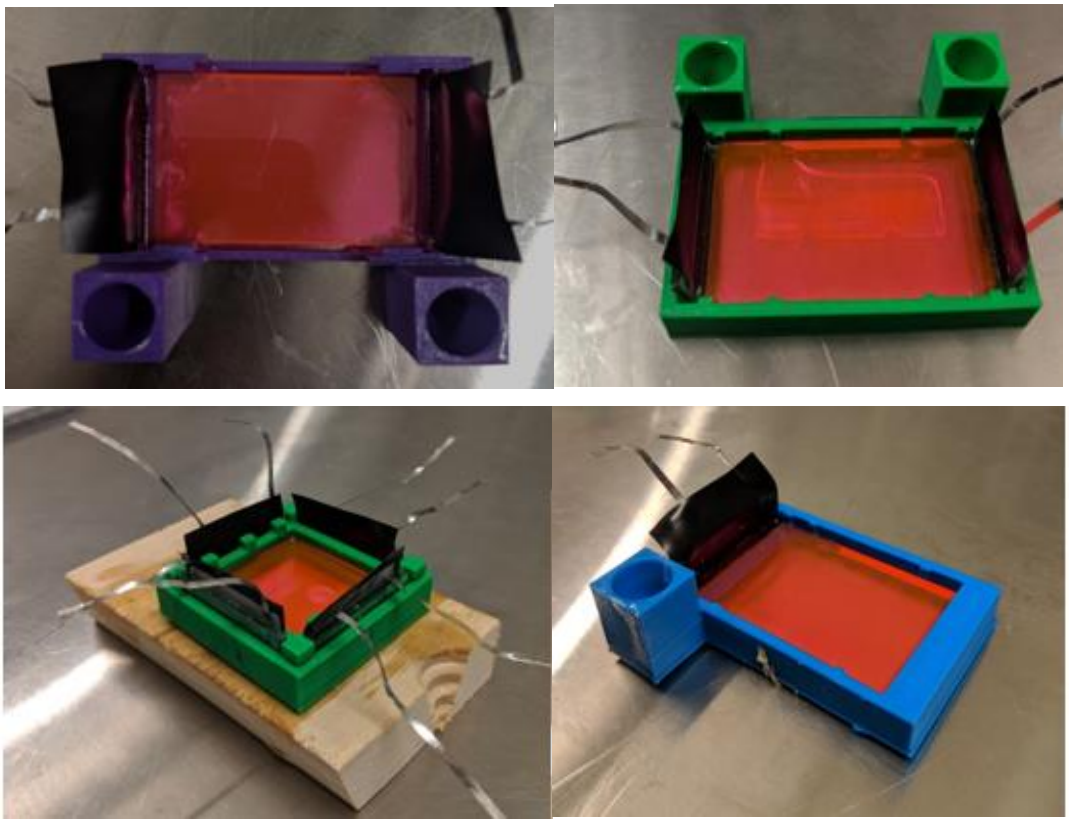

**Figure 4.5.** Various assembled LSCs samples

**Figure 4.6.** Cross-section of Funnel Design

For the larger 12 cm x 12 cm LSCs, a modification of the moulds used in the glue gap method had to be created to accommodate the larger size, referred to as the "3D printed frame method". A frame was designed using solid works to hold the sample, allowing for a 2 mm gap around all edges of the acrylic. The frame had a 5 mm ledge to hold the acrylic from the bottom and prevent glue leakage and a 1 mm offset along the outside edge to allow space for the PV cell tabbing, as shown in **Figure 4.7**. The frame was designed as a single edge with a 45-degree cut at each end to allow for the assembly of a square frame. One end was created with a hole and the other with a pin, allowing for the pieces to be easily assembled with good alignment. The frame pieces were printed in ABS using a 3D printer.

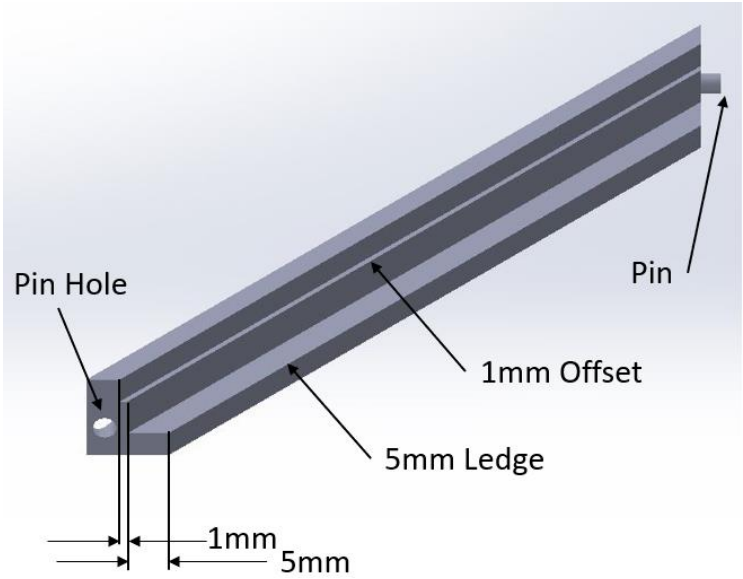


**Figure 4.7.** 3D printed frame design. The image shows one edge of the frame. Four of these parts can be attached using the pin and the pinhole to create a square frame.

The solar cells (mono c-Silicone cells) were cut into 11.5 cm long strips and tabbing was added. They were then glued (using super glue) to the outside edge of the frame to hold them in place. The four frame edges were then assembled and glued together using super glue to prevent leakage of glue through the cracks during the next process. Aluminum foil was cut and inserted along the bottom ledge of the frame to act as a mirrored surface between the frame and the waveguide. The cut acrylic was then inserted into the frame and centered, leaving a small gap around the edge between the PV cell and the acrylic panel. The panel was clamped tightly against the bottom ledge of the frame and the gap between the acrylic and solar cell was filled with AA bond epoxy using a needle and syringe. The resulting panel is shown in **Figure 4.8**.

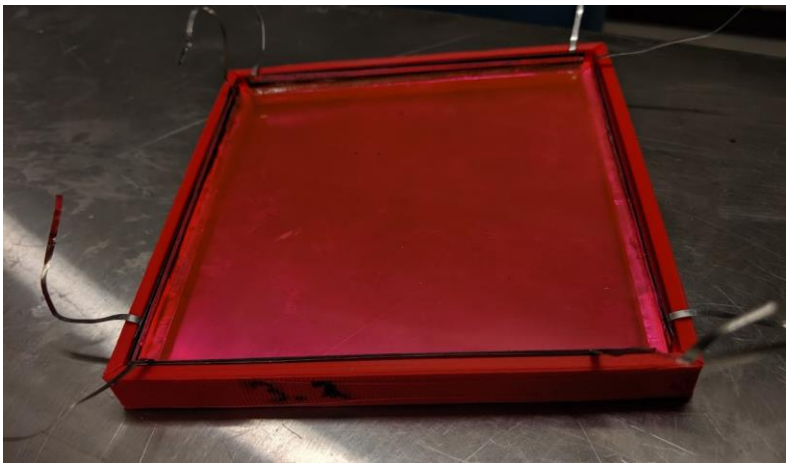

**Figure 4.8**. 12 cm x 12 cm LSC assembly

### 3.2.6 LSC assembly

The method used to attach the PV cells for the creation of each small LSC is detailed below. Some samples had a cell on two edges, while others had a cell on just one. Any edge without a PV cell was left as an open-air boundary. 17 cells were used in total, using the specific methods detailed below in Table 4.1.

**Table 4.1.** Waveguide size and method used to attach each PV cell to create LSC samples.

| Cell # | Waveguide size | Glue Used | Method used |
|---|---|---|---|
| **Small LSCs** | | | |
| 1 and 2 | 35 x 60 x 4.7 $mm^3$ | AA-Bond Epoxy | Both 35 mm edges, glue gap method |
| 3 | 35 x 50 x 4.7 $mm^3$ | AA-Bond Epoxy | Single 35 mm edge, glue gap method |
| 4 and 5 | 35 x 60 x 4.7 $mm^3$ | AA-Bond Epoxy | Both 35 mm edges, glue gap method |
| 6 and 7 | 35 x 50 x 4.7 $mm^3$ | AA-Bond Epoxy | Both 35 mm edges, glue gap method |
| 8 | 35 x 35 x 4.7 $mm^3$ | Krazy Glue | Single 35 mm edge, direct gluing method |
| 9 and 10 | 35 x 35 x 4.7 $mm^3$ | Krazy Glue | Opposite 35mm edges, direct gluing method |
| 11 | 35 x 35 x 4.7 $mm^3$ | Krazy Glue | Single 35 mm edge, glue gap method |
| 12 and 13 | 35 x 35 x 4.7 $mm^3$ | Gorilla Glue | Single 35 mm edge, direct glue method |
| **Large LSC** | | | |
| 14-17 | 12 x 12 x 0.47 $cm^2$ | AA-Bond Epoxy | All 4 edges, 3D printed frame method |

### 3.2.7 Light source

Two light sources were used. The first was used for the smaller samples (samples number 1-17). The light source used was an SF300C solar simulator lamp from Science Tech with a listed intensity of 1000 W/m$^2$ and a spectrum similar to the solar spectrum. The irradiance was measured using a power meter (ThorLabs PM16-401) for verification, with the results indicating an irradiance of 970 W/m$^2$. For calculations, the irradiance value of 970 W/m$^2$ was used. This data was used in combination with the sample size to determine the efficiency of each sample. The illuminated area was a circle with a size of 55 mm in diameter. This means that for the larger samples (55 and 60 mm long), a portion of the sample is not illuminated, as shown in **Figure 4.9.** Position of rectangular LSC samples under SF300C solar simulator lamp illumination area. For efficiency calculations, only the illumination area is included.

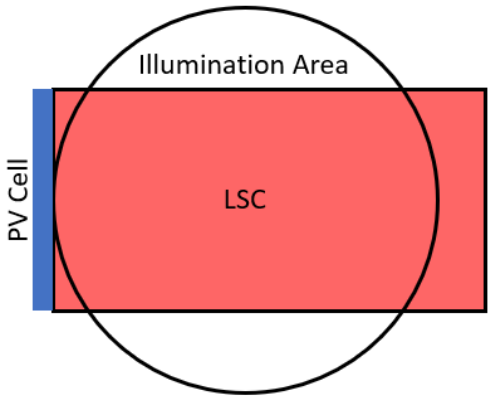


**Figure 4.9.** Position of rectangular LSC samples under SF300C solar simulator lamp illumination area

Due to the larger size, the 12 cm x 12 cm panel could not be tested under the solar simulator used previously. Instead, a 1000 W Sunmaster FullNova MH light bulb (41983 SM. 1000W.FullNova) was used. The lamp was mounted 36 inches above a reflective aluminum table. The irradiance from the lamp was measured using a power meter (ThorLabs PM16-401) in multiple spots over the surface of the panel and the average irradiance was determined. The spectral profile of the lamp was obtained from the manufacturer and is provided in Appendix A: Section 10.1. Further, according to the manufacturer, 50% of the light is emitted between 360-1000 nm. In comparison, for the solar AM 1.5 spectrum almost 75% of the light falls between 360 – 1000 nm. The power meter, on the other hand, measures all irradiance with wavelength greater than 190 nm.

### 3.2.8 Measurements

The solar cells were placed under the light source and their open-circuit voltage and short circuit current were measured using a voltmeter prior to being attached to the LSC. The solar cells were measured again under the light source after being attached to the LSC panel with the short circuit current and the open-circuit voltage recorded. The power was calculated both before and after being attached to the waveguide by multiplying the output voltage by the current (initial) and applying the fill factor (0.7984). The power measured before the cell was attached to the waveguide is denoted $P_{cell}$ whereas the power measure after the cell was attached to the waveguide is $P_{LSC}$. The difference between both measurements is called ΔP and is used to allow the performance of the cell to be compared directly to itself. This method of comparing each cells performance before and after attaching it to the PV cell allows for an accurate measurement of performance gains/losses without the errors attributed to variations between different cells. This method also allows for measuring the edge illumination profile for current matching purposes, as described in Appendix A: Section 9.5.

## 3.3 Results and Discussion

### 3.3.1 Small LSC results and discussion

Table 4.2 shows the measured open-circuit voltage, short circuit current, and total power produced by each PV cell before and after being attached to an LSC. The table also indicates the method used for attaching the cell and the overall efficiency (using a fill factor of 0.7854).

**Table 4.2**. Results from small LSC samples.

| Sample | $V_{cell}$ (V) | $I_{cell}$ (mA) | $P_{cell}$ (mW) | $V_{LSC}$ (V) | $I_{LSC}$ (mA) | $P_{LSC}$ (mW) | ΔP (%) | Illuminated LSC Area ($cm^2$) | Overall efficiency (%) |
|---|---|---|---|---|---|---|---|---|---|
| 1 | 0.55 | 56.5 | 24.41 | 0.54 | 29.5 | 12.51 | 51.3 | 17.85 | 0.72 |
| 2 | 0.56 | 63.5 | 27.93 | 0.55 | 25.2 | 10.89 | 39.0 | 17.85 | 0.63 |
| 3 | 0.561 | 43.6 | 19.21 | 0.53 | 21.2 | 8.82 | 45.9 | 16.78 | 0.54 |
| 4 | 0.568 | 41.9 | 18.69 | 0.53 | 28.5 | 11.86 | 63.5 | 17.85 | 0.69 |
| 5 | 0.568 | 49 | 21.86 | 0.52 | 23 | 9.39 | 43.0 | 17.85 | 0.54 |
| 6 | 0.57 | 42.9 | 19.21 | 0.544 | 21.2 | 9.06 | 47.2 | 16.78 | 0.56 |

| | | | | | | | | | |
|---|---|---|---|---|---|---|---|---|---|
| 7 | 0.57 | 56.8 | 25.43 | 0.53 | 27.6 | 11.49 | 45.2 | 16.78 | 0.71 |
| 8 | 0.56 | 49.2 | 21.64 | 0.55 | 28 | 12.10 | 55.9 | 12.25 | 1.02 |
| 9 | 0.58 | 57 | 25.97 | 0.55 | 27 | 11.66 | 44.9 | 12.25 | 0.98 |
| 10 | 0.55 | 48.5 | 20.95 | 0.55 | 21.3 | 9.20 | 43.9 | 12.25 | 0.77 |
| 11 | 0.56 | 52.8 | 23.22 | 0.53 | 24.4 | 10.16 | 43.7 | 12.25 | 0.85 |
| 12 | 0.55 | 51.2 | 22.12 | 0.55 | 27.3 | 11.79 | 53.3 | 12.25 | 0.99 |
| 13 | 0.56 | 48.5 | 21.33 | 0.54 | 20.5 | 8.69 | 40.8 | 12.25 | 0.73 |
| Average | 0.56 | 50.88 | 22.46 | 0.54 | 24.98 | 10.59 | 47.50 | | 0.75 |

*Cell denotes the measured solar cell before being attached, whereas LSC denotes measurements after being attached to the LSC.

** % $\Delta P$ column compares the power observed by the cell before being attached to the power measured after being attached to the LSC.

*** Irradiance = 970 W/m$^2$, fill factor is 0.7854.

It was noted that during gluing while using the gap-filling method, the glue would leak out from beneath the bottom of the mould and the LSC waveguide. This led to significant losses due to the glue gap not being completely filled. Efforts were made to minimize this effect by re-filling the gap, increasing performance from the re-tested modules. The use of a gasket material between the bottom of the LSC and the mould may aid in preventing glue leakage in future attempts.

The largest ratio of power ($\Delta P$) measured for a PV cell before and after it was attached to an LSC was seen in cell 4 (63.5%). This cell was attached to a 35 mm x 60 mm LSC using the AA bond Epoxy and glue gap method. It was expected that the larger samples would show a larger increase in the power ratio due to larger concentration ratios. By averaging the $\Delta P$ measured from each LSC, grouped by size, and comparing them together, as shown in Table 4.3, it can be seen that the largest sample (35 x 60 mm$^2$) saw the largest $\Delta P$, although the results are too close to draw any significant conclusions.

Table 4.3 also shows that the smallest sample size had the highest overall efficiency when compared with the larger samples which is an expected characteristic of LSCs. The best efficiency from a sample was 1.02% from cell 8. The small area samples tend to have a higher

overall efficiency than the larger samples, with an average efficiency of 0.89%, compared with 0.6% and 0.64% for the 12.25, 17.5 and 19.25 $cm^2$ LSC samples, respectively. This result is as expected and demonstrates the decreasing efficiency with increasing size.

**Table 4.3.** A comparison between average ΔP and efficiency based on LSC size.

| LSC Size | Illuminated Area ($cm^2$) | ΔP (%) | Efficiency (%) |
|---|---|---|---|
| 35 x 60 $mm^2$ | 17.85 | 49.2 ± 2.7 | 0.64 ± 0.02 |
| 35 x 50 $mm^2$ | 16.78 | 46.1 ±0.33 | 0.60 ± 0.03 |
| 35 x 35 $mm^2$ | 12.25 | 47.1 ±1.0 | 0.89 ± 0.02 |

Where the ± value is based on the standard error of the sample.

Using the average efficiency from single cells measured on the various 12.25 $cm^2$ samples of 0.89% and multiplying by 4 (to compare it to the case where all 4 edges are used), it is estimated that the LSC could have a total efficiency of ~ 3.6%. Note that this is an estimate since the interaction of light may change with the addition of solar cells to the open edges. This is within 12.1% of the 4.1% overall efficiency estimated by the C++ Raytracer code [35] for an equal-sized LSC with Lumogen Red 305 dye. For additional comparison, a 5 cm x 5 cm LSC using Rot 305 and blue perylene with an overall efficiency of 4.2% was reported by Desmet et al [60].

### 3.3.2 Large LSC results and discussion

The initial measurements taken from the 12 cm x 4.7 mm cells under the lamp are shown in Table 4.4 and the measurements taken from each cell after being attached to the LSC are shown in Table 4.5.

**Table 4.4.** Initial PV cell measurement (not attached to the LSC)

| Cell # | Irradiance ($mW/cm^2$) | Area ($cm^2$) | $I_{Cell}$ (mA) | $V_{Cell}$(V) | $P_{Cell}$ (mW) | Initial Efficiency |
|---|---|---|---|---|---|---|
| 14 | 44 | 6.524 | 111.3 | 0.55 | 48.36 | 16.85 |
| 15 | 44 | 6.524 | 111.8 | 0.56 | 49.46 | 17.23 |
| 16 | 44 | 6.1215 | 105.2 | 0.56 | 46.54 | 17.28 |
| 17 | 44 | 6.006 | 100.5 | 0.53 | 42.08 | 15.92 |

**Table 4.5.** PV cell measurements attached to 12 x 12 $cm^2$ LSC

| Cell # | Area ($cm^2$) | $I_{LSC}$ (mA) | $V_{LSC}$ (V) | $P_{LSC}$ (mW) | ΔP % | Module Efficiency % |
|---|---|---|---|---|---|---|
| 14 | 144 | 65.7 | 0.55 | 28.55 | 59.03 | 0.50 |
| 15 | 144 | 66.4 | 0.53 | 27.80 | 56.21 | 0.48 |
| 16 | 144 | 82.3 | 0.53 | 34.46 | 74.04 | 0.60 |
| 17 | 144 | 84.7 | 0.53 | 35.46 | 84.28 | 0.62 |
| | | | Total | 126.27 | | 2.19 |

*Where, I = current, V = voltage, P = power

The overall efficiency observed from the 12 cm x 12 cm panel was found to be 2.19%. This value is low compared to the value predicted using Raytraver of 3.65%, however, this is attributed to the light spectral profile. The solar AM1.5 spectrum has a high intensity between 400-700 nm, which is where the absorption range of the LSC falls, compared with the lamp used for this experiment, which has a much flatter and more even distribution between 300-1000 nm. The lamp also produced a higher percentage (50%) of its irradiance at wavelengths above 1000 nm, far past the absorption range of the dye, compared with the AM 1.5 solar spectrum (25%).

Applying the spectral transmission modeling methods described in section 2.2 “Spectral Modeling Methods”, in which the measured transmission spectrum of the LSC is multiplied by the lamp irradiance spectrum, it is estimated that 0.75 Watts of power is absorbed by the dye. Applying the optical dye efficiency of 38.5% predicted by Raytracer [35] and a spectral response of 0.48 (approximate average for red light @650 nm for Si cells, estimated using Equation 1.1), it is estimated that 0.144 W of electricity can be produced. The actual LSC module produced 0.126 W. The difference could be due to a variety of factors, including the epoxy used for bonding the cells, fabrication defects, solar cells used, actual dye efficiency, losses due to contact between the LSC and the frame or irradiance variation across the panel. For additional comparison, a similar-sized 10 cm x 10 cm LSC using Lumogen Red 305 dye (state of the art) was reported to have an efficiency of 2.9% by B. Vishwanathan et al [61].

## 3.4 Conclusion

This chapter demonstrated methods that can be used to create LSC for testing purposes, as well as demonstrated proof of concept and verification of previous authors work. Efforts were made to expand on areas that have previously been skipped over such as attachment methods, glue fillets and solar cell cutting techniques. Purchased fluorescent acrylic was shown to be able to produce satisfactory results, performing with 12% of the predicted efficiency reported by Raytracer using state of the art dye (BASF Lumogen series Rot 305), with collector size of 35 x 35 $mm^2$. The net overall efficiency achieved from a larger 12 cm x 12 cm LSC falls within 25% of the reported efficiency for a similar-sized LSC reported in the literature using state of the art dye, despite using a sub-optimal light source. Using spectral modeling methods to estimate the performance under the light source and using the dye efficiency for the state of the art Lumogen ROT (red) 305 dye (predicted by Raytracer) the observed performance of the 12 cm x 12 cm deviated from the predicted value by 12.5% or 0.018 W. This shows that the purchased fluorescent acrylic demonstrates the expected LSC properties and can perform as an LSC waveguide for future experiments, allowing researchers to fast track proof of concept tests and application prototyping. It should be noted that this acrylic used was purchased through Plastic World–results may differ if purchased from different sources. The use of these easily obtainable waveguides allows for high-quality large-sized sheets which would be difficult to produce in a lab setting. Additionally, this work allows for the use of purchased fluorescent acrylic in subsequent experiments done throughout this thesis, such as in the following chapter, Characterization and Modeling of Luminescent Solar Concentrators using Newton's law of Cooling.

# 4. Characterization and Modeling of Luminescent Solar Concentrators Using Newton's Law of Cooling

## 4.1 Introduction

The solar energy concentrated at the sidewalls of LSCs can also be used as a heat source, rather than for electrical generation [62]. W. Stahl et al have shown that temperatures of 550 °C can be achieved in a 3 mm thick absorber pipe under vacuum when attached to an LSC with an area of 0.8 $m^2$ when subjected to a total irradiation of 850 $W/m^2$ [63]. In the same study, temperatures higher than 250 °C were reached under diffuse light conditions at an intensity of 150 $W/m^2$. Moreover, in a theoretical comparison between LSC thermal collectors and conventional flat plate collectors, A.Goetzberger showed that fluorescent collectors show lower thermal efficiencies at low temperatures but retain higher efficiencies at high operating temperatures [64]. Despite these promising results, very little research has been done to investigate the thermal applications of LSCs.

The objective of this chapter is to measure the thermal energy output from LSCs under practical conditions for building applications. These conditions include normal temperatures and pressures and an absorber at the LSC edges that is comparable to the size of a typical window frame. The performance of LSCs using fluorescent acrylic was examined using both single dye sheets and cascading multi-panel LSCs. The use of the purchased fluorescent acrylic was explored for its suitability and use as an LSC by measuring the efficiency of PV cells attached to their sidewalls in Chapter 3. In this chapter the LSCs are tested using a thermal approach and utilizing Newton's law of cooling to determine the optical (dye) efficiency. A model was created using the transmission and reflection spectrum from LSC samples which was able to accurately estimate the performance of the LSC and provide insight into losses and energy pathways in the LSC. Moreover, the amount of thermal energy generated by single and multi-panel LSCs is used to evaluate the potential of harnessing thermal energy from LSCs to make a meaningful contribution towards alleviating energy demands in an urban environment.

**Figure 4.1** re-illustrates various mechanisms of light and heat transfer as an incident photon interacts with an LSC panel. The photons impinging on the sidewalls of the LSC are typically harvested using photovoltaic cells to produce electricity, however, these devices suffer from low efficiencies [29] [36]. These low electrical efficiencies due to various loss mechanism is a contributing factor to why these devices have failed to be adopted into the solar industry. This chapter explores a new method of testing and modeling LSC devices to aid with the design and optimization of devices, with the focus on future design for solar thermal heating applications.

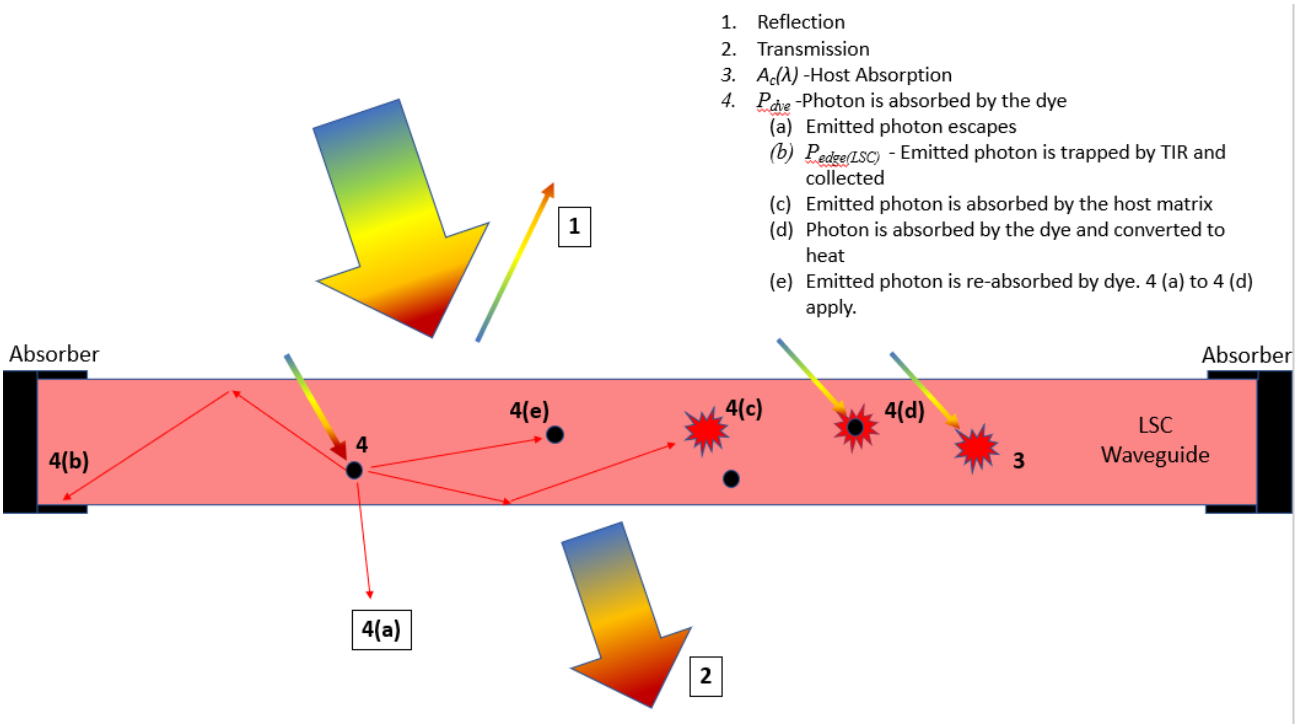


**Figure 4.1**. Mechanisms of LSCs. $P_{dye-internal\ loss}$ is sum of 4(c) and 4(d) and includes Stokes shift energy losses that occur during emission.

The efficiency of converting solar energy to heat at the edges of LSCs is expected to be greater than solar-to-electric power conversion efficiencies because all light energy transmitted to the LSC edges can potentially be converted to heat. That is, energy losses due to the quantum efficiency of the PV cells is avoided for thermal applications of LSCs. The other losses are shown in **Figure 4.1**, including reflection, transmission, Stokes shift, and host absorption losses do still apply to thermal generation applications of LSCs. It is important to note that the efficiency of the thermal applications of LSCs depends on the size of the LSCs. Thus, changing

the size of the panel investigated in this chapter would change the experimental results. This is due to multiple factors such as increased travel distances and re-absorption losses, as described by Lindsay Wilson [29]. Nonetheless, the avoidance of the aforementioned quantum efficiency losses is significant, and a promising application of LSCs is high-temperature solar heaters.

## 4.2 Methods

In this chapter, a combination of experimental and numerical methods are used to investigate the extent to which thermal energy can be generated at the edges of LSC panels. The methods used for the optical characterization of the LSCs are reported in Section 2.2 and are not repeated here. The methods used for LSC panel fabrication, experimentation, and numerical modeling are described subsequently.

### 4.2.1 LSC panel fabrication

To measure the thermal power generated at the edges of the LSCs ($P_{edge(LSC)}$) a black absorbing frame was built around a square 0.5 x 0.5 m acrylic sheet for each colour of fluorescent LSC to be tested. A similar black frame was also built around the clear acrylic panel to measure the thermal energy generated at the edge of the clear acrylic sheets ($P_{edge(host)}$). The framed acrylic sheets, referred to herein as panels, were then placed under a light of known spectral irradiance, and the temperature at the frame was measured. When the panel reached steady-state, the light source was removed, and the panel was allowed to cool. Newton's law of cooling was used to calculate the thermal power provided at each absorber frame when the modules were subjected to illumination.

The absorbing frames used to make the LSC modules were made from 3 pieces of aluminum sheet metal sandwiched together as shown in
**Figure 4.2**(a). The outer aluminum sheets were 1.5 mm thick and the inner piece was 3 mm thick, which is the same thickness as the acrylic sheets. Both the inner and outer aluminum sheets were 25 mm wide. The 3 pieces were glued (using gorilla glue) and clamped together with a 5 mm offset, creating a channel that is the same width as the panels. The inside of the channel was painted with flat black spray paint. The outer sides of the two 1.5 mm thick pieces were also painted.

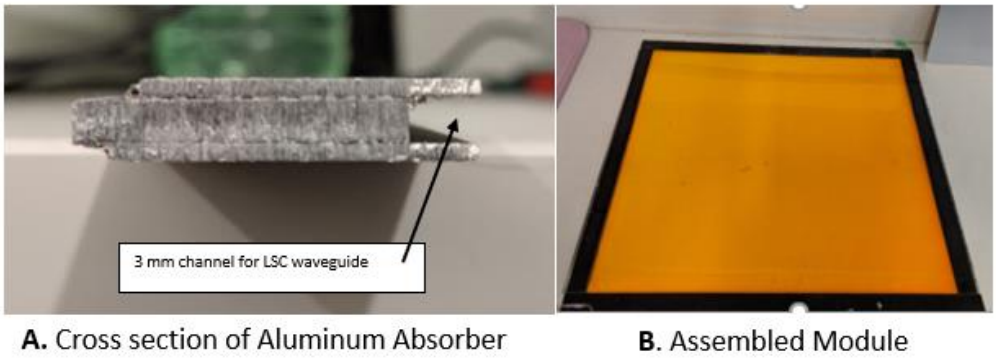


**Figure 4.2.** LSC panel with Aluminium Absorber

The channel was then filled with clear epoxy and the edge of the acrylic sheet was inserted into the channel and clamped until the epoxy set. This created an optically transparent bond between the absorber and the acrylic sheet that allowed photons incident onto the edge of the acrylic sheet to impinge upon and be absorbed by the aluminum frame. The epoxy should have a similar index of refraction to that of the acrylic (1.5) to prevent internal reflection at the boundary. The index of refraction for epoxy is generally between 1.45 and 1.57, which is well-matched with the index of refraction of the acrylic to provide for minimal reflection. In this study, Art Resin's two-part clear epoxy was used for its optical clarity, non-yellowing protection and UV resistance. The resulting panel has an absorber surrounding each edge as shown in **Figure 4.2** (b). In this work, it was assumed that all light incident onto the edge of the fluorescent acrylic sheets contributed to the thermal energy generated at the frame of the modules.

### 4.2.2 Experimental set-up

To measure the thermal energy generated at the edges of the fluorescent LSC modules, they were placed under two 1000 W Sunmaster FullNova MH light bulbs (41983 SM. 1000W.FullNova). The frames were supported at their corners such that the LSC modules resided 5 cm above a table to prevent conductive heat losses from their underside. The temperature of the absorbing frame and acrylic panels were measured in 3 and 4 locations, respectively, and the position of the thermocouples is shown in **Figure 4.3**. A 1 mm thin aluminum reflective shield was placed 5 cm above the absorbing frame to prevent it from receiving light directly from the lamps. The modules were left under the lamps for approximately 2 hours, allowing them to reach steady-state. Once at steady state, the lamps were turned off and the modules were left to cool to room

temperature. The temperature at all points indicated in **Figure 4.3** were measured and recorded every 5 seconds throughout the experiments. A fan (6-inch VIVOSUN 390 CFM inline Duct Fan) was used to provide forced convection cooling across the modules to maintain a constant heat loss condition and mitigate the effects of natural convection currents. An aluminum surface placed on the table beneath the module was painted black to prevent the reflection of light that passed through the modules. The size of the module is 50 x 50 cm, for a total area of 0.25 $m^2$. Each coloured LSC module was tested 3 times and the clear module was tested 5 times. In addition to each coloured LSC module, several combinations of stacked modules were tested. This was done by simply stacking two or more modules and clamping their aluminum frames together.

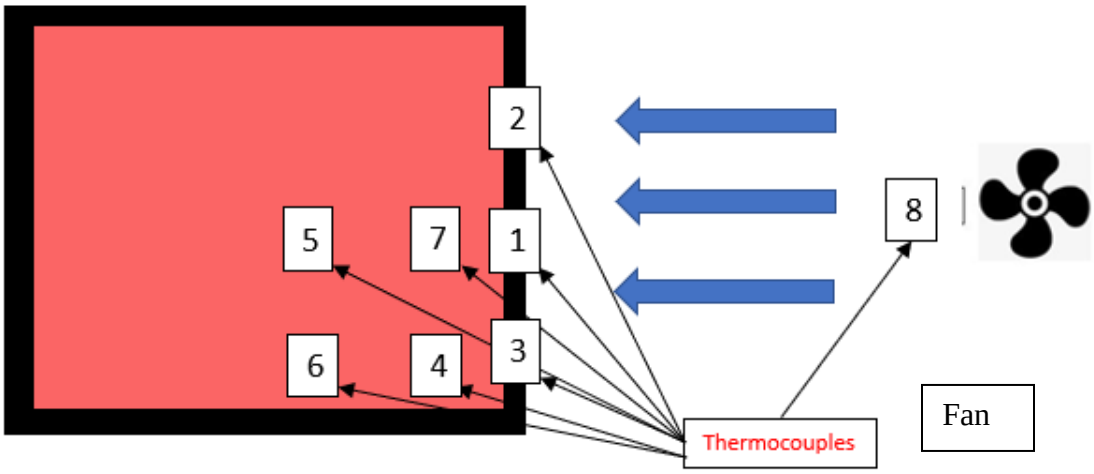


**Figure 4.3.** Experimental set-up. Location of thermocouples and the fan are indicated.

### 4.2.3 Light source

Two Sunmaster 1000W FullNova MH grow lamps were used as the light source for all experiments. The lamps were placed 60 cm above the modules. To determine the amount of radiant power incident onto the module surface, 16 measurements were taken using a ThorLabs PM16-401 power meter in a grid pattern over the area of the panel. The spectrum of the lamps used for the experiment was obtained by contacting the manufacturer. The relative spectrum was provided, and the total measured irradiance was used to find the energy at each wavelength. The total energy over the panel surface was found by using the sum calculated individually for each of the 16 sections. A detailed analysis of the light spectrum can be found in Appendix A:10.1 Light Source.

## 4.3 Numerical Methods

Newton's law of cooling states that the temperature difference between a cooling body and its surroundings decreases exponentially with time. Newton's law of cooling is applicable when the temperature difference between the object and its surroundings is small compared to the temperature of the object and when heat loss is dominated by forced convection [65] [66]. The temperature of an object that obeys Newton's law is given by Equation 4.1.

Equation 4.1

$$T(t) = T_a + (T_0 - T_a) \cdot e^{-kt}$$

Where $T(t)$ is the temperature at time $t$, $T_a$ is the ambient temperature, and $T_0$ is the initial temperature of the object under consideration. Furthermore, $k$ represents the cooling constant, which is proportional to the area, $A$, and convective heat transfer coefficient, $h$, of the object, and inversely proportional to the objects heat capacity, $Cp$. As per Newton's law of cooling, the cooling rate will remain constant as long as all geometric and heat transfer properties remain the same, as is the case for the experiments performed in this work.

Herein, we measure the cooling rate of the acrylic host and absorber frame after the lamps have been turned off, using the thermocouples indicated in **Figure 4.3** to determine their cooling constants. For example, the cooling curves and coefficient of determination for the orange LSC module are shown in **Figure 4.5**. As described subsequently, once the cooling constant for the aluminum frame, $k_f$, has been determined the heating power provided by the modules ($P_{edge(LSC)}$ or $P_{edge(host)}$) can be calculated using temperature measurements of the ambient and aluminum frame attained during steady-state illumination conditions.

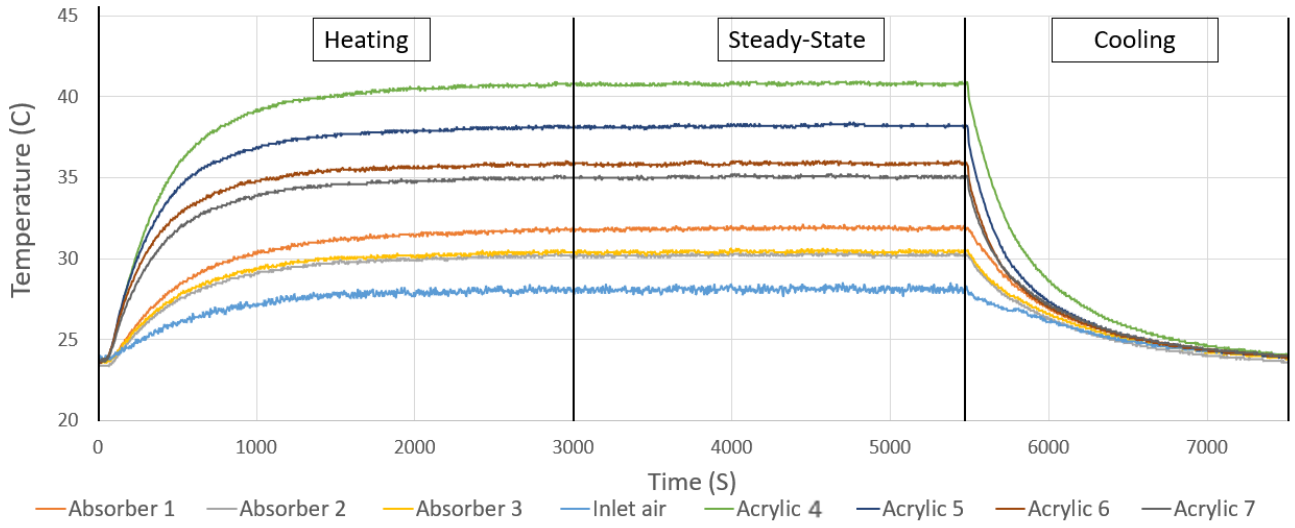


**Figure 4.4.** Thermocouple data from an orange LSC panel. The numbers correspond to the thermocouple numbers indicated in **Figure 4.3**.

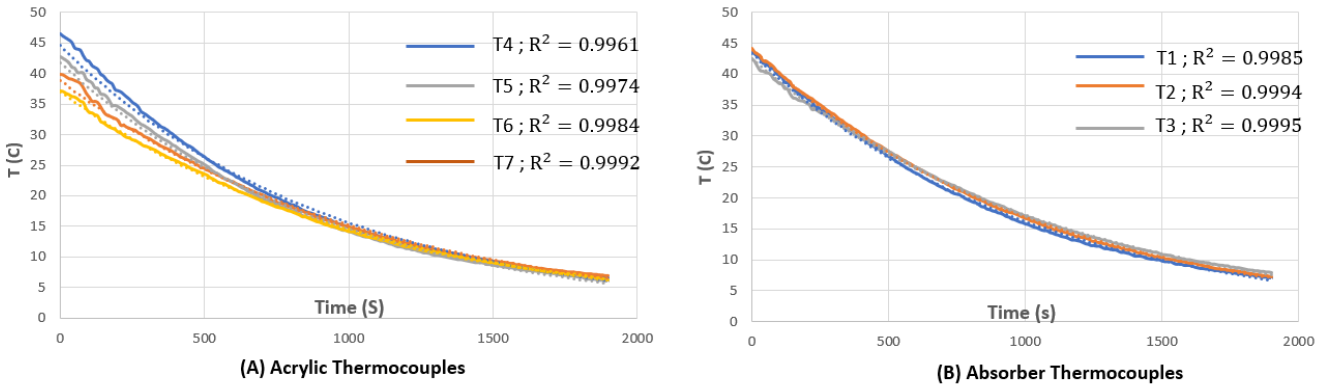


**Figure 4.5**. Cooling curves from Orange LSC panel. $R^2$ values are shown to illustrate the accuracy of the model.

Given the cooling constant for the absorber frame, $k_f$, its rate of temperature change can be calculated using Equation 4.2.

Equation 4.2

$$\frac{dT_f}{dt} = -k_f \cdot (T_f - T_a)$$

Where $T_f$ is the temperature of the aluminum frame. Furthermore, the heat transferred from the frame to the ambient, $Q_{out}$, during the cooling experiments can be related to the rate of temperature change of the frame according to Equation 4.3.

Equation 4.3

$$Q_{out} = M_f \cdot Cp_f \cdot \frac{dT_f}{dt}$$

Where $M_f$ and $Cp_f$ are the mass and heat capacity of the aluminum frame, respectively. Combining Equation 4.2 and Equation 4.3 leads to an expression for $Q_{out}$ in terms of the cooling constant and the temperature of the frame, as shown in Equation 4.4:

Equation 4.4

$$Q_{out} = -k_f \cdot M_f \cdot Cp_f \cdot (T_f - T_a)$$

Furthermore, at steady-state illumination conditions $Q_{in} = -Q_{out}$, where $Q_{in}$ is the energy from the lamp that is absorbed in the dye or acrylic host and ultimately transferred to the aluminum frame, either via reemission from the dye or thermal conduction through the acrylic matrix. That is, under steady-state illumination conditions $Q_{in}$ is equal to the thermal power provided by the frame of the LSC module, $P_{edge(LSC)}$ (or $P_{edge(host)}$ for the clear module) and is given by Equation 4.5.

Equation 4.5

$$P_{edge(LSC)} \ (or \ P_{edge(host)}) = k_f \cdot M_f \cdot Cp_f \cdot (T_{f(steadystate)} - T_a)$$

Where $T_{f\text{-}steady\text{-}state}$ is the temperature of the aluminum frame measured under steady-state illumination conditions. Once the heating power has been calculated for each module, the module heating power from the reference (clear) panel, $P_{edge(host)}$, was subtracted from that of the LSC modules, $P_{edge(LSC)}$ to determine the power contribution from the dye, $P_{dye\text{-}Optical}$.

### 4.3.1 Experimental determination of host absorption loss

Equation 4.1 to Equation 4.5 can be used to determine the heat generated in the acrylic host by using the temperature measurements from the thermocouples placed on the acrylic sheets. This value for the thermal power of the acrylic can be considered the experimental value for $P_{host(abs)}$. $P_{host(abs)}$ can also be found using by using Equation 4.6 if the optical dye efficiency has already been determined. Geometrically, for a planar acrylic (PMMA) host with an index of refraction of 1.5, 25% of the light emitted by the dye is within the escape cone and is lost through the top or bottom of the panel [16] [17] [67]. Escape cone losses are dependant on the probability of total internal reflection. The probability of total internal reflection can be calculated using Snell's laws of refraction and is based on the difference in the refractive indices of the host material used in the waveguide and the surrounding air. Thus, the total amount of light absorbed by the host material for each panel is the percentage of power absorbed by the dye that neither reaches the edge or is lost through the escape cone, plus the light power absorbed as photons emitted from the dye propagate towards the sidewalls of the acrylic panel. Note that 25% represents the fraction of photons lost and does not take into account energy losses due to Stokes shift. The amount of energy lost from Stokes shift can be estimated by applying the ratio between the peak absorption, $\lambda_a$, and peak emission, $\lambda_e$, wavelengths for each dye. Since the exact dye used is unknown, this is estimated by using the values for similar coloured BASF Lumogen dyes, with absorption and emission peaks reported by L. R. Wilson et al [39].

Equation 4.6

$$P_{host(abs)} = P_{dye} * \left(1 - \eta_{dye-Optical} - \left(0.25 - \left(0.25 * \frac{\lambda_a}{\lambda_e}\right)\right)\right) + \sum_{\lambda=220\,\mathrm{nm}}^{3600\,nm} I(\lambda) \cdot A_c(\lambda)$$

### 4.3.2 Estimating escape losses from experimental data

Once the absorption ($P_{dye}$ and $P_{host(abs)}$) and power output ($P_{dye\text{-}edge}$) have been determined experimentally, the escape losses can be determined using Equation 4.7.

Equation 4.7

$$P_{dye} = P_{dye-optical} + P_{dye-internal\ loss} + P_{dye-escape}$$

Where $P_{dye-internal\ loss}$ is the portion of the radiant energy absorbed by the dye ($P_{dye}$) that is converted to thermal energy within the acrylic sheet due to non-unity quantum yield, Stokes shift, and absorption of reemitted photons in the acrylic sheet. In this work $P_{dye-internal\ loss}$ is estimated to be the difference between the heat generated in an LSC panel and the heat generated by the clear panel. Numerically, it can also be expressed as the first term of Equation 4.6.

### 4.3.3 Monte Carlo simulations

Raytracer is a C++ program written by L. R. Wilson for modeling the performance of LSC and is described in [29]. The program generates photons and uses a raytracing Monte-Carlo logic to determine the outcome. Input parameters include the size and shape of the LSC, the type of dye (BASF Lumogen series dyes area available options), the dye concentration, and the number of photons generated for the simulation. The default host material is PMMA. Data from this program was used to generate dye efficiencies of LSC panels for comparison with the panels used in this study. The dyes selected to represent each panel were chosen based on similar colour (i.e. Lumogen Red is used to represent the red fluorescent acrylic) as shown in

Table 4.1. BASF Lumogen series dyes are often used in LSCs, with lumogen red (ROT 305) often considered the gold standard for LSC dyes. The data used from this program is meant to compare the samples used in the experiments herein with the expected performance of similar coloured LSC panels using known dyes. Dye concentrations were kept at the default 400 ppm. The size of the panel was changed to represent the size used in the experiments (50 cm x50 cm x 3 mm). Note that for all raytracer efficiency simulations, 500,000 photons were simulated which was shown in Chapter 2 to be sufficient.

**Table 4.1.** Available dyes in raytracer

| LSC panel | Dye used in Raytracer (based on BASF Lumogen Dyes) |
|---|---|
| Red | Rot 305 |
| Blue | Violette 570 |
| Green | Gleb 083 |
| Yellow | Gleb 170 |
| Orange | Orange 240 |

### 4.3.4 Cascading LSC multi-panel calculations

For multi-module configurations, the model and calculations are done by applying similar steps as those used for a single module. The incident light spectrum on each panel is multiplied by its absorption spectrum and the optical dye efficiency for that panel is applied. The transmission spectrum through the first module becomes the incident spectrum for the second module, and so on. The transmission spectrum through each module is calculated by multiplying the transmission spectrum of each panel by the incident irradiance upon that panel.

In comparison to the single-panel LSCs, additional power is expected to be generated in the multi-panels due to various mechanisms including (1) emitted photons that escape one panel may be captured in the other panels, (2) light that is diffusely scattered and transmitted by one panel may be captured by another panel, and (3) light that is reflected from lower panels may be captured by the dye in upper panels, and ultimately contribute to the heating at the edge of the module frame.

Emitted photons that escape LSC panels within the multi-panel configuration may be captured by adjacent LSCs. Emitted photons have undergone Stokes shift, and have an increased chance of being absorbed by LSC panels that absorb at longer wavelengths (i.e. the emissions from the blue panel are likely to be absorbed by the yellow panel, and the yellow panel's emissions are likely to be absorbed by the red). This is illustrated in **Figure 4.6**.

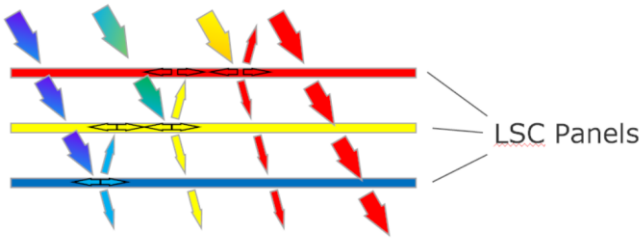


**Figure 4.6.** Light interaction in multi-panels. The dye in the yellow panel may absorb light emitted by the blue panel and convert it into yellow light. Escaped yellow light can now be absorbed by the red panel, which absorbs yellow/green light, thus increasing the amount of light it can use.

The interactions between panels become quite complicated and thus a simplified model is used to estimate the additional contribution from these interactions based on some simplified assumptions. To account for this aspect in the calculations, all emitted photons traveling from a panel with shorter emission wavelengths to one with longer emission wavelengths (i.e., blue to yellow, yellow to red) are assumed to be absorbed by the dye in that panel. The fraction of these re-captured photons that are re-emitted and propagate to the sidewalls of the multi-panel is determined using the optical dye efficiency of the LSC panel they are absorbed in. Higher-order emission and recapture events (i.e. incident light energy that is absorbed and re-captured twice or more) are not considered.

The effect of diffusely transmitted or scattered light must also be investigated. The amount of diffusely transmitted light ($T_d$) from each surface of the panels in the stack can be estimated by using the $T_d$ spectrum obtained from taking $TD_c - TS_c$ and multiplying by the incident light spectrum on each panel. The diffuse light is assumed to be scattered evenly between 0° and 180 ° from each surface of the panel. Using Fresnel's equations to determine the reflection of light of the diffusely transmitted light from underlying panels at angles between 0° and 90 ° and integrating the curve to find the average, the average reflectance of diffuse light at a PMMA/Air interface was found to be ~17.9% (note that this is a two-dimensional model and diffuse light scattered out of the plane of the image shown in **Figure 4.6** is not considered). Thus, taking the sum of reflected light from diffuse transmission from the top LSC panel to the bottom of the module, which crosses 4 air interfaces before exiting the module, results in 63% of the diffusely transmitted light being reflected. This light can either be absorbed, it can escape, it can be scattered (again) or it can be reflected again, repeating for a number of iterations until it reaches the absorber or is lost. For simplicity, it is assumed that all diffuse light reflected into the module after the first iteration makes it to the absorber and contributes to the captured power. This same method is applied to the middle and bottom panels. Note that the average Td value is 0.49 W from the top panel and 0.34 W from the middle panel, with only a fraction of that being counted for the additional contribution and thus the impact from these assumptions is small. The total contribution of this assumption is explicitly presented in the results.

The reflection of incident light off the surface of each panel must be considered as well. The amount of reflected light can be estimated by multiplying the reflection spectrum (RD) by the incoming irradiance on each panel (or the transmission through the panel above it). The light reflecting off the middle panel is directed back towards the top panel, where the reflection spectrum (RD) can again be applied to determine the amount of light redirected back to the lower panels. Likewise, the light reflected from the bottom panel can be again multiplied by the reflection spectrum to determine the amount of light reflected from the middle panel. Furthermore, light that is reflected off the bottom panel that is transmitted through the middle panel can be multiplied by the reflection spectra of the top panel to determine the amount of light that returned to the middle panel. This process could be repeated indefinitely, until all the light either escapes or reaches the edge of the multi-panel. Moreover, with each pass through one of the LSCs, there is a chance of  light being scattered, diffusely reflected, absorbed by the dye, or absorbed by the host material.

Approximately 4% of the incident perpendicular rays are reflected at each air-surface interface in PMMA (thus 7.84%  are reflected from each panel due to the double boundary) [68]. With a total module thickness of 15mm (3mm x 3 + 2mm (air gap) x 3) and an incident angle of 4°, the light will only travel ~1mm per travel thus making it unlikely that this light will make it to the edge.

However, in the experimental set up the light source is located directly above the middle of the module with a diffuse back reflector– thus the incident light will likely strike the panel at higher than 4% angle of incidence, increasing the travel distance and reflection chance, thus increasing the chance on contributing to the edge power.

Additionally, some of the reflected light will be reflected diffusely rather than purely spectral reflection.  With many unknowns, an estimation must be used, such that it is assumed that the reflected light still trapped within the panel after following the process described above is captured and contributes to edge power.

For sensitivity analysis, the amount of trapped reflected light is also calculated using the above method, but assuming all the reflected light is reflected diffusely, and thus a reflection of 17.9%

is applied rather than ~4%. Both scenarios are presented in the results with an S to denote spectral reflection (4%) and a D for values calculated assuming diffuse reflection (17.9%).

The reflected light from lower panels can also be absorbed by the dye. To account for this, the reflected light entering the top panel (as a result of reflection from the middle panel) is multiplied by the dye absorbance of the top LSC panel. The dye efficiency of the top panel is then applied to determine the edge contribution. The reflected light from the bottom panel is multiplied by the dye absorbance of the middle panel, and the portion of this reflected light that is not absorbed by the middle panel is then multiplied by the absorbance of the top panel. The light reflected from the bottom panel that is absorbed in the middle and top panels is multiplied by the respective dye efficiencies to determine the edge contribution.

## 4.4 Results and Discussion

### 4.4.1 Transmission and absorption spectrum

**Figure 4.7** illustrates the heating power measured at the absorbing frame for each LSC module and

| Module | Pedge (W) | $Pedge_{(LSC)}$ - $Pedge_{(Ref)}$ (W) | $Pedge_{(LSC)}$ - $Pedge_{(host)}$ (W) | *Pdye* (W) | ηdye-optical **(**dye efficiency **%)** |
|---|---|---|---|---|---|
| Reference (Frame) | 5.78 ± 0.24 | 0 | n/a | n/a | n/a |
| Clear (host) | 8.83 ± 0.13 | 3.05 | 0 | 0.0 | n/a |
| Orange | 10.51 ±0.03 | 4.73 | 1.68 ±0.16 | 19.6 | 9.2% ±0.8% |
| Yellow | 11.95 ±0.05 | 6.18 | 3.13 ±0.18 | 17.7 | 17.7% ±1% |
| Green | 11.64 ±0.07 | 5.87 | 2.82 ±0.2 | 11.6 | 24.1% ±1.7% |
| Blue | 11.24 ±0.11 | 5.46 | 2.41 ±0.24 | 6.1 | 39.7% ±3.9% |
| Red | 13.44 ±0.12 | 7.66 | 4.61 ±0.25 | 16.3 | 28.3% ±1.5% |
| BY | 14.58 ±0.28 | 9.28 | 5.75 ±0.41 | 20.0 | 28.75% ±2% |
| BYO | 16.93 ± 0.35 | 11.16 | 8.11 ±0.48 | 23.2 | 34.9% ±2.1% |
| BYR | 19.76 ± 0.1 | 13.98 | 10.94 ±0.23 | 26.6 | 41.2% ±0.86% |

| | | | | | |
|---|---|---|---|---|---|
| RYB | 20.00 ±0.33 | 14.22 | 11.20 ±0.46 | 26.9 | 41.7% ±1.7% |

shows a summary of the data from these measurements. The value shown is the power for all 4 sides of the frame, with the assumption that the edge measured represents an average condition. In addition to the five coloured LSC modules that were tested individually, four stacked-module configurations were also tested. The stacking sequence for the multi-module configurations is denoted using the first letter of the colour of the LSCs they are comprised of (i.e. BYR represents a stacked module with a blue LSC on top, a yellow LSC in the middle, and a red LSC at the bottom). Moreover, "Reference 1" (frame) is the heat generated in an absorbing aluminum frame without an acrylic sheet attached to identify background heating. The background heating is caused by heat produced by the lamps/fan which becomes trapped in the experimental workspace.

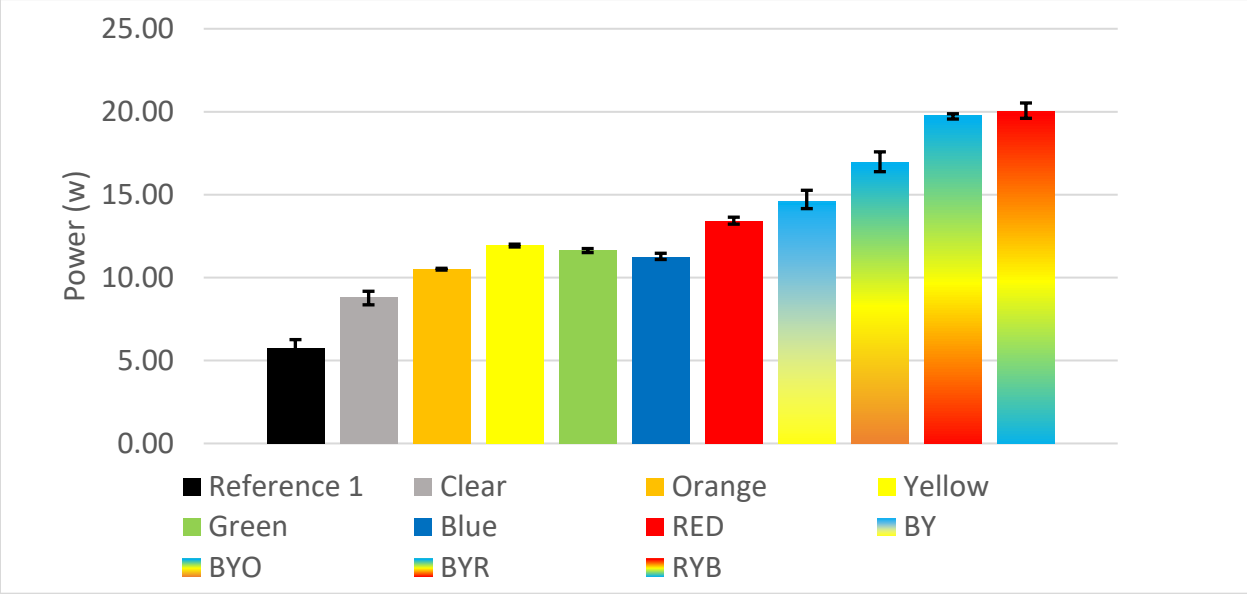


**Figure 4.7.** Absorber Power. Panel Area = 0.25 $m^2$ and the average irradiance between 300-1000nm = 23.95 $mW/cm^2$. Error bars represent the maximum and minimum values observed.

**Table 4.2**. Data summary from LSC heating experiments with standard error shown

| Module | $P_{edge}$ (W) | $P_{edge(LSC)}$ - $P_{edge(Ref)}$ (W) | $P_{edge(LSC)}$ -$P_{edge(host)}$ (W) | $P_{dye}$ (W) | $\eta_{dye\text{-}optical}$ **(**dye efficiency **%)** |
|---|---|---|---|---|---|
| Reference (Frame) | 5.78 ± 0.24 | 0 | n/a | n/a | n/a |

| | | | | | |
|---|---|---|---|---|---|
| Clear (host) | 8.83 ± 0.13 | 3.05 | 0 | 0.0 | n/a |
| Orange | 10.51 ±0.03 | 4.73 | 1.68 ±0.16 | 19.6 | 9.2% ±0.8% |
| Yellow | 11.95 ±0.05 | 6.18 | 3.13 ±0.18 | 17.7 | 17.7% ±1% |
| Green | 11.64 ±0.07 | 5.87 | 2.82 ±0.2 | 11.6 | 24.1% ±1.7% |
| Blue | 11.24 ±0.11 | 5.46 | 2.41 ±0.24 | 6.1 | 39.7% ±3.9% |
| Red | 13.44 ±0.12 | 7.66 | 4.61 ±0.25 | 16.3 | 28.3% ±1.5% |
| BY | 14.58 ±0.28 | 9.28 | 5.75 ±0.41 | 20.0 | 28.75% ±2% |
| BYO | 16.93 ± 0.35 | 11.16 | 8.11 ±0.48 | 23.2 | 34.9% ±2.1% |
| BYR | 19.76 ± 0.1 | 13.98 | 10.94 ±0.23 | 26.6 | 41.2% ±0.86% |
| RYB | 20.00 ±0.33 | 14.22 | 11.20 ±0.46 | 26.9 | 41.7% ±1.7% |

* Panel Area = 0.25 $m^2$, Average irradiance between 300-1000nm = 23.95 mW/cm^2

** (±) calculated by using standard error formula

Considering the individual modules, the most heat generated in the aluminum frame was 13.4 W (averaged) for the red LSC module. Its performance was followed by the yellow, green, blue and then orange LSC modules which generated an average of 11.9, 11.6, 11.2 and 10.5 W, respectively. In contrast, considering the average amount of energy absorbed by the dye, the orange LSC absorbs the most (19.6 W), followed by the dye within the yellow (17.7 W), red (16.3 W), green (11.6 W) and then the blue (6.1 W) LSC. The efficiency with which light energy absorbed by the dye within the LSC modules is ultimately converted to heat at the module frame, $\eta_{dye\text{-}optical}$, is provided in the last column of

| Module | $P_{edge}$ (W) | $P_{edge(LSC)}$ - $P_{edge(Ref)}$ (W) | $P_{edge(LSC)}$ -$P_{edge(host)}$ (W) | $P_{dye}$ (W) | $\eta_{dye\text{-}optical}$ **(**dye efficiency **%)** |
|---|---|---|---|---|---|
| Reference (Frame) | 5.78 ± 0.24 | 0 | n/a | n/a | n/a |
| Clear (host) | 8.83 ± 0.13 | 3.05 | 0 | 0.0 | n/a |
| Orange | 10.51 ±0.03 | 4.73 | 1.68 ±0.16 | 19.6 | 9.2% ±0.8% |
| Yellow | 11.95 ±0.05 | 6.18 | 3.13 ±0.18 | 17.7 | 17.7% ±1% |
| Green | 11.64 ±0.07 | 5.87 | 2.82 ±0.2 | 11.6 | 24.1% ±1.7% |
| Blue | 11.24 ±0.11 | 5.46 | 2.41 ±0.24 | 6.1 | 39.7% ±3.9% |
| Red | 13.44 ±0.12 | 7.66 | 4.61 ±0.25 | 16.3 | 28.3% ±1.5% |

| | | | | | |
|---|---|---|---|---|---|
| BY | 14.58 ±0.28 | 9.28 | 5.75 ±0.41 | 20.0 | 28.75% ±2% |
| BYO | 16.93 ± 0.35 | 11.16 | 8.11 ±0.48 | 23.2 | 34.9% ±2.1% |
| BYR | 19.76 ± 0.1 | 13.98 | 10.94 ±0.23 | 26.6 | 41.2% ±0.86% |
| RYB | 20.00 ±0.33 | 14.22 | 11.20 ±0.46 | 26.9 | 41.7% ±1.7% |

. This efficiency was estimated by subtracting the thermal power generated at the aluminum frame for the clear acrylic module from the power generated by the LSC modules ($P_{edge(LSC)}$ - $P_{edge(host)}$) and then dividing by the power absorbed by the dye ($P_{dye}$). The experimentally determined dye efficiency is compared with the simulated results attained using the Raytracer program [29] in **Table 4.3**.

**Table 4.3.** Optical dye efficiencies of a 0.25 $m^2$ LSC panel.

| Dye Efficiency | Red | Blue | Yellow | Green | Orange |
|---|---|---|---|---|---|
| Experimental | 28.33% | 39.72% | 17.71% | 24.15% | 9.21% |
| Simulated using Raytracer | 29.3% | 51.43% | 24.35% | 26.0% | 25.39% |

The experimental and simulated optical dye efficiencies are very close, within 2 %, for the red and green acrylic sheets, whereas the measured and modeled dye efficiencies for the blue and yellow acrylic sheets are reasonably close. The results also show that the red, blue, yellow, and green samples perform well as LSCs. However, the orange panel performed exceptionally bad, exhibiting an experimental efficiency of just 9.2%, and is the only panel to show a large difference between the experimentally and theoretically determined values. This could be due to a variety of factors, such as excessive dye concentration which will increase self-absorption and escape losses or poor quantum yield for the type of dye used.

### 4.4.2 Acrylic absorption

In addition to the thermal energy generated at the module frame, the thermal energy generated within the acrylic sheet was also determined. The experimental results are compared to the theoretical results (calculated from Equation 4.6) in **Table 4.4**.

**Table 4.4** Acrylic thermal power

| Panel colour | Power (acrylic) (W) (experimental) | Power (acrylic) (W) (Theoretical modeling) |
|---|---|---|
| Clear (reference case) | 34.0 | 33.7 |
| Orange | 46.3 | 46.2 |
| Red | 42.3 | 41.4 |
| Yellow | 43.5 | 43.1 |
| Green | 39.8 | 39.8 |
| Blue | 35.8 | 35.3 |

The results in **Table 4.4** show that Equation 4.6 produces similar values to those found experimentally, with a maximum difference between the experimental and theoretical results of 3.0% for the red LSC module. Note that the assumptions used to calculate the clear absorption power provided a value that differs from the experimental results by 0.7%.

### 4.4.3 Escape losses

The estimated dye loss and escape loss for each panel is shown below in

**Table 4.5** The escape losses range from 16.8% to 27.3%, with an average of 23.2 %. This is relatively close to the expected 22.5% escape losses (accounting for Stokes shift) for an LSC. Appendix B:10.2 provides a complete chart that includes the breakdown of energy pathways through each panel.

**Table 4.5.** Dye loss and escape losses

| | Red | Blue | Yellow | Green | Orange |
|---|---|---|---|---|---|
| (1) Observed Acrylic heating ($P_{host(abs)}$ - $P_{host}$) (W) | 8.9 | 2.0 | 9.7 | 6.1 | 12.6 |
| (2) Observed absorber heating (W) | 4.6 | 2.4 | 3.1 | 2.8 | 1.7 |
| (3) Total observed heating (W) (1) + (2) | 13.5 | 4.4 | 12.8 | 8.9 | 14.3 |
| (4) Total W absorbed by dye (Estimated from UV-Vis measurements) | 16.3 | 6.1 | 17.7 | 11.6 | 18.2 |
| Escape loss [(4) – (3)] | 2.7 | 1.6 | 4.8 | 2.7 | 4.0 |
| Escape Loss (% of dye absorption) | 16.8% | 26.7% | 27.3% | 23.6% | 21.9% |

### 4.4.4 Multi-panels

Four different multi-module configurations were tested to determine the effects of stacking modules on the amount of thermal energy generated at the module frame. The module configurations tested were blue/yellow (BY), blue/yellow/orange (BYO), blue/yellow/red (BYR) and Red/yellow/blue (RYB). **Figure 4.8** shows the transmission and absorption of light as it travels through the RYB multi-module, based on transmission and absorption spectra and plotted over the lamp irradiance spectrum. A detailed analysis of the data obtained for various multi-panel modules are shown in **Table 4.6**.

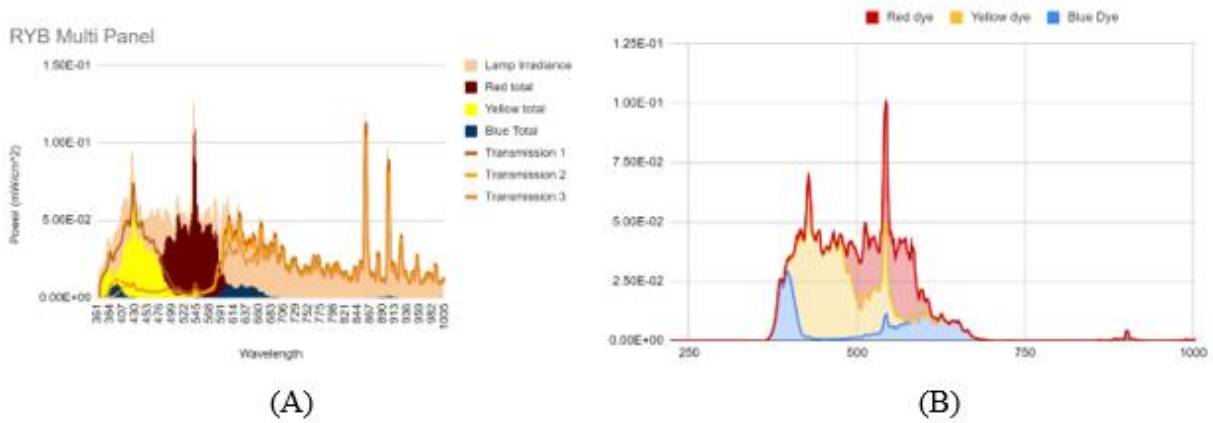


**Figure 4.8.** Absorbed irradiance through each panel. (A) a plot showing the absorption of energy as light travels through the multi-panel. (B) a plot showing the sum of energy absorbed from each panel

**Table 4.6.** Multi-panel observations. Total lamp irradiance on modules = 59.975 W

| RYB Module | Power absorbed by dye (W) | Dye Efficiency | $P_{Optical}$ (W) (Calculated) | $P_{Optical}$ ($P_{absorber} - P_{Clear}$) (W) (Observed) |
|---|---|---|---|---|
| Red | 16.3 | 28.33 % | 4.6 | - |
| Yellow | 9.24 | 17.71% | 1.5 | - |
| Blue | 2.23 | 39.72 % | 0.81 | |
| Additional contribution | - | - | 3.52 | |
| Total | 26.60 | 25.98% | 6.91+ ($3.52^S$ , $2.86^D$ ) | 11.2 ± 0.46 |
| Total Efficiency (300-1000 nm) | - | - | 11.52% ($17.4^S$ %) $16.3^D$ % | 18.67% ±0.82% |
| BYR Module | | | | |
| Blue | 6.07 | 39.72 % | 2.41 | - |
| Yellow | 13.96 | 17.71% | 2.47 | - |
| Red | 6.52 | 28.33% | 2.19 | - |
| Additional Contribution | - | - | 3.94 | |
| Total | 26.56 | 25.34% | 6.73+$3.94^S$, $3.09^D$ | 10.94 ± 0.23 |
| Total Efficiency (300-1000 nm) | - | - | 11.22% (17.79%$^S$ ,16.4%$^D$) | 18.24% ±0.4% |
| BYO Module | | | | |
| Blue | 6.07 | 39.72% | 2.41 | - |
| Yellow | 13.96 | 17.71% | 2.47 | - |
| Orange | 3.76 | 9.21% | 0.35 | - |
| Additional Contribution | - | - | 3.54 | |
| Total | 23.79 | 21.98% | 5.23+$3.54^S$ $2.65^D$ | 8.1 ±0.48 |
| Total Efficiency (300-1000nm) | - | - | 8.72% (14.6%$^S$ , 13.13%$^D$) | 13.5% ± 0.8% |
| BY Module | | | | - |
| Blue | 6.07 | 39.72 % | 2.41 | - |
| Yellow | 13.96 | 17.71% | 2.47 | - |
| Additional Contribution | - | - | 1.94 | |
| Total | 20.03 | 24.36% | 4.88+$1.94^S$, $1.47^D$ | 5.75 ±0.41 |
| Total Efficiency (300-1000 nm) | | | 8.2% (11.4%$^S$) 10.58%$^D$ | 9.6% ± 0.68% |

** $^S$ is used to denote the additional contribution assuming spectral reflection, whereas $^D$ is used for values calculated assuming diffuse reflection.

Calculated values are obtained using the transmission spectrum and measured dye efficiency to estimate power, whereas the observed values are those seen in the experiment.

The most apparent observation is that the observed power is significantly higher than the calculated value obtained using the spectra modeling data, as expected, with an average difference of 37.5% for the 3-panel modules. This difference is expected because light emitted and captured between adjacent panels has not yet been taken into account, thus demonstrating the need to calculate the additional contributions from reflection in the stacked panel configurations.

Using the method which assumes that the reflected light is scattered diffusely and captured after the first iteration of reflection, the estimated power for the RYB module becomes 10.43 W compared with the experimental power of 11.175 W and the calculated power for the BYR module becomes 10.66 W, compared to 10.94 W observed. The percent difference between these values is 6.67% and 2.5% for the RYB and BYR modules, respectively. In the case of the BYO module, the calculated value becomes 8.77 W vs the observed 8.11 W, with a percent difference of 8.1%. Applying this same method to the BY module, the estimated output becomes 6.82 W, a 9% difference from the measured value. Thus, the method used to estimate the additional contribution caused by interactions between panels using this specific set up can predict the observed power within 10%. Variation in the experimental setup may require changes to the assumptions made and thus this method is simply a first step estimation and as such should be verified for different applications. It should also be noted that this method underestimates the power from the BYR and RYB but overestimates the power for the BYO and BY modules. Assuming spectral reflection in the contribution estimations, the estimated additional contribution shrinks, thus increasing the difference between estimated and observed values for the BYR and RYB modules and decreasing the difference for the BYO and BY modules, when compared with the diffuse reflection assumption. If it was assumed that all the reflected light escapes, this would further increase the difference in predicted/observed values for all modules, except the BY module. This makes sense because the two-panel module has fewer chances to reflect/scatter light and thus it is more likely for all reflected light to escape.

The total contribution from the assumption that all of the diffusely transmitted light (Td) that is reflected is trapped after the first iteration, resulted in 0.57 W, 0.64 W and 0.64 W of power for the RYB, BYR and BYO modules, which represent 16%, 16.2% and 18% of the total calculated additional power contribution.

For multi-panel modeling used within this thesis, the assumption that the light is reflected diffusely and captured after the first iteration will be used, along with the other assumptions used in calculating the additional contribution. Although the predicted power is within 10% of the observed power, it should again be noted that changing the parameters may change the accuracy of this model. This is an area that should be explored in more detail in future work.

## 4.5 Conclusions

The methods for characterizing and modeling LSC panels described in this chapter conform fairly close to expected values and are suitable for an initial approximation. The performance of multi-panel LSC configurations was able to be predicted to within ~10% of values observed experimentally using transmission and reflection spectrum modeling. However, the accuracy of this prediction may change in different scenarios, nevertheless, it can provide an initial estimate and provides a closer approximation than simply ignoring the additional power contribution from interactions between stacked panels. Newton's law of cooling was applied to estimate the thermal output at the edge of the LSC panels under a controlled environment. By substituting the solar spectrum for the lamp spectrum used, data for sunlight conditions could be generated. Verification of the performance under sunlight should be done if a high degree of certainty is desired. The methods for modeling the performance and energy flow in LSCs in various configurations/orders can aid in the optimization, design and simulation of multi-panel LSC for various applications, such as the integration into solar heaters, windows, or spectral splitting LSC PV designs. One such application, flat-plate solar thermal collectors, is investigated in Chapter 5.

# 5. LSC Solar Thermal Heating Systems

## 5.1 Introduction

In a study by W. Stahl et al [69], the thermal conversion of solar energy using LSCs was shown to produce temperatures as high as 555 °C using LSCs coupled to vacuum tube absorbers. In a comparison between flat plate collectors and LSC thermal collectors, A. Goetzberger [15] concluded that fluorescent collectors show lower thermal efficiencies at low temperatures, but retain their efficiency at high operating temperatures. LSC thermal collectors can reduce heat losses compared to traditional flat plate collectors by reducing the size of the absorber and moving it to a location that can be easily insulated while maintaining the simple flat plate profile. This allows for the reduction of the two main loss mechanisms from flat plate collectors – convection and radiation losses through the transparent cover. This is due to the optical transmission of energy to an insulated absorber rather than conductive heat transfer to provide thermal energy at the collector. Despite promising results for the thermal application of LSCs, little work has been done in this area. This chapter aims to develop and verify a mathematic model of LSC flat-plate thermal collectors using heat transfer principals. The model is then used in combination with work done in Chapter 4 to design and evaluate LSC flat-plate thermal collector performance with comparisons made to traditional solar thermal systems.

## 5.2 Introduction to Flat-Plate Solar Collectors

Traditional solar heating systems, such as a black-plate absorber, are comprised of a black-plate with a transparent outer cover to reduce heat losses. Fluid channels run under the black plate to collect heat, with thick insulation covering the backside to reduce heat losses. **Figure 5.1** illustrates a typical black plate absorber.

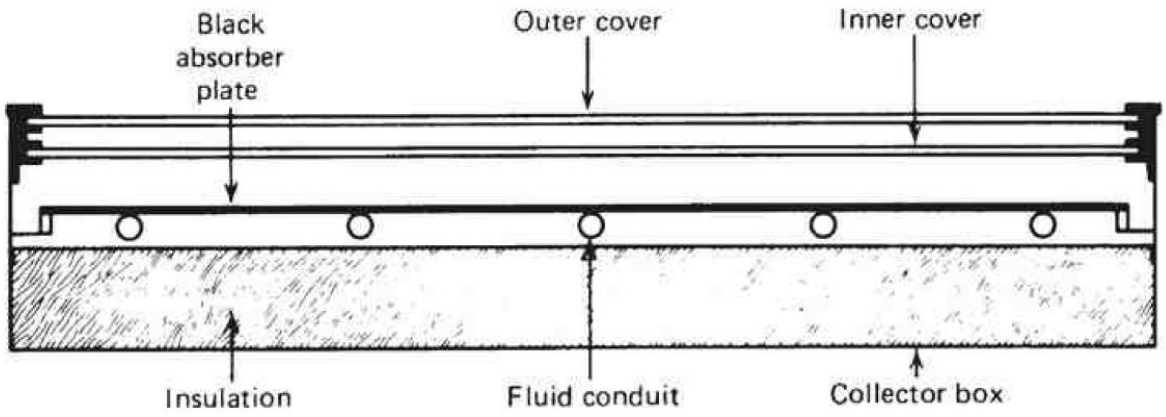


**Figure 5.1.** Black plate absorber. Image from J. A. Duffie and W. A. Beckman, Solar Engineering of Thermal Processes, Fourth Edition, US: John Wiley & Sons, ©2013. Ch. 6, p. 2.

In a black plate absorber system, heat loss represents the most significant reduction in efficiency, due to the large surface area of the absorber which leads to high radiation and convective heat losses through the top of the absorber. A basic equation for determining the rate of useful thermal energy provided by a solar collector is given in Equation 5.1, adapted from [70].

Equation 5.1 $$Q_u = A_c[S - U_L(T_{pm} - T_a)]$$

Where $S$ is the solar irradiance absorbed by the collector in W/m$^2$, $U_L$ is the heat loss coefficient in W/m$^2$·K, $T_{pm}$ is the mean plate temperature, $T_a$ is the ambient temperature and $A_c$ is the collector area. This equation has limited usefulness due to the difficulty in obtaining the mean plate temperature, however, it can be adapted to become an expression for the fluid temperature at the inlet of the collector and will be discussed later. The efficiency of a solar heater can be expressed as the ratio of useful energy gain over time to the incident energy on the collector over time, as shown in Equation 5.2, where $I_T$ is the irradiance.

Equation 5.2 $$\eta = \frac{Q_u}{I_T A_c}$$

For this analysis, simulation methods will be the dominant tool used and thus detailed heat transfer calculations are not required, however, knowledge of the process should be used to

confirm simulation results. A detailed analysis of heat transfer in black-plate absorbers can be obtained from J. A. Duffie and W. A. Beckman, Solar Engineering of Thermal Processes, Fourth Edition, US: John Wiley & Sons., 2013.

### 5.2.1 Important design parameters

Several design parameters to consider while designing a flat-plate absorber are the number of covers, the spacing of fluid conduits and the spacing of covers. The addition of covers will reduce heat losses but will also increase optical losses from reflection and absorption as the light travels through each cover. Typically, 1-3 covers are used [70]. Fluid conduit spacing can influence the efficiency of heat transfer from the plate to the fluid, with wide spacing causing hotspots between conduits which leads to higher losses. Spacing of cover plates influences the conductive heat transfer between the covers and impacts heat loss. **Figure 5.2** shows the effect that the number of plate covers has on the total loss coefficient at various temperatures and with a convective heat loss coefficient at the top surface of 5 and 10 W/m$^2$·K.

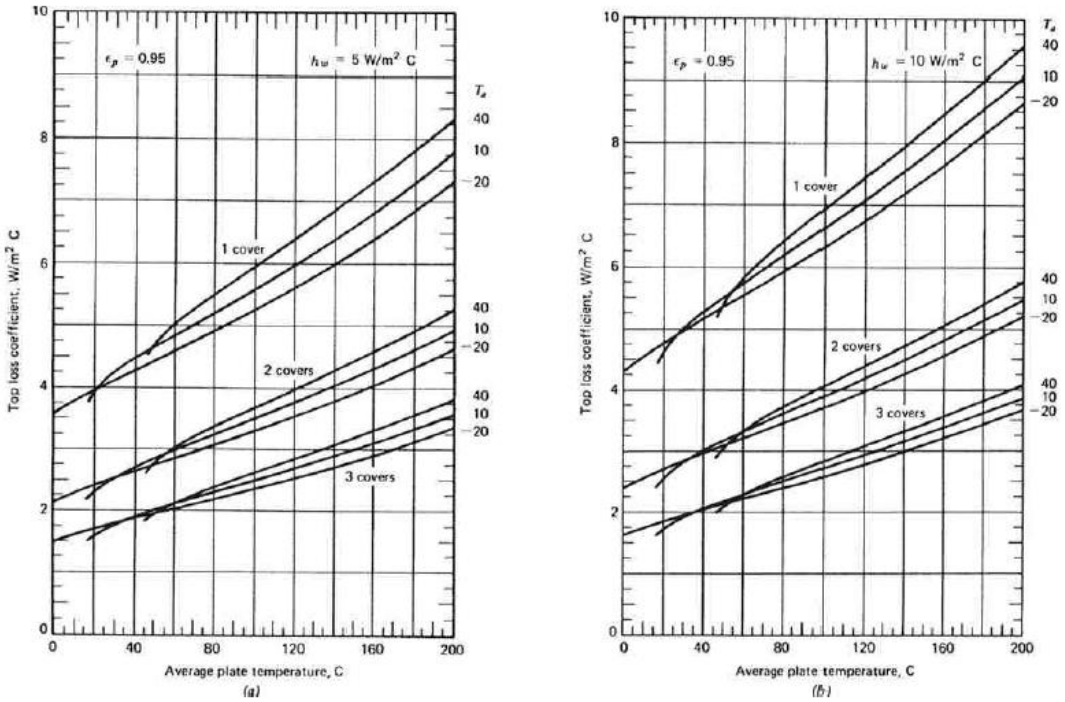


**Figure 5.2.** Top Loss co-efficient. Image from J. A. Duffie and W. A. Beckman, Solar Engineering of Thermal Processes, Fourth Edition, US: John Wiley & Sons, ©2013. Ch. 6, p. 11.

This image shows that the addition of the second cover has a larger effect on reducing the top heat loss coefficient than the addition of a third cover does. **Figure 5.3** shows the effect of plate spacing on the top heat loss coefficient. For spacings less than 15 mm, heat transfer is dominated by gap conduction and radiation which contributes to a sharp increase in losses and the spacing decreases [70]. For spacing over 15 mm, fluid motion and conduction starts to increase, contributing to a small rise in the top heat loss coefficient between 15-20 mm, which reaches a maximum at around 20 mm [70]. Plate spacing should thus be 15 mm or 25 mm or greater to reduce losses.

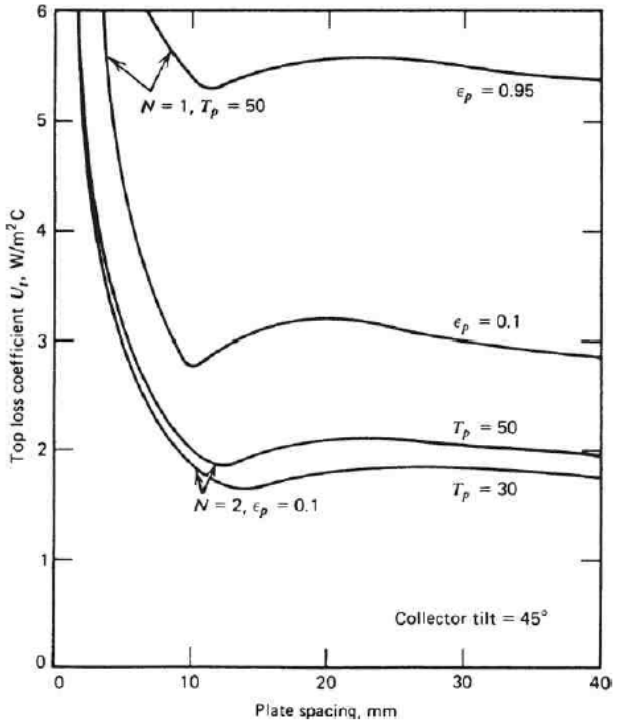


**Figure 5.3.** Variation of top loss coefficient with plate spacing. Image from J. A. Duffie and W. A. Beckman, Solar Engineering of Thermal Processes, Fourth Edition, US: John Wiley & Sons, © 2013. Ch. 6, p. 13.

The temperature difference between collector tubes can be calculated by treating the black plate as a fin and applying relevant equations. Plate thickness, thermal conductance, and distance between tubes can be used to create a classic fin problem. Note that it is generally assumed that due to the small thickness and high thermal conductance of the absorber that the temperature gradient through the plate is negligible. It is suggested that the plate thickness should be between 0.5-1 mm and that additional thickness does not significantly increase collector efficiency [70].

The heat transfer rate to the fluid is given by Equation 5.3, wherein $T_b$ is the local base temperature, *F* is the standard fin efficiency for straight fins which is provided by Equation 5.4 [70], *W* is the width between collector tubes, *D* is the diameter of the tubes, and *m* is given by Equation 5.5, wherein $\delta$ and $\kappa$ are the thickness and thermal conductance coefficient of the plate, respectively [70].

Equation 5.3 $$q'_{fin} = (W - D)F[S - U_L(T_b - T_a)]$$

Equation 5.4 $$F = (\tanh [m(W - D)/2]/m(W - D)\,)/2$$

Equation 5.5 $$m = \sqrt{\frac{U_L}{\delta\kappa}}$$

The effect of various fin spacing and sizing on fin efficiency and collector efficiency is shown in **Figure 5.4** and **Figure 5.5**.

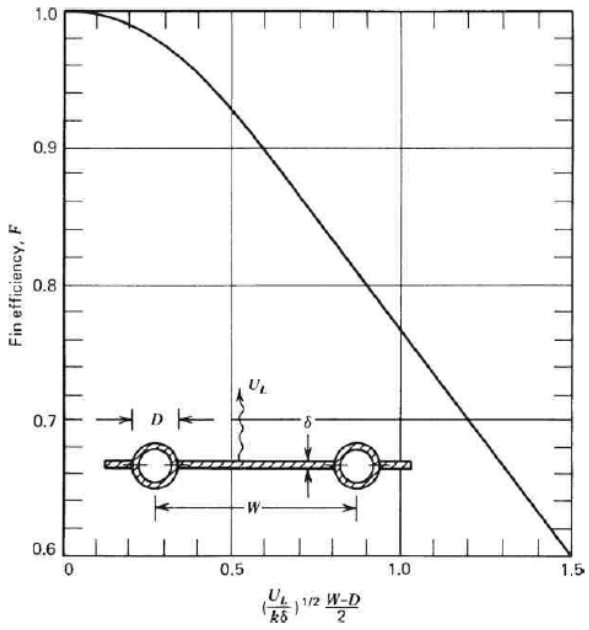


**Figure 5.4**. Fin efficiency for tube and sheet solar collectors. Image from J. A. Duffie and W. A. Beckman, Solar Engineering of Thermal Processes, Fourth Edition, US: John Wiley & Sons, ©2013. Ch. 6, p. 19.

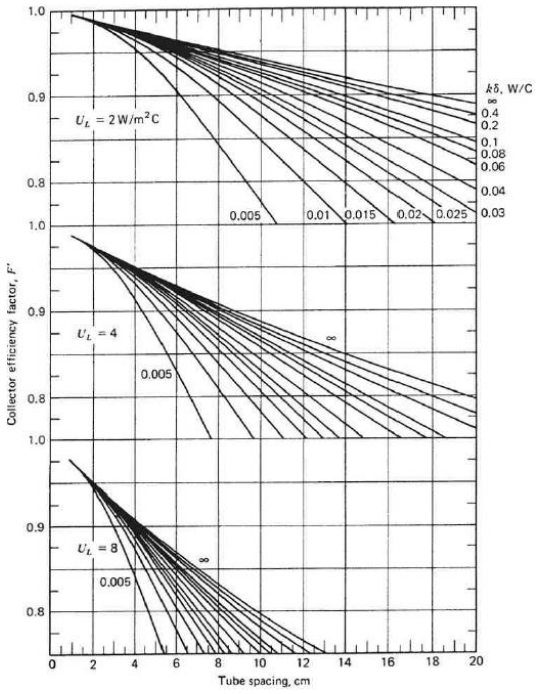


**Figure 5.5.** Collector efficiency factor versus tube spacing for 10 mm diameter tubes. Image from J. A. Duffie and W. A. Beckman, Solar Engineering of Thermal Processes, Fourth Edition, US: John Wiley & Sons, ©2013. Ch. 6, p. 21.

In addition to fluid collector tube spacing, the useful gain per unit flow length can be used to determine the length of the collector tubes. As fluid enters the tube at $T_{in}$ its temperature progressively increases towards $T_{plate}$, reducing the heat gain due to decreasing heat transfer as it progresses along the tube. Combining this with the fin efficiency factor, these parameters can be grouped into a collector heat removal factor, which is given in Equation 5.6 [70].

Equation 5.6 $$F_R = \frac{\dot{m}C_p}{A_c U_L}[1 - \exp\left(-\frac{A_c U_L F'}{\dot{m}C_p}\right)]$$

Where *F'* is the collector efficiency factor, $F_R$ is the collector heat removal factor and $\dot{m}$ is the mass flow rate. $F_R$ can also be the effectiveness of a heat exchanger, which is the ratio of actual heat transfer to maximum possible heat transfer. Combining this all together leads to Equation 5.7 which can be used to describe the useful energy gain of any flat-plate collector and is a function of inlet temperature vs ambient temperature.

Equation 5.7 $$Q_u = A_c F_R [S - U_L(T_i - T_A)]$$

## 5.3 Methods

Using the transmission/spectrum model based on the spectra measured in Chapter 2 and developed in Chapter 4, the parameters of a solar thermal heating system can be estimated. To do this, the lamp spectrum used for the calculations in Chapter 4 are replaced with the AM 1.5 Spectrum (downloaded from nrel.gov [71]). Applying Equation 2.1 to Equation 2.6 and Equation 4.1 to Equation 4.7, the profile of energy as it passes through various combinations of panels can be found. Table 5.1 shows an example of the calculation results for a RYB panel under solar irradiance (total 858.42 W/m$^2$ from 280 to 3400 nm).

**Table 5.1.** RYB panel under the AM 1.5 solar spectrum. All units in W/m$^2$

| W/m$^2$ | Total energy blocked by panel | Dye absorption | Refection | Transmission (includes bottom escape loss) | Power, Edge | Dye absorption loss | host absorption | Dye Escape (top) |
|---|---|---|---|---|---|---|---|---|
| Red | 176.61 | 141.00 | 56.23 | 624.36 | 44.69 | 74.98 | 48.22 | 21.32 |
| Yellow | 82.12 | 59.53 | 40.83 | 501.40 | 12.98 | 39.29 | 25.55 | 7.26 |
| Blue | 29.23 | 19.15 | 33.27 | 438.90 | 9.67 | 7.22 | 12.49 | 2.26 |
| sum | 287.96 | 219.67 | 130.34 | 438.90 | 67.34 | 121.49 | 86.26 | 30.84 |

Using this data, various flat-plate solar thermal collector designs using LSCs can be explored. Note that the size of each LSC module must be kept consistent to maintain the same dye efficiencies as found in Chapter 4. Changes in LSC size can be accounted for by modifying the dye efficiency using results from raytracer, although these results are less reliable unless the actual dye efficiency is verified. Traditionally LSCs are used with a focus on electricity generation, however, they may also have potential for use in solar thermal heating systems.

### 5.3.1 Solar thermal collector equations

This section describes the methods used to determine the comparison between energy losses associated with a flat black plate solar collector to those of an LSC thermal collector. Using Equation 5.8 we can estimate the useful thermal energy output from LSC SAHs and traditional SAHs. For these calculations, it is assumed that there is no fluid flow within the collector.

Equation 5.8

$$Q_u = A_c[S - U_L(T_{pm} - T_a)]$$

Where *S* is equal to the solar irradiance *I*, minus the optical losses. The optical losses for LSCs are estimated using Chapter 4 methods. The thermal energy loss coefficient from a flat black plate collector $U_L$, is comprised of radiative and convective losses through the top side of the plate, $U_t$, and losses through insulation at the bottom, $U_b$, and edges, $U_e$, of the plate.

Equation 5.9

$$U_L = U_t + U_b + U_e \qquad \left(\frac{W}{m^{2\circ}C}\right)$$

The top losses can be estimated within ± 0.3 W/m$^2$ using Equation 5.10, which was created to allow for computer calculations [70].

Equation 5.10

$$U_t = \left( \frac{N}{\frac{C}{T_{pm}} * \left[\frac{T_{pm} - T_a}{N + f}\right]^e} + \frac{1}{h_{air}} \right)^{-1} + \frac{\sigma(T_{pm} + T_a)(T_{pm}^2 + T_a^2)}{\frac{1}{\varepsilon_p + 0.00591\, N h_w} + \frac{2N + f - 1 + 0.133\varepsilon_p}{\varepsilon_g} - N}$$

Where, *N* = Number of glass covers

$f$ = (1+0.089$h_w$ – 0.1166 $h_w\varepsilon_p$) (1+0.07866N)

$C$ = 520(1-0.000051$\beta^2$) for 0° < $\beta$ <70°

$e$ = 0.430(1-100/$T_{pm}$)

$\beta$ =tilt angle of the collector

$\varepsilon_p$ = emittance of the plate

$\varepsilon_g$ = emittance of the cover

$T_a$= ambient temperature (K)

$T_{pm}$= mean plate temperature (K)

$h_{air}$ = wind heat transfer coefficient (W/m$^2$ °C)

$\sigma$ = Stefan-Boltzmann constant

To evaluate the $T_{pm}$ in this equation, an iterative mathematic method or simulation work can be done. Additionally, for solar air heaters, it is suggested that $T_{pm}$= 20 + $T_{in}$ as a rough estimate [70].

The heat loss coefficient for the bottom of the collector, $U_b$, can be calculated using Equation 5.11 [70].

Equation 5.11

$$U_b = \frac{k}{L} \qquad \left(\frac{W}{m^2 °C}\right)$$

Where *k* and *L* are the conductance and thickness of the insulation, respectively.
The heat loss coefficient for the edge of the plate, $U_e$, is given by Equation 5.12 [70].

Equation 5.12

$$U_e = \frac{\frac{k}{L} * Pl * t}{A_C} \qquad \left(\frac{W}{m^2 °C}\right)$$

Where *Pl* and *t* are the perimeter and thickness (or height) of the plate, respectively, and $A_C$ is the collector Area.

Using these equations, $U_T$ can be calculated at various values of $T_{pm}$.

For an LSC SAH, the thermal heat losses, $U_T$, are the sum of heat transfer losses from the absorber. To illustrate these losses, a simple geometry is created in which an absorber is attached to an LSC and surrounded by insulated round ducting, as shown in **Figure 5.6**.

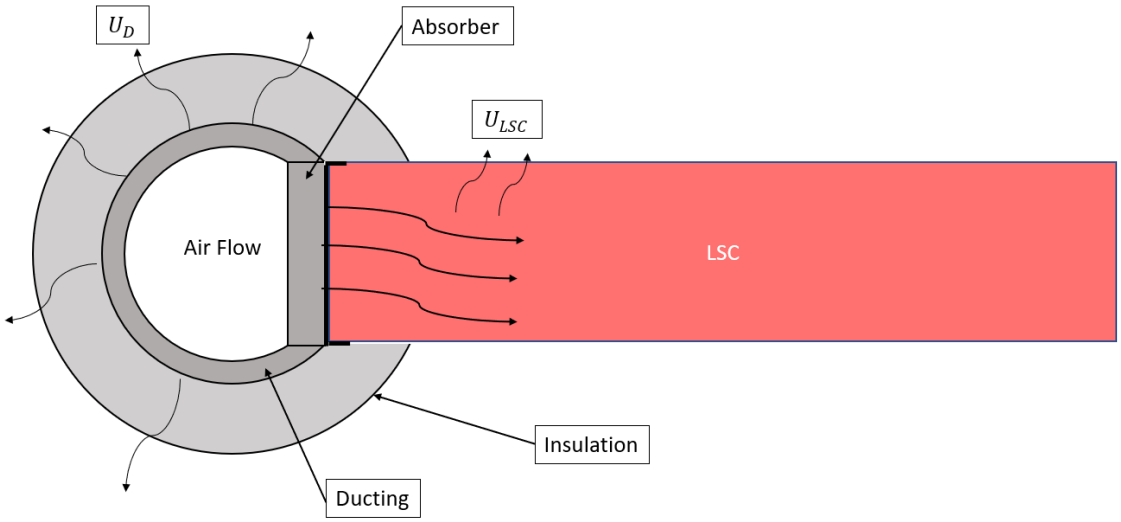


**Figure 5.6.** Single LSC thermal collector design

The heat loss coefficient from the absorber can be found as the sum of the heat loss coefficient through the ducting, $U_D$, and the heat loss coefficient through the LSC itself, $U_{LSC}$. The heat loss through the LSC can be calculated using the fin equation for an infinitely long rectangular fin, given as Equation 5.13. The assumption of an infinite fin is made due to the large profile of the LSC.

Equation 5.13

$$Q_{fin} = \sqrt{h * P * A_{cross\ section} * k} * (T_{pm} - T_a)$$

Equation 5.14

$$u_{LSC} = \sqrt{h * Pl * A_{Cross\ section} * k} \quad \left(\frac{W}{°C}\right)$$

Where *Pl* is the perimeter (2 x width + 2 x thickness), *h* is the convection co-efficient and *k* is the thermal conductance co-efficient of the fin. Note that the units here are in $\left(\frac{W}{°C}\right)$ rather than $\left(\frac{W}{m^2 °C}\right)$ which was the case for the flat plate collector.

It is assumed that there is no heat loss to the insulation as the heat travels through the covered portion of the LSC. Under this assumption, the total heat loss co-efficient through the LSC becomes the sum of the thermal resistance, as described by Equation 5.15 and Equation 5.16.

Equation 5.15

$$U_T = \frac{1}{R_T} = \frac{1}{R_{LSC} + R_{fin}}$$

Equation 5.16

$$a.\ \ R_{LSC} = \frac{L_{overlap}}{k_{lsc} * A} \qquad\qquad b.\ \ R_{fin} = 1/u_{LSC}$$

To determine the heat loss through an insulated pipe, $U_D$, Equation 5.17 is needed.

Equation 5.17

$$Q_D = \frac{2\,\pi * L * (T_i - T_a)}{\frac{1}{r_1 * h_{in}} + \frac{\ln(r_2/r_1)}{k_{pipe}} + \frac{\ln(r_3/r_2)}{k_{Insulation}} + \frac{1}{r_3 * h_{air}}}$$

Where $r_3$ is the outer diameter of the insulation,
$r_2$ is the outer diameter of the pipe.
$r_1$ is the inner diameter of the pipe.
$h_{in}$ is the heat transfer coefficient for the fluid flowing in the pipe.
$h_{air}$ is the heat transfer coefficient of the surrounding air.
$L$ is the length of the pipe.
Note that the contact resistance between the pipe and insulation is ignored.

For our purposes, it is assumed that there is no fluid flow in the pipe. This means that any positive $Q$ value calculated is the maximum amount of energy that could be removed by a heat transfer fluid and thus the first term of the denominator can be removed. Because the inside pipe

(i.e. the ducting shown in **Figure 5.6**) is made from metal and has a high thermal conductance, it is assumed that the inside pipe has the same temperature as the absorber. To verify this assumption, the *k* value for aluminum is 205 W/m·K and 0.0299 W/m·K for polyurethane foam. Thus, in the absence of heat loss from the inside of the piping, the conductance through the piping is ~6856 times larger than the conductance through the insulation. This allows the previous equation to be simplified to Equation 5.18.

Equation 5.18

$$U_D = \frac{2\,\pi * L}{\frac{\ln\,(r_3/r_2)}{k_{Insulation}} + \frac{1}{r_3 * h_{air}}}$$

Equation 5.18 applies to an entire pipe, but only part of the ducting is comprised of piping; the rest is the absorber and experiences heat loss through the LSC. To account for this, a ratio was created to represent the percentage of pipe that this equation applies too. This ratio can be created using simple geometry based on the circumference of the actual ducting versus the circumference of a pipe with the same radius. This ratio is given by
Equation 5.19, where *t* is the thickness of the LSC sheet.

Equation 5.19

$$R = \frac{\pi - \sin^{-1}\left(\frac{t}{2r_3}\right)}{\pi}$$

The final equation for the LSC solar heaters becomes:

Equation 5.20

$$Q_u = S_{LSC} * A_C - (u_{LSC} + R *\ U_D)\left(T_{pm} - T_a\right)$$

Where $S_{LSC}$ is equal to the amount of light captured by the LSC dye multiplied by the optical efficiency of the panel.

### 5.3.2 Initial parameters for the LSC collector and the flat plate collector:

The thermal energy from an LSC collector is first compared to that from a traditional flat-plate collector assuming the same amount of solar energy is absorbed. That is, to keep it fair, initially, the *S* term for the flat plate collector is set to be the same as the amount of energy captured by the LSC panel. For example, if a red LSC panel is used, which absorbed 141 W/m$^2$ of light from the AM 1.5 Solar spectrum, then 141 W/m$^2$ is also used for the *S* value of the flat plate collector. This comparison is motivated by the fact that the portion of the AM 1.5 Solar spectrum not absorbed by the LSC panel can be used for other purposes, such as lighting in greenhouses or underlying LSC collectors in a multi-panel configuration. Additionally, this comparison also provides initial validation for the design of hybrid SAHs, which are comprised of both LSCs and flat black plates and are presented later in this chapter; if the results from this initial comparison show the flat black outperforms the LSC SAH when the absorbed solar irradiance is the same, then pursing the design of hybrid LSCs would not be sensible.

The initial parameters for $Q_{out}$ as a function of the mean plate temperature for both the flat plate SAH and the LSC SAH are given below. The melting temperature of PMMA and the heat collection efficiency of each collector is not considered. This initial comparison allows for a proof of concept type analysis, to compare "apples to apples" to determine the advantages, if any, of the LSCs energy capture mechanism in LSC SAHs compared to that in traditional flat-plate SAHs. Following this initial comparison, the spectrum is expanded to include the entire solar spectrum for additional comparison in subsequent multi-panel configurations.

Initial parameters for the LSC collector and the flat plate collector:

**RED LSC SAH**

LSC thickness = 3mm

Material = PMMA

$k_{PMMA}$ = 0.2 W/m·k

Area = 0.25 m$^2$

Side length = 0.5 m

Insulation thickness: r = 25mm

$h_{air}$ = 10 (W/m$^2$ °C)

$k_{insulation}$ = 0.0299 W/ m·k

$T_a$= 0 °C

$r_1$= 1 mm

$r_2$= 1.5 mm

$r_3$= 26.5 mm

Absorber/piping = Aluminum

$K_{Al}$ = 205.0 W/m K

LSC colour: Red

Dye absorption = 141.0 W/m$^2$

Optical efficiency = 29.3%

S = 0.293 * 141.0= 41.313W/m$^2$

**It is assumed that all 4 side of the LSC have an absorber and ducting

**Flat plate collector:**

Area = 0.25 m$^2$

$\varepsilon_p$ = 0.9

$\varepsilon_g$ = 0.88

$T_a$ = 0 °C

N = 1

$T_{pm}$ = to be plotted

$h_{air}$ = 10 (W/m$^2$ °C)

Insulation thickness = 50mm

$k_{insulation}$ = 0.0299 W/m K

Side length = 0.5 m

Height = 15mm

S = 141.0W/m$^2$

### 5.3.3 Multi-panel LSCs

Multi-panel LSCs are simply different coloured LSCs stacked on top of one another which can enhance the total amount of energy captured by the LSCs. In practice, there should be an air gap between each to minimize the light from one panel cascading into the next and driving up re-absorption losses. However, it is assumed that there is no gap between the panels in this analysis. All multi-panels used in this analysis are composed of theoretical red green and blue LSCs, stacked in that order and with the same transmission, reflection and absorption as the LSC measured in Chapter 2. The addition of a fourth panel using near-infrared dye is (denoted NIR) was also used. It is assumed that all LSC panels are made from acrylic and are 3 mm thick, thus the LSC thickness becomes 9 mm for a 3-panel Multi-Panel LSC and $r_2$ becomes 4.5 mm.

### 5.3.4 Energy flow

The amount of energy absorbed by each LSC panel is estimated using the methods presented in Chapter 4. The dye efficiencies were estimated at various sizes using Raytracer. **Table 5.2** shows the expected dye efficiencies generated by Raytracer [29] using 500,000 photons in a square 3 mm PMMA LSC for various BASF dyes with concentrations of 400 ppm. Note that the dyes available on raytracer may not be the same dyes used in the measured samples, leading to a possible source of error; However, thermal testing of samples in Chapter 4 (with an area of 0.25m$^2$) has shown that the dye efficiencies of the samples are close to that predicted by the program.

**Table 5.2** Dye efficiencies using Raytracer

| Size ($m^2$) | Red<br>Rot 305 | Blue<br>Violett 570 | Yellow<br>Gleb 170 | Green<br>Gleb 083 | Orange<br>Orange 240 |
|---|---|---|---|---|---|
| 0.01 | 38.50% | 62.39% | 40.40% | 37.84% | 37.40% |
| 0.1 | 32.10% | 55.23% | 31.40% | 29.00% | 28.71% |
| 0.25 | 29.30% | 51.59% | 27.72% | 26.16% | 25.75% |
| 0.5 | 27.29% | 49.93% | 25.74% | 24.33% | 23.77% |
| 1 | 25.30% | 46.74% | 24.50% | 23.50% | 21.30% |

**Table 5.3** gives the estimated edge power and subsequent transmission for stacked LSCs in the following order: red, green, blue, NIR. Values are based on the AM 1.5 Solar spectrum (Direct + circumsolar) from ASTM G173-03 Reference Spectra [72]

**Table 5.3** Absorption, transmission and edge power of stacked RGB + NIR LSCs.

| $W/m^2$ | Total<br>Absorbed | Reflection | Transmission | Dye<br>Absorb | Dye Efficiency<br>at 1 $m^2$ | Edge<br>power |
|---|---|---|---|---|---|---|
| Red | 176.61 | 56.23 | 624.36 | 141.00 | 25.3% | 35.67 |
| Green | 70.52 | 40.47 | 513.37 | 53.38 | 23.5% | 12.59 |
| Blue | 35.68 | 34.00 | 443.68 | 23.24 | 46.7% | 10.85 |
| NIR (estimated) | - | 28.74 | 295.40 | 104.31 | 28.8% | 30.04 |

### 5.3.5 Double LSC Collector

To further increase the temperature, two LSC collectors could be placed on either side of the ducting, as illustrated in **Figure 5.7**.

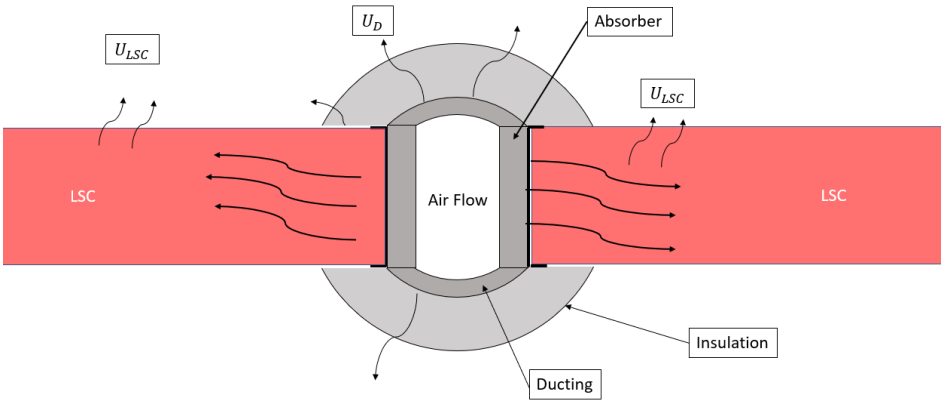


**Figure 5.7**. Illustration of a double LSC collector

The relevant heat transfer equations can be easily modified by doubling the LSC related losses and adjusting the ducting ratio R for the reduced ducting area. This setup uses 3 LSC panels (RGB) and adds the restriction that the diameter must be greater than the thickness of the LSC to allow for a gap to exist between the two absorbers. Thus, for a small 2 mm air channel between the 9 mm absorbers (3 mm x 3 panels), the inner diameter of the ducting must be 9.22 mm.

### 5.3.6 Hybrid LSC design

To further improve the amount of light harvested by an LSC collector, a flat black plate can be placed behind the LSC panels and used to pre-heat the working fluid prior to entering the ducting surrounding the LSC. This configuration is demonstrated in **Figure 5.8** and **(A)** which shows a cross-section view to illustrate fluid flow through the collector.

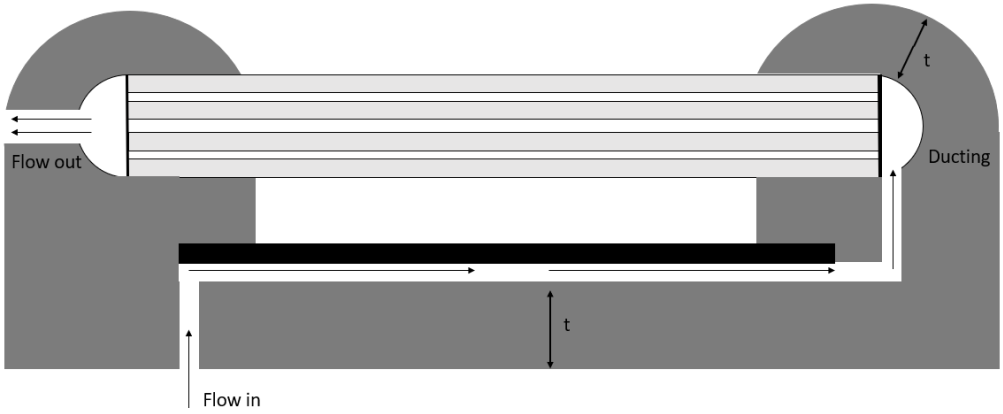


**Figure 5.8.** Cross-section of a hybrid collector using 4 LSC panels and a flat black plate. (Illustration, not to scale. Note that an air gap is included to add distinction between panels)

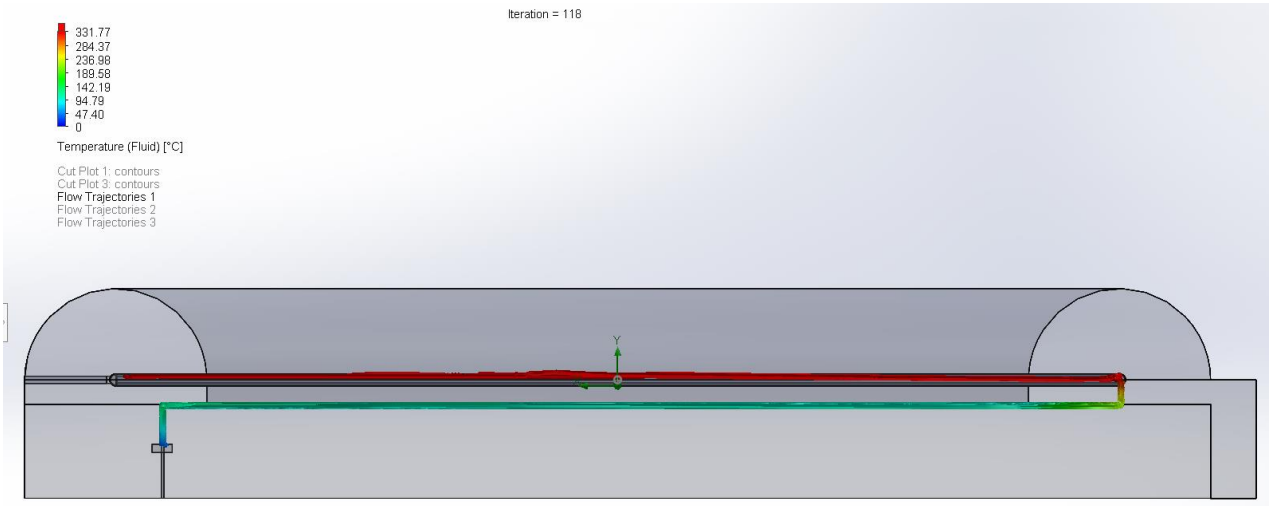


**(A)**

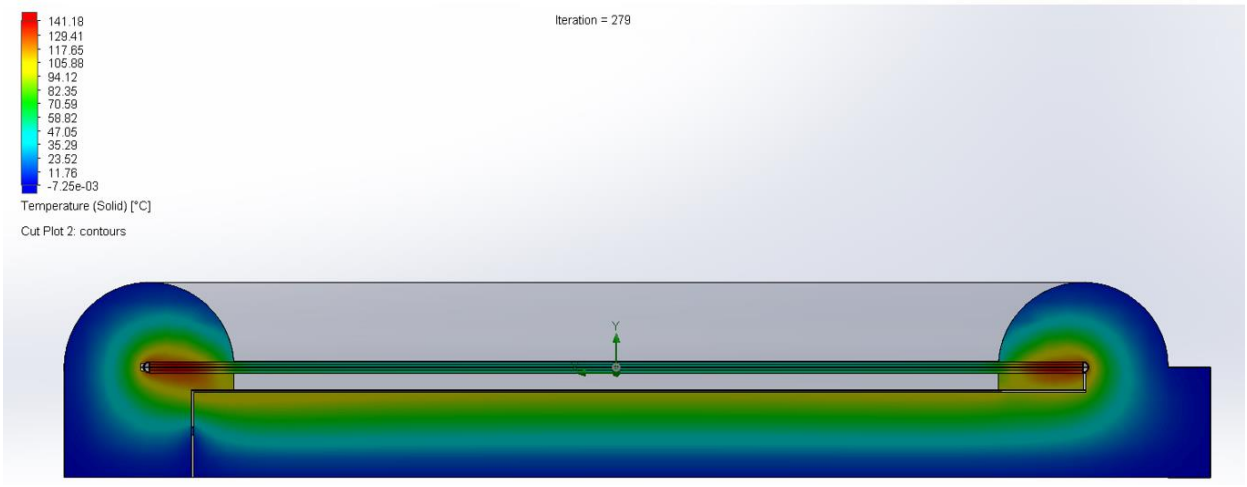


**(B)**

**Figure 5.9**. **(A)** Cross-section of a 1 $m^2$ hybrid collector, modelled using SOLIDWORKS. Fluid temperature is shown in colour scale. **(B)** Cross-section of a 1 $m^2$ hybrid collector, modelled using SOLIDWORKS. Solid temperature is shown in colour scale.

The hybrid configuration was modelled for a 1 $m^2$ RGB LSC with a flat plate collector, using the parameters given in **Table 5.3** which are estimated by using a combination of Raytracer [29] and transmission measurements from samples. For a 3 panel RGB hybrid heater, the transmission through the 3rd panel (443.68 W) is applied as the irradiance on the flat black plate. For a 4-panel RGB+NIR hybrid heater the irradiance on the flat black plate becomes 295.4 W. Because

the LSC panels are now being heated from the bottom (from the flat black plate) it is assumed heat loss in this direction is zero, thus the fin losses from the LSC are cut in half.

## 5.4 Results and Discussion

### 5.4.1 LSC collectors vs flat plate collectors

**Figure 5.10** shows the results of plotting $Q_U$ as a function of the mean plate temperature for both the flat plate collector and the LSC SAH. The point at which the lines cross zero indicates the max temperature of the collector with zero fluid flow. Recall that the irradiance for both collectors has been limited to the absorption of the red dye (141 W/m$^2$); this allows for a direct proof of concept comparison.

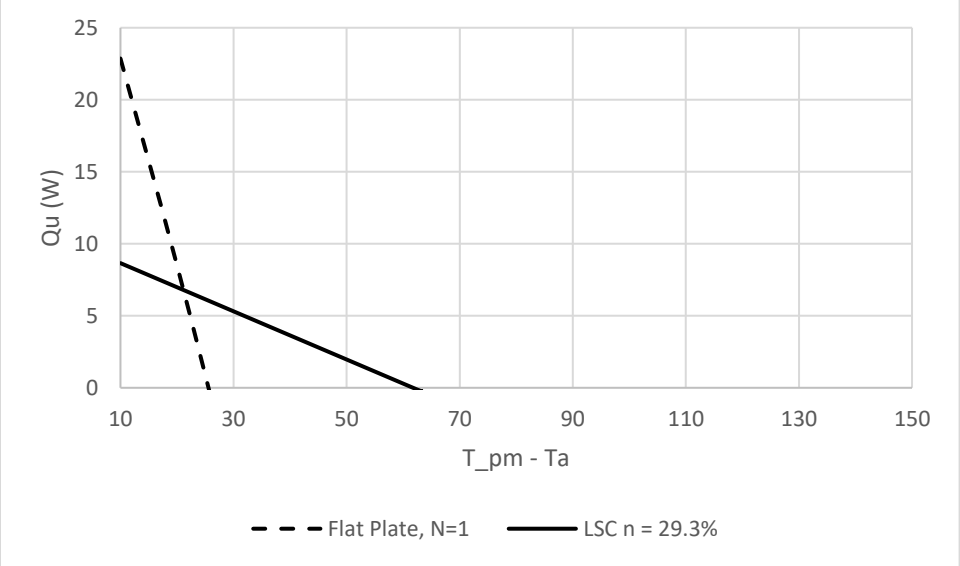


**Figure 5.10.** A comparison between the useful heat energy $Q_u$ and the mean plate temperature for flat plate collectors and an LSC collector. 0.25 m$^2$ LSC collector, with $h_{air}$ =10 W/m$^2$ K.

The results demonstrate that the flat plate collector provides more usable thermal energy than the LSC collector when the difference between the mean plate temperature and the temperature of the surrounding environment is small. Furthermore, when this temperature difference is ~27 °C or larger the flat plate collector does not supply usable thermal energy. In comparison, the LSC

collector provides a lower amount of usable thermal energy when the difference between the mean plate and ambient temperatures is small. However, when this temperature difference is ~22 °C or greater, the LSC SAH outperforms the flat plate collector. Notably, the maximum temperature the thermal collector in the LSC SAH can reach is ~61.5 °C, which is significantly larger than the maximum temperature attainable using the flat plate collector. The ability for the LSC to outperform the flat black plate under these conditions indicates that it may be worth perusing for use in real-world conditions.

Various parameters of both the flat plate collector and LSC SAH were examined. The largest and most realistic improvement for the flat plate collector is to add additional covers, which reduces the heat losses $U_L$ and is shown in **Figure 5.11**. This also reduces the S value by ~10% for each additional cover, due to added reflection and absorption.

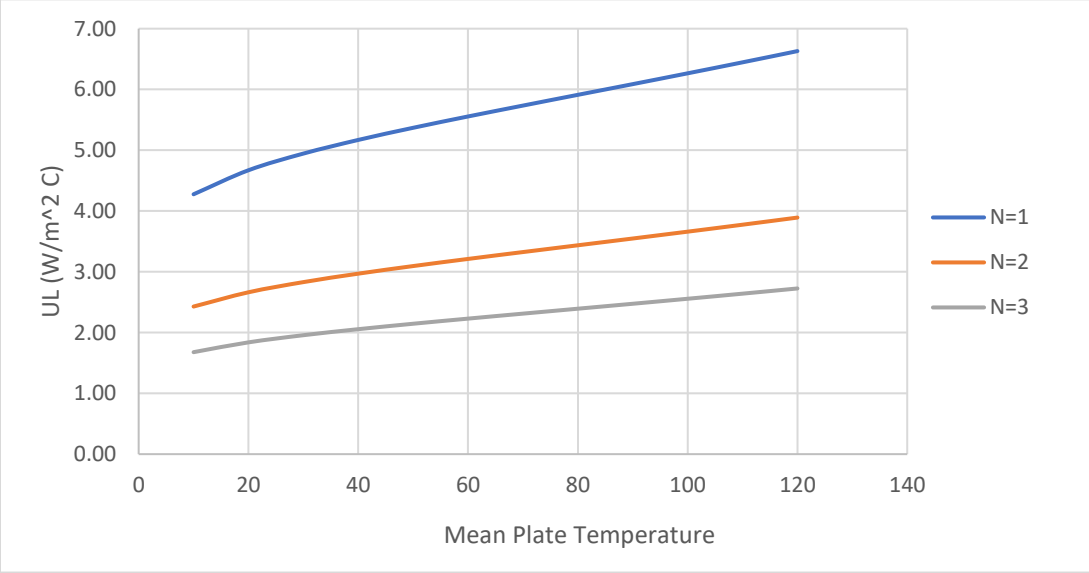


**Figure 5.11.** Effects of the number of covers on $U_L$ for $h_{air}$ = 10, $T_a$ = 0 °C, A = 0.25 $m^2$

For the LSC collector, the parameters that affect performance are the optical efficiency and the size of ducting $r_2$. The larger the size of the ducting, the more heat is lost. The smallest possible size of $r_2$ is half of the thickness of the LSC, due to geometric constraints. At this size, (1.5 mm for a 3 mm thick LSC), the amount of heat lost through the ducting insulation is 2.9 times larger than the heat lost through the LSC. **Figure 5.12** shows this effect on $Q_u$ (useful energy output).

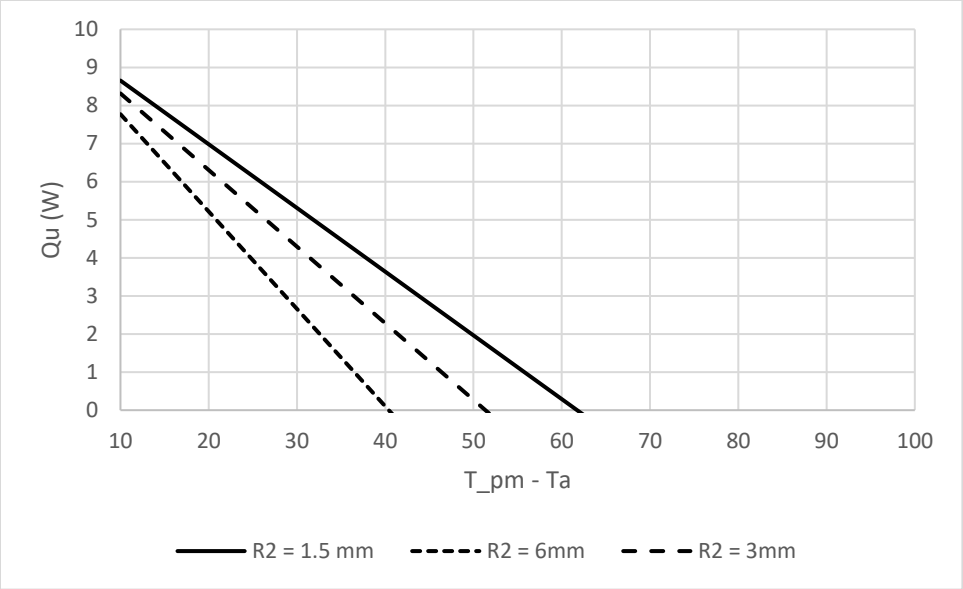


**Figure 5.12.** Effect of $r_2$ on useful heat output. 0.25 $m^2$ LSC collector, with $h_{air}$ =10 $W/m^2$ K

The effects of optical efficiency of the LSC are relatively obvious; as the optical efficiency increase, so does the S value in Equation 5.20, thus increasing the amount of useful energy output. The maximum possible efficiency of an LSC is around 75%, with the remaining 25% lost due to escape cone losses. In addition, Stokes shift must be included to account for the shift in emission wavelength. The amount of energy lost due to Stokes shift can be estimated by taking the ratio between the peak absorption wavelength and the peak emission wavelength. For Lumogen ROT 305 dye, the absorption peak is at 574 nm and the average emission is at 622 nm [39] and thus ~8% of the energy is lost due to Stokes shift. This brings the maximum possible efficiency down to 67%. The effects of increased optical efficiency on useful heat output ($Q_u$) are plotted in **Figure 5.13** against the performance of a black plate collector for collectors with the parameters described previously.

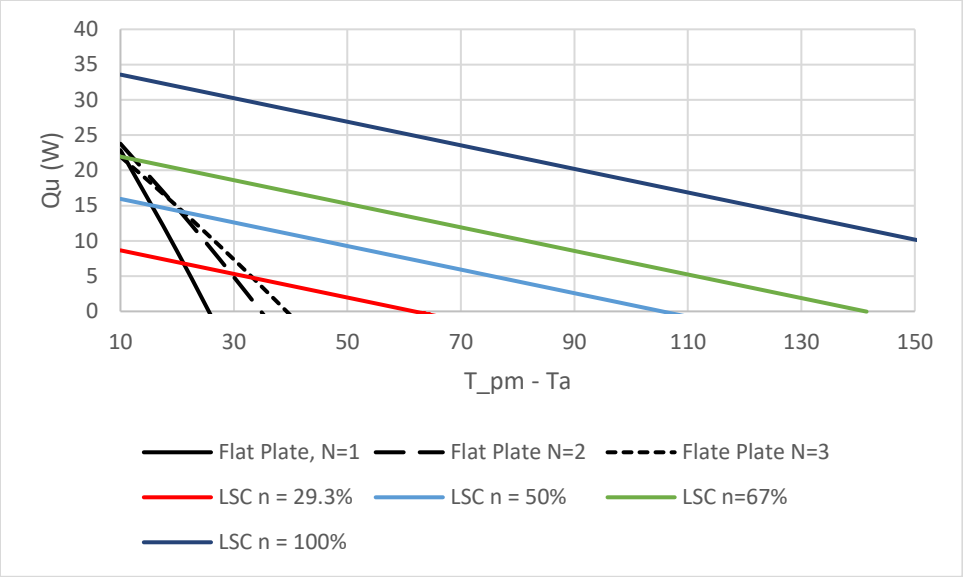


**Figure 5.13**. Comparison of the useful heat output from a flat plate collector with N covers and LSC collectors with an optical efficiency of n. Collector area = 0.25 $m^2$ with $h_{air}$ =10 $W/m^2$ K

The plot in **Figure 5.13** shows that the LSC collectors show benefits in high-temperature applications or cold environments when compared with the flat plate collectors. The flat plate collector losses are dominated by heat transfer losses whereas the losses from the LSC collectors are dominated by optical losses. Efforts to increase the optical efficiency of LSC panels are crucial for LSC collectors to become competitive with 2 or 3 cover flat plate collectors at lower temperatures. It is worth noting that decreasing the size of the LSC collectors improves the optical performance. Using Raytracer [29] to predict the optical efficiency of a 10 cm x 10 cm x 3 mm LSC with Lumogen Red 305 dye, the optical efficiency is estimated to be ~38.5%. Thus, a possible solution is to create a network of small heating panels connected in a network of ducting.

To verify the mathematic model created is correct, an LSC heater with matching parameters to the one previously described was created using SOLIDWORKS and simulated using SOLIDWORKS Flow Sim. The results for the max temperature at three different dye efficiencies were calculated and compared, as shown in **Table 5.4**.

**Table 5.4.** Max temperature comparison between the mathematic model and SOLIDWORKS Flow Simulations

| | n = 29.3% | n = 50% | n=67% |
|---|---|---|---|
| Mathematic Model | 61.5 °C | 105.5 °C | 141.25 °C |
| SOLIDWORKS Flow | 59.9 °C | 102.17 °C | 136 °C |

The results in **Table 5.4** show the mathematic based model closely correlates to the SOLIDWORKS Flow Simulation. With the additional variation of changing the insulation thickness around the ducting to 50 mm rather than 25 mm, the mathematical model predicted a max temperature of 87 °C compared with 80.3 °C from the SOLIDWORKS Flow simulation (a difference of less than 10%).

It is important to recall that for this comparison the flat plate is only being exposed to the same amount of light that the LSC panel can absorb. In reality, the flat plate will absorb nearly the entire spectrum whereas the LSC only absorbs a fraction of it. Thus, for LSC collectors to be competitive with flat plate collectors, the absorption spectrum of LSCs must be greatly increased. This can be done to some degree by stacking different LSC sheets to increase the absorption range. Additionally, a hybrid collector could be designed which utilized both LSCs and a flat black plate to create a solar heater for higher temperature/cooler climate applications.

The useful heat output, Qu, is plotted as a function of the difference between the plate temperature and the ambient temperature, $T_{pm} - T_a$, for an LSC collector with 3 stacked LSCs (RGB) and a flat black plate that absorbs the entire spectrum in **Figure 5.14.** It was assumed there is no gap between LSC sheets, which are 3 mm thick, the radius of the ducting is equal to half the thickness of the LSCs and the area is 0.25 $m^2$. The RGB LSC is expected to absorb 57.1 W per 0.25$m^2$ and produce 16.8 Watts of power at the edge.

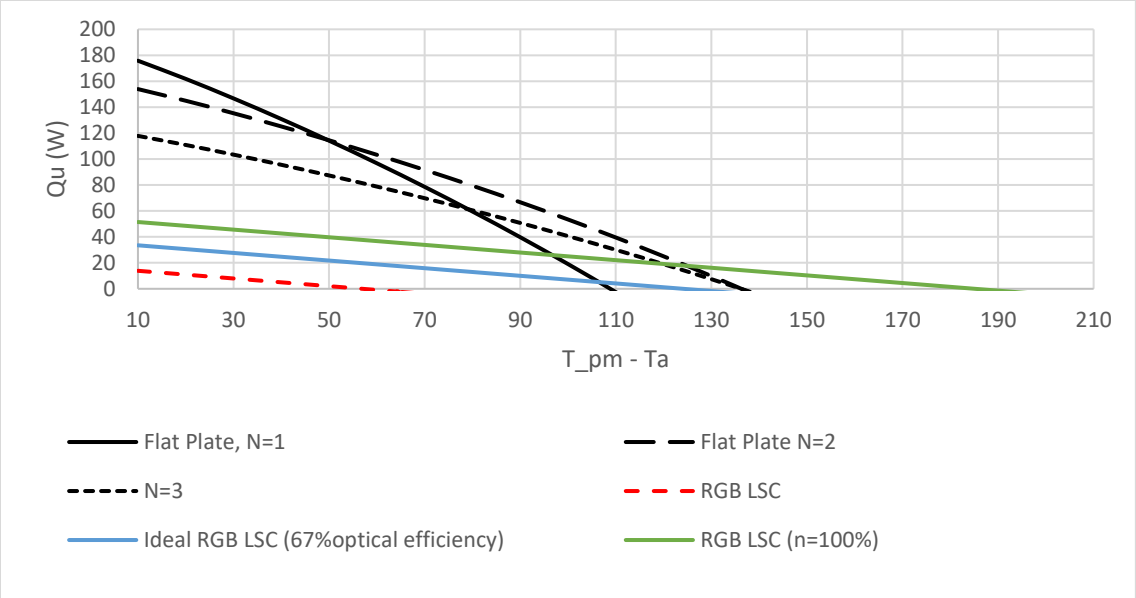


**Figure 5.14.** Useful heat output of an RGB LSC vs a flat black plate collector (0.25$m^2$ collector, $h_{air}$ =10 W/$m^2$ K).

**Figure 5.14** demonstrates that even with 3 LSC sheets, the LSC heaters do not produce as much heat as the flat plate collector at low plate temperatures. However, they can produce comparable temperatures at 67% optical efficiency and outperform the black plate at 100% optical efficiency. Despite the increase in absorbed light by the RGB collector, the required increase in the ducting size drives up the heat losses and prevents the temperature from increasing. The max temperature for the RGB LSC was predicted to be 56 ° C by the mathematic model and 59.7 °C by the SOLIDWORKS Flow Simulation. In comparison, the flat black plate collector can achieve temperatures of 108 °C with one cover, and up to 135 °C with 3 covers. The case for LSCs gets worse when low emittance (e=0.1) black paint is used, driving up the max temperature of the flat plate collectors to ~187 °C, as shown in **Figure 5.15**.

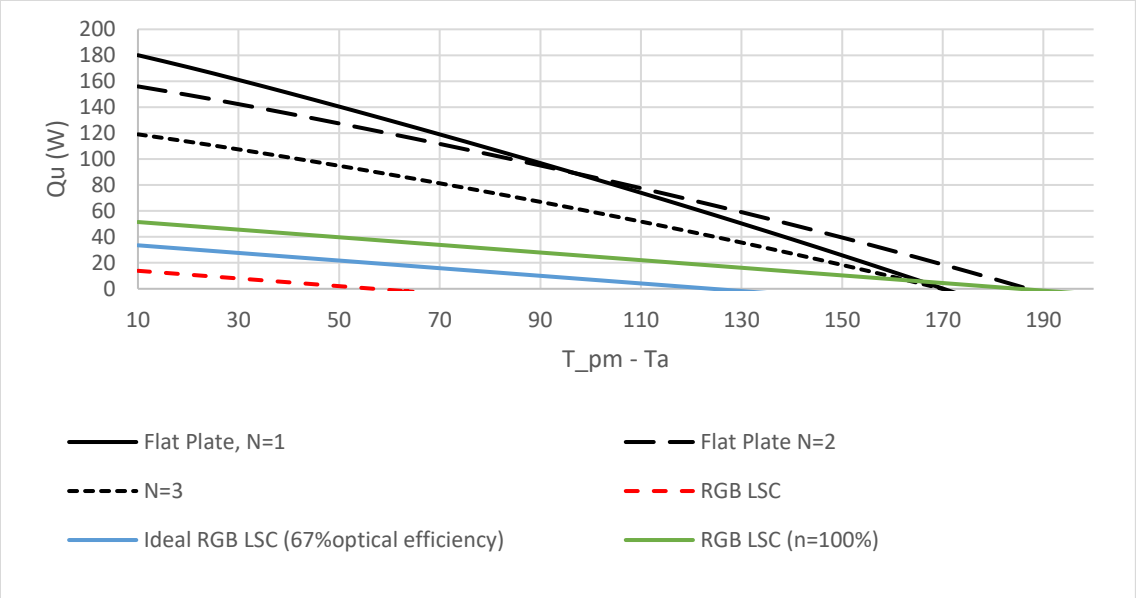


**Figure 5.15.** Flat black plate collector with low emittance (0.1) black paint. (0.25m$^2$ collector, $h_{air}$ =10 W/m$^2$ K).

Interestingly, the max temperature of the flat plate collector stays almost the same (with a small change due to change in edge losses) as the size increases, due to proportionally increasing heat losses with increasing area. However, the maximum useful heat output increases relative to the increase in the collector area. In comparison, the size of the LSC panels can be scaled up increasing the concentration ratio without significantly increasing the amount of heat losses. It should be noted that increasing LSC size correlates to a decrease in the optical efficiency.

The useful heat out and max temperature for flat plate collectors and LSC collectors is plotted in **Figure 5.16** for a 1 m$^2$ panel. Three LSC collectors are modeled, one with a dye efficiency of 67%, another considering the hypothetical case of using 100% dye efficiency and finally one using the dye efficiency predicted by raytracer for a 1m$^2$ panel, as shown in **Table 5.2**.

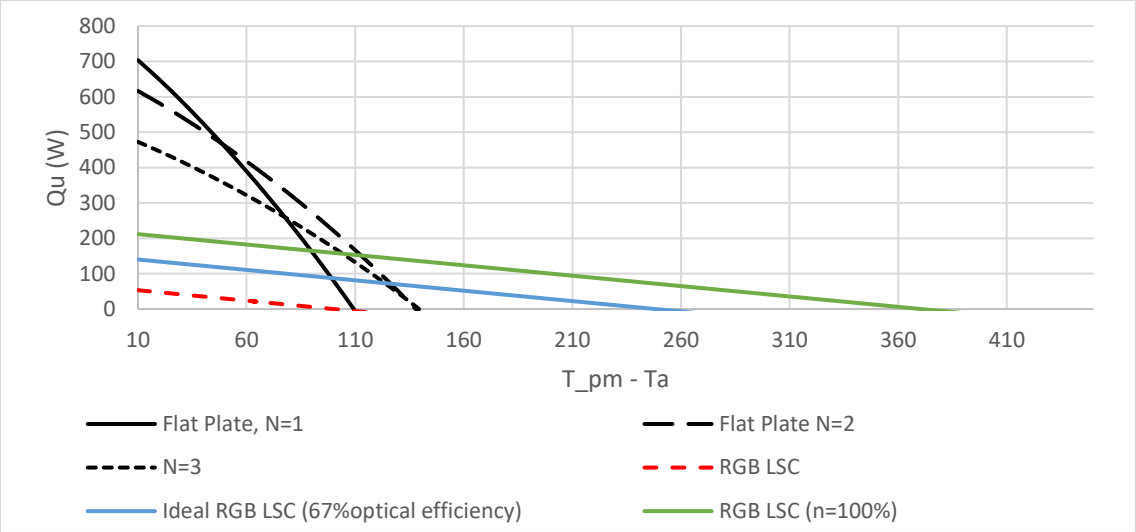


**Figure 5.16.** Output from 1 $m^2$ solar collector using flat plates or LSCs, $h_{air}$ = 10 $W/m^2$ K.

A large increase in the maximum temperature obtainable by the LSC collectors is observed, with the optimal collector (n = 67%) reaching temperatures of ~250 °C and the real collector reaching a temperature of 110 °C. It should be noted that these temperatures can be further increased by increasing the thickness of the insulation around the ducting. The effect of doubling the insulation ducting to 50 mm from 25 mm is shown in **Figure 5.17**.

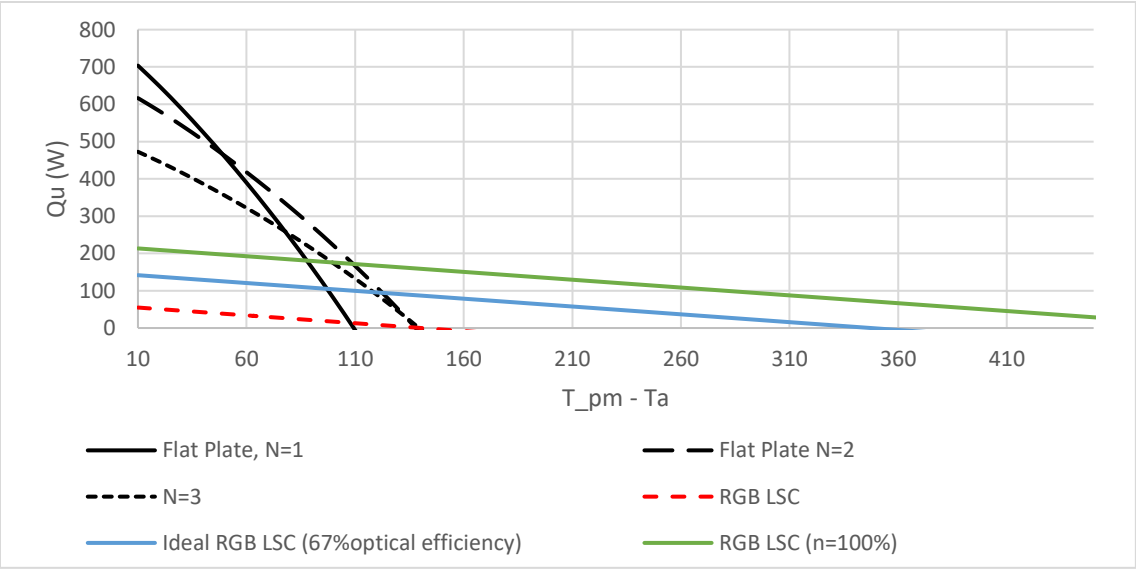


**Figure 5.17** Output from 1 $m^2$ solar collectors using flat plates or LSCs with 50 mm insulation, $h_{air}$ = 10 $W/m^2$ K.

Interestingly, an LSC heater using one panel can achieve similar max temperatures as a 3-panel module. **Figure 5.18** shows the results of a 1 $m^2$ red LSC panel at various efficiencies. This is likely caused by the increase in heat losses associated with the increased ducting size to accommodate the extra panels for multi-panel collectors. Despite having similar maximum temperatures, the multi-panels have a higher useful heat output.

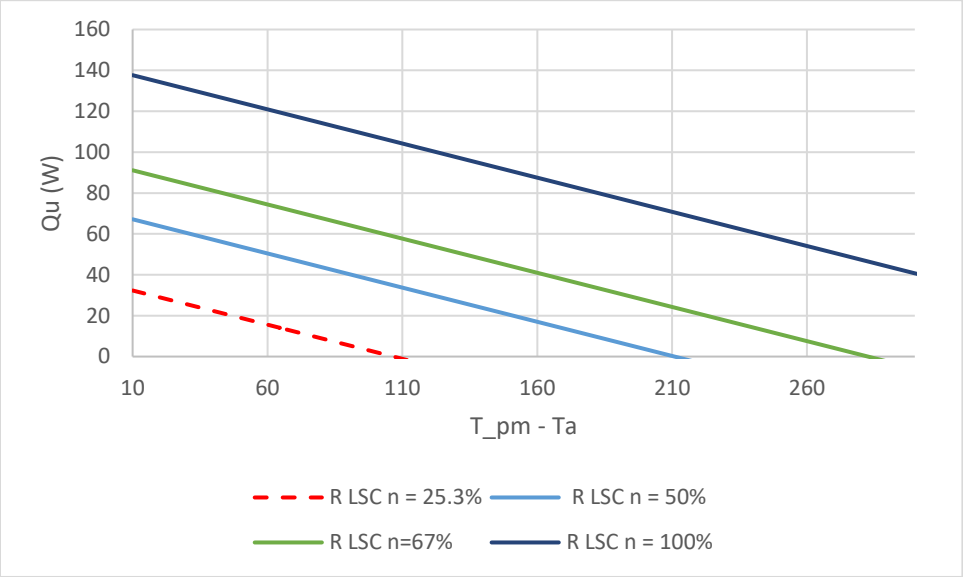


**Figure 5.18.** 1 $m^2$ Red LSC heater with 25 mm thick insulation, $h_{air}$ = 10 W/$m^2$ K.

### 5.4.2 Double LSC collectors

Applying the parameters for a double-sided LSC collector, the maximum temperature for a 0.25 $m^2$ RGB collector (using two 0.125 $m^2$ RGB modules) becomes 62 °C compared to 56 °C for the single-sided RGB collector with the same area (with 25 mm insulation). Using two 0.25 $m^2$ collectors for a total area of 0.5 $m^2$, the max temperature becomes 89 °C. If two 1 $m^2$ panels are used, the maximum temperature reaches 158°C.

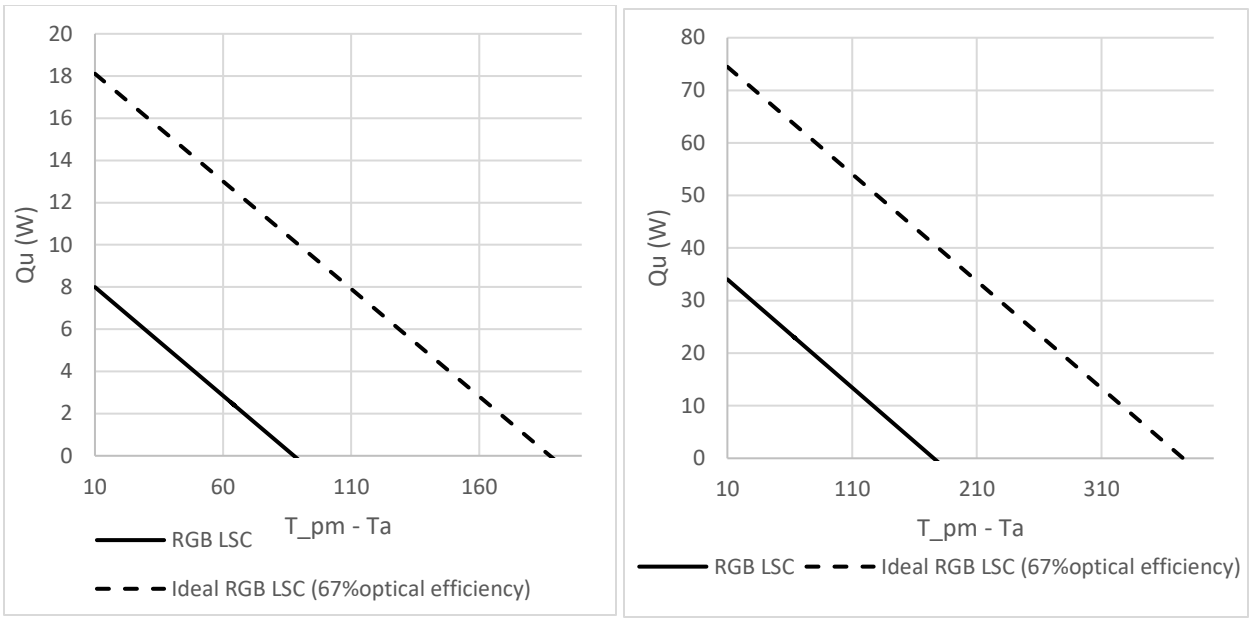


(A) (B)

**Figure 5.19.** Double LSC collectors. (A) collector area = 0.5 $m^2$ (2 x 0.25 $m^2$) and (B) collector area = 2 $m^2$ (2 x 1 $m^2$)

Note that using 50 mm insulation, the max temperature becomes 229 °C for the 2 x 1 $m^2$ RGB collector and 425 °C if 100 mm thick insulation is used. This indicates that double LSC collectors can achieve higher temperatures than flat plate absorbers whether the flat plate absorbers are using low emissivity black paint or not, if the ducting can be insulated adequately. This data also indicates that the larger the LSC, the higher the achievable temperature, however, lower usable heat is achieved due to the decrease inefficiency. It is also likely that larger panels have higher than predicted optical losses. It is for these reasons that larger panels are rarely reported in literature. The results generated using the 0.25 $m^2$ panels are more reliable due to extensive experimentation with panels of these sizes to confirm optical losses. It should be noted that black plate absorbers can produce more usable heat in all situations whereas double LSC collectors offer value for high-temperature applications or cold/windy climates. Additionally, the increase in dye efficiency can drastically improve the output from LSC collectors.

LSC heaters may find use in an application in which transparency and selective spectra absorption is a desirable trait, such as windows. In such an application, they could provide a cooling effect by capturing part of the heat that would have otherwise been transmitted into the

building. This heat could be used for water heating, saving costs on water heating costs and building cooling costs during the summer or in hot climates. In addition, IR (infrared) dyes could be added to expand the range of absorption in the LSC panels.

### 5.4.3 NIR dyes

By using the absorption data for two IR dyes, (BASF l nir1 and nir3) found in the data files of raytracer [29], it was found that a fourth panel consisting of both nir1 and nir3 dyes could capture as much as 104.31 W/m$^2$. Using raytracer [29] with 500,000 simulated photons and dye concentrations of 800 ppm (400 ppm of each dye), it is estimated that an additional 30.4 W/m$^2$ of power could be collected at the edges from a 1 m$^2$ panel. In the case of an optimal dye with 67% dye efficiency, an additional 69.88 W/m$^2$ could be collected. This represents an increase of 30-70% in the amount of energy incident on the absorber. This situation is illustrated in **Figure 5.20** and **Figure 5.21**. The addition of the NIR dyes significantly increases the maximum useful heat output as well as the maximum temperature for both the single and double plane LSC heaters.

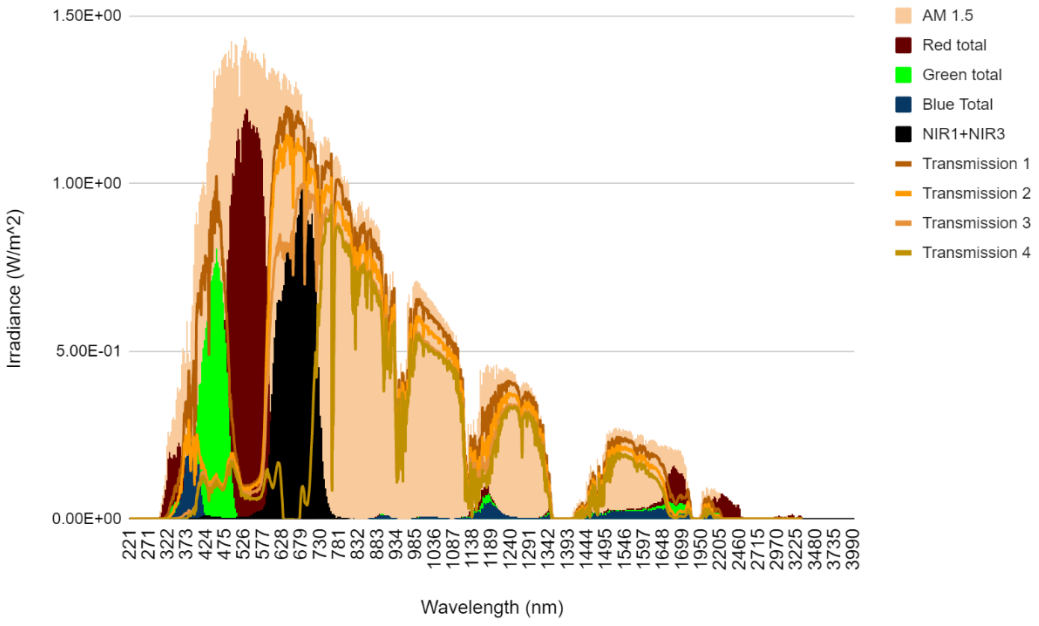


**Figure 5.20** Absorbed energy by four stacked LSC panels, red, green, blue, and NIR1+NIR3. Where the solar irradiance spectrum is shown by AM 1.5, and the total energy absorbed by each dye is shown by “Red total”, “Green total”, “Blue Total” and “NIR1 + NIR3”. Transmission 1,2,3 and 4 show the remaining irradiance spectrum after passing through each panel (red, green, blue, NIR).

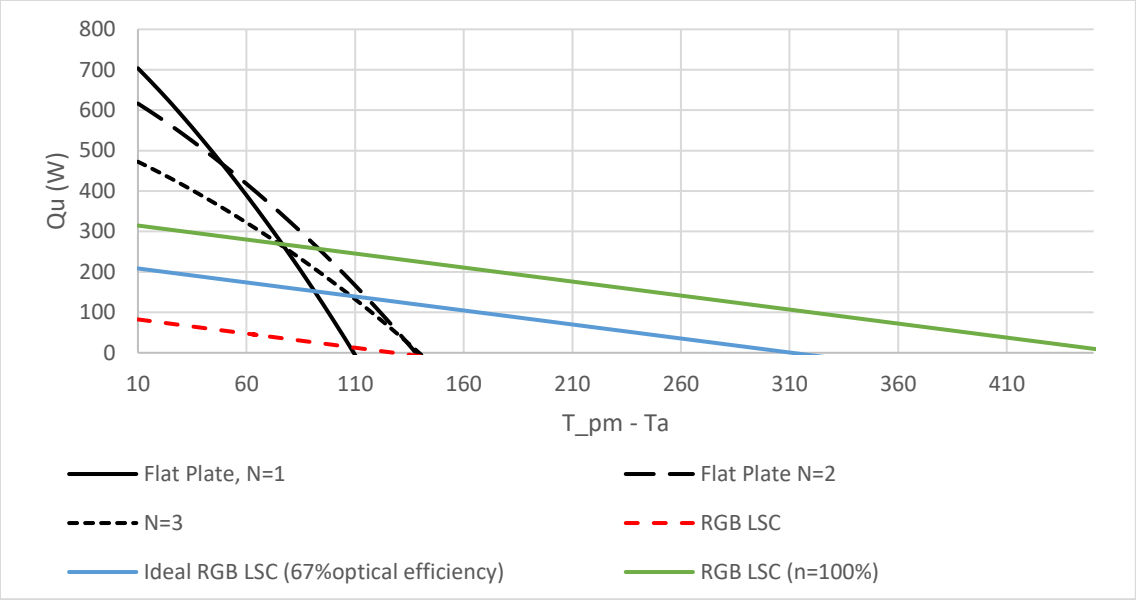


**Figure 5.21.** Useful heat output from a 1 $m^2$ LSC SAH (red green blue and NIR) vs a flat plate collector.

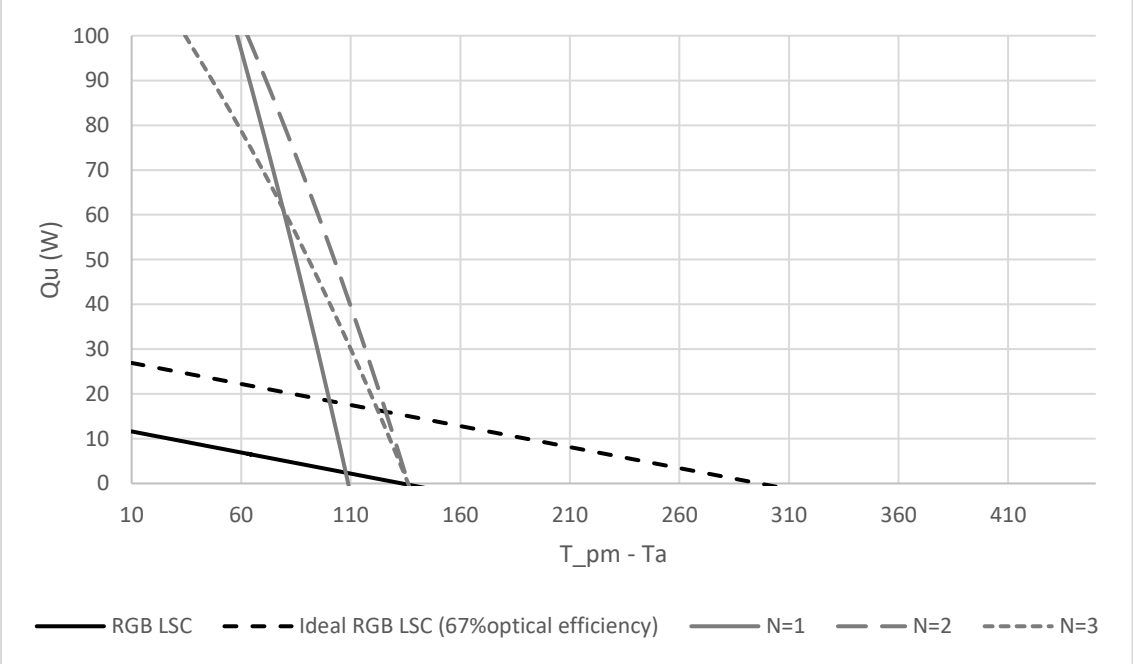


**Figure 5.22.** Useful heat output and max temperature of a double plane LSC collector (2x0.25$m^2$) using Red, Green Blue and NIR panels (50 mm insulation).

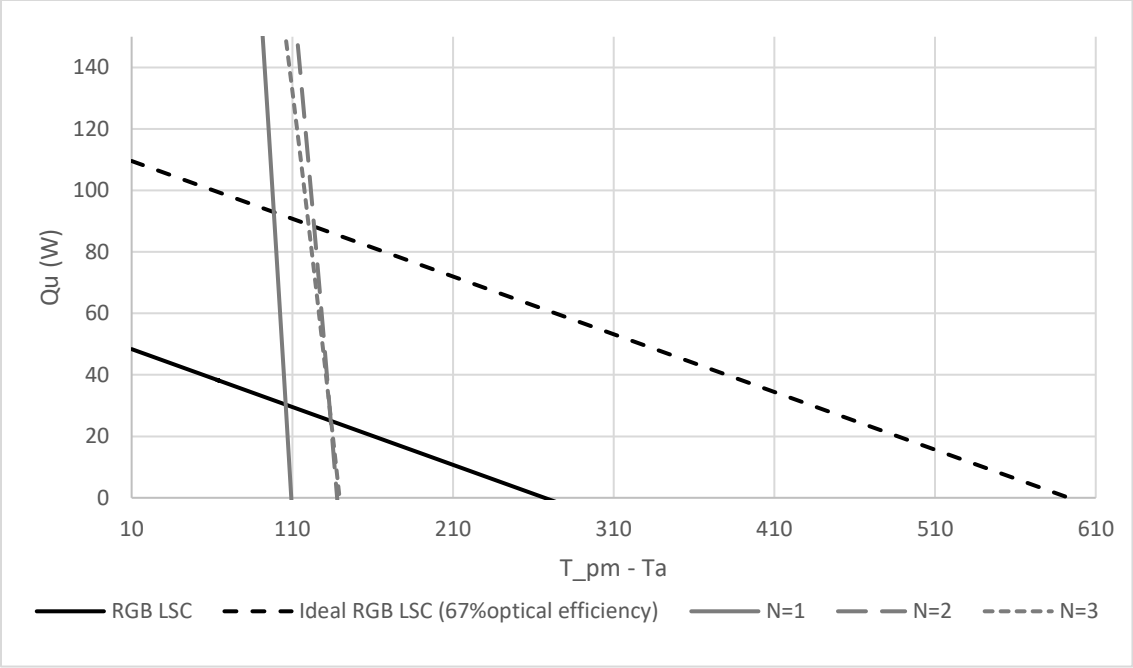


**Figure 5.23.** Useful heat output and max temperature of a double plane LSC collector (2x1 $m^2$) using Red, Green Blue and NIR panels (50mm thick insulation).

For a single transparent panel (1 $m^2$) utilizing just NIR dyes with an optical power output at the edge of 30.4 $W/m^2$ (with insulation thickness of 25 mm), a maximum temperature of 91.5 °C is achievable. For a double plane, transparent collector with the same parameters (using two 1 $m^2$ panels), a maximum temperature of 142 °C can be reached.

### 5.4.4 Transparent applications

IR (infrared) dyes opens the potential for use in applications where transparency is desirable, such as windows, where they could provide a cooling effect by utilizing the captured heat for water heating. Transparent applications may be the most promising area of LSCs because their low performance limits their competitiveness against existing technologies. The temperature for most hot water tanks is 48 °C and at this temperature, a 1$m^2$ single NIR panel could provide 14.34 $W/m^2$ of useful heat output.

It is estimated that 51.624 $kJ/m^2$ can be captured each hour under full sunlight, enough to heat 0.26 kg of water to 48 °C (the temperature of most hot water tanks). According to Energy Star [73] window area is ~15% of the floor area for a house. For an average house of 2600 square

feet, (242 $m^2$) this equates to 36.15 $m^2$ of window area. A 36.15 $m^2$ LSC solar heater window could then produce 9.4 kg of hot water per hour and up to 56.6 kg over 6 hours of full sunlight. The average family of 4 uses 125-250 L of hot water a day, thus the window could provide 22.6%-45.3% of the heating requirements. In addition to water heating, the heat captured by the windows may reduce the cooling costs for air conditioning. Improvements in the optical efficiency of IR dyes or the absorption range would further increase the ability of these windows to provide hot water capacity. The expected performance of a single NIR panel is shown below in **Figure 5.24**.

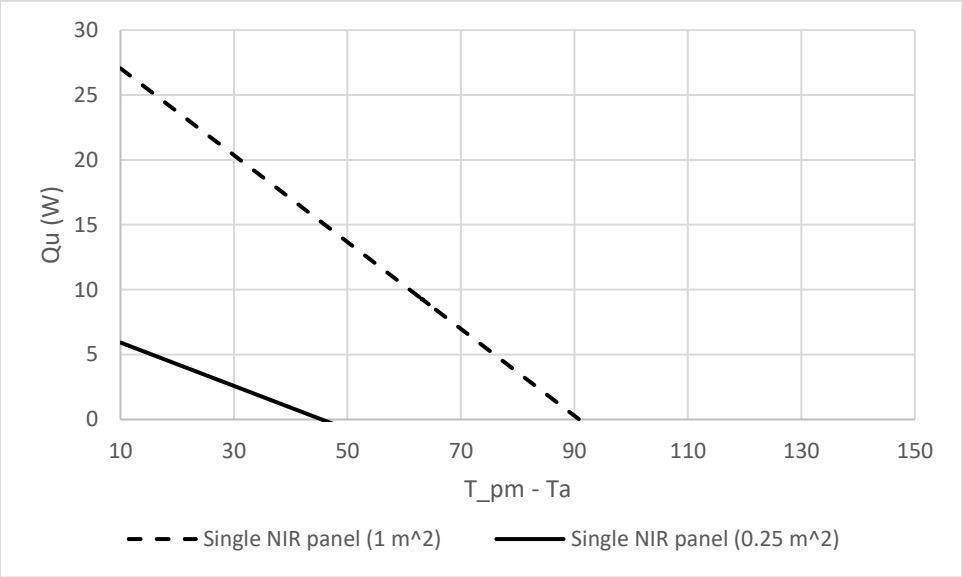


**Figure 5.24.** Performance of a single panel LSC thermal collector using NIR dyes.

It has been suggested that red LSCs may find use in greenhouses, due to their ability to utilize green light (Stokes shift causes it to appear red) with minor impacts on the growth of the crops. For use in greenhouses, a red LSC panel would be able to remove 41.313 W/$m^2$ of heat that could be pumped out of the greenhouse during hot seasons and represents a 5% reduction in cooling requirements. At 48 °C, 25.25 W of useful heat out could be utilized for hot water. This energy could be used to produce 0.46 kg/$m^2$ of hot water (@48 °C) per hour of full sunlight which could be utilized by surrounding residential units. A greenhouse with a 100 $m^2$ roof could thus provide 46 kg of hot water per hour, filling a 180-liter residential hot water tank in just 4 hours of full sunlight. Additionally, NIR panels could be added to further increase the captured heat, leading to a combined 43.05 W/$m^2$ of useful heat output at 48°C, (0.78 kg/$m^2$ of 48°C water

per hour of full irradiance). The performance of a NIR + Red LSC thermal collector is shown in **Figure 5.25**.

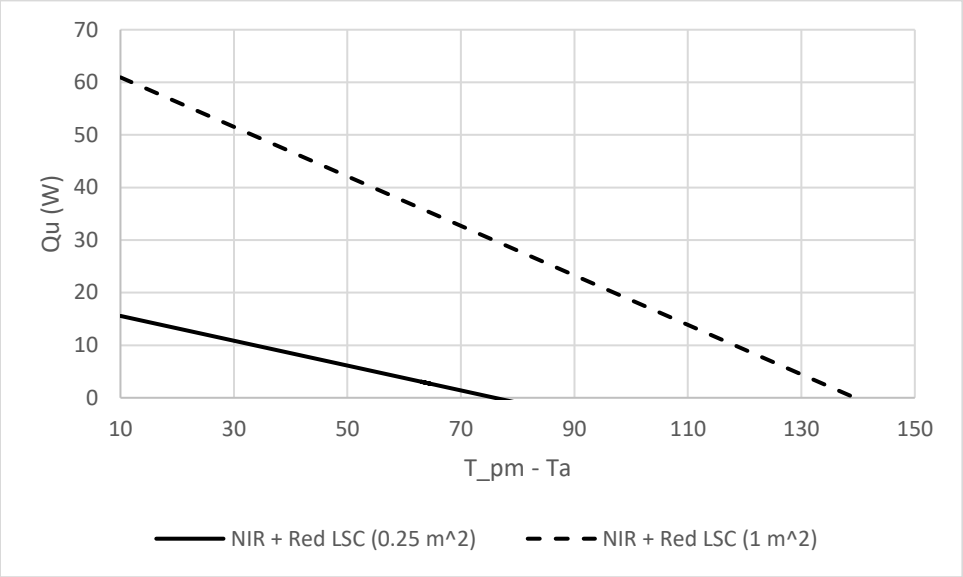


**Figure 5.25**. NIR + Red LSC thermal collector performance

Note that the useful heat output can be utilized by enabling a flowrate within the ducting to remove the excess heat. The flow rate can be calculated based on the collection efficiency of the fluid and the amount of heat to be removed to maintain the desired temperature. Removed heat can be used for countless thermal applications, such as thermal energy storage, water heating, and industrial processes.

### 5.4.5 Hybrid LSC heaters

The resulting performance curves of various hybrid LSC heaters are plotted in **Figure 5.26**.

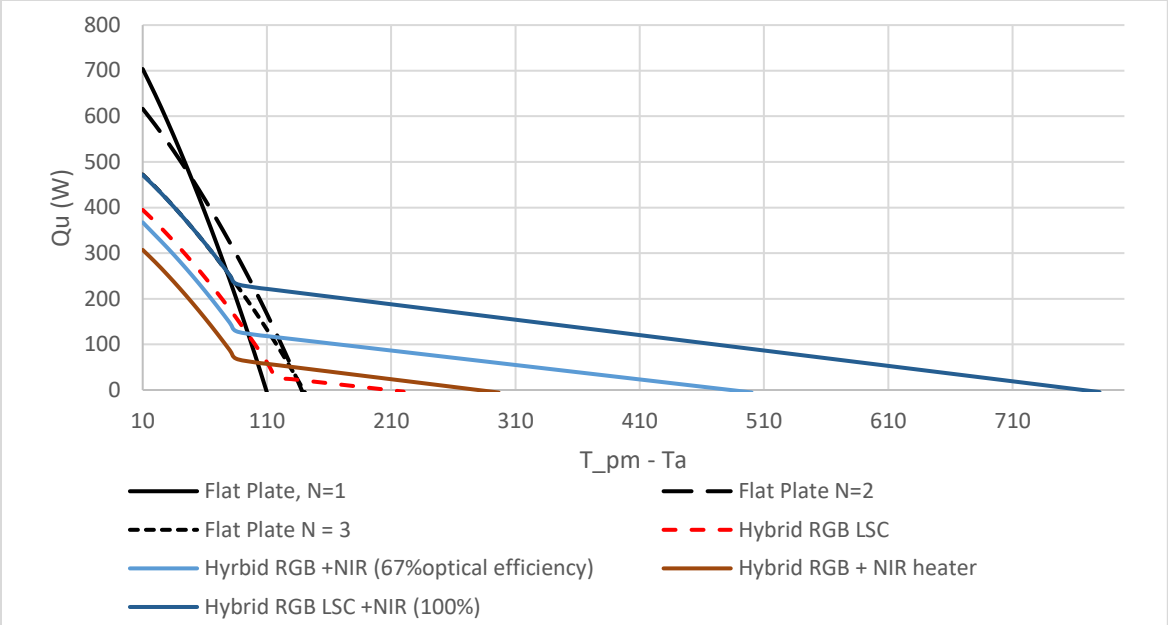


**Figure 5.26**. Performance of hybrid LSC heaters (1 $m^2$ with 100 mm thick insulation).

The results show that the hybrid collectors have much better useful heat output in the low-temperature range due to the increase in collected energy from the flat black plate. Once the flat plate has reached is max temperature, its only contribution is to minimize the fin losses through the LSC thus, the performance curve is dictated solely by the LSC collector equations. Using SOLIDWORKS Flow Simulations, the maximum temperature of the Hybrid RGB + NIR heater was predicted to be 256.45°C whereas the mathematic model predicts the max temperature to be 279.5°C. It should be noted that for a simulation that included LSC absorption heating (caused by the energy that is absorbed by the host material through Stokes shift, host absorption, non-unity quantum yield, etc.), the max achievable temperature predicted increases to 356 °C, indicating that the actual performance of a hybrid LSC heater may be better than that predicted by the mathematical model due to the additional heating in the LSC panels. This effect should be explored further in future works and refinement of the mathematical model.

## 5.5 Conclusion

LSC thermal solar collectors are shown to have reduced heat transfer losses compared with traditional flat plate collectors, thus showing potential for high-temperature applications. When the incoming light spectrum is limited to match the absorption of the dye, the LSC collector can reach more than double the temperature of a flat plate collector, demonstrating the potential for

LSCs to outperform flat plate collectors if the dye absorbance range can be expanded to match that of the flat black plate. Under the full spectrum, a 0.25 $m^2$ multi-panel LSC collector utilizing 3 differently coloured LSC collectors is unable to be competitive with flat plate collectors in heat output and temperature unless improvements can be made in the dye efficiency of the LSC devices. At $1m^2$, the three colour LSC collector can produce higher temperatures than a flat black plate collector but severely underperforms in the amount of useful heat output when the difference between the mean plate temperature and the ambient temperature are low. Future work to verify the edge power output from 1 $m^2$ LSCs should be completed to verify the estimated dye efficiency. Additionally, it was shown that double-sided LSC collectors can further increase the maximum temperature to close to 230 °C, which is higher than can be achieved using a flat plate collector. Like the single-sided LSC collector, this too suffers from low useful heat output at low and moderate temperatures. The addition of a fourth panel using NIR dyes is shown to further increase both the amount of useful heat output and the maximum temperature, although testing of large NIR panels should be completed to confirm power output.

Hybrid LSC collectors are shown to have improved low-temperature (the difference between the mean plate temperature and ambient temperature is low) performance over LSC collectors and improved high-temperature (large difference between the mean plate temperature and ambient) performance compared with both flat plate collectors and LSC collectors. This indicated that hybrid LSC collectors may provide a benefit for applications in high-temperature applications, and in applications where both high and low temperatures may be required.

For transparent applications such as windows, NIR LSC heaters are shown to have the potential to supply between 22.3-45.5% of the average household hot water requirements

# 6. Integration of LSCs Into a Traditional Flat Plate Thermal Collector

Chapter 5 has shown that LSCs can offer advantages for solar thermal collectors, such as high temperatures and low heat losses. Herein, this chapter investigates taking a slightly different approach by investigating the effect on the performance of integrating LSC covers and ducting with existing flat plate thermal collector designs and examines the case for co-generation LSC electric/thermal collectors.

## 6.1 LSC Integration into Flat Plate Solar Heaters

The dominant heat losses from a flat plate absorber occur through the covers to the surroundings due to the high temperature and large exposed surface area of the absorber (black plate) [70]. By replacing the covers of the solar heater with LSCs, some of the heat can be concentrated and directed to an absorber along the edges of the collector where it can be collected by the heat transfer fluid. The LSC absorber can be fully insulated resulting in low heat losses to the surroundings. The photoluminescent heat transfer to the collector at the LSC sidewalls also reduces the flat plate temperature and thus reduces heat losses to the surroundings.

### 6.1.1 Solar air heater

Solar Air Heaters (SAHs) are designed for low-grade heating with temperatures under 60 °C [74]. SAHs are typically used in applications such as space heating or drying. SAHs are similar to the flat-plate tube collectors described in Chapter 5 but use air as the working fluid and generally allow for the fluid to travel over the entire surface of the absorber plate rather than through collector tubes. **Figure 6.1** shows an example of a typical solar air heater. Herein, LSCs are integrated into solar heaters to determine their suitability in this application.

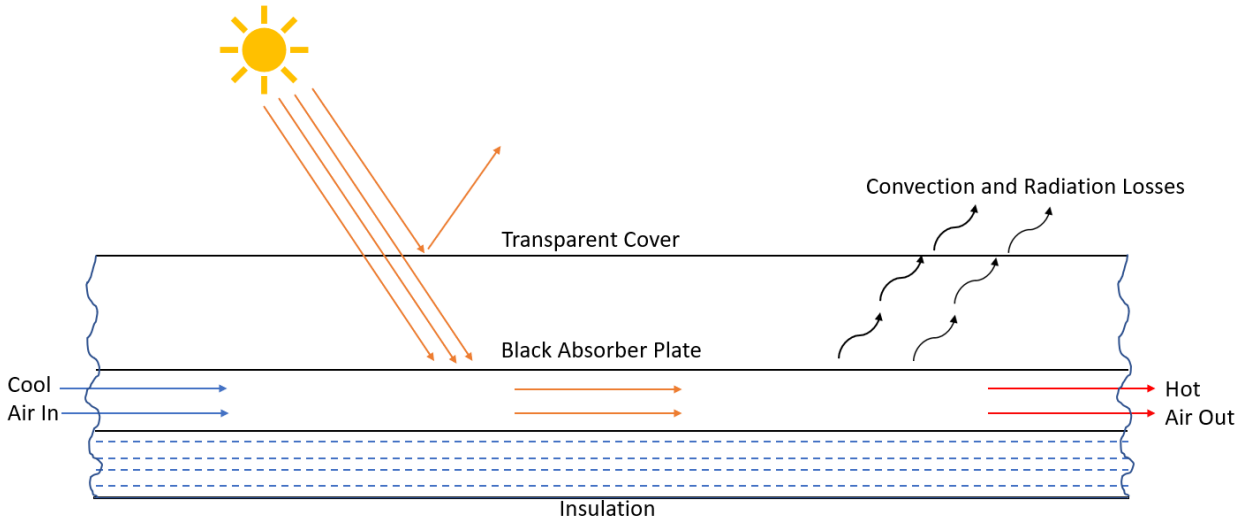


**Figure 6.1** Typical solar air heater

### 6.1.2 Hybrid LSC/flat plate heater

A hybrid LSC/flat plate heater was designed and simulated using Solid Works Flow Simulation modeling, which includes radiative heat transfer in addition to conductive and convective heat transfer between fluids and solids. Three designs were created and numerically analyzed for comparison. The first design incorporates a cover comprised of 3 LSC panels (LSC SAH), the second design (clear SAH) uses the same set-up but replaces the LSCs with clear acrylic panels, and the third design uses a more traditional SAH configuration (reference SAH). All designs were simulated using the same parameters (area, convection, mass flow, irradiance). The area for all designs used in the simulation are 0.25 $m^2$ to correlate with the data from Chapter 4. The irradiance is modeled after the AM 1.5 Solar spectrum, which is used to replace the lamp spectrum from Chapter 4 to estimate LSC performance. The mass flow rate and external convection coefficient are varied between 0.001 Kg/s to 0.0025 kg/s and from 10 $W/m^2 \cdot K$ to 20 $W/m^2 \cdot K$ for each design to build performance curves.

## 6.2 Materials and Methods

All designs use a low emissivity paint on the flat plate absorber, with an emissivity coefficient of 0.1. The insulation used is 2-inch thick UF Foam 2, with a conduction coefficient of 0.0299 $W/m^2 \cdot K$. The absorber plate is 2 mm thick and made from aluminum, and the covers are made from 3 mm thick acrylic panels. Heating parameters were added according to the performance

results predicted by the LSC modeling. Heating power from the edge of the panels was applied to the contact points between the absorbing framework and the LSC panels. The heat generated in the LSC panels, due to both host absorption and dye absorption losses (e.g. due to Stokes shift) was modelled as a volumetric heat source within the LSC panels. The heat generated in the aluminum black plate at the underside of the SAH was determined by assuming all light incident onto its surface is absorbed and converted to heat. The light incident onto the aluminum black plate includes the solar radiation transmitted through all panels within the LSC SAH and a fraction of the light emitted from the dye within the LSC panels. For all simulations, it is assumed that the LSC SAHs are at a 45-degree incline with respect to the ground. The angle of incidence is assumed to be perpendicular to the surface of the collector. Turbulent flow is modeled using a modified K-epsilon flow. The K-Epsilon model is commonly used in CFD simulations.

### 6.2.1 Multi-panel LSC solar air heater design

This design uses 3 LSC panels over a flat black plate absorber to maximize heat collected. In order to make use of the energy captured by the LSC panels, absorbers must be located at the edges of the LSC panels. This results in the requirement for additional ducting and fluid flow around the outside edges of the collector. The ducting around the collector will benefit from reduced losses compared to the flat plate due to the reduction of radiation losses and the ability to insulate nearly all the exposed surface area. To maximize the efficiency of this design, the plate should be kept as cool as possible (to reduce heat losses) with higher temperatures being reached in the edge ducting. Thus, cool ambient air is first drawn across the flat plate before being drawn into the edge ducting for additional heating. Due to the limitations of having ducting surrounding the panels, the air cannot be drawn through the side edges as is typical for a SAH. Instead, the inlet is located as a 3mm slot in the back insulation, which is located 35 mm away from the side edge.

The ducting around the edges of the collector draws in air from the middle of the collector edge and then is split into two ducts which wrap around the collector before merging and exiting on the opposite side of the collector. The ducts are made from round piping that has been cut to attach to the absorber plate. The LSC covers are separated by 15 mm to minimize convection

losses from the black plate, as is suggested for minimizing black plate heat losses. The unfortunate side effect of this is the increase in the required size of edge ducting, boosting the heat losses in this area and minimizing the advantages of the LSCs. **Figure 6.2** shows a top view of the collector with the simulated flow to demonstrate its operation, **Figure 6.3** and **Figure 6.4** show a cross-section view.

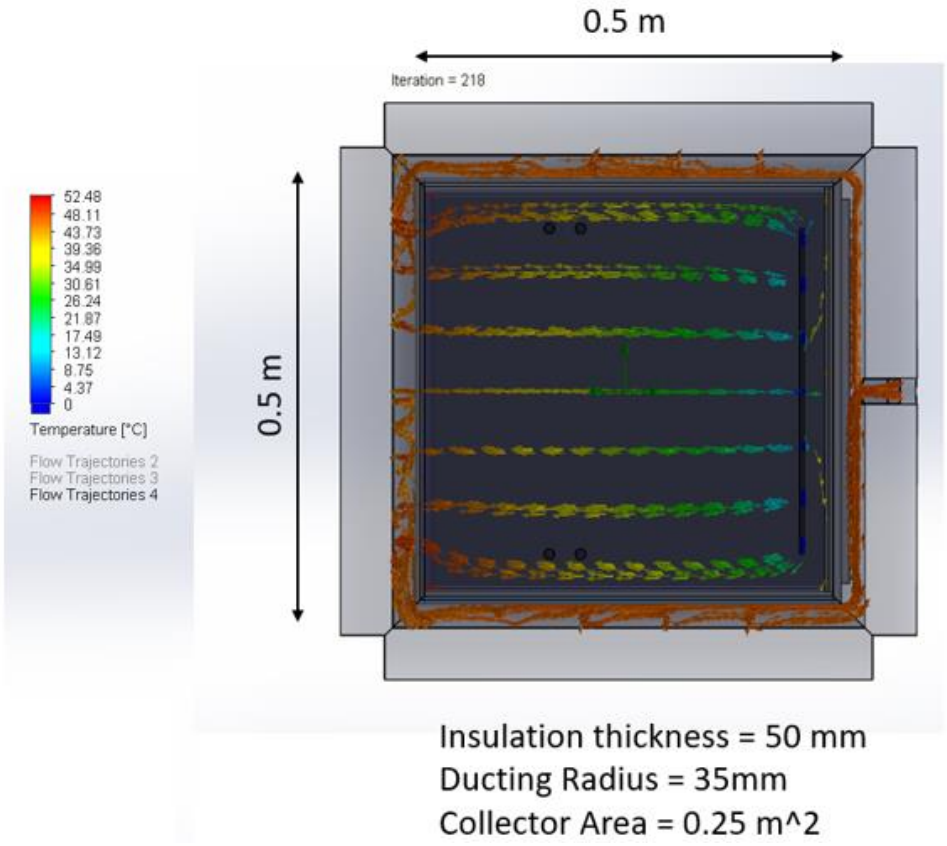


**Figure 6.2**. Top view of LSC solar air heater with simulated airflow.

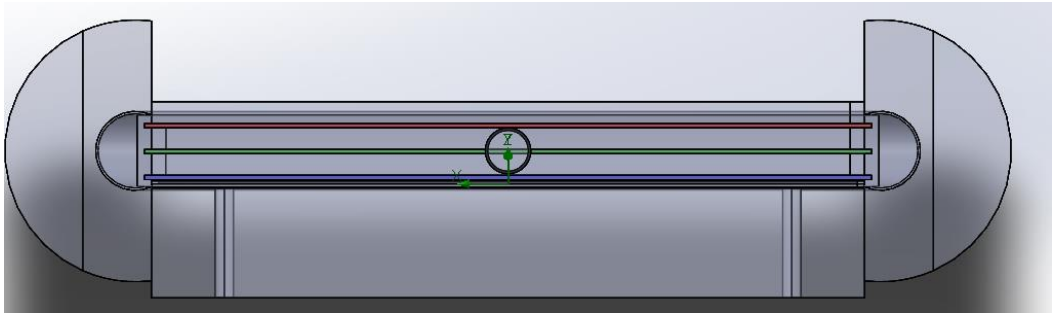

**Figure 6.3**. Cross-section of the LSC SAH design, with insulation. The gap between the top sheets is 15 mm with a 2 mm gap between the bottom (blue) LSC and the black absorber plate. Fluid flow is allowed on both the top and bottom sides of the black absorber plate.

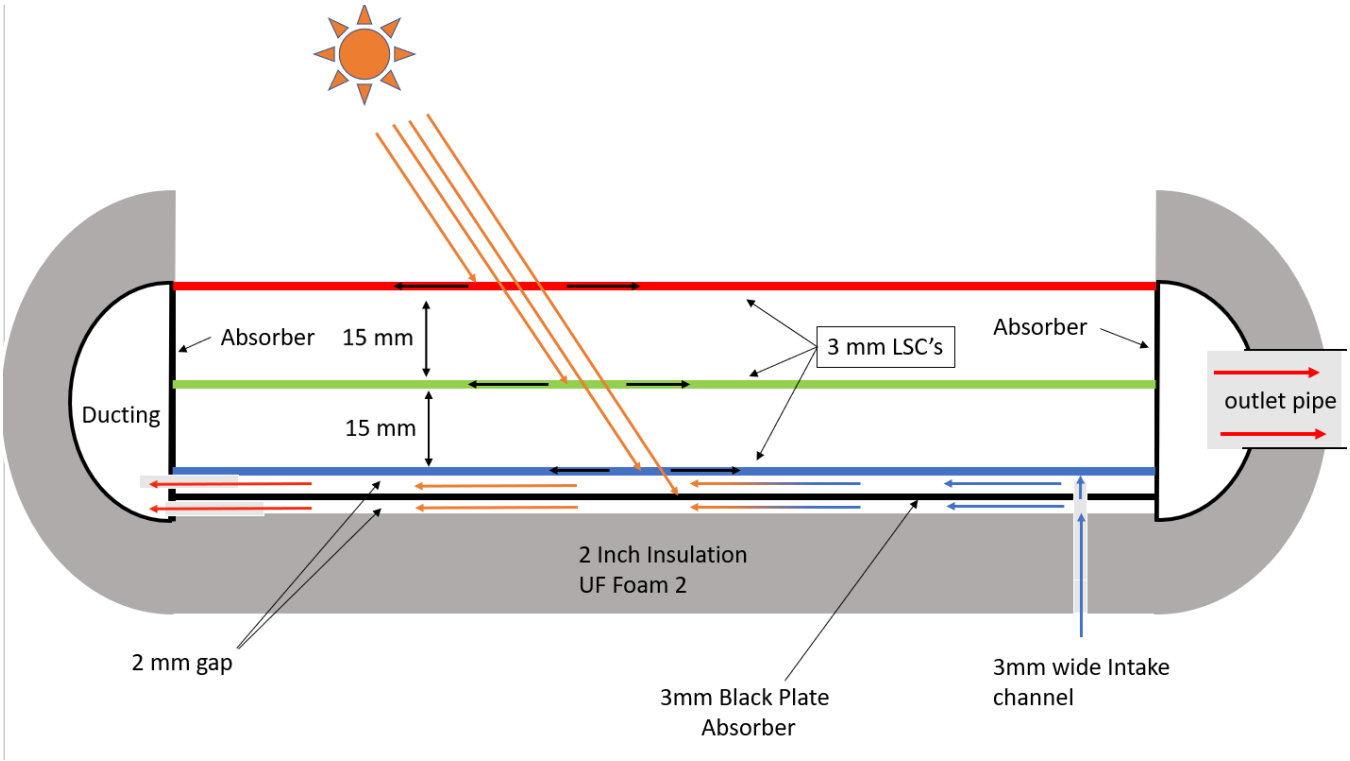


**Figure 6.4.** Cross-section view of LSC SAH with Dimensions. Not to scale.

Due to the ducting around the edges of the collector, air must be drawn in through the surface of the collector. This was done by drawing air through the back of the collector through a 3 mm wide and 400 mm long air channel and disbursed over the absorber sheet. The inlet channel runs parallel to the absorber and is located 35 mm away from the edge of the black plate. It is located on the side of the outlet. The mass flow rate at the exit is set as a constant (0.0025,0.002 or 0.001 kg/s) for all simulations. It is assumed a fan is used to pull air through the collector. **Figure 6.5**, **Figure 6.6** and **Figure 6.7** show an example of simulation results and general layout. **Figure 6.5** shows the fluid temperature gradient as is travels through the collector, where as **Figure 6.6** shows the heat gradient through the insulation. **Figure 6.7** shows a view looking directly at the surface of the collector to demonstrate the temperature gradient across the collector surface.

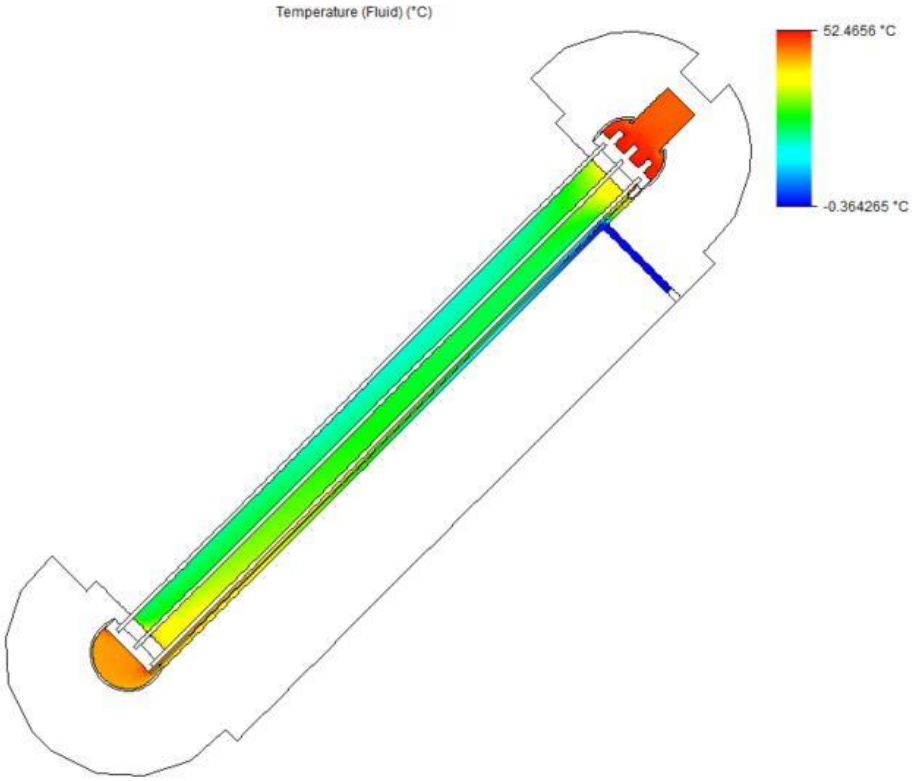


**Figure 6.5.** Cross-section of RGB LSC SAH, showing the fluid temperature and general layout

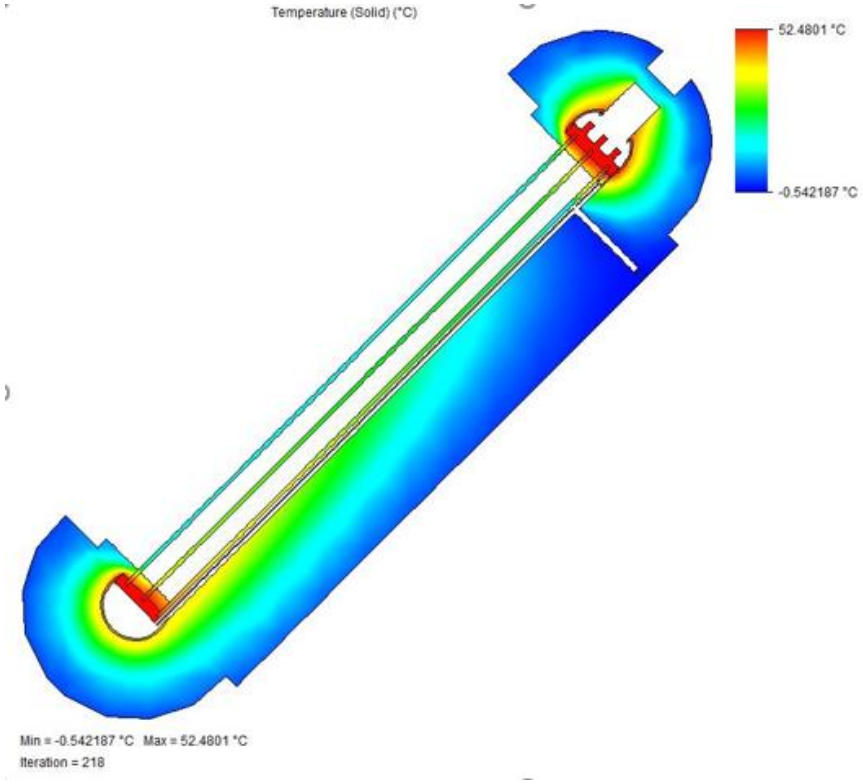


**Figure 6.6**. Cross-section of RGB SAH, showing the temperature of the solid components.

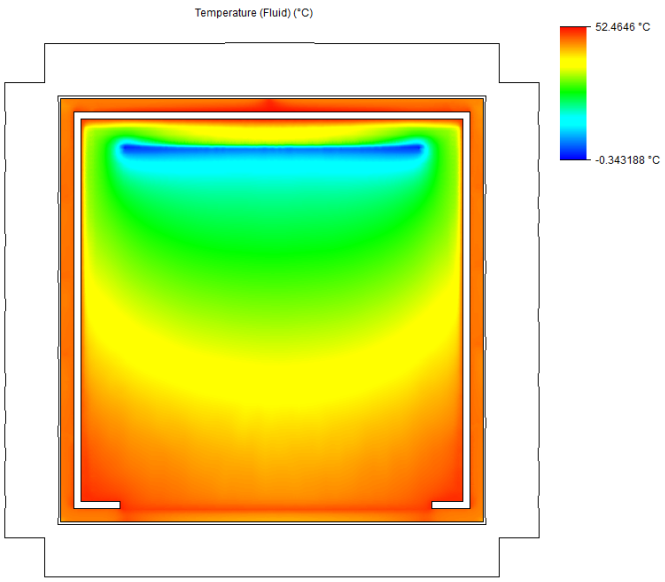


**Figure 6.7.** Top view of the fluid temperature as it travels over the black absorber and around the edge ducting.

### 6.2.2 Clear SAHs design

For comparison purposes, a second model was designed for use as a traditional black plate absorber (sometimes called a Clear SAH in this document to describe the use of clear covers rather than dyed LSC panels). In this model, the cover spacing, and insulation thickness and area is kept the same as the LSC SAH, but the edge ducting is removed. Air enters through a header tube along the bottom edge and is disbursed over the black plate. It is then collected in a header tube along the opposite (top) edge, where it then exits in the collection tube.

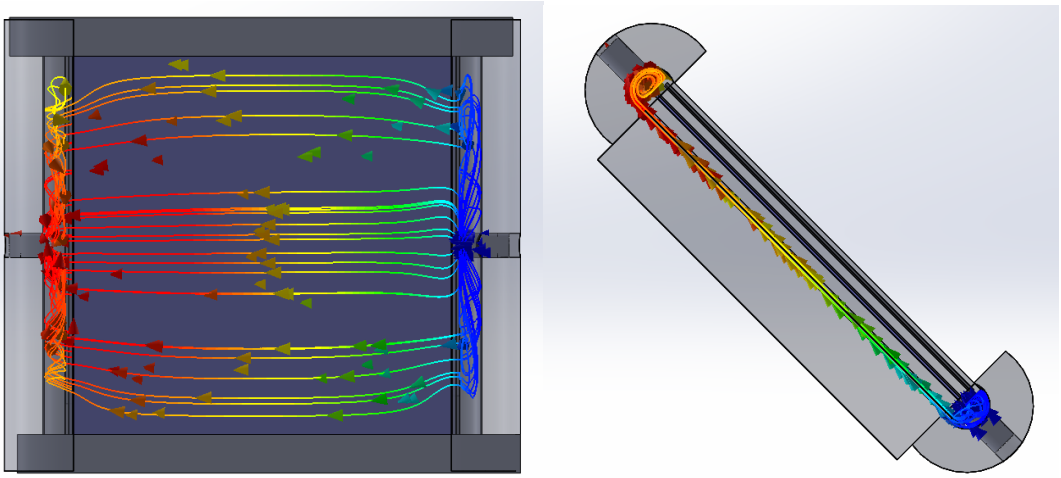

**Figure 6.8.** Top-view and cross-section view of reference SAH with illustrated fluid flow.

In addition to the clear collector described above, a clear collector was designed with two covers rather than 3 to represent the most common case for solar heaters. For this version, fluid flow is limited to the bottom side of the black plate.  A cross-section view with the insulation hidden is shown in **Figure 6.9**.

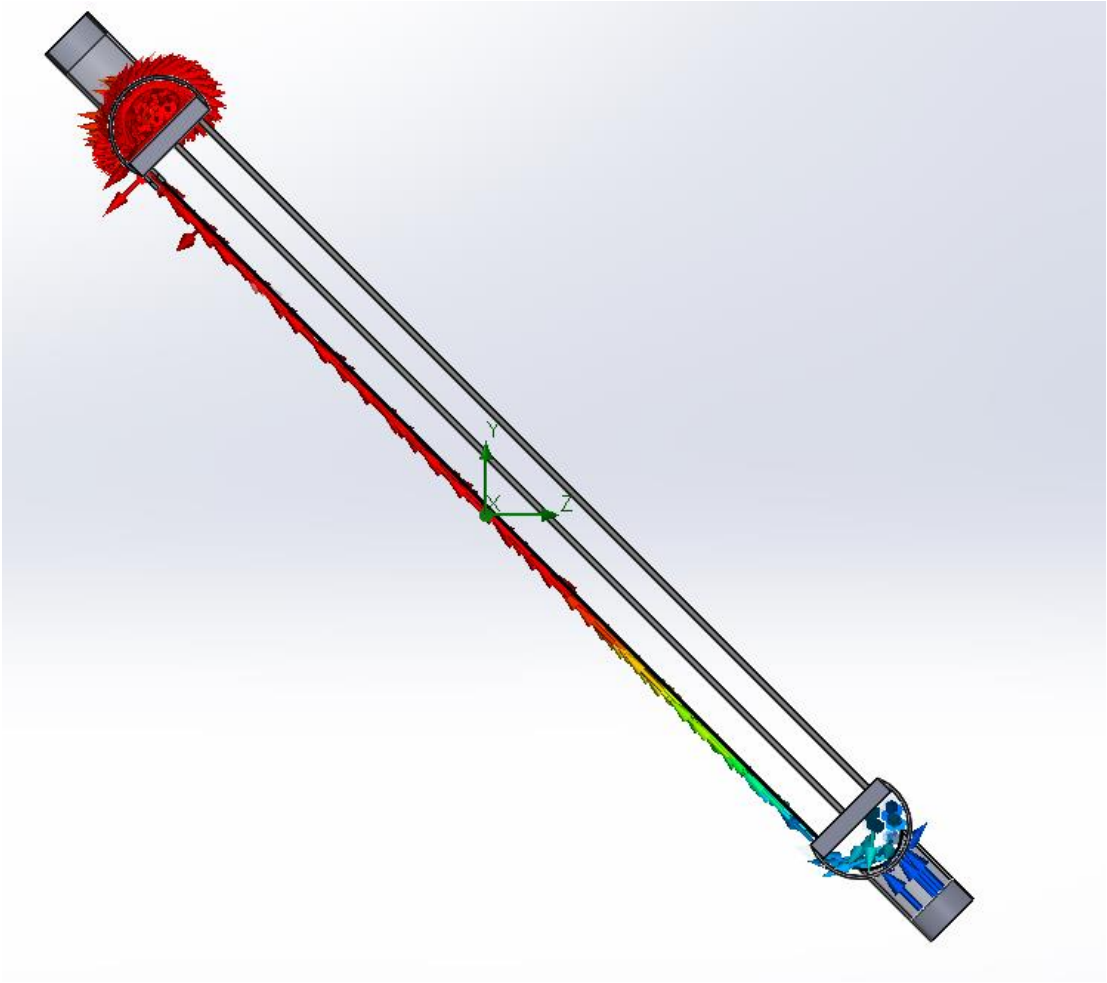


**Figure 6.9.** Cross-section fluid flow through a multi-panel LSC hybrid thermal collector

## 6.3 Results

Modeling results show that the combinations of 3 LSC panels which transmits the most light to the sidewalls is RGB and BGR. Results from the RGB model under solar irradiance is shown in **Table 6.1**, with results from the transmission of 3 clear panels is shown in **Table 6.2** and BGR results are shown in **Table 6.3**.

**Table 6.1.** RGB transmission.

| All units in $W/m^2$ | Total Light blocked by panel | Reflection | Transmission | Dye Absorb | Edge | Dye absorption loss | host absorption | Dye Escape |
|---|---|---|---|---|---|---|---|---|
| Red | 176.61 | 56.23 | 624.36 | 141.00 | 44.69 | 79.00 | 48.22 | 17.31 |
| Green | 70.52 | 40.47 | 513.37 | 53.38 | 15.61 | 32.20 | 25.55 | 5.57 |
| Blue | 35.68 | 34.00 | 443.68 | 20.81 | 10.50 | 7.84 | 17.62 | 2.47 |
| sum | 282.81 | 130.71 | 443.68 | 215.19 | 70.81 | 119.04 | 91.39 | 25.35 |

**Table 6.2** Clear panel transmission.

| All units in $W/m^2$ | Total blocked | Reflection | Transmission | Absorption |
|---|---|---|---|---|
| Clear | 105.74 | 57.53 | 751.58 | 48.22 |
| Clear | 70.40 | 51.80 | 681.05 | 18.60 |
| Clear | 60.83 | 47.36 | 620.18 | 13.48 |
| sum | 236.98 | 156.68 | 620.18 | 80.30 |

**Table 6.3.** BGR transmission.

| All units in $W/m^2$ | Total Light Blocked by panel | Reflection | Transmission | Dye absorption | Edge | Dye absorption loss | host absorption | Dye Escape |
|---|---|---|---|---|---|---|---|---|
| Blue | 87.10 | 57.27 | 712.83 | 43.36 | 21.88 | 16.33 | 48.22 | 5.15 |
| Green | 83.08 | 47.33 | 582.42 | 68.83 | 20.13 | 41.53 | 17.83 | 7.18 |
| Red | 100.08 | 38.65 | 443.68 | 90.13 | 28.57 | 50.50 | 12.91 | 11.07 |
| sum | 270.27 | 143.25 | 443.68 | 202.32 | 70.58 | 108.35 | 78.96 | 23.39 |

The net thermal efficiencies from each simulation are shown in **Table 6.4** for a convection coefficient of 10 W/m$^2$·K and **Table 6.5** for a convection coefficient of 20 W/m$^2$·K.

**Table 6.4** Thermal efficiencies of SAH @ h=10 W/m$^2$·K

| Flow Rate (kg/s) | 0.0025 | | | | 0.002 | | | | 0.001 | | |
|---|---|---|---|---|---|---|---|---|---|---|---|
| $T_{in}$-$T_a$ °C | RGB | BGR | Clear X3 | Clear X2 | RGB | Clear X3 | Clear X2 | RGB | BGR | Clear X3 | Clear X2 |
| 0°C | 55.62 | 56.73 | 58.33 | 59.66 | 52.12 | 54.70 | 56.06 | 37.27 | 38.07 | 39.01 | 40.81 |
| 10°C | 51.58 | 52.80 | 53.80 | 55.41 | 48.78 | 50.59 | 52.16 | 34.23 | 35.06 | 35.82 | 37.70 |
| 20°C | 47.51 | 48.69 | 49.39 | 51.24 | 44.28 | 46.19 | 48.18 | 31.18 | 32.01 | 32.53 | 34.69 |
| 30° C | 43.39 | 44.56 | 44.81 | 46.86 | 40.29 | 41.87 | 44.17 | 28.10 | 28.92 | 29.34 | 31.54 |

**Table 6.5.** Thermal efficiencies of SAH @ h=20 W/m$^2$·K

| Flow Rate | 0.0025 kg/s | | | | 0.002 kg/s | | | | 0.001kg/s | | |
|---|---|---|---|---|---|---|---|---|---|---|---|
| $T_{in}$-$T_a$ | RGB | BGR | Clear X3 | Clear X2 | RGB | Clear X3 | Clear X2 | RGB | BGR | Clear X3 | Clear X2 |
| 0°C | 53.96 | 55.61 | 56.09 | 56.92 | 50.26 | 52.60 | 53.09 | 35.83 | 36.71 | 36.22 | 37.28 |
| 10°C | 49.79 | 51.35 | 51.27 | 52.10 | 46.31 | 48.18 | 48.86 | 32.76 | 33.55 | 32.86 | 33.70 |
| 20°C | 45.58 | 47.07 | 46.51 | 47.52 | 42.30 | 43.65 | 44.55 | 29.65 | 30.42 | 29.47 | 30.48 |
| 30°C | 41.28 | 42.73 | 41.63 | 42.81 | 38.22 | 39.05 | 40.21 | 26.49 | 27.33 | 26.08 | 27.17 |

**Figure 6.10** shows the thermal performance of the RGB SAHs at various flow rates as the difference between intake temperature and ambient temperature increases.

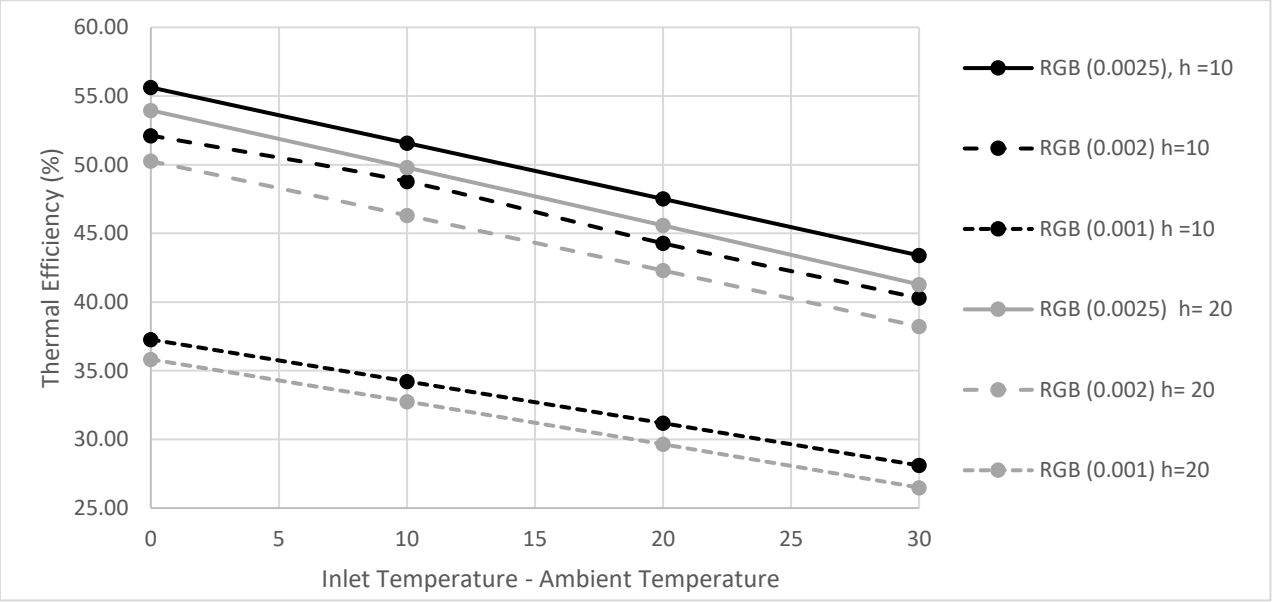


**Figure 6.10.** RGB thermal collector at flow rates of 0.0025 kg/s, 0.002 kg/s and 0.001 kg/s. Convection co-efficient = 10 W/m$^2$ K (black) and 20 W/m$^2$ K (gray).

From **Figure 6.10**, the thermal efficiency of the RGB SAH is 55.62% , 52.12 % and 37.27 % at 0.0025, 0.002 and 0.001 kg/s mass flow rates, respectively at $T_{in}$-$T_a$ = 0 and h=10 W/m$^2$ K. As expected, the heater performs better at h=10 W/m$^2$ K than at h =20 W/m$^2$ K .

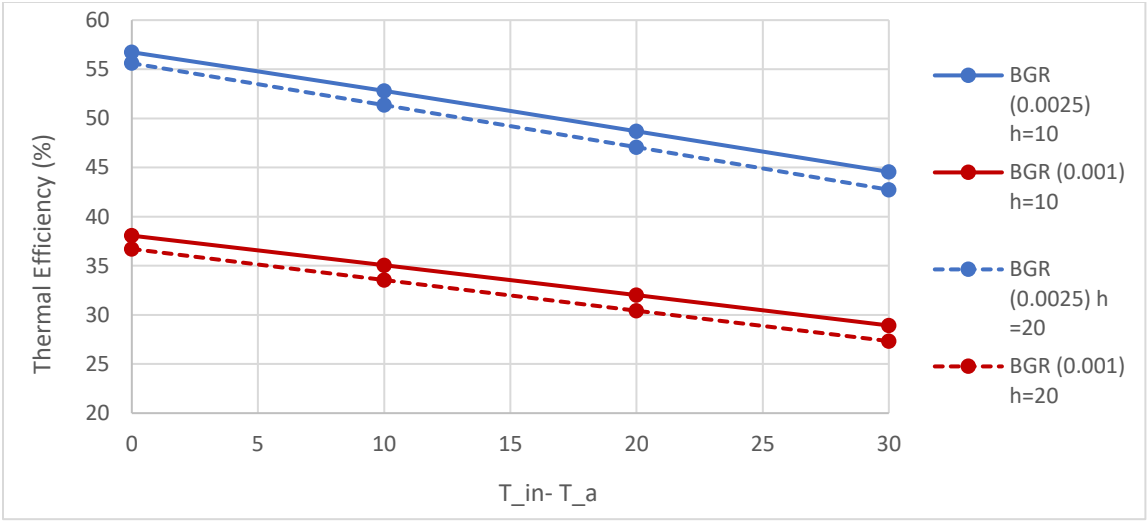


**Figure 6.11.** BGR performance curves at various mass flow rates. Mass flow rate varied between 0.0025 kg/s and 0.001 kg/s. Convection co-efficient = 10 W/m$^2$ K (solid line) and 20 W/m$^2$ K (dashed line).

The maximum and minimum performance of the BGR at 0.0025 and h=10 W/m$^2$ K was 56.73% and 44.56%. Additionally, the thermal efficiency from the clear reference cases with the clear 3-cover and clear 2-cover SAH, are plotted on the same graph as the RGB and BGR curves at the various mass flow rates and k values and shown in **Figure 6.12** and **Figure 6.13**. The clear 2-cover SAH heater outperforms all others at high flow rates and low thermal conduction coefficient; however, as the thermal coefficient (h) increases and the flow rate decreases, the performance becomes much closer to the performance of the 3-panel modules. This is because the addition of the 3$^{rd}$ cover panel increases the amount of light lost through reflection and absorption, with only minor decreases of thermal heat transfer. Under all conditions, the thermal efficiency slope of the LSC SAH is less steep than the slope of the clear panels, indicating that the ability for the LSC to transfer heat directly into the ducting while maintaining a cooler plate temperature provides beneficial effects reducing heat transfer losses.

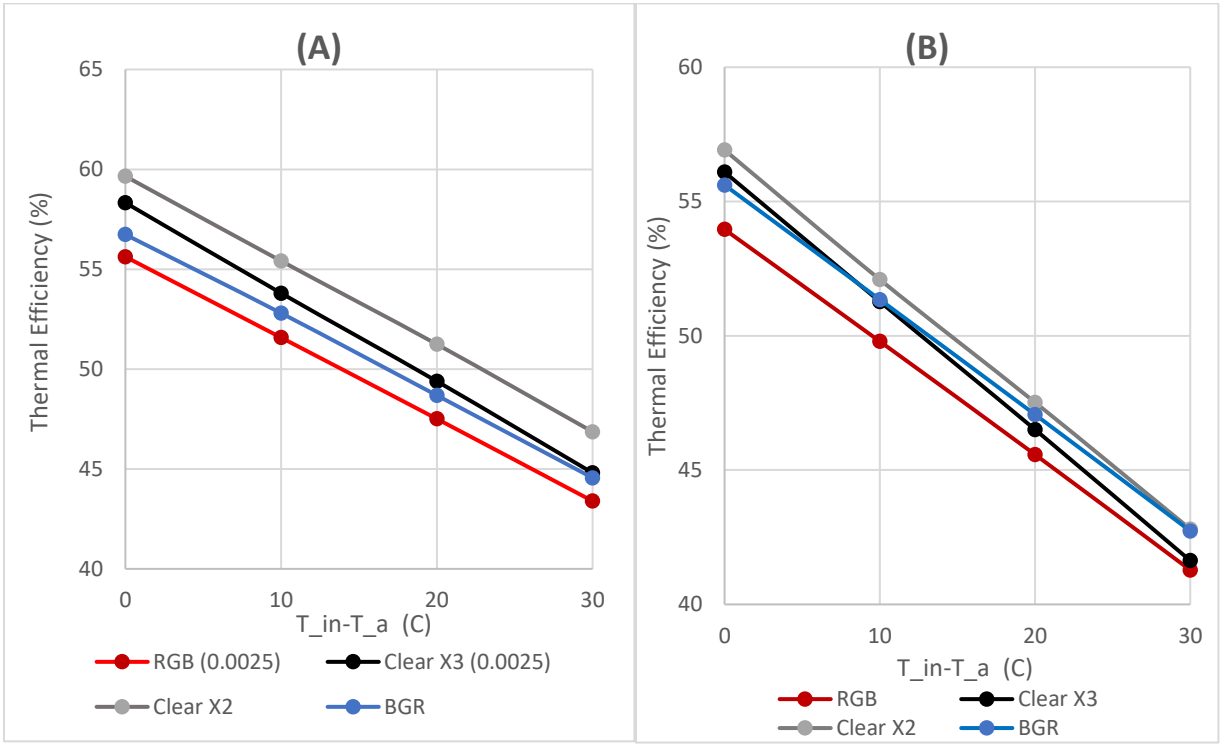


**Figure 6.12** Efficiency of thermal collectors at 0.0025 kg/s. (A) h = 10 W/m$^2$. (B) h = 20 W/m$^2$

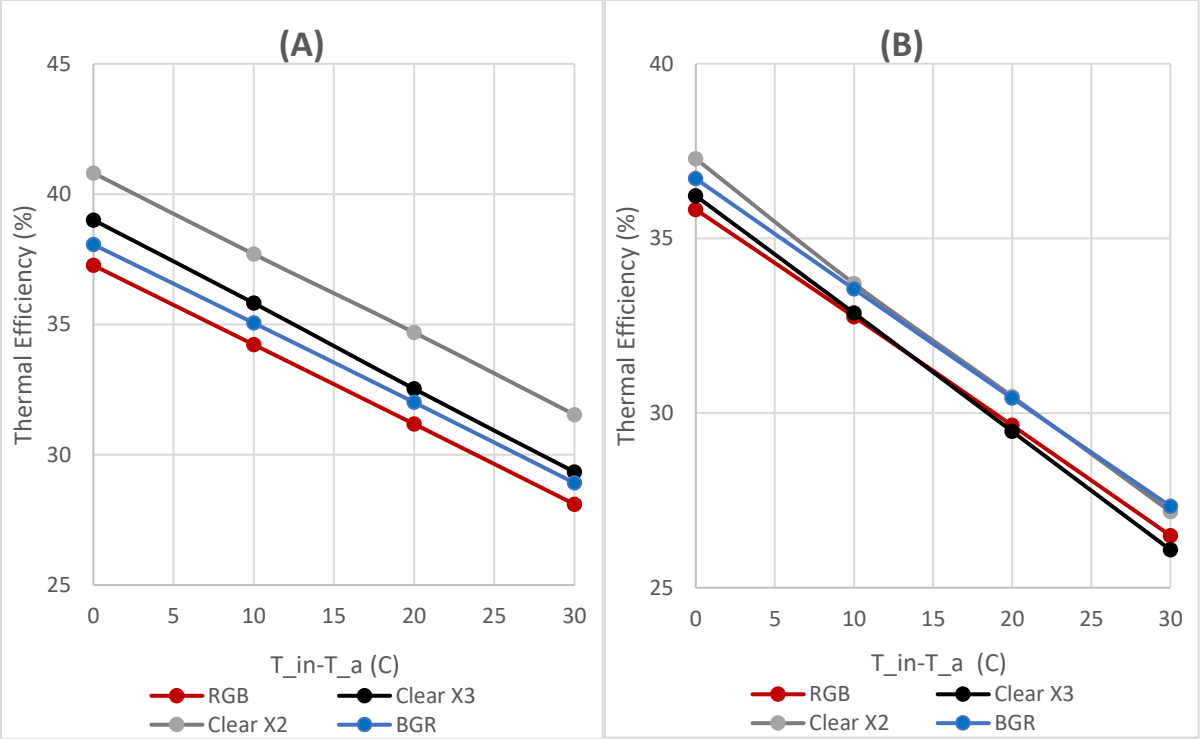


**Figure 6.13.** Efficiency of thermal collectors at 0.001 kg/s. (A) h = 10 W/m$^2$. (B) h = 20 W/m$^2$

**Table 6.6.** Outlet temperature (°C) of SAH with h = 10 W/m$^2$ K

| Flow Rate | 0.0025 kg/s | | | | 0.001 kg/s | | | |
|---|---|---|---|---|---|---|---|---|
| $T_{in}$-$T_a$ °C | RGB | BGR | Clear X3 | Clear X2 | RGB | BGR | Clear X3 | Clear X2 |
| 0 | 47.3 | 47.3 | 49.6 | 50.7 | 79.2 | 80.9 | 82.9 | 86.8 |
| 10 | 53.9 | 53.7 | 55.8 | 57.1 | 82.8 | 84.5 | 86.1 | 90.1 |
| 20 | 60.4 | 60.0 | 62.0 | 63.6 | 86.3 | 88.1 | 89.2 | 93.8 |
| 30 | 66.9 | 66.3 | 68.1 | 69.9 | 89.7 | 91.5 | 92.4 | 97.1 |

**Table 6.7.** Outlet temperature (° C) of SAH with h = 20 W/m$^2$ K

| Flow Rate | 0.0025 kg/s | | | | 0.001 kg/s | | | |
|---|---|---|---|---|---|---|---|---|
| $T_{in}$-$T_a$ °C | RGB | BGR | Clear X3 | Clear X2 | RGB | BGR | Clear X3 | Clear X2 |
| 0 | 45.9 | 47.3 | 47.7 | 48.4 | 76.16 | 78.04 | 76.99 | 79.25 |
| 10 | 52.3 | 53.7 | 53.6 | 54.3 | 79.64 | 81.32 | 79.86 | 81.65 |
| 20 | 58.8 | 60.0 | 59.6 | 60.4 | 83.02 | 84.68 | 82.66 | 84.79 |
| 30 | 65.1 | 66.3 | 65.4 | 66.4 | 86.32 | 88.10 | 85.45 | 87.77 |

## 6.4 Discussion

The results indicate that the LSC modules are more resilient to high thermal k coefficients and $T_{in}$-$T_a$ differences. With h=10 W/m$^2$ K, both clear modules outperformed both the LSC SAHs, but at h = 20 W/m$^2$ K and a mass flow rate of 0.0025 kg/s, the BGR panel outperforms the clear 3 cover module after a $T_{in}$-$T_{out}$ difference greater than ~10 °C. At a flow rate of 0.001 kg/s, the BRG panel outperforms the clear 3 cover panel over all temperature ranges, and the RGB panel overtakes it after a $T_{in}$-$T_{out}$ difference greater than ~15 °C. This indicated that LSC SAH could be utilized in cold/windy climates.

As mentioned earlier, the clear double cover module outperformed all others in low heat transfer conditions. This result would also be expected of a single cover clear SAH, due to reduced incident light losses and low thermal losses. A double or single cover LSC SAH is expected to perform with similar aspects as the triple LSC and triple clear SAH, wherein the LSC modules may start to outperform the clear modules at higher h values and temperatures. The BGR module performs better than the RGB module. This is likely due to a more even distribution of light captured by each LSC pane in the BRG configuration. In comparison with the RGB modules, most of the light is captured by the red panel (~64%), with only 15% being captured by the blue panel.

Improvements in LSC performance would further amplify the ability for LSC to be integrated into solar heaters. In these models, only ~ 70 W/m$^2$ of the ~200 W/m$^2$ of energy absorbed by the dye makes it to the edge of the panels. Increasing the optical dye efficiency by even a few percent could significantly increase the performance of the LSC SAHs, making them competitive with the clear SAH under all conditions. In retrospect, it was noticed that by adding a 15 mm separation between LSC covers significantly increases the losses from the ducting, thus minimizing the potential benefits of using the LSCs.

### 6.4.1 Combined co-generative solar electric/ solar heater

Rather than generating extra heat through the addition of an LSC to a SAH, the LSC panels could be used to generate electricity in a co-generative solar heater. The amount of electricity generated can be estimated by using the spectral response of a solar cell at the estimated

emission peak for each panel multiplied by the light intensity at the edge of each panel, calculated using the methods described in Chapter 2 using the transmission and reflection measurements. **Table 6.8** shows the resulting estimate for electricity that could be generated by the RGB and BGR panels (0.25 $m^2$) using Si cells. The emission peak is estimated by using data for BASF Lumogen series dyes [39].

**Table 6.8**. Electricity generated by RGB and BGR panels using Si cells.

| | RGB Edge ($W/m^2$) | BGR Edge ($W/m^2$) | Emission Peak (nm) | QE | Spectral Response (Si cells) | Electricity RGB ($W/m^2$) | Electricity BGR ($W/m^2$) |
|---|---|---|---|---|---|---|---|
| Red | 44.69 | 21.88 | 600 | 0.98 | 0.474 | 21.20 | 10.38 |
| Green | 15.61 | 20.13 | 525 | 0.99 | 0.419 | 6.54 | 8.44 |
| Blue | 10.51 | 21.88 | 425 | 0.94 | 0.322 | 3.39 | 7.05 |
| Sum | | | | | | 31.13 | 25.87 |

The SAH simulation was modified to model a co-generative panel. The effects of heat on the efficiency of the solar cells were not included in the simulation and it is assumed that the solar cells will receive adequate cooling through an effective design. The results are shown in **Table 6.9** and depicted in **Figure 6.14** for an RGB co-generation SAH with a convection co-efficient of 10 $W/m^2 \cdot K$ and a mass flow rate of 0.0025 kg/s.

**Table 6.9**. Co-generation efficiency at various temperature differences for an RGB co-generation SAH with a convection co-efficient of 10 $W/m^2 \cdot K$ and a mass flow rate of 0.0025 kg/s.

| $T_{in}$-$T_a$ | Thermal Efficiency | Electrical Efficiency | Total Efficiency |
|---|---|---|---|
| 0°C | 47.15 | 3.63 | 50.78 |
| 10°C | 42.82 | 3.63 | 46.45 |
| 20°C | 38.45 | 3.63 | 42.08 |
| 30°C | 33.99 | 3.63 | 37.62 |

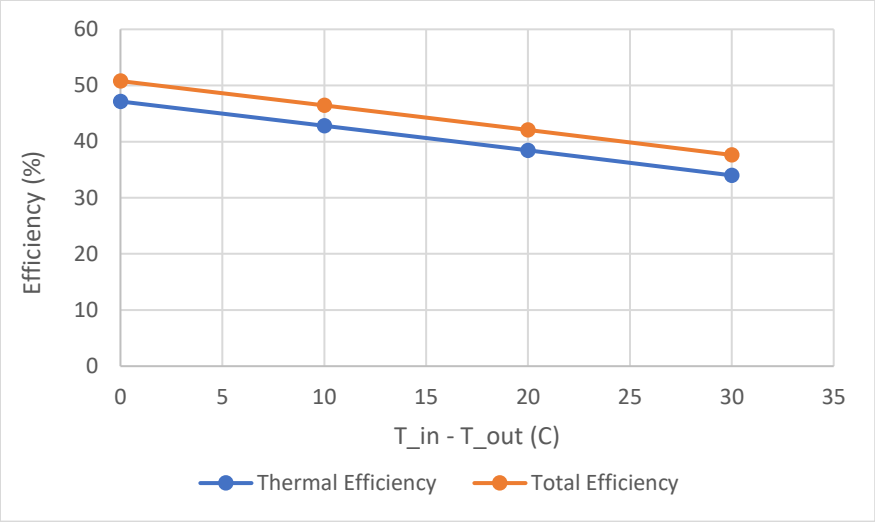


**Figure 6.14** Co-generation efficiency for an RGB co-generation SAH with a convection co-efficient of 10 W/m$^2$·K and a mass flow rate of 0.0025 kg/s.

The resulting RGB panel has an electrical efficiency of 3.63% and a thermal efficiency profile as shown in **Figure 6.14**, with a max thermal efficiency of 47.15%. This means that the co-generation panel has 8.5% lower thermal efficiency when compared to the RGB SAH and a 12.5% lower thermal efficiency than typical double cover solar heater under the same conditions. However, the addition of the 3.63% electrical efficiency narrows this difference and holds additional value due to the high-grade energy medium. The electrical efficiency could be further increased by matching the dye emission wavelengths from each panel to solar cells with an optimal spectral response spectrum.

For comparison purposes, the following scenarios are proposed; two different set-ups of the same size, with one using traditional solar cells and traditional solar heater and the other using a co-generation heater, described above.

Scenario one: Solar cells are assumed to be 18% efficient, with a power output of 154.3 W/m$^2$ under the AM 1.5 solar spectrum. The solar heater with the double cover at h=10 W/m$^2$ K and a mass flow rate of 0.0025 kg/s operates with an efficiency of 59.6%, producing 511 W/m$^2$ of heat.

Scenario two: Using the RGB co-generation panel with the performance above under the same conditions as scenario one. The RGB co-generation panel will produce an estimated 31.13 W/$m^2$ of electric power and operates at 47.15% thermal efficiency, or 404.1 W/$m^2$.

Using these parameters, 0.202 $m^2$ of solar PV is required to produce the same amount of electricity as 1 $m^2$ of the co-generation panels. The remaining 79.8% of the area could be used to produce 408.08 W thermal heat, outperforming the co-generation panel (404.1 W thermal) by 0.25%. The same procedure was replicated to produce **Table 6.10** for results at different h values and different $T_{in}$-$T_a$ values.

**Table 6.10** Co-generation performance comparison

| Parameters | Description | Electric (W/$m^2$) | Thermal (W/$m^2$) |
|---|---|---|---|
| h = 10 W/$m^2$ K<br>ΔT = 0 °C | Traditional 2 cover black plate heater + solar cells | 31.13 | 408.08 |
| | RGB Co-generation | 31.13 | 404.08 |
| h = 10<br>ΔT =30 | Traditional 2 cover black plate heater +solar cells | 31.13 | 320.571 |
| | RGB Co-generation | 31.13 | 291.26 |
| h= 20<br>Δ T = 0 | Traditional 2 cover black plate heater + solar cells | 31.13 | 389.35 |
| | RGB Co-generation | 31.13 | 387.3 |
| h = 20<br>ΔT = 30 | Traditional 2 cover black plate heater +solar cells | 31.13 | 292.8 |
| | RGB Co-generation | 31.13 | 263 |

The performance of these two scenarios is remarkably similar, however, the traditional proven method of using solar PV outperforms the LSC co-generation predictions. Improvements in the optical efficiency of LSC dyes will be required to tip the scale in favour of using LSCs.

A quick analysis shows that if all the power absorbed by the dye in a 3-layer RGB multi-panel is directed to the edge with 75% optical efficiency (only escape losses) and collected using Si cells, 71.96 W/m$^2$ of electricity could be generated and 443.68 W/m$^2$ will be transmitted. This is less than the 154.26 W/m$^2$ of electricity that can be generated by traditional Si PV cells with a conversion efficiency of 18%, making them less desirable on a pure electrical perspective. The thermal efficiency of the transmitted light can be estimated based on the total thermal efficiency of a triple clear SAH (58.33%) removing the efficiency loss attributed to reflection (18.28%) and absorption (9.37%) as the light passes through the covers to isolate for transmitted light efficiency. Applying the estimated thermal efficiency of 83.74% for the transmitted light, an additional 371.53 W/m$^2$ of thermal energy can be harvested from the RGB co-generation collector. In comparison, 0.467 m$^2$ of dedicated Si PV cells could produce the same amount of electricity, leaving the remaining 0.533 m$^2$ available for a traditional black plate collector; generating 260.21 W/m$^2$ of thermal power. This equates to an efficiency of 38.75% for the separate PV/heating and 51.7% for the LSC co-generation method, thus building the case for future improved LSC in this application.

## 6.5 Conclusion

The methods used to integrate LSCs into SAHs resulted in a small difference in performance compared to traditional 2 and 3 cover flat plate solar air heaters. The slope of the LSC SAH was shown to be slightly less steep, indicating that they may have advantages at high-temperature differences or windy conditions. The large size of edge ducting required in this design minimized the beneficial effect of using the optical transmission through the LSC panels when compared to the flat plates resulting in sub-par performance improvements. When the optical energy generated captured by the LSC is used to generate electricity rather than heat, it was shown that this co-generation setup underperforms when compared to simply using a traditional solar PV and flat plate thermal collector. Extrapolating data to explore the future case with optimal LSC panels, it is speculated that LSCs co-generation collectors could outperform the traditional technology if the efficiency of LSCs could be improved.

# 7. Conclusion

A case was built to further pursues the application of the integration of LSCs into greenhouse roofs by showing that red LSCs may improve the microclimate of the greenhouse while matching with typical shading values used by growers during hot sunny months. Spectral modeling methods were developed based on using transmission and reflection spectra through florescent acrylic samples. This method was used to estimate the effect of red LSC panels on greenhouse crops, where it was found that the addition of commercially purchased red fluorescent LSC panels resulted in a 35% shading factor. However, due to the selective properties, the LSC reduces the net photosynthetic action of the crops by only 27% (at 35% shading), rather than by 1% for each percent of shading caused by whitening. This shading value is less than the shading factor achieved through techniques commonly used during hot months, which can provide shading values higher than 40%. The ability to have a high net shading with reduced impact on the photosynthetic action indicates that the LSCs may improve the crop yields due to improved microclimate and improved energy efficiency over traditional shading methods. It should be noted that the dye concentration used in the LSCs could be varied causing different amounts of shading and effecting LSC collection performance. It is worth pointing out that traditional shading techniques have the advantage of being removable, thus allowing them to be used only when required; in contrast, integrating LSCs into the roof may be permanent, which could limit their suitability to hot, sunny climates. Additionally, a simple profit model shows that the integration of LSCs into a theoretical greenhouse can raise the profits from a greenhouse by as much as 40.7% if the generated electricity is sold at wholesale Ontario prices, under the assumptions described. This model could be adapted and used to estimate profits on a case by case basis but would benefit from supporting data such as actual LSC impact on crops and real-world performance data.

Chapter 3 demonstrated the ability for commercially available florescent acrylic to be used as an LSC, performing within 12% of the expected efficiency predicted by Raytracer using BASF Lumogen series ROT 305 dye, at a size of 35 x 35 x 4.7 $mm^3$. The ability to use commercially available fluorescent acrylic for LSCs can allow researchers to bypass the fabrication of LSCs for design and prototyping for proof of concept in applications. The large sizes available can

speed up large scale testing in applications such as greenhouse roofs or thermal collectors, although it does impose limitations on the dye choices available and may not have the optimal efficiency.

Newton's law of cooling was adapted to measure the thermal power output from LSCs, showing a new and unique method of determining LSC performance. This data was matched with spectral modeling data for additional verification and used to simultaneously develop the spectral model, allowing for additional knowledge about the performance of the fluorescent acrylic. This data can be used to estimate the performance of the LSC under varying configurations and light sources, providing a starting point for the design of panels for thermal applications, such as solar thermal windows, thermal greenhouse panels, and solar thermal collectors. Designs should be tested in real-world settings to confirm the performance values to add verification to the results.

The performance of multi-panel LSC configurations was able to be predicted to within ~10% of values observed experimentally using transmission and reflection spectrum modeling; however, the accuracy of this prediction may change in different scenarios. The model can provide an initial estimate and provides a closer approximation than simply ignoring the additional power contribution from interactions between stacked panels. The methods described for measuring and modeling the performance and energy flow in LSCs in various configurations/orders can aid in the optimization, design, and simulation of multi-panel LSC for various applications, such as the integration into solar heaters, windows, or spectral splitting LSC PV designs. Care should be used to acknowledge the limitations of these methods, because it provides an estimate based on lab conditions and has not been validated for all conditions or scenarios.

Hybrid LSC collectors are shown to have improved low-temperature performance over LSC collectors and improved high-temperature performance over both flat plate collectors and LSC collectors for modules with the parameters (area, insulation, LSC performance, irradiance and black plate emittance) described in chapter 5. This indicated that Hybrid LSC collectors may provide a benefit in high-temperature applications, and in applications where a large operating temperature range is required.

Applying the thermal collector design to transparent NIR LSC heaters which could be used as solar thermal windows in houses and buildings, it is estimated that they could supply between 22.3-45.5% of the average household hot water requirements, limited to the assumptions described. With nearly 40% of the energy use in the USA being used by residential units and buildings and nearly half of that being used for water and space heating [7], these windows could provide a significant reduction to national energy requirements. Improvements to either the IR dye efficiency or the absorption range would further improve the attractiveness of this solution.

LSCs were first proposed in the 1970s and since then little progress has been made in terms of largescale high efficiency/low-cost modules. Efforts made in this thesis to create a case for applications in which LSC add additional benefit have demonstrated the potential for LSC use in greenhouse applications, solar thermal collectors and solar windows, however, they also emphasize the same conclusion as previous authors; new dyes with higher performance must be developed to see the full potential of LSCs and to make them competitive enough against traditional solar systems. The methods demonstrated within this thesis provide the initial steps for designing LSCs for the explored applications, but future research into these applications should be conducted.

It should be noted that transparent solar PV cells have shown strong development and will be in direct competition with LSCs for transparent, spectral selective electrical generation systems. This puts pressure on further development for LSC technologies to avoid becoming obsolete in these applications.

## 7.1 Future Work

The use of LSCs in greenhouses has thus been shown to be worth further investigation, especially when used in hot, sunny conditions, and as such, further research into the implementation of such a system should be conducted with a focus on electricity output and crop yields. Future work to build and test a greenhouse with integrated LSC panels should be completed to determine the actual crop yields and electrical yields; the methods described within this thesis can provide a starting place. It is suggested that two similar greenhouses be

constructed, one using a traditional roof, and one using an LSC roof, where crop yields from each greenhouse could be studied and compared, along with electricity production, thus laying the groundwork for future commercialization and implementation in the climate zone.

Testing the performance of solar thermal LSC collectors under sunlight conditions should be conducted to verify that the performance predicted in this work. Future work to integrate the solar thermal LSC collectors into specific applications, such as hot water heating and solar windows should be completed. Further testing of NIR panels should be completed to reduce reliance on second-hand data for NIR calculations. Real-world prototyping for specific applications could be completed to increase the impact of these results and take the next step towards commercial implementation.

A closer look at the interactions between multi-panel configurations could be done to provide a more accurate model allowing for improved design and simulation ability.

# 8. References


[1] EIA. Energy Information Administration, "International Energy Outlook 2019," EIA, 2019.

[2] J. Tsao, N. Lewis and G. Crabtree, "Solar FAQs," U.S Department of Energy, 2006.

[3] IEA, "World Energy Outlook 2019," IEA, 2019. [Online]. Available: https://www.iea.org/reports/world-energy-outlook-2019/electricity. [Accessed 12 05 2020].

[4] R. F. Service, "Skyscrapers could soon generate their own power, thanks to see-through solar cells.," Science, AAAS, 28 june 2018. [Online]. Available: https://www.sciencemag.org/news/2018/06/skyscrapers-could-soon-generate-their-own-power-thanks-see-through-solar-cells. [Accessed 12 05 2020].

[5] International Energy Agency, "Energy Efficiency, Buildings," Availible: https://www.iea.org/topics/energyefficiency/buildings, 2019.

[6] Office of Energy Efficiency, "Energy Efficiency Trends In Canada 1990 to 2013," Natural Resources Canada, 2016.

[7] U.S Department of Energy., 2011 Buildings Energy Data Book, 2001.

[8] P. Emrath and J. Miller, "How much Energy Homes Use and Why," National Association of Home Builders, 2014.

[9] NREL, "Estimating Rooftop Suitability for PV: a Review of Methods, Patents and Validation Techniques," NREL, Denver, 2013.

[10] CSIRO, "Windows will soon generate electricity," CSIRO, April 2020. [Online]. Available: https://www.csiro.au/en/News/News-releases/2020/Windows-will-soon-generate-electricity. [Accessed 12 05 2020].

[11] "Solar Window Technologies," Solar Window Technologies, [Online]. Available: https://www.solarwindow.com/technology/. [Accessed 12 05 2020].

[12] C. J. Traverse, R. Pandey, M. C. Barr and R. R. Lunt, "Emergence of highly transparent photovoltaics for distributed applications," *Nature Energy*, vol. 2, pp. 849-860, 2017.

[13] J. Yu, J. Sun, N. Chandrasekaran, C. Dunn, A. Chesman and J. Jasieniak, "Semi-transparent Perovkite solar cells with a cross-linked hole transport layer," *Nano Energy,* no. https://doi.org/10.1016/j.nanoen.2020.104635, 2020.

[14] A. Goetzberger and V.Wittwer., "Flourescent planar collector-concentrators: A Review.," *Solar Cells,* vol. 4, no. 3, p. 23, 1981.

[15] A. Goetzberger, "Thermal Energy Conversion With Fluorescent Collector-Concentrators," *Solar Energy ,* vol. 22, pp. 435-438, 1979.

[16] A. P. Green, "Optical Properties of Luminescent Solar Concentrators," in *University of Sheffield*, England, 2014.

[17] L. R. Wilson, B. C. Rowan, N. Robertson, B. Richards, A. C. Jones and O. Moudam, "Characterization and reduction of re-absorption losses in luminescent solar concentrators," *Applied Optics*, vol. 49, no. 9, pp. 651-1661, 01 03 2010.

[18] B. S. Richards and K. R. McIntosh, "Ray-tracing simulations of luminescent solar concentrators containing multiple luminescent species," *Proceedings of the 21st EU PVSEC, Dresden,* pp. 185-188, 2006.

[19] M. Gajic and G. Rosengarten, "Non-imaging technologies for designing a hybrid photovoltaic and solar thermal collector," *RMIT University, Thesis. ,* 2018.

[20] G. Griffini, L. Brambilla, M. Levi, M. DelZoppo and S. Turri, "Photodegradation of a perylene-based organic Luminescent solar concentrator: Molecular Aspects and device implications," *Solar Energy Materials and Solar Cells,* vol. 111, pp. 41-48, 2013.

[21] J. R. Lakowicz, "Introduction to," in *Principles of Fluorescence Spectroscopy*, Springer US, 2006, pp. 1-23.

[22] F. Holtrup, G. M• uller, S. H. Quante, d. Feyter, F. d. Schryver and k. Mullen, "Terrlenimides: New NIR flourescent dyes.," *Chem. EUR. J. ,* vol. 3, no. 2, pp. 219-225, 1997.

[23] F. Nolde, J. Qu, C. Kohl, N. Pschinirer, E. Reuther and K. Mullen, "Synthesis and modification of terrylenendiimides as high-performance fluorescent dyes.," *Chem. Eur. J.,* no. 11, pp. 3959-3967, 2005.

[24] G.Wagenblast and G.Seybold, "New Perlene and Violanthrone Dyestuffs for Flourescnets collectors.," *Dyes and Pigments,* vol. 11, pp. 303-317, 1989.

[25] R. Sah and G. Baur, "Influence of the solvent matrix on the overlapping of the absorption and emission bads of soulte fluorescnet dyes.," *Appl. Phys.,* vol. 23, pp. 369-372, 1980.

[26] W. G. v. Stark, K. W. J. Barnham, L. H. Slooff, A. J. Chatten, A. Buchtemann, A. Meyer, S. J. McCormack, R. Koole, D. J. Farrell, R. Bose, E. E. Bende, A. R. Burgers, T. Budel and J. Quilitz, "Luminescent solar concentrators- A review of recent results," *Optics Express,* vol. 16, no. 26, pp. 21773-21792, 2008.

[27] C. Corrado, S. W. Leow, M. Osborn, I. Carbone, K. Hellier, M. Short, G. Alers and S. A. Carter., "Power Generation Study of Luminescent Solar Concentrator Greenhouse," *Renewable Sustainable Energy,* vol. 8, no. 043502-10, 2016.

[28] BASF, "Lumogen F Dyes," BASF, [Online]. Available: http://www2.basf.us/additives/pdfs/lumvio570.pdf. [Accessed 20 03 2020].

[29] L. R. Wilson, "Luminescent Solar Concentrators: A study of Optical properties re-absorbtion and device optimization," *Heriot-Watt University, School of Engineering and Physical Sciences,* vol. Doctor of Philosphy Thesis Submission, 2010.

[30] A. Zastrow, "Ph.D Thesis," *Frieburg,* 1981.

[31] M. Currie., "High-efficiency organic solar concentrators for photovoltaics," *Science,* vol. 321, no. 226, 2008.

[32] L. Sloof, E. Bende, A. Burgers, T.Budel, M.Pravettoni, R. Kenny and E. Dunlop, "A luminescent solar concentrator with 7.1% power conversion efficiency," *Phys. Stat. Sol. (RRL),* vol. 2, no. 6, pp. 257-259, 2008.

[33] L. Slooff, R. Kinderman, A. Burgers, A. Buchtemann, R.Danz, T. Meyer, A. Chatter, D. Farrell, K. Barnham and J. V. Roosmalen, "The luminescent concentrator illuminated," *Proc. SPIE 6197 Photonics for Solar Energy Systems,* 2006.

[34] M. Kastelijn, M. Bastiaansen and C. Debije, "Influence of waveguide material on light emission in luminescent solar concentrators," *Optical Materials,* vol. 31, no. 11, pp. 1720-1722, 2009.

[35] L. R. Wilson, *LSC Simmulation Code.,* 2010.

[36] C. Tummeltshammer, A. Taylor, A. Kenyon and I. Papkonstantinou, "Losses in Luminescent Solar Concentrators Unveiled," *Solar Energy Materials and Solar Cells,* vol. 144, pp. 40-47, 2016.

[37] C.Honsberg and S. Bowden, "IV curve," PV Education, 2019. [Online]. Available: https://www.pveducation.org/pvcdrom/solar-cell-operation/iv-curve. [Accessed 23 03 2020].

[38] C. Honsberg and S. Bowden, "PV Education - Spectral Response," [Online]. Available: https://www.pveducation.org/pvcdrom/solar-cell-operation/spectral-response. [Accessed 29 3 2020].

[39] L. R. Wilson and B. Richards, "Measurement method for PLQY of fluorescent organic dyes," *Applied Optics,* vol. 48, pp. 212-220, 2009.

[40] J. Mugnier, Y.Dordet, J. Pouget and B. Valeur, "A photometric approach of fluorescent solar Concentrators. Role of Diffuse Reflectors and Spectral Sensitivity of Solar Cells," *Revue Phys. Appl.,* vol. 22, pp. 89-100, 1987.

[41] R. Nave, "Light Absorption for Photosynthesis," HyperPhysics Project, Georgia State University, [Online]. Available: http://hyperphysics.phy-astr.gsu.edu/hbase/Biology/ligabs.html. [Accessed 29 07 2020].

[42] R. Hassanien, E. Hassanien, M. Li and F. Yin, "The integration of semi-transparent photovoltaics on greenhouse roof for energy and plant production," *Renewable Energy,* vol. 121, pp. 377-388, 2018.

[43] D. R. Holding and A. M. Striech, "Plant Growth Processes: Transpiration, Photosynthesis and Respiration," University of Nebraska, 2013.

[44] O.Korner, E. HeuVelink and Q.Niu, "Quantification of temperature, CO2 and light effects on crop photosythesis as a basis for model-based greenhouse climate control," *Journal of Horticultural science and biotechnology,* vol. 84, no. 2, pp. 233-239, 2009.

[45] K. Aberkani, X. Hao, D. d. Halleux, M. Dorais, S. Vineberg and A. Gosselin, "Effects of Shading Using a Retractable Liquid Foam Technology on Greenhouse and Plant Micro-Climates," *HorTechnology,* vol. 20, no. 2, pp. 283-291, 2010.

[46] R. Hassanien and E. Hassanien, "Influences of greenhouse-integrated semi-transparent photocoltaics on microclimate and lettuce growth," *International Journal of Agricultural and Biological Engineering,* vol. 10, no. 6, pp. 11-20, 2017.

[47] D. Dannehl, J.Suhl, S. Huyskens-Keil, C. Ulrichs and U. Schmidt, "Effects of a special solar collector greenhouse on water balance, fruit quantity and fruit quality of tomatoes," *Agricultural Water Management.,* vol. 134, pp. 14-23, 2014.

[48] R. Hassanien, M. Li and F. Yin, "The integration of semi-transparent photovoltaics on greenhouse roof for energy and plant production," *Renewable Energy,* no. https://doi.org/10.1016/j.renene.2018.01.044, 2018.

[49] NRC, "Photovoltaic and Solar Resource Maps," Natural resources Canada, 2019. [Online]. Available: https://www.nrcan.gc.ca/18366. [Accessed 04 02 2019].

[50] "Commercial Greenhouse Tomato Production," Alberta, [Online]. Available: https://www.alberta.ca/commercial-greenhouse-tomato-production.aspx. [Accessed 02 02 2019].

[51] Statistics Canada, "Table 32-10-0364-01. Area, Production and farm gate value of marketed fruits," [Online]. Available: https://doi.org/10.25318/3210036401-eng.

[52] Statistics Canada, "Tables 22-202-X; Greenhouse, Sod and Nursery Industries," Stats Canada, 2018. [Online]. Available: https://www150.statcan.gc.ca/n1/en/catalogue/22-202-X. [Accessed 02 02 2019].

[53] K. Mcree, "The Action Spectrum, Absorbance and Quantum Yield of Photosynthesis in Crop Plants," *Agric. Meterol. ,* vol. 9, pp. 191-216, 1970.

[54] A. Baille, C. Kittas and N. Katsoulas, "Influence of whitening on greenhouse microclimate and crop energy partitioning," *Agricultural and Forest Meteorology,* vol. 107, no. 01681923, pp. 293-306, 2001.

[55] R. Hassanien, E. Hassanien and L. Ming, "Influences of greenhouse-integrated semi-transparent photovoltaics on microclimate and lettuce growth," *Int J Agric & Biol Eng,* vol. 10, no. 6, 2017.

[56] M. Cossu, L. Murgia, L. Ledda, P. Deligios, A. Sirigu, F. Chessa and A. Pazzona, "Solar radiation distribution inside a greenhouse with south-oriented photovoltaic roofs and effects on crop productivity," *Applied Energy,* 2014.

[57] Y. Araki and S. I. k. Murakami, "Effects of Shading on Suimmer Spinach," *Journal of Agricultural Engineering,* 2017.

[58] M. d. l. Á. Moreno-Teruel, D. Valera, F. D. Molina-Aiz, A. López-Martínez, A. Peña, P. Marín and A. Reyes-Rosas, "Effects of Cover Whitening Concentrations on the Microclimate and on the Development and Yeild of Tomato Inside Mediterranean Greenhouses," *Agronomy,* vol. 10, no. 237, 2020.

[59] B. Rowan, L. R. Wilson and B. Richards, "Advanced Material concepts for Luminescent Solar Concentrators," *IEEE Journal of Selected Topics in Quantum Electronics,* vol. 14, no. 5, pp. 1312-1322, 2008.

[60] L. Desmet, A. J. M. Ras, D. k. .. deBoer and M. Debijie, "Monocrystalline silicon photovoltaic luminescent solar concentrator with 4.2% power conversion efficiency," *Opt. Lett. 37, 3087-3089 (2012).*

[61] B. Wishwanathan, A. reinders, D. deBoer, L. Desmet, A. Ras, F. Zahn and M. Debije, "A comparison of performance of flat and bent photovoltaic luminescent solar concentrators," *Solar Energy,* vol. 112, pp. 120-127, 2015.

[62] W. G. A. Geotzberger, "Solar Energy Conversion with Flourescent Collectors," *Appl. Phys.,* vol. 14, pp. 123-139, 1977.

[63] W.Stahl, V.Wittwer and A.Goetzberger, "Thermal Conversion With Fluorscent concentrators," *Solar Energy Vol. 36,* vol. 36, no. 1, pp. 27-35, 1986.

[64] A.Goetzberger, "Thermal Energy Conversion With Fluorescent Collector-Concentrators," *Solar Energy,* vol. 22, pp. 435-438, 1979.

[65] C. T. O'Sullivan, "Newtons Law of Cooling- A critical Assessment,," *AM.J Phys.,* vol. 58, no. 10, p. 956.

[66] M. Vollmet, "Newton's Law of Cooling Revisted," *Eur. J. Phys.,* pp. 10063-1084, 2009.

[67] A.Goetzberger and V.Wittwer., "Flourescent planar collector-concentrators: A Review.," *Solar Cells,* vol. 4, no. 3, p. 23, 1981.

[68] Arkema, "Plexiglas," Altuglas Internation. Arkema Inc. , Philadelphia, 2000.

[69] W. Stahl, V.Wittwer and A. Goetzberger, "Thermal Conversion With Fluorscent concentrators," *Solar Energy Vol. 36,* vol. 36, no. 1, pp. 27-35, 1986.

[70] J. A. Duffie and W. A. Beckman, Solar Engineering of Thermal Processes, Fourth Edition, US: John Wiley & Sons., 2013.

[71] NREL, "Reference Solar Spectral Irradiance: ASTM G-173," Gov., [Online]. Available: https://rredc.nrel.gov/solar//spectra/am1.5/ASTMG173/ASTMG173.html. [Accessed 01 08 2019].

[72] NREl, "Reference Solar Spectral Irradiance: ASTM G-173," [Online]. Available: https://rredc.nrel.gov/solar//spectra/am1.5/ASTMG173/ASTMG173.html. [Accessed 05 11 2019].

[73] Energy Star, "ENERGY STAR® for Windows, Doors, and Skylights Version 6.0".

[74] R. L. a. B. Krittakom, "A study: Thermal Efficiency of Solar Air heater with Wire mesh Stainless Installation: Using Solar Simulator," *Journal of Physics: Conference Series,* vol. 1039 012044, 2018.

[75] E. Loh and D. Scalapino, "Luminescent solar concentrators: effects of shape on efficiency," *Appl. Opt.,* vol. 25, no. 2, pp. 1901-1907, 1986.

[76] M. S. D. Cardona, M.Carrascosa, F. Meseguer, F. Cusso and F. Jaque, "Edge Effect on Luminescent Solar Concenctrators," *Solar Cells,* vol. 15, pp. 225-230, 1985.

[77] ThorLabs, [Online]. Available: Thorlabs.com. [Accessed 08 2019].

[78] "Flourescent Acrylic - Alibaba," 20 01 2020. [Online]. Available: https://www.alibaba.com/trade/search?fsb=y&IndexArea=product_en&CatId=&SearchText=fluorescent+acrylic.

[79] F. Struckmann, "Analysis of a Flat-plate Solar Collector," *Heat and Mass Transport,* 2008.

[80] E. E. a. R. E. U.S Department of Energy, "Energy Efficiency Trends in Residential and Commercial Buildings," U.S Department of Energy, 2008.

[81] G. Liu, R. Mazzaro, Y. Wang, H. Zhao and A. Vomiero, "High Efficiency sandwich structure luminescent solar concentraotrs based on colloidal quantum dots," *Nano Energy,* vol. 60, pp. 119-126, 2019.

[82] N. Aste, L. Tagliabue, C. Pero and D. T. R. Fusco, "Performance analysis of a large-area luminescent solar concentrator module," *Renewable Energy,* vol. 76, pp. 330-337, April 2015.

[83] L. Witmer, Solar Thermal Energy for Utilities and Industry, PennState, Department of Energy and Mineral Engineering, 2013.

[84] H. Bhowmilk and R. Amin, "Efficiency Improvement of flat plate solar collector using reflector," *Energy Reports,* vol. 3, pp. 119-123, 2017.

[85] S. Agbo and E. Okoroigwe, "Analysis of Thermal Losses in the Flat-Plate Collector of a Thermosyphon Solar Water Heater," *Research Journal of Physics,* vol. 1, pp. 35-41, 2007.

[86] L. &. B. A. &. D. M. Slooff, "Reduction of escape cone losses in luminescent solar concentrators with cholosteric mirrors.," *Proc SPIE,* no. 10.1117/12.794522. , 2008.

[87] "Fluorescence guide," Abcam, 2020. [Online]. Available: https://www.abcam.com/secondary-antibodies/fluorescence-guide. [Accessed 18 03 2020].

[88] J. R. Lakowicz, "Principles of Flourescence Spectroscopy," vol. 3, Springer Science + Business Media, 1983.

[89] G. S. a. G. Wagenblast., "New perylene and violanthrone dyestuff for flourescent collectors.," *Dyes and pigments,* vol. 11, pp. 303-317, 1989.

[90] M. Debije, K. -P. Tuenissen, M. Kastelijin, P. Verbunt and C. Bastiaansen., "The effect of a scattering layer on the edge output of a luminescent solar concentrator," *Solar Energy Materials and Solar Cells,* vol. 93, pp. 1345-1350, 2009.

[91] L. H. Slooff, E. E. Bende1, A. R. Burgers, T. Budel, M. Pravettoni, R. P. Kenny and E. D. Dunlop, "A luminescent Solar Concentrator with a 7.1% power conversion Efficiency," *Phys. Stat. Sol,* vol. 2, no. 6, pp. 257-259, 2008.

[92] Lexico, "UK Dictionary: Definition: Quantum Dot," Oxford. [Online].

[93] M. Samadpour, "Efficiency of CdS/CdSe/ZnS quantum dot sensitized solar cells perpared by ZnS Treatment from methanol Solvent," *Solar Energy,* vol. 144, pp. 63-70, 2016.

[94] M. G. Hydahl, S. T. Bailey and B. P. Wittmershaus, "Photo-stability and performance of CdSe/ZnS quantum Dots in Luminescent Solar Concentrators," *Solar Energy,* vol. 83, no. 4, pp. 566-573, 2009.

[95] Z. Krumer, S. J. Pera, R. J. v. Dijk-Moes, Y. Zhao, A. F. d. Brouwer, E. Groeneveld and W. G. v. Stark, "Tackling self-absorption in luminescent solar concentrators with type-II

colloidal quantum dots," *Solar Energy Materials and Solar cells,* vol. 111, pp. 57-65, 2013.

[96] C. D. M. Donega, "Formation of nanoscale spatially indirect excitons: evolution of the type-ii optical character of CdTe/CdSe heteronanocrystals," *Physical Review B,* vol. 81, p. 165303, 2010.

[97] K. Knowles, T. Kilburn, D. Alzate, S. McDowall and D. Gamelin, "Bright CuInS2/CdS nanoCrystal phosphors for high-grain full spectrum luminescent solar concentrators," *Chemical Communications,* vol. 51, no. 44, pp. 9129-32, 2015.

[98] D. Waldron, A. Preske and J. Zawodny, "PbSe quantum dot based luminescent solar concentrators," *nanotechnology,* vol. 28, no. 9, p. 095205, 2017.

[99] L. R. Wilson, "Luminescent Solar Concentrators: A Study of Optical Properties, Re-Absorption and Device Optimization," Heriot-Watt University, School of Engineering and Physcial Sciences, Edinburgh, 2010.

[100] D. Holding and A. Streich, Plant Growth Processes; Transpiration, Photosynthesis and Respiration, Universityof Nebraska, 2013.

[101] L. Wilson, B. Rowan, N. Robertson, B. Richards, A. Jones and O. Moudam, "Chareacterization and reduction of reabsorption losses in luminescent solar concetrators," *Applied Optics,* 01 03 2010.

[102] W. Stahl, V. Wittwer and A. Goetzberger, "Thermal Converions with Flourescent Concentrators," *Solar Energy,* vol. 36, no. 1, pp. 27-35, 1986.

[103] International Energy Agency, "Energy Technology Perspectives," IEA, Availible: https://www.iea.org/etp2017/, 2017.

[104] A.P.Green, "Optical Properties of Luminescent Solar Concentrators," in *University of Sheffield*, England, 2014.

[105] L. Slooff, A. Burgers and M. Debije, "Reduction of escape cone losses in luminescent solar concentrators with cholosteric mirrors.," *Proc SPIE,* no. 10.1117/12.794522., 2008.

[106] L. R. Wilson, *LSC simmulation Code,* 2010.

[10 F. Meinardi, H. MCDaniel, F. Carulli, A. Colombo, K. A. Velizhanin, N. S. Makarov, R. 7] Simonutti, V. I. Klimov and S. Brovelli, "Highly Efficiency large area colourless Luminescent solar concentrators using heavy-metal-free colloidial quantuym dots," *Nature Nanotechnology*, vol. 10, 2015.

[10 F. Mateen, M. Ali, S. Y. Lee, S. H. Jeong, M. J. Ko and S. Hong, "Tandem Structured 8] luminescent solar concentrator based on inorganic carbon quantum dots and organic dyes," *Solar Energy*, vol. 190, pp. 488-494, 2019.

[10 A. I. Olivia, R. Castro-Rodriguez, O. Solis-Canto, V. Sosa, P. Quintana and J. L. Pena, 9] "Comparison of properties of CdS thin films grown by two techniques," *Applied Science,* vol. 205, no. 1-4, pp. 56-64, 2003.

[11 C. Chou, M. Hsu and F. Chen, "Flexible luminescent waveguiding photovoltaics exhibiting 0] strong scattering effects from the dye aggregation," *nano energy,* vol. 15, pp. 729-736, 2015.

[11 C. Corrado, S. Leow, M. Osborn, I. Carone, K. Hellier, M. Short, G. Alers and S. Carter, 1] "Power generation study of luminescent solar concentrator Greenhouse," *Renewable and Sustainable Energy,* vol. 8, p. 043502, 2016.

# 9. Appendix A: Fabrication Methods for LSC Waveguides

## 9.1 PMMA Polymerization Casting

PMMA is fabricated by following the water bath method present by Lindsay Robert Wilson [29] which involves polymerizing a methyl methacrylate and dye mixture. The steps used to produce the waveguide samples are presented below:

1. Monomer (MMA) and polymer (PMMA) are measured by weight using a 9:1 ratio of monomer to polymer.
2. Dye is added to the monomer solution and stirred using a magnetic stirrer to ensure it is fully mixed.
3. The monomer/dye solution is heated to 60 °C on the magnetic stirrer, and the polymer powder is added slowly to prevent clumping. The mixture is stirred for 1 h and the solution transforms to a casting syrup, containing the monomer, polymer, and dye.
4. The syrup is removed from the heat source and allowed to cool.
5. Once the casting syrup has cooled, AIBN (Azobisisobutyronitrile) is added at a ratio of 0.08% by weight of the casting syrup. It is mixed into the casting syrup using the magnetic stirrer. AIBN is a free radical initializer used for initializing free radical polymerization. (Note that if the initiator (AIBN) is added before you allow the syrup to cool polymerization would begin and the syrup would thicken making it difficult to pour into the mould.)
6. The casting syrup is poured into a readied mould, and the mould is sealed. (see Section “9.1.1 waveguide mould”)
7. The mould is placed in a water bath at 60 °C, allowing polymerization to begin. It is left for 18 h.
8. Post curing is then commenced to complete the polymerization. The mould is transferred into an oven at 80 °C for 2 h. Next, the temperature is increased to 100 °C for 1 h. The temperature is increased again to 110 °C for another hour, and finally to 120 °C for one more hour.
9. The mould is removed from the oven and left to cool. The PMMA sheet is removed from the mould.

### 9.1.1 Waveguide mould

The mould used for the above waveguide fabrication method was composed of two sheets of glass, a rubber gasket, and several clips. The gasket is placed between the two sheets of glass, making a loop with a small opening. Extra gasket length is left on each side of the gap to allow it to be pinched closed after filling. The glass sheets are clamped together using clips. **Figure 9.1** shows a demonstration of the set-up used. The PMMA samples created through this method are shown in **Figure 9.2** and **Figure 9.3**. Once the sample has been created and machined, the solar cells can be attached using optically compatible adhesives.

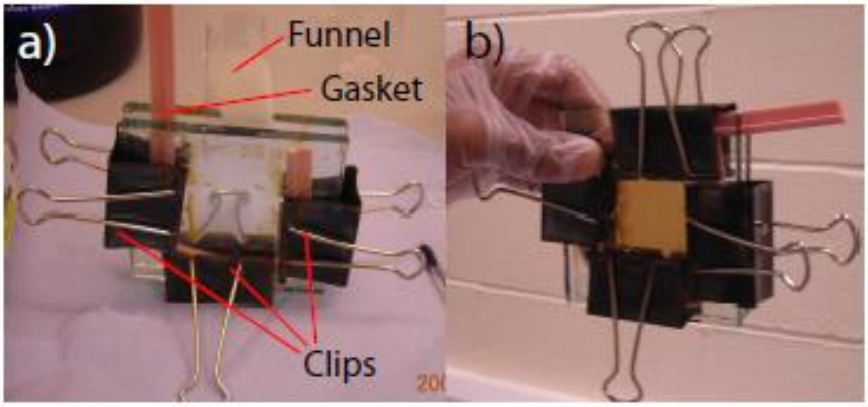


**Figure 9.1**. Mould gasket assembly. Figure from L. R. Wilson, "Luminescent Solar Concentrators: A Study of Optical Properties, Re-Absorption and Device Optimization", page 56. ©2010 [29]

**Figure 9.2.** Waveguide sample after being removed from the mould

**Figure 9.3.** Waveguide sample after machining

## 9.2 Post Processing of PMMA Samples

Some experimentation was done with post-processing the PMMA after retrieving it from the moulds. The surface of the samples often had defects, likely due to the shrinking of the PMMA during solidification. Additionally, bubbles were sometimes present within the material, however, once present there is no solution to removing these. Bubbles can likely be prevented by degassing of the casting syrup in a vacuum before pouring or by careful mixing and pouring of the syrup into the mould to prevent trapped gas. The PMMA was cut in a mill to experiment with cutting it into various shapes and subsequently improving its surface finish. Laser cutting and polishing using an acrylic polish was also attempted. The results were that the surface finish is best left untouched by polishing and machining as both of these steps have a visibly negative effect on the quality of the finished surface. Laser cutting produced fairly good results, but the cut edges had a small angle, rather than being square. Machining produced flat edges; however, the surface quality of the edges was not as good. The resulting sample is 4 cm x 8 cm and ~5 mm thick.

## 9.3 Spin Coating

In addition to the casting method, spin coating was investigated to create the LSC waveguide. For this method, PMMA was dissolved into Chloroform and mixed with the dye using a magnetic stirrer. A sheet of glass was cut to size (~5 cm x 5 cm) and placed in the spin coating machine. The surface of the glass was completely covered with the PMMA/Dye/Chloroform

mixture. The spin coater was turned on, spinning the sample at 1000-2000 rpm for 30 s. Several coats were used to increase the resulting thickness.

The resulting samples had a visibly non-uniform surface due to the improper dissolving of the dye in the solution. Several attempts were made to create a uniform surface, but none were successful. This could be a result of the oxidization of the dye used. **Figure 9.4** shows a sample created by the spin coating method and illuminated under a light. Note the uneven surface texture.

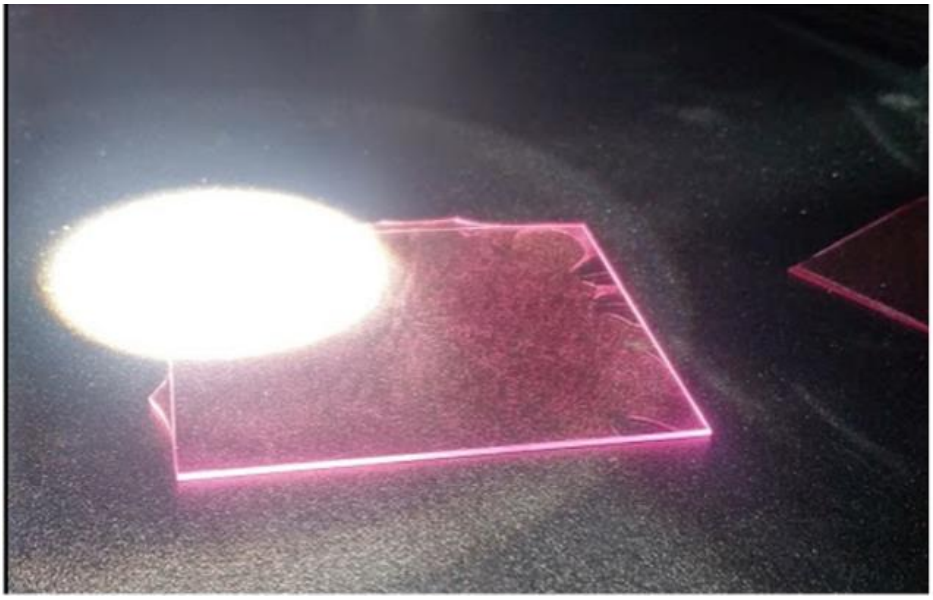

**Figure 9.4.** LSC spin coating sample

Due to added difficulty of cutting and shaping glass, poor uniformity across the surface, cost, and the desire for a larger thickness to facilitate attaching the PV cells to the edges, it was decided to pause work on spin coating samples.

## 9.4 Aluminum Mould Polymerization

As noted previously attaching the solar cell to the edge of the waveguide can cause problems with glue fillets and can be difficult to align properly. Additionally, the selection of an adhesive with the desirable properties must be used. The following describes a method used in an attempt to cast the solar cells directly into a PMMA waveguide to simplify the assembly process.

A mould was machined out of two pieces of aluminum. One piece of Aluminum featured a negative cut out to be filled with the casting syrup. The other piece was flat with a small slit cut into it to allow a solar cell to be added during the casting process. The slit was designed to hold the top of the solar cell (where the tabbing is) to prevent it from being cast into the waveguide. A gasket was cut from a $1/16^{th}$ piece of rubber to fit between the two sides and it was bolted together using pre-tapped holes along the edges of the mould. A small hole was machined into the top edge to allow for filling the mould. The inside of the mould was sanded using 3500 grit sandpaper and then polished for a good surface finish. Ideally, a mirrored finish would be used, although it was not possible to achieve this using the available tools. The aluminum mould and design are shown in **Figure 9.5** and **Figure 9.6**. The dimensions of the cast were 3 mm x 5 cm x 10 cm.

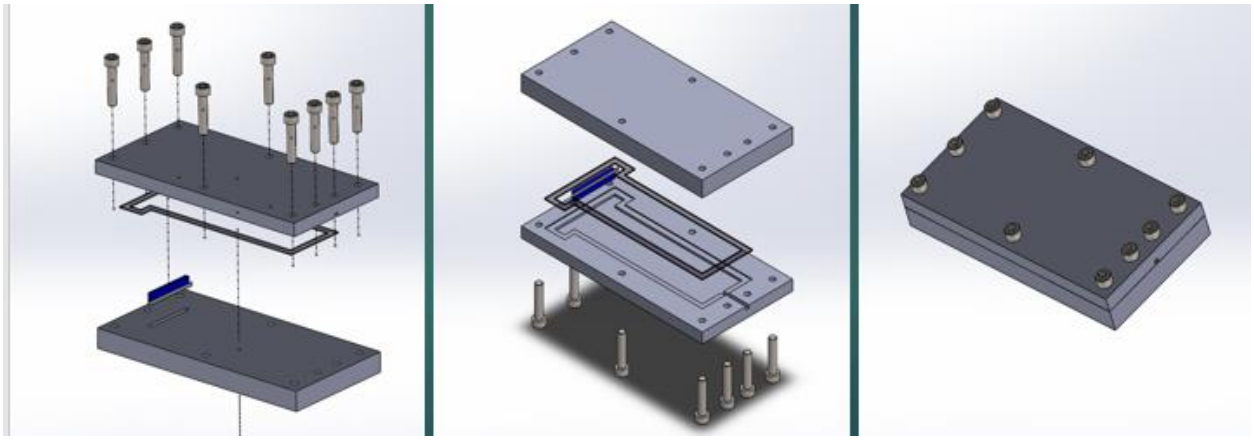

**Figure 9.5.** CAD design showing the aluminum mould

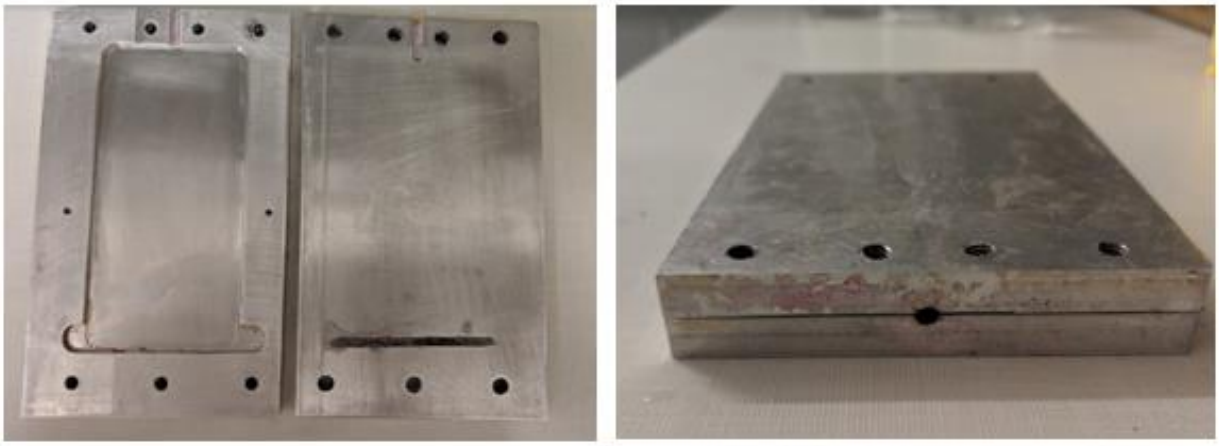

**Figure 9.6.** Aluminum mould

Despite several attempts, the LSCs fabricated using the aluminum mould were of poor quality in comparison to the LSCs fabricated using the glass sheet/gasket moulds as described in Section 9.1.1. The PV cells consistently broke inside the mould or became stuck inside the slot, causing them to break during removal efforts. No samples were created in which the solar cell was successfully bonded to the waveguide. **Figure 9.7** shows a sample created using this method.

**Figure 9.7.** PMMA sample created using the aluminum mould

The surface finish of LSCs fabricated using the aluminum mould was not as good as that of the LSCs produced using the glass mould, and required additional polishing using plastic polish. The resulting PMMA sample looked cloudy and had several bubbles in it, likely due to trapped gasses from the filling process. This could be reduced by increasing the thickness of the sample, which would allow better movement of the casting fluid and thus allow trapped gases to escape. A black substance was observed around the edges of the LSC waveguide, which may have been caused by the gasket, indicating that a different material must be used. It was thus decided to no longer pursue this method, as the best LSC created using this method had a single cell efficiency of 1%.

## 9.5 Current Matching and Edge Illumination Profile

### 9.5.1 Current matching in large cells

For large LSC modules, multiple solar cells must be used to span the length of the edge, which are generally connected in series. This can cause a problem because there is an inconsistent light intensity along the edge which has been described by other researchers [75] [76] in which the middle of the LSC edge receives more light than the corners do. The non-uniformity of light intensity causes different short circuit currents across the cells which can reduce the overall power because the current is limited by the cell with the lowest short circuit current [76] [29]. As a solution to this problem, it has been suggested that the length of the solar cells could be varied

such that the middle cell is the shortest and the edge cells are longest so that the total current produced by each cell is the same [29]. It has been estimated that for a large 60 cm x 60 cm module, the light intensity at the corner of the LSC is 40% lower than the middle [29]. The current matching of cells was shown to produce a 15% higher power output compared to an LSC with unmatched cells by L. R. Wilson [29].

### 9.5.2 Simulations

To simulate the edge illumination profile, COMSOL Optics was used. A square PMMA waveguide was created with dimensions 3 mm x 30 cm x 30 cm. $10^8$ photons were generated at random locations and in a random direction inside the waveguide. 10 collectors were placed in 10 even sections along one edge of the waveguide, from corner to corner (positions 5 and 6 being in the middle). The resulting plot shows the collected photons from each position (**Figure 9.8**).

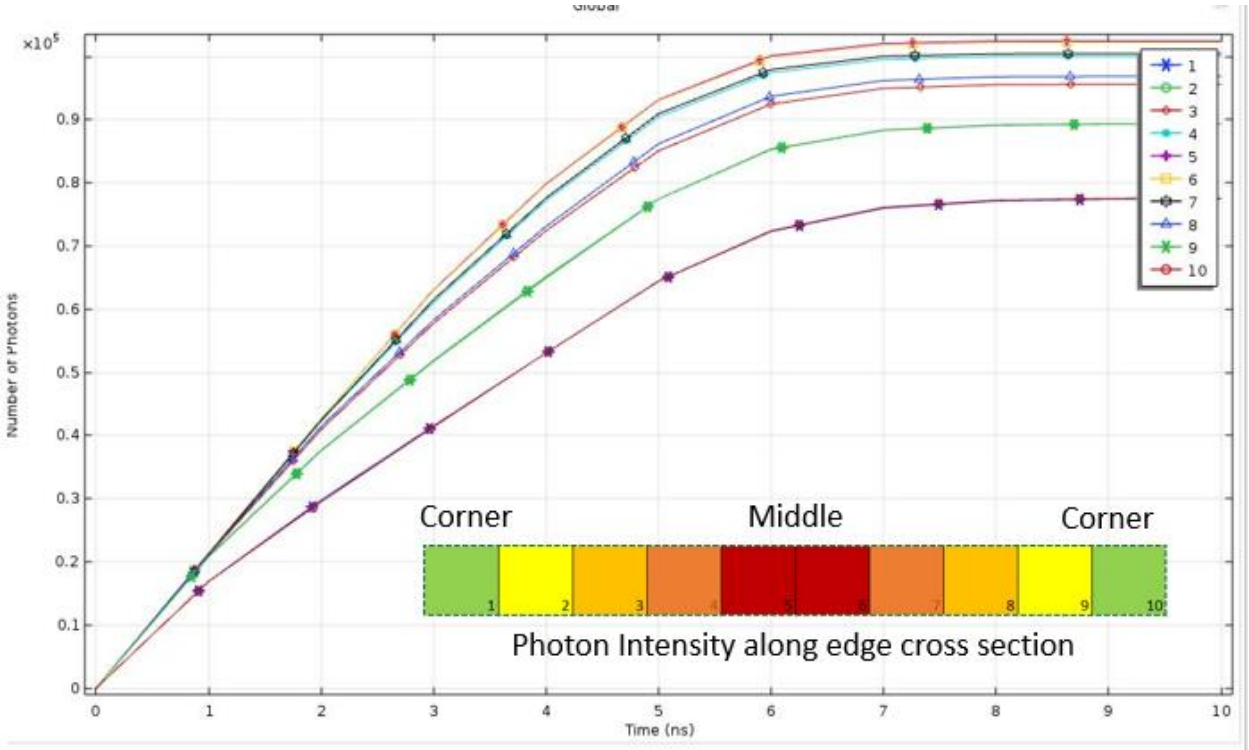


**Figure 9.8.** Edge illumination intensity of an LSC, generated using COMSOL Mutliphysics® simulations.

The difference in illumination between the middle cells and the corner cells was found to be ~25%. Normalizing the results so that the middle position has an intensity of 1 and plotting the

intensity in the middle of each position (ie. Position 1 is plotted at 0.5, positions range from 1 to 10) **Figure 9.9** is obtained. The profile is nearly quadratic, with ~ 35% decrease in intensity between the middle and corner of the edge.

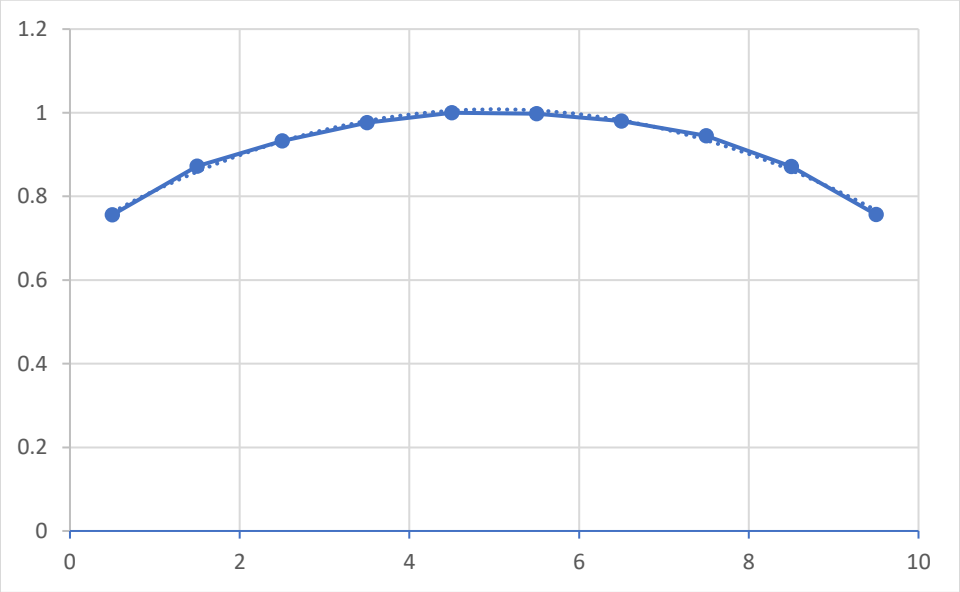


**Figure 9.9**. Edge illumination profile of LSCs. Position 0 and 10 are the corners, with position 5 representing the middle.

### 9.5.3 Current matching methods

To verify the intensity profile a 12 cm x 12 cm LSC was fabricated following the "3d printed frame method" described in Chapter 3. However, in this case, instead of using a single solar cell to span the length of each edge, 3 solar cells were used on each edge, for a total of 12. The cells were cut to be 3.5 cm long and were placed at either the corner or middle of each edge as shown in

**Figure 9.10**. A 0.75 cm gap was left between each cell.

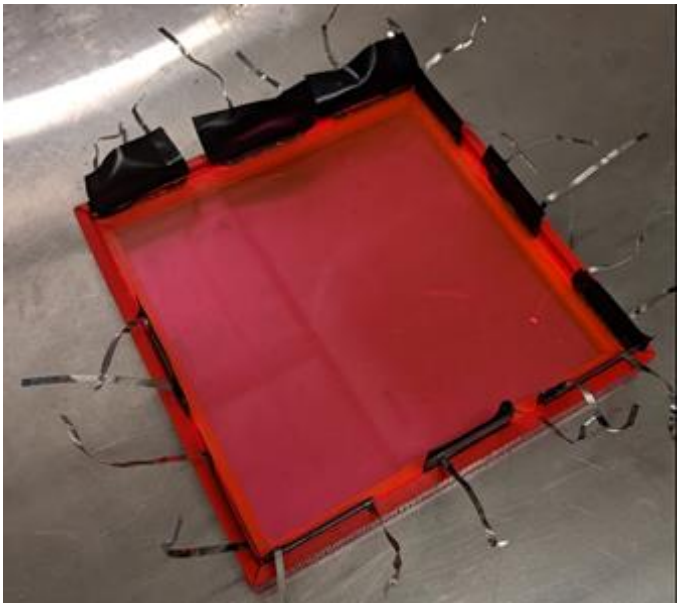

**Figure 9.10.** 12 x 12 $cm^2$ LSC with 12 PV cells for experimentally measuring the edge power distribution.

The power from each cell was measured while being exposed to the SunMaster Full Nova lamp before being attached to the LSC. The power from each cell was measured again after being attached to the LSC, with the LSC exposed to the same Sun Master Full Nova Lamp. The position of the cells and LSC under the light was kept consistent throughout the experiment. The power difference before and after were compared for each cell to determine the power ratio. The ratio of power generated by the cell before being attached and after being attached is used because each cell has a slightly different base performance; by comparing the performance of each cell to itself and using that ratio to compare between cells, the effect of the LSC can be compared without interference from individual cell differences.

### 9.5.4 Current matching results

**Table 9.1** shows the measurements taken for each cell. Note that cells 1 to 6 were tested at a different time than cells 8-12, resulting in a difference irradiance, and thus the results from each test will be compared separately. It can be seen that cells 1-6 perform better than cells 7-12; this is likely due to a light gradient across the panel (due to the nature of the light source) in which the sides where cells 1-6 are located received a higher than average irradiance. (note that the irradiance was measured in the direct middle of the panel).

**Table 9.1.** Measured results from each cell.

| Samples: | Position | Irradiance $mW/cm^2$ | $V_{Cell}$ | $I_{Cell}$ (mA) | $P_{Cell}$ (mW) | $V_{LSC}$ | $I_{LSC}$ (mA) | $P_{LSC}$ (mW) | % Power Ratio |
|---|---|---|---|---|---|---|---|---|---|
| 1 | corner | 42 | 0.5 | 27.2 | 13.6 | 0.52 | 25.7 | 13.4 | 98.3 |
| 2 | middle | 42 | 0.53 | 25.8 | 13.674 | 0.54 | 30.5 | 16.5 | 120.4 |
| 3 | corner | 42 | 0.52 | 30.1 | 15.652 | 0.52 | 29.5 | 15.3 | 98.0 |
| 4 | corner | 42 | 0.52 | 31.5 | 16.38 | 0.55 | 30.2 | 16.6 | 101.4 |
| 5 | middle | 42 | 0.53 | 25.1 | 13.303 | 0.55 | 30.2 | 16.6 | 124.9 |
| 6 | corner | 42 | 0.53 | 30.2 | 16.006 | 0.53 | 25.7 | 13.6 | 85.1 |
| 7 | BROKEN | | | | | | | | |
| 8 | middle | 39 | 0.55 | 26.7 | 14.685 | 0.55 | 25.6 | 14.1 | 95.9 |
| 9 | corner | 39 | 0.52 | 17.5 | 9.1 | 0.53 | 13.9 | 7.4 | 81.0 |
| 10 | corner | 39 | 0.53 | 26.7 | 14.151 | 0.53 | 19.7 | 10.4 | 73.8 |
| 11 | middle | 39 | 0.5 | 16.9 | 8.45 | 0.52 | 14.6 | 7.6 | 89.8 |
| 12 | corner | 39 | 0.53 | 28.2 | 14.946 | 0.52 | 19.4 | 10.1 | 67.5 |

It is observed that the middle cells saw a larger power ratio than the corner cells, indicating a higher light intensity. The average difference between the power ratio observed by the middle cells and the edge cells was 27% for cells 1-6 and 18.8% for cells 7-12. Combined, the middle cells saw a power ratio of 107.75% compared to only 84.89% for the corner cells, a difference of 22.87%. Using data from the simulation to extrapolate the expected difference based on the position of the solar cells, the expected variation would be ~19.5%. The difference between the expected and observed values is relatively close. The small deviation observed is likely due to fabrication defects or non-uniform lighting.

### 9.5.5 Conclusion

The illumination profile along the edge of the LSC module was demonstrated by using COMSOL verified using experimental methods. The difference in illumination demonstrates the need for current matching of cells for large panels that require 3 or more solar cells along each edge for optimal efficiency.

# 10. Appendix B: Additional Information

## 10.1 Light Source

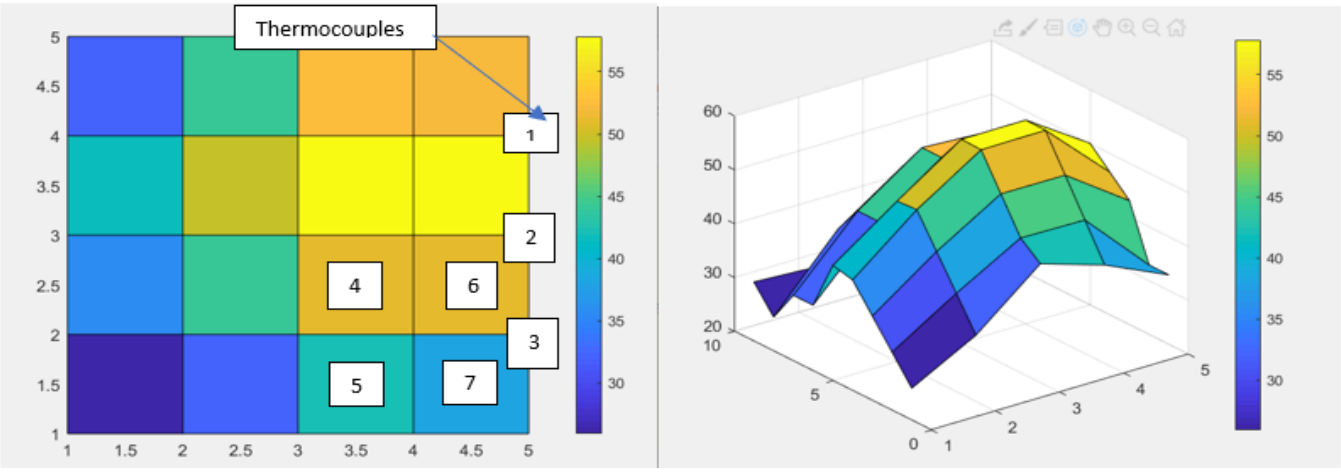


**Figure 10.1**. Measured light intensity across the panel surface under solar lamps (mW/cm$^2$)

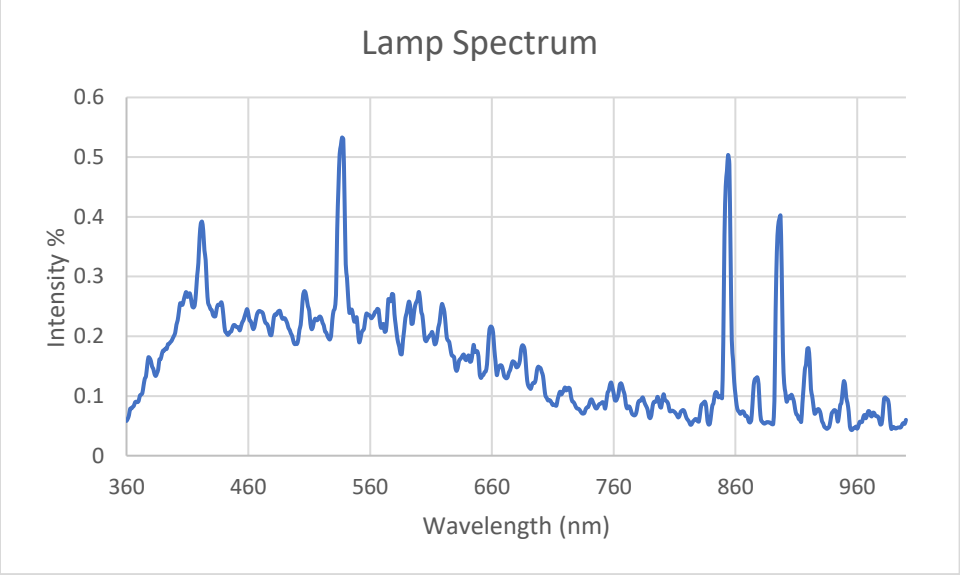


**Figure 10.2.** Spectrum of the Sunmaster 1000W FullNova Solar lamp

It is important to note that the spectrum obtained for the Full Nova Solar lamp only covers the range of 360-1000 nm, whereas the power meter measures all incident light with wavelengths greater than 190 nm. Using the data obtained from the manufacturer, it was found that 50% of the light that is emitted is in the range of 360-1000nm. The dye absorption of the panels to be tested is well within the 360-1000 nm range and thus this level of detail is satisfactory. For the

clear (reference) absorption more detail is required. The transmission spectrum between 300-3300 nm for clear acrylic was obtained from Thorlabs-acrylic substrate transmission [77] and was compared to the measurements taken by the UV-Vis to ensure compatibility. The average absorption of the acrylic between 1000-3300 nm was found to be 61 % and the average weighted absorption using Plank's law for photon energy is 49.5%. These two numbers were averaged to obtain an estimated absorption of 55.5% between 1000-3300 nm. Using the assumption that the remaining 50% of the power emitted by the lamp is evenly distributed through the 1000-3400 nm spectrum, the energy absorbed can be estimated.

## 10.2 Tables and Charts

**Table 10.1**. Observed and calculated power from single panel LSCs with an area of 0.25$m^2$

| | | Red | Blue | Yellow | Green | Orange | Method |
|---|---|---|---|---|---|---|---|
| LSC host thermal losses $P_{dye\text{-}internal\_loss}$ (W) | Theoretical | 7.6 W | 1.6 W | 9.4 W | 6.0 W | 9.5 W | Calculated using raytracer efficiency |
| LSC host thermal losses $P_{dye\text{-}internal\_loss}$ (W) | Experimental | 8.8 W | 1.9 W | 9.6 W | 5.9 W | 12.4 W | Observed |
| LSC host thermal losses $P_{dye\text{-}internal\_loss}$ (W) | Experimental | 8.0 W | 2.3 W | 10.6 W | 6.2 W | 12.5 W | Calculated using measured efficiency |
| Edge Power $P_{edge(LSC)}$- $P_{edge(host)}$ (W) | Theoretical | 5.0 W | 3.1 W | 4.3 W | 3.0 W | 4.6 W | raytracer efficiency |
| Edge Power $P_{edge(LSC)}$- $P_{edge(host)}$ (W) | Experimental | 4.6 W | 2.4 W | 3.1 W | 2.8 W | 1.7 W | measured (Observed) |
| Total thermal Watts ($P_{dye\text{-}internal\_loss}$ + ($P_{edge(LSC)}$- $P_{edge(host)}$) (W) | Theoretical | 12.6 W | 4.7 W | 13.7 W | 9.0 W | 14.1 W | Calculated based on raytracer Efficiency |
| Total thermal Watts ($P_{dye\text{-}internal\_loss}$ + ($P_{edge(LSC)}$- $P_{edge(host)}$) (W) | Experimental | 12.6 W | 4.7 W | 13.7 W | 9.0 W | 14.1 W | Calculated based on measured Efficiency |

| | | | | | | | |
|---|---|---|---|---|---|---|---|
| Total thermal Watts ($P_{dye\text{-}internal\_loss}$ + ($P_{edge(LSC)}$- $P_{edge(host)}$) (W) | Experimental | 13.4 W | 4.3 W | 12.7 W | 8.7 W | 14.1 W | Observed (absorber +acrylic heating) |
| Watts absorbed by Dye ($P_{dye}$) (W) | | 16.3 W | 6.1 W | 17.7 W | 11.6 W | 18.2 W | Using methods from Chapter 2 |
| Escape loss (W) ($P_{dye}$ – Total thermal Watts) | Theoretical | 3.7 | 1.4 | 4.0 | 2.6 | 4.1 | |
| Escape loss (W) ($P_{dye}$ – Total thermal Watts) | Experimental | 2.88 | 1.77 | 4.97 | 2.89 | 4.14 | |
| Escape Loss % (Escape Loss / $P_{dye}$ )% | Theoretical | 25.0% | 25.0% | 25.0% | 25.0% | 25.0% | Accounting for Stokes shift |
| Escape Loss % (Escape Loss / $P_{dye}$ )% | Experimental | 19.7% | 32.4% | 31.3% | 27.7% | 25.2% | Accounting for Stokes shift |
| Edge Efficiency (Edge Power/ $P_{dye}$ )% | Theoretical | 30.5% | 51.43% | 24.4% | 26.0% | 25.4% | Raytracer |
| Edge Efficiency (Edge Power/ $P_{dye}$ )% | Experimental | 28.33% | 39.72% | 17.71% | 24.15% | 9.21% | measured |
| Dye absorption loss | Theoretical | 44.5% | 23.6% | 50.7% | 49.0% | 49.6% | |